

NEW PIGMENTS AND ADDITIVES FOR CORROSION PROTECTION BY ORGANIC COATINGS

EDITED BY: Flavio Deflorian, Michele Fedel and Victoria Johnston Gelling
PUBLISHED IN: *Frontiers in Materials*



frontiers

Frontiers eBook Copyright Statement

The copyright in the text of individual articles in this eBook is the property of their respective authors or their respective institutions or funders. The copyright in graphics and images within each article may be subject to copyright of other parties. In both cases this is subject to a license granted to Frontiers.

The compilation of articles constituting this eBook is the property of Frontiers.

Each article within this eBook, and the eBook itself, are published under the most recent version of the Creative Commons CC-BY licence.

The version current at the date of publication of this eBook is CC-BY 4.0. If the CC-BY licence is updated, the licence granted by Frontiers is automatically updated to the new version.

When exercising any right under the CC-BY licence, Frontiers must be attributed as the original publisher of the article or eBook, as applicable.

Authors have the responsibility of ensuring that any graphics or other materials which are the property of others may be included in the CC-BY licence, but this should be checked before relying on the CC-BY licence to reproduce those materials. Any copyright notices relating to those materials must be complied with.

Copyright and source acknowledgement notices may not be removed and must be displayed in any copy, derivative work or partial copy which includes the elements in question.

All copyright, and all rights therein, are protected by national and international copyright laws. The above represents a summary only. For further information please read Frontiers' Conditions for Website Use and Copyright Statement, and the applicable CC-BY licence.

ISSN 1664-8714

ISBN 978-2-88966-213-5

DOI 10.3389/978-2-88966-213-5

About Frontiers

Frontiers is more than just an open-access publisher of scholarly articles: it is a pioneering approach to the world of academia, radically improving the way scholarly research is managed. The grand vision of Frontiers is a world where all people have an equal opportunity to seek, share and generate knowledge. Frontiers provides immediate and permanent online open access to all its publications, but this alone is not enough to realize our grand goals.

Frontiers Journal Series

The Frontiers Journal Series is a multi-tier and interdisciplinary set of open-access, online journals, promising a paradigm shift from the current review, selection and dissemination processes in academic publishing. All Frontiers journals are driven by researchers for researchers; therefore, they constitute a service to the scholarly community. At the same time, the Frontiers Journal Series operates on a revolutionary invention, the tiered publishing system, initially addressing specific communities of scholars, and gradually climbing up to broader public understanding, thus serving the interests of the lay society, too.

Dedication to Quality

Each Frontiers article is a landmark of the highest quality, thanks to genuinely collaborative interactions between authors and review editors, who include some of the world's best academicians. Research must be certified by peers before entering a stream of knowledge that may eventually reach the public - and shape society; therefore, Frontiers only applies the most rigorous and unbiased reviews. Frontiers revolutionizes research publishing by freely delivering the most outstanding research, evaluated with no bias from both the academic and social point of view. By applying the most advanced information technologies, Frontiers is catapulting scholarly publishing into a new generation.

What are Frontiers Research Topics?

Frontiers Research Topics are very popular trademarks of the Frontiers Journals Series: they are collections of at least ten articles, all centered on a particular subject. With their unique mix of varied contributions from Original Research to Review Articles, Frontiers Research Topics unify the most influential researchers, the latest key findings and historical advances in a hot research area! Find out more on how to host your own Frontiers Research Topic or contribute to one as an author by contacting the Frontiers Editorial Office: researchtopics@frontiersin.org

NEW PIGMENTS AND ADDITIVES FOR CORROSION PROTECTION BY ORGANIC COATINGS

Topic Editors:

Flavio Deflorian, University of Trento, Italy

Michele Fedel, University of Trento, Italy

Victoria Johnston Gelling, Other

Citation: Deflorian, F., Fedel, M., Gelling, V. J., eds. (2020). New Pigments and Additives for Corrosion Protection by Organic Coatings.

Lausanne: Frontiers Media SA. doi: 10.3389/978-2-88966-213-5

Table of Contents

- 04 Editorial: New Pigments and Additives for Corrosion Protection by Organic Coatings**
Flavio Deflorian, Michele Fedel and Victoria Johnston Gelling
- 06 Next-Generation Composite Coating System: Nanocoating**
Weiwei Bao, Zhifeng Deng, Shaodan Zhang, Zhuoting Ji and Haichang Zhang
- 12 Application of Scanning Kelvin Probe in the Study of Protective Paints**
Andrej Nazarov and Dominique Thierry
- 29 Recent Development of Corrosion Protection Strategy Based on Mussel Adhesive Protein**
Fan Zhang and Jinshan Pan
- 36 A Review of Modern Assessment Methods for Metal and Metal-Oxide Based Primers for Substrate Corrosion Protection**
Matthew E. McMahon, Raymond J. Santucci Jr., Carol F. Glover, Balaji Kannan, Zachery R. Walsh and John R. Scully
- 60 Assessment of Self-Healing Epoxy-Based Coatings Containing Microcapsules Applied on Hot Dipped Galvanized Steel**
Evangelia K. Karaxi, Ioannis A. Kartsonakis and Costas A. Charitidis
- 77 Corrosion Assessment of Zn-Rich Epoxy Primers With Carbon Nanotube Additions in an Electrolyte With a Bacteria Consortium**
Homero Castaneda and Monica Galicia
- 89 Epoxy Self-Healing Coating by Encapsulated Epoxy Ester Resin in Poly (Urea-Formaldehyde-Melamine) Microcapsules**
Fernando Cotting, André Koebsch and Idalina Vieira Aoki
- 101 Effects of TiO_2 Nanoparticles on the Overall Performance and Corrosion Protection Ability of Neat Epoxy and PDMS Modified Epoxy Coating Systems**
Ammar Shafaamri, Chiam H. Cheng, Iling A. Wonnice Ma, Shahid B. Baig, Ramesh Kasi, Ramesh Subramaniam and Vengadaesvaran Balakrishnan
- 120 Polypyrrole/Metal Oxides-Based Composites/Nanocomposites for Corrosion Protection**
Niteen Jadhav, Subramanyam Kasisomayajula and Victoria Johnston Gelling
- 127 Protective and Suppressing Electromagnetic Interference Properties of Epoxy Coatings Containing Nano-Sized NiZn Ferrites**
Andrzej Miszczyk



Editorial: New Pigments and Additives for Corrosion Protection by Organic Coatings

Flavio Deflorian^{1*}, Michele Fedel¹ and Victoria Johnston Gelling²

¹ Department of Industrial Engineering, University of Trento, Trento, Italy, ² Department of Coatings and Polymeric Materials, North Dakota State University, Fargo, ND, United States

Keywords: organic coatings, corrosion protection, pigments, nanotechnology, environmentally friendly

Editorial on the Research Topic

New Pigments and Additives for Corrosion Protection by Organic Coatings

Corrosion protection of over- and under-ground structures as well as industrial products by protective coatings is one of the most widely employed methods. The durability of the protective coatings is commonly prolonged thanks to the addition of pigments or specific compounds which are able to provide the substrate with improved corrosion protection. During the past 20 years, the field of corrosion protection science and technology has developed, produced, and tested a variety of novel pigments and compounds whose full potential as well as their long-term efficiency are as yet unknown. Pigments in paints are not only added to improve the barrier properties but they can be designed also to provide passivation, galvanic protection, pH buffering, or self-healing of the polymeric matrix. Corrosion inhibition can be achieved by adding to the polymeric matrix partially soluble pigments or stimuli sensitive reservoir of chemical species in which the leakage depends on an electrochemical or chemical trigger. Along with the development of modern paints, technologists have been also focused on new pigments for the development of the so called “smart coatings.” These new coatings are to address the environmental concerns related to traditional pigments and compounds (such as chromates and phosphates), to provide self-healing and to improve the longevity of the coatings. This objective can be accomplished by combining the polymeric phase with innovative pigments/compounds with tailored properties. In this frame, there is a significant ongoing research seeking to improve the functionality of protective pigmented organic layers often employing a nanotechnology based approach.

This special issue of the Frontiers in Materials—section Environmental Materials—is motivated by the need to update the state-of-the-art in the development of completely new pigments for corrosion protection and to establish a milestone by taking a snapshot of the efficiency of the current cutting-edge solutions.

The ten papers in this collection give an in-depth picture of the state of the art and future developments in the field of new pigments and additives for corrosion protection by organic coatings, coming from research groups from around the world engaged in research in this area. Two articles in particular are interesting as they present an accurate review of the new generation of nano-composites for corrosion protection (Bao et al.) and on methods of assessment of protective performance in this field (McMahon et al.). In fact, it is important to emphasize that innovation in this area, on one side, involves the development of new materials, but also needs accurate and scientifically rigorous evaluation and verification methods to predict their behavior in the field. Still considering the methods of investigation, the article by Nazarov et al. provides an focus on the use of one of the most powerful electrochemical techniques in this area, namely the use of the Scanning Kelvin Probe.

OPEN ACCESS

Edited and reviewed by:

Changdong Gu,
Zhejiang University, China

*Correspondence:

Flavio Deflorian
flavio.deflorian@unitn.it

Specialty section:

This article was submitted to
Environmental Materials,
a section of the journal
Frontiers in Materials

Received: 14 September 2020

Accepted: 22 September 2020

Published: 13 October 2020

Citation:

Deflorian F, Fedel M and Gelling VJ
(2020) Editorial: New Pigments and
Additives for Corrosion Protection by
Organic Coatings.
Front. Mater. 7:606256.
doi: 10.3389/fmats.2020.606256

The other articles are more focused on the development of new protective systems based on organic coatings with new pigments, where nanotechnologies already play a fundamental role, and will be even more relevant in the future.

One of the most advanced technology for corrosion protection by coatings is the use of microcapsules, with inhibitors inside, able to stop the corrosion and having a self-healing capability or containing chemical compounds polymerizing and repairing the scratches. A first example of a protective system based on microcapsules containing chemical compounds with inhibitory action is the paper by Karaxi et al.

The paper of Cotting et al. represents a study that develops a new coating with self-healing capacity thanks to the chemical properties of microcapsules that polymerize in the event of damage to the coating itself.

Inorganic pigments, which are traditionally used in organic coatings, are showing relevant developments in particular at nano-scale, giving a relevant contribution to innovation in this area, as shown in the case titania nanopigments in the paper of Shafaamri et al. Also conductive polymers, extensively studied in the last decade to develop new composite coatings for corrosion protection, are promising materials as demonstrated in the paper by Jadhav et al.

One of the more effective driving forces for innovation in pigments for organic coatings for corrosion protection are the environmental issues associated with most of the corrosion inhibitors currently used in industry. Several pigments used in the past have a significant impact on the environment and human health and must be substituted. A way to find new environmentally friendly products is to give a look to the natural biological products and use it as additives in coatings. This is the approach of the paper of Zhang et al., using mussel proteins as effective additives in organic coatings.

A further, very relevant, field of innovation is the development of multifunctional coatings. The concept can be considered from different points of view. In some cases, multifunctional coatings

can be considered materials using more than one strategy for improving corrosion protection. An example is the paper of Castaneda et al., where both Zn particles and nanotubes are employed in organic coatings to reduce the risk of microbiologically induce corrosion. Moreover, the traditional, and still essential, function of the pigments, to contribute to the corrosion protection action of the organic coatings, is sometime combined with new technological functions. An example of this new trend in multifunctional coatings is the paper of Miszczyk where nano-sized ferrites are studied to improve coating durability, but also to act as microwave absorber.

This collection of works represents an important opportunity to provide an updated view of innovation in the sector of new pigments and additives for corrosion protection with organic coatings. This overview is considering both the point of view of new materials and of investigation techniques and evaluation, highlighting how nanotechnologies on the one hand, and multifunctionality on the other, are the keywords for a future where coatings for corrosion protection will improve our quality of life while taking care of the environment.

AUTHOR CONTRIBUTIONS

All authors contributed equally to the Editorial.

Conflict of Interest: The authors declare that the research was conducted in the absence of any commercial or financial relationships that could be construed as a potential conflict of interest.

Copyright © 2020 Deflorian, Fedel and Gelling. This is an open-access article distributed under the terms of the Creative Commons Attribution License (CC BY). The use, distribution or reproduction in other forums is permitted, provided the original author(s) and the copyright owner(s) are credited and that the original publication in this journal is cited, in accordance with accepted academic practice. No use, distribution or reproduction is permitted which does not comply with these terms.



Next-Generation Composite Coating System: Nanocoating

Weiwei Bao, Zhifeng Deng, Shaodan Zhang, Zhuoting Ji and Haichang Zhang*

School of Materials Science and Engineering, Shaanxi University of Technology, Hanzhong, China

Nanocoating combines the protective properties of conventional coating system with effects on nanoscale such as high hardness, UV scattering, and uniform dispersing. Their facile and low-cost synthesis, together with superior protective properties and multi-functionalities, makes nanocoating attractive candidates for next-generation coating systems. In this review, a brief introduction regarding mainstream nanocoating and its related challenges including the zinc oxide-, titanium dioxide-, silica dioxide-, graphene-, carbon nanotube-based nanocoating system is presented. Finally, a perspective of the nanocoating is demonstrated.

Keywords: corrosion resistance, protection, nanocoating, nanoparticle, coating system

OPEN ACCESS

Edited by:

Flavio Defforian,
University of Trento, Italy

Reviewed by:

Changdong Gu,
Zhejiang University, China
Santiago Fajardo,
Centro Nacional De Investigaciones
Metalurgicas (CENIM), Spain

*Correspondence:

Haichang Zhang
haichangzhang@hotmail.com

Specialty section:

This article was submitted to
Environmental Materials,
a section of the journal
Frontiers in Materials

Received: 25 February 2019

Accepted: 01 April 2019

Published: 17 April 2019

Citation:

Bao W, Deng Z, Zhang S, Ji Z and
Zhang H (2019) Next-Generation
Composite Coating System:
Nanocoating. *Front. Mater.* 6:72.
doi: 10.3389/fmats.2019.00072

INTRODUCTION

Nanocoating is defined as having either the thickness of the coating or the second phase particles that are dispersed into the matrix in the nanosized range, which is a trend in the application of nanotechnology for the prevention and control of corrosion. This technology is growing rapidly in the field of corrosion protection and wear resistance of steel substrate materials compared to conventional coating (Bugnicourt et al., 2016). Conventional coating, organic, or inorganic coating, have been widely applied for the protection of metals against corrosion, which has made significant progress in recent years. However, despite significant improvements in coating technologies, problems continue in the long-term protection of metal from aggressive environments (Sørensen et al., 2009). For the purpose of addressing this issue, the introduction of nanoparticles, nanocomposites, or nanocontainers in the coating formulation has been developed to enhance the wear resistance, shock, or pressure resistance and improve thermal conductivity of offshore structures, vessels, and drilling equipment (Müller et al., 2017). In addition, nanomaterials in the coating system can enable coating with superhydrophobic performance which endows the nanocoating with multi-functionalities such as anti-corrosions, anti-icing, and anti-fogging etc., (Das et al., 2018). Since nanocoating equips the substrate with special functions, the key results of nanocoating are summarized in several good reviews (Bugnicourt et al., 2016; Müller et al., 2017; Das et al., 2018). However, a comprehensive overview of nanocoating, with special emphasis on the distinct nano-pigment systems and their challenges, has not been yet thoroughly covered by the recent report.

In this review, we will briefly introduce mainstream nanocoating, its related challenges and applications including the zinc oxide (ZnO)-, titanium dioxide (TiO₂)-, silica dioxide (SiO₂)-, graphene-, and carbon nanotube (CNT)-based nanocoating system. Finally, our perspective on the potential further development trends for the next generation nanocoating is provided.

DISTINCT NANOCOATING SYSTEM

ZnO-Based Nanocoating

Nanocoating systems provide corrosion protection of metallic substrates via barrier effect, inhibitive effect, or anodically active metal effect (galvanic effect) (Müller et al., 2017). The Zn-based nanocoating protective mechanism belongs to one of the galvanic effects, in which it sacrificially corrodes by the oxygen and moisture from the coating surface and forms a corrosion product such as ZnO. This corrosion product provides protection similar to a barrier effect. Recently, Ramezanza et al. reported different proportion of ZnO nanoparticles (0, 2, 3.5, 5, and 6.5 wt%) into the epoxy-polyamide coating (Ramezanzadeh et al., 2011). The studies showed that the physical interaction between the nanoparticles and coatings resulted in improved resistance against hydrolytic degradation in comparison with the blank epoxy coating. In addition, introducing ZnO-nanoparticles into the coating system could increase the coating curing degree resulting in the ZnO-based nanocoating with lower curing enthalpy. When adding the ZnO nanoparticles, the barrier properties of the coating has been significantly improved due to the increasing crosslinking density of the coating and the formation of corrosion product. The nanocoating with the best barrier properties was observed with ZnO composite of 3.5%. Once the ZnO nanoparticles were increased above 3.5% volume concentration, the barrier properties, typically the corrosion resistance, was decreased due to the weakened crosslinking density and the high loading aggregations. Another reason might be that the amount of resin was insufficient to wet all the pigments; therefore, the coating did not form a continuous film, which resulted in extensive defects throughout the coating. When constructing ZnO-based nanocoating, the size of ZnO particles considerably affects the nanocoating anticorrosion properties. ZnO particles with 20 nm in the polyurethane coatings showed better protective performance than that of the ones with 400 nm (Yang et al., 2005). This could be explained by the fact that small size particles have greater surface activity, such as borders and corners, which can absorb more resin on their surfaces.

Except enhancing the anticorrosion properties, nano-ZnO in the coating could also improve its UV resistance. When exposing alkyd-based water borne coating under UV-radiation for 110 h, there were several cracks and pinholes on the surface, while for the ZnO-based nanocoating under the same condition, no cracks were observed (Dhoke et al., 2009). Nano-ZnO particles, typically between 20 and 40 nm, could scatter UV radiation between 200 and 400 nm, thereby providing good UV blocking property to the coating system without interacting with the UV radiation. It should be noticed that the size of the nanoparticles plays a key role in enhancing the UV resistance.

The oxygen and water were the main reasons that caused the metal materials to corrode. Thus, the development of superhydrophobic coating, which has nearly non-wetting results with easy rolling of water droplets from the surface, is of utmost important. Superhydrophobic coating with water contact angle (WCA) $>150^\circ$ and sliding angle (SA) $<10^\circ$ are often difficult to be obtained. Introducing modified nano-ZnO particles into the coating is a simple and inexpensive

approach to obtain superhydrophobic coating (Das et al., 2018). Traditionally pure nano-ZnO are hydrophilic due to many hydroxyl groups existing on its surface (Qing et al., 2015). Modification the nano-ZnO particles with stearic acid obtaining hydrophobic nano-ZnO was reported by Qing et al. (2015). Using the modified nano-ZnO particles to construct fluorinated polysiloxane (FPDHS) nano-ZnO nanocoating showed superhydrophobicity with WCA as high as 166° (Figure 1a), while the pure FPDHS coating exhibited hydrophobicity with WCA of only 143° . Recently, various approaches to develop superhydrophobic ZnO-based nanocoating have been reported, such as using polydimethylsiloxane, hexadecyltrimethoxysilane, and aminopropyltriethoxysilane etc., (Wu et al., 2005; Chakradhar et al., 2011; Li et al., 2015; Velayi and Norouzebeigi, 2018). Appropriate modification ZnO-nanoparticles can not only enhance the coating hydrophobicity, but also increase its corrosion resistance, for instance the corrosion rate of modified ZnO-based nanocoating showed 11-fold decrease compared to the pure coating. When constructing superhydrophobic nanocoating, it should be noticed that the coating superhydrophobic improved with the increase in surface roughness, meanwhile introducing small size and appropriate amount of nanoparticles is quite important for forming high surface roughness.

SiO₂-Based Nanocoating

Silicon dioxide, one of the most complex and most abundant families of materials, exists as a synthetic product and as a compound of several minerals. The first commercial-grade surface-modified silica nanoparticles were produced into market in 2002, which were introduced into the epoxy resin by a modified sol-gel process and had a very narrow particle size distribution (Sprenger, 2013). Many metal-O-Si bonds were generated on the surface of substrate, which provided not only the supplement of the good physical barrier effect, but also the improvement of adhesion force between coating and substrate. Silica with inherent strong hardness and resistance against chemicals and alteration characteristics allow the nano-SiO₂ particles in coatings to improve various properties such as modulus, stiffness, toughness, scratch resistance, and anti-corrosions. Conradi et al. presented a 0.5 kg load on the surface of the pure epoxy and 130 nm SiO₂/epoxy coating, separately, which showed the indents in the epoxy coating were significantly large compared to those in the SiO₂/epoxy coating, and the hardness was enhanced by almost 40% (Conradi et al., 2013). Improvement of the Vickers hardness could be due to the strong hardness of Nano-SiO₂ into the coatings considerably affected the morphology, the area roughness parameters S_a from 16 to 329 nm. This further influenced the surface hydrophobicity with the WCA from 84.6° to 94.2° . The hydrophobicity affected by the surface roughness could be due to trapped air between the surface and the water droplet, which can minimize the contact area by creating micro/nano structures. Improved hydrophobicity resulted in the nano-SiO₂/epoxy coating with enhanced anti-corrosion effect.

As discussed in section ZnO-Based nanocoating, coating hydrophobicity plays a key role in the anti-corrosion, hence

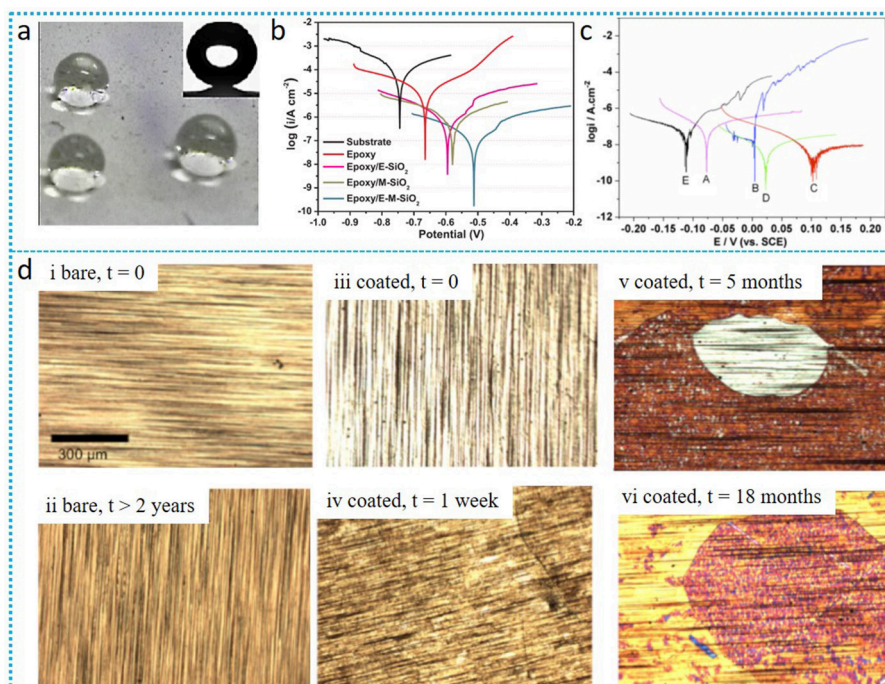


FIGURE 1 | (a) Image of water droplets on the modified-ZnO/FPDHS superhydrophobic surface (Qing et al., 2015); (b) The polarization curves of bare substrate and all coating system based on SiO₂-nanocoating after the immersion of 80 days (Ye et al., 2018); (c) polarization curves for pure TiO₂/316L (A), Cl-TiO₂/316L (B), N-TiO₂/316L (C), S-TiO₂/316L (D) and bare 316L coating (E) in 0.5 M NaCl solution (Yun et al., 2007); (d) image of graphene-covered Cu and bare Cu in ambient condition (Schrivier et al., 2013).

modification nano-SiO₂, resulting in the nanocoating with superhydrophobicity and improvement compatibility can significantly increase the nanocoating corrosion resistance. Very recently, Ye and colleagues compared the performance of different nano-SiO₂ based coating systems such as electrodeposited oligoaniline modified silica/epoxy coating (E-M-SiO₂) and electrodeposited pure silica coating/epoxy (E-SiO₂). The E-M-SiO₂ coating exhibited superhydrophobicity with WCA of 167°, while E-SiO₂ exhibited hydrophobicity with WCA of 143.5° (Ye et al., 2018). Superhydrophobicity could available inhibit the diffusion of corrosive medium, hence E-M-SiO₂ coating showed better corrosion protection compared to E-SiO₂. The author also compared the performance between E-M-SiO₂ with sol-gel oligoaniline modified silica/epoxy coating (M-SiO₂), in which the E-M-SiO₂ showed better hydrophobicity and corrosion protection performance (Figure 1b). This could be due to most silica coating obtained by sol-gel approach with low surface roughness, which seriously restricts the thickness of coating, thereby the physical barrier of pre-process coating was weak.

For conventional coating, there is no protective effect once it is damaged, protection only lasts for the first damage. Self-healing coatings, possessing the internal capability to repair sustained damage by themselves or with some outside stimulation, is in the trend due to its providing feedback active healing ability to a scratch on metal surfaces for long term protection. Introducing self-healing microcapsules,

such as perfluorooctyl triethoxysilane-urea-formaldehyde (POT-UF) shell, ethanolamine-polystyrene (ETA-PS) shell or diethanolamine-polystyrene (DEA-PS) shell, into the modified nano-silica/epoxy nanocoating and enhancing the coating anti-corrosion performance was reported by Kongparakul's group (Kongparakul et al., 2017). Among all the three systems, the POT-UF shell microcapsules performed the best corrosion prevention due to the increased length of the diffusion pathways, as well as decreased the oxygen permeability of the coating. Other approaches, such as using nanocontainers, self-healing additive, layer-by layer deposition, etc. could also obtain self-healing nanocoating (Shchukin et al., 2006; Li et al., 2013). Hydrophobic coating is unstable and easy to lose its ability to resist water (Zhang et al., 2006). Hence, self-healing coating combined with superhydrophilicity behavior are promising due to its long-term protection properties.

TiO₂-Based Nanocoating

Titanium dioxide, one of the most commonly occurring oxides of titanium, received a lot of attention due to its easily available, relatively inexpensive, chemical stability, and harmless nature which was widely applied in several fields such as paints, coatings, inks etc. (Munafò et al., 2015). Introducing nano-TiO₂ into coating systems can lead the nanocoating with improvement protection and can even endow it with self-cleaning properties. Shen et al. reported that covering a uniform TiO₂ nanoparticles films on the surface of 316L stainless steel could sufficiently

improve its corrosion resistance properties, the corrosion resistance increasing over three order of magnitudes (Shen et al., 2005). The protection mechanism of TiO₂-based nanocoating is that electron and hole are generated in the coating once exposing nano-TiO₂ to UV-irradiation, in which the electrons transferred to the metal substrate thereby making its electrode potential more negative than its corrosion potential, meanwhile, TiO₂ does not get consumed. Nano-TiO₂-based coating is promising to protect metal with anti-corrosion. However, the protection mechanism suggests that pure TiO₂ nanocoating cannot be used under dark conditions due to the photo effect. In addition, once small defects appear in the nanocoating, these nanocoating are no longer able to protect the exposed zone, which means the nanocoating works only until their surface is intact. Numbers of works attempt to address this issue through the modification nano-TiO₂ coatings such as noble metal deposition, doping of metallic and non-metallic ions, etc. (Hoffmann et al., 1995; Park and Choi, 2004). Yun and colleagues reported TiO₂-nanocoating without photo-effect using doped TiO₂ with N, S, and Cl (Yun et al., 2007). Electrochemical polarization was conducted in 0.5 M NaCl solution under dark conditions for the different coating systems. Comparing this to the bare 316L, the pure TiO₂-nanocoating slightly improved the corrosion-resistance, while the corrosion-resistance performance for the dopant-modified TiO₂ coating was significantly enhanced. This could be due to the eliminating photo effect of the modified nano-TiO₂ coating (**Figure 1c**). Other research regarding modification nano-TiO₂ particles improving the nanocoating corrosion resistance has also been reported, such as polypyrrole/Sn-doped TiO₂, thermal oxidation, introducing polyaniline in the coating system etc. (Krishna and Sun, 2005; Radhakrishnan et al., 2009; Mahmoudian et al., 2011).

TiO₂ is normally hydrophobic. However, once it is exposed under UV-illumination, it becomes both oleophilic and hydrophilic, which will decrease the organic liquid angle or WCA until there is almost complete flattening of organic liquids or water droplets on the surface. This property prevents the external dirty directly contacting the coating surface and allowing an easier removal of stain. Based on this performance, TiO₂-based nanocoating as self-cleaning effect coating was widely used, such as on glass, stone, and photovoltaic module (Munafò et al., 2015). A single-layer (SL) and three-layer (ML) treatment nanocoating were obtained through spraying the nano-TiO₂ product directly on the stone surface with different amounts obtained (Goffredo et al., 2013). Under UV illumination, there was no significant degradation of stains on untreated surfaces, while the photocatalytic degradation of the strain was very rapid for the SL and ML coating, the rhodamine B losing almost 50% of its original color after 4 h. TiO₂-based nanocoating are transparent, hence it can be applied directly on architectural surface for protection without altering their original aspect. Numbers of works on the TiO₂ nanoparticles into different coating systems for optimizing its self-cleaning performance have been reported (Kaplani et al., 2015; Crupi et al., 2018). However, the analyses carried on the TiO₂ self-cleaning efficiency up to now still lack a more complete approach. The system studied on the relationship between the self-cleaning and the size or amount of nano-TiO₂, the further optimization of the

nano-TiO₂ particles and extending the lifepath of the coating are still a challenge.

Carbon (Graphene and Carbon Nanotube)-Based Nanocoating

Nanoscale carbon, graphene and CNT, are potential useful applications as nanocoating in materials protection due to its inherent characters, such as the high stiffness and conductivity capacity (Hu et al., 2014). Chen et al. first time successfully used as-grown graphen to protect the surface of metallic growth substrate of Cu or Cu/Ni alloy away from air oxidation (Chen et al., 2011). The covered graphene resulted in a passivation of metal underneath, which offered an inserted block between the reactants and the protected metal. Except the oxidation resistance, graphene-based nanocoating could also effectively extend materials thermal stability and corrosion-resistance. Kwon et al. used graphene and metal-chloride-doped graphene over layers on 25 um thick copper foil, in which the chlorine evaporation was almost blocked, and maintained the doped state even after thermal annealing (Kwon and Kim, 2014). Yu and co-workers introduced graphene, typically metronidazole modified graphene oxide, on the metal surface which exhibited better corrosion resistance than the bare metal (Yu et al., 2016).

It should be noticed that graphene offers an impressive oxidation barrier for the short-term, however, for long-term scales, graphene promoted the metal corrosion instead of preventing it. Schriver et al. compared the sample surfaces between bare Cu and graphene-coated Cu under ambient conditions for up to 2 years (Schriver et al., 2013). The results showed that slight color changing happened for the bare Cu after 2 years. For the graphene-protected Cu, it was shiny and free of oxide within 1 week. However, the surface started to tarnish non-uniformly with small patches after 1 month, which gradually caused high oxide after 5 months. Finally heavy oxidization on virtually all of the surface was observed at 18 months (**Figure 1d**). Non-uniform oxidation or defects of graphene will lead to stress and cracking of the oxidation layer, which often opens a new avenue for corrosion. In addition, the monolayer graphene often exhibited wetting transparency (Hu et al., 2014). These characteristics result in monolayer graphene with bad protection properties. To address this issue, multi-layered graphene or nanocomposite such as mixture with epoxy were used, which showed good protective performance (Rafiee et al., 2012; Tang et al., 2013). Yang et al. studied epoxy coating on a copper substrate modified by fluorographene nanosheet, which showed superhydrophobicity with WCA up to 154° (Yang et al., 2017). The superhydrophobicity characteristic of this nanocoating was ascribed to the irregular microstructure constructed by randomly stacked fluorographene.

CNT, allotropes of graphene, was used in coating effect protection performance typically on the anti-oxidation and corrosion resistance. Recent studies showed the CNT-based nanocoating exhibited similar protection performance as graphene-based nanocoating (Janas and Koziol, 2013). In many cases, the CNT not only acts as a physical barrier to the corrosion

process, but also improves the electrochemical properties to anti-oxidation (Ates, 2016). Epoxy composite coatings filled with different multiwalled CNT contents was reported by Frankel's group, which indicated that multiwalled CNT can influence the coating performance such as improvement adhesion strength, increasing wear resistance and the total impedance enhancement (Khun et al., 2013). Nanocoating containing modified CNT composite should be in the trend.

CONCLUSION AND PERSPECTIVES

The ever-growing interest in nanocoating and its fascinating protective properties makes it a promising candidates for next-generation protecting system. In this review, we have given an overview of the recently popular composite nanocoating system based on ZnO, SiO₂, TiO₂, grapheme, and CNT. On the basis of the literature findings above, it is noticeable that introducing the modified-nanoparticles into the conventional coating system could significantly improve the coating protective characters, typically the corrosion-, UV-, and oxidation-resistance performance, and even self-cleaning functionality. However, the amount of introduced nanoparticles should be proper, otherwise, it will reduce the protective properties. When using a carbon-based nanocoating system, it should be the CNT or graphene modification, or compositing it with other coating systems to extend its corrosion resistance.

REFERENCES

- Ates, M. (2016). A review on conducting polymer coatings for corrosion protection. *J. Adhes. Sci. Technol.* 30, 1510–1536. doi: 10.1080/01694243.2016.1150662
- Bugnicourt, E., Kehoe, T., Latorre, M., Serrano, C., Philippe, S., and Schmid, M. (2016). Recent prospects in the inline monitoring of nanocomposites and nanocoating by optical technologies. *Nanomaterials* 6:150. doi: 10.3390/nano6080150
- Chakradhar, R. P. S., Kumar, V., Dinesh, R. J. L., and Basu, B. J. (2011). Fabrication of superhydrophobic surfaces based on ZnO-PDMS nanocomposite coatings and study of its wetting behavior. *Appl. Surf. Sci.* 257, 8569–8575. doi: 10.1016/j.apsusc.2011.05.016
- Chen, S., Brown, L., Levendorf, M., Cai, W., Ju, S. Y., Edgeworth, J., et al. (2011). Oxidation resistance of graphene-coated Cu and Cu/Ni alloy. *ACS Nano* 5, 1321–1327. doi: 10.1021/nn103028d
- Conradi, M., Kocijan, A., Kek-Merl, D., Zorko, M., and Verpoest, I. (2013). Mechanical and anticorrosion properties of nanosilica-filled epoxy-resin composite coatings. *Appl. Surf. Sci.* 292, 423–437. doi: 10.1016/j.apsusc.2013.11.155
- Crupi, V., Fazio, B., Gessini, A., Kis, Z., Russa, M. F. L., Majolino, D., et al. (2018). TiO₂-SiO₂-PDMS nanocomposite coating with self-cleaning effect for stone material: finding the optimal amount of TiO₂. *Constr. Build. Mater.* 166, 464–471. doi: 10.1016/j.conbuildmat.2018.01.172
- Das, S., Kumar, S., Samal, S. K., Mohanty, S., and Nayak, S. K. (2018). A review on superhydrophobic polymer nanocoatings: recent development and applications. *Ind. Eng. Chem. Res.* 57, 2727–2745. doi: 10.1021/acs.iecr.7b04887
- Dhoke, S. K., Khanna, A. S., and Sinha, T. J. M. (2009). Effect of nano-ZnO particles on the corrosion behavior of alkyd-based waterborne coatings. *Prog. Org. Coat.* 64, 371–382. doi: 10.1016/j.porgcoat.2008.07.023
- Goffredo, G. B., Quagliarini, E., Bondioli, F., and Munaf, Ò. (2013). TiO₂ nanocoatings for architectural heritage: self-cleaning treatments on historical stone surfaces. *Proc. Int. Mech. E Part N: J. Nanoeng. Nanosyst.* 228, 1–9. doi: 10.1177/1740349913506421
- Hoffmann, M. R., Martin, S. T., Choi, W., and Bahnemann, D. W. (1995). Environmental applications of semiconductor photocatalysis. *Chem. Rev.* 95, 69–96. doi: 10.1021/cr00033a004
- Hu, J., Ji, Y., Shi, Y., Hui, F., Duan, H., and Lanza, M. (2014). A review on the use of graphene as a protective coating against corrosion. *Annu. Mater. Sci. Eng.* 1:16.
- Janas, D., and Koziol, K. K. (2013). A review of production methods of carbon nanotube and graphene thin films for electrothermal applications. *Nanoscale* 6, 3037–3045. doi: 10.1039/c3nr05636h
- Kaplani, K., Panayiotatos, Y., and Kaldellis, J. K. (2015). "TiO₂-based nanocoating with self-cleaning and anti-reflective properties: effects on PV performance," in *Photovoltaic Technical Conference-Advanced Materials and Processes to Innovative Applications*, 2015-05-27–2015-05-29.
- Khun, N. W., Troconis, B. C. R., and Frankel, G. S. (2013). Effects of carbon nanotube content on adhesion strength and wear and corrosion resistance of epoxy composite coatings on AA2024-T3. *Prog. Org. Coat.* 77, 72–80. doi: 10.1016/j.porgcoat.2013.08.003
- Kongparakul, S., Kornprasert, S., Suriya, P., Le, D., Samart, C., Chantarasiri, N. C., et al. (2017). Self-healing hybrid nanocomposite anticorrosive coating from epoxy/modified nanosilica/perfluorooctyl triethoxysilane. *Prog. Org. Coat.* 104, 173–179. doi: 10.1016/j.porgcoat.2016.12.020
- Krishna, D. S. R., and Sun, Y. (2005). Thermally oxidised rutile-TiO₂ coating on stainless steel for tribological properties and corrosion resistance enhancement. *Appl. Surf. Sci.* 252, 1107–1116. doi: 10.1016/j.apsusc.2005.02.046
- Kwon, K. C., and Kim, S. Y. (2014). Extended thermal stability in metal-chloride doped graphene using graphene overlayers. *Chem. Eng. J.* 244, 355–363. doi: 10.1016/j.cej.2014.01.100

Nanocoating with a wide branch of genuine properties has been intelligently used by the scientific community and industries. The future research on this field should be focus on further improving its protecting properties combined with multi-functionalities, such as self-cleaning, self-healing, UV-resistance, antibacterial, thermal resistance, color-changing in one single nanocoating. In addition, studies on the relationship between minimization of the size, optimization of the modification and the amount, uniform dispersion of the nanoparticles and the nanocoating performance are important, and finally development of a new nanocoating system. Furthermore, introducing organic nano-pigment or multi-different pigments into one coating system to enhance the coating properties is a growing trend.

AUTHOR CONTRIBUTIONS

All authors listed have made a substantial, direct and intellectual contribution to the work, and approved it for publication.

FUNDING

The authors acknowledge the support from the Natural Science Foundation of China, under Grant 21805151, the Natural Science Foundation of Shandong Province, China, under Grant ZR2018MB024, and Special Scientific Research Planned Projects of Education Department of Shaanxi Province (No. 17JK0161).

- Li, G. L., Zheng, Z., Möhwalk, H., and Shchukin, D. G. (2013). Silica/polymer double-walled hybrid nanotubes: synthesis and application as stimuli-responsive nanocontainers in self-healing coatings. *ACS Nano* 7, 2470–2478. doi: 10.1021/nn305814q
- Li, S., Sun, Z., Li, R., Dong, M., Zhang, L. Q., W. et al. (2015). ZnO nanocomposites modified by hydrophobic and hydrophilic silanes with dramatically enhanced tunable fluorescence and aqueous ultrastability toward biological imaging applications. *Sci. Rep.* 5:8475. doi: 10.1038/srep08475
- Mahmoudian, M. R., Basirun, W., Alias J., and Ebadi, Y. (2011). Synthesis and characterization of polypyrrole/Sn-doped TiO₂ nanocomposites (NCs) as a protective pigment. *Appl. Surf. Sci.* 257, 8317–8325. doi: 10.1016/j.apsusc.2011.03.075
- Müller, K., Bugnicourt, E., Latorre, M., Jorda, M., Sanz, Y. E., Lagaron, J. M., et al. (2017). Review on the processing and properties of nanocomposites and nanocoating and their applications in the packing, automotive and solar energy fields. *Nanomaterials* 7:74. doi: 10.3390/nano7040074
- Munafò, P., Goffredo, G. B., and Quagliarini, E. (2015). TiO₂-based nanocoatings for preserving architectural stone surfaces: an overview. *Constr. Build. Mater.* 84, 201–218. doi: 10.1016/j.conbuildmat.2015.02.083
- Park, J. S., and Choi, W. (2004). Enhanced remote photocatalytic oxidation of surface-fluorinated TiO₂. *Langmuir* 20, 11523–11527. doi: 10.1021/la048051n
- Qing, Y., Yang, C., Hu, C., Zheng, Y., and Liu, C. (2015). A facile method to prepare superhydrophobic fluorinated polysiloxane/ZnO nanocomposite coatings with corrosion resistance. *Appl. Surf. Sci.* 326, 48–54. doi: 10.1016/j.apsusc.2014.11.100
- Radhakrishnan, S., Siju, S. R., Mahanta, D., Patil, S., and Madras, G. (2009). Conducting polyaniline-nano-TiO₂ composites for smart corrosion resistant coatings. *Electrochim. Acta* 54, 1249–1254. doi: 10.1016/j.electacta.2008.08.069
- Rafiee, J., Gullapalli, H., Thomas, A. V., Yavari, F., Shi, Y., Ajayan, P. M., et al. (2012). Wetting transparency of graphene. *Nat. Mater.* 11, 217–222. doi: 10.1038/nmat3228
- Ramezanzadeh, B., Attar, M. M., and Farzam, M. (2011). A study on the anticorrosion performance of the epoxy-polyamide nanocomposites coating ZnO nanoparticles. *Prog. Org. Coat.* 72, 410–422. doi: 10.1016/j.porgcoat.2011.05.014
- Schrivver, M., Regan, W., Gannett, W. J., Zaniewski, A. M., Crommie, M. F., and Zetti, A. (2013). Graphene as a long-term metal oxidation barrier: worse than nothing. *ACS Nano* 7, 5673–5678. doi: 10.1021/nn4014356
- Shchukin, D. G., Zheludkevich, M., Yasakau, K., Lamaka, S., Ferreira, M. G. S., and Möhwalk, H. (2006). Layer-by-layer assembled nanocontainers for self-healing corrosion protection. *Adv. Mater.* 18, 1672–1678. doi: 10.1002/adma.200502053
- Shen, G. X., Chen, Y. C., and Lin, C. J. (2005). Corrosion protection of 316 L stainless steel by a TiO₂ nanoparticle coating prepared by sol-gel method. *Thin Solid Films* 489, 130–136. doi: 10.1016/j.tsf.2005.05.016
- Sørensen, P., Kill, S., Johansen, D. K., and Weinell, C. (2009). Anticorrosive coating: a review. *J. Coat. Technol. Res* 6, 135–176. doi: 10.1007/s11998-008-9144-2
- Sprenger, S. (2013). Epoxy resin composites with surface-modified silicon dioxide nanoparticles: a review. *J. Appl. Polym. Sci.* 130, 1421–1428. doi: 10.1002/app.39208
- Tang, L. C., Wan, Y. J., Yan, D., Pei, Y. B., Zhao, L., Li, Y. B., et al. (2013). The effect of graphene dispersion on the mechanical properties of graphene/epoxy composites. *Carbon* 60, 13–27. doi: 10.1016/j.carbon.2013.03.050
- Velayi, E., and Norouzebeigi, R. (2018). Annealing temperature dependent reversible wettability switching of micro/nano structured ZnO superhydrophobic surfaces. *Appl. Surf. Sci.* 441, 156–164. doi: 10.1016/j.apsusc.2018.02.005
- Wu, X., Zheng, L., and Wu, D. (2005). Fabrication of superhydrophobic surfaces from microstructured ZnO-based surface via wet-chemical route. *Langmuir* 21, 2665–2667. doi: 10.1021/la050275y
- Yang, L. H., Liu, F. C., and Han, E. H. (2005). Effects of P/B on the properties of anticorrosive coating with different particle size. *Prog. Org. Coat.* 53, 91–98. doi: 10.1016/j.porgcoat.2005.01.003
- Yang, Z., Wang, L., Sun, W., Li, S., Zhu, T., Liu, W., et al. (2017). Superhydrophobic epoxy coating modified by fluorographene used for anti-corrosion and self-cleaning. *Appl. Surf. Sci.* 401, 146–155. doi: 10.1016/j.apsusc.2017.01.009
- Ye, Y., Liu, Z., Liu, W., Zhang, D., Zhao, H., Wang, L., et al. (2018). Superhydrophobic oligoaniline-containing electroactive silica coating as preprocess coating for corrosion protection of carbon steel. *Chem. Eng. J.* 348, 940–951. doi: 10.1016/j.cej.2018.02.053
- Yu, Z., Lv, L., Ma, Y., Di, H., and He, Y. (2016). Covalent modification of graphene oxide by metronidazole for reinforced anti-corrosion properties of epoxy coatings. *RSC Adv.* 6, 18217–18226. doi: 10.1039/C5RA23595B
- Yun, H., Li, J., Chen, H. B., and Lin, C. J. (2007). A study on the N-, S- and Cl-modified nano-TiO₂ coatings for corrosion protection of stainless steel. *Electrochim. Acta* 52, 6679–6685. doi: 10.1016/j.electacta.2007.04.078
- Zhang, J., Gu, C., Tong, Y., Yan, W., and Tu, J. (2006). A smart superhydrophobic coating on coating on AZ31B magnesium alloy with self-healing effect. *Adv. Mater. Interfaces* 3:1500694. doi: 10.1002/admi.201500694

Conflict of Interest Statement: The authors declare that the research was conducted in the absence of any commercial or financial relationships that could be construed as a potential conflict of interest.

Copyright © 2019 Bao, Deng, Zhang, Ji and Zhang. This is an open-access article distributed under the terms of the Creative Commons Attribution License (CC BY). The use, distribution or reproduction in other forums is permitted, provided the original author(s) and the copyright owner(s) are credited and that the original publication in this journal is cited, in accordance with accepted academic practice. No use, distribution or reproduction is permitted which does not comply with these terms.



Application of Scanning Kelvin Probe in the Study of Protective Paints

Andrej Nazarov* and Dominique Thierry

French Corrosion Institute, Brest, France

OPEN ACCESS

Edited by:

Michele Fedel,
University of Trento, Italy

Reviewed by:

Ole Øystein Knudsen,
Norwegian University of Science and
Technology, Norway
Wolfram Fürbeth,
DECHEMA Forschungsinstitut
(DFI), Germany

*Correspondence:

Andrej Nazarov
andrej.nazarov@institut-corrosion.fr

Specialty section:

This article was submitted to
Environmental Materials,
a section of the journal
Frontiers in Materials

Received: 28 March 2019

Accepted: 25 July 2019

Published: 08 August 2019

Citation:

Nazarov A and Thierry D (2019)
Application of Scanning Kelvin Probe
in the Study of Protective Paints.
Front. Mater. 6:192.
doi: 10.3389/fmats.2019.00192

Industrial coatings are composed of layers of different polymers (top coats, primers) containing pigments, corrosion inhibitors, and fillers as well as additives. For corrosion protection, it is vitally important to preserve the strong adhesion and long-term stability of the metal-polymer interface in corrosive environments. In recent decades, the performance of painted materials increased, which requires the application of advanced methods for quick assessing, ranking and predicting corrosion stability. Scanning Kelvin probe (SKP) is a highly sensitive and non-invasive technique to analyze *in situ* the metal-polymer interface of high-performance industrial coatings. SKP is able to monitor the adhesion and corrosion underneath different kinds of paints without the need for long-term corrosion tests. SKP is a localized electrochemical technique with a spatial resolution in the range of 70–100 μm . Hence, it is possible to obtain information about the intact and corroding portions of the interface at defect sites, corrosion blisters, contaminants, and intermetallics, quality of pretreatments, and the development of galvanic couples that lead to corrosion de-adhesion of the polymeric coatings. This article reviews the application of SKP to the determination of the mechanisms of corrosion de-adhesion of model paints, thick marine paints, coatings with zinc rich primers, automotive paints, and coil coatings applied on galvanized steel substrates.

Keywords: SKP, polymeric coatings, corrosion protection, adhesion, pigments, pretreatments

INTRODUCTION

Historically, polymeric coatings were assumed to protect the substrate from corrosion by acting as a barrier toward water, oxygen and ions. However, later studies found that oxygen and water relatively quickly saturated the coating and could not be rate determining factors in corrosion protection (Leidheiser and Granata, 1988; Thomas, 1991). Kinsella and Mayne (1969) and Mayne and Scantlebury (1970) found that ionic resistance is a key factor in polymer coating stability, known as “resistance inhibition.” The relationship between the ionic resistance of a coating and its protective ability has been identified (Kinsella and Mayne, 1969; Mayne and Scantlebury, 1970). Ionic resistance has been highlighted as an important (even critical) property of a coating in modern works (Kendig and Mills, 2017; Mills and Jamali, 2017).

Funke placed great emphasis on the importance of wet adhesion to the substrate, claiming “adhesion is performance” and that it is a key factor in determining the overall coating lifetime (Funke, 1979; Negele and Funke, 1996).

The high importance placed on ionic resistance has been criticized in an article of Sykes et al. (2017). The existence of micro galvanic couples underneath the coating leads to the rapid failure of resistive coatings. Coating failure normally initiates at a local defects, which can be the result of application errors, chemical heterogeneities in the coating

or other defects, such as bubbles, under film deposits or mechanical damages. The corrosion of steel at a defect can lead to cathodic delamination of the surrounding coating (Leidheiser et al., 1983; Hamade and Dillard, 2005; Sørensen et al., 2010). On the other hand, coating de-adhesion can result from anodic undermining or filiform corrosion (Sharman, 1944; Funke, 1981). Schematics illustrating these two modes of coating de-adhesion are given in **Figure 1**. Leidheiser et al. (1983) described the mechanism for the cathodic delamination of polymeric coatings. The corrosion of steel at a defect due to the presence of an aqueous electrolyte can lead to spreading of the cathodic oxygen reduction reaction to the surrounding interface (**Figure 1A**). Delamination is effective for metals (e.g., Fe, Zn), which are covered by electron conducting surface oxide films. Considering a coated steel substrate immersed in an electrolyte at a near-neutral pH, the half-cell reaction responsible for the coating delamination process is oxygen reduction (Leidheiser et al., 1983). A linear relationship has been found between the diffusion coefficients of the different cations in an aqueous solution and the delamination rate (Leidheiser et al., 1983). The adhesion instability has been explained by the reduction of the metal oxide film at the interface or by chemical degradation of the polymer chains by products of oxygen reduction such as alkali or peroxide species. Three locus of failure have been suggested: in the oxide, in the layer of polymer or the interface (Leidheiser et al., 1983). After a weakening of the interface due to cathodic processes, residual stresses concentrated at the metal-polymer interface can cause peeling of the coating (Negele and Funke, 1996; Hamade and Dillard, 2005).

Anodic undermining or filiform corrosion has been found in polymer-coated metals exposed to humid atmospheres and is enhanced by artificial or natural impurities, such as sulfur dioxide or chloride (Sharman, 1944; Funke, 1981). It is supposed that the galvanic cell governs the growth of the filament (**Figure 1B**). Although filiform corrosion usually occurs on organic-coated aluminum parts, it has also been observed on magnesium and cold rolled steel. Filiform corrosion normally initiates at small, sometimes microscopic, scratches or defects in the coating. In the case of iron and zinc, cathodic oxygen reduction takes place at defect sites on the surface of rust, and anodic oxidation and formations FeCl_2 or ZnCl_2 develop underneath the coating prior to de-adhesion (**Figure 1B**). There is only one certain way to prevent filiform corrosion, which is to dehydrate the rusted steel surface by reducing the relative humidity of the air to below ~60% (Funke, 1981). On the other hand, the stability of metal-paint interfaces can be enhanced by treating the metal surface, and these types of conversion coatings have a beneficial effect toward preventing filiform corrosion (Stratmann, 2005).

The electrochemical heterogeneity of the metal surface governs the spatial separation of the cathodic and anodic corrosion reactions. The stability of the coatings to corrosion driven deadhesion is determined by formation of galvanic elements and the local electrochemical methods can obtain spatially resolved information related to metal-polymer interface. The local techniques that have been applied to metals covered by organic coatings have been reviewed (Grundmeier et al., 2000; Ogle et al., 2000; Philippe et al., 2003; Stratmann,

2005; Hausbrand et al., 2008; Rossi et al., 2008; Huang et al., 2011; Upadhyay and Battocchi, 2016). A very important advantage of local scanning techniques is the possibility of comparing the map of the electrochemical parameters with the topographic information (presence of defects or rust clusters), metal microscopy data (microstructure and contaminants), differences in surface treatments, etc. DC current techniques (the scanning vibrating electrode technique and scanning electrochemical microscopy) are mainly applicable for assessing relatively low resistive paths, such as defects in the coating. Techniques based on AC current measurements (local electrochemical impedance spectroscopy and SKP) are effective for obtaining information from the interfaces underneath intact and highly resistive polymeric coatings. The objective of this particular review is to discuss the growing information concerning the application of SKP to analyze the properties of paints and paint additives that influence their stabilities and protective properties. Industrial paints have increased corrosion stabilities, and the application of highly sensitive and non-invasive *in situ* methods for quick assessment and ranking is highly important.

SKP PRINCIPLES AND APPLICATION

SKP is a non-destructive local electrochemical technique that measures the contact potential difference between a working electrode (e.g., the polymer-coated metal) and a vibrating reference electrode (e.g., a CrNi alloy or gold). A schematic of the Kelvin probe is shown in **Figure 2A**. When two metals are in contact, electrons move to reach equilibrium that creates the contact potential difference (CPD). This potential difference (ΔV , Equation 1) is proportional to the difference in the electron work functions (Φ) of the two materials. Φ is defined as the minimum work necessary to extract an electron from the Fermi level of a metal and transfer it to a point just outside the metal surface (carrying no net charge) (Hölzl and Schulte, 1979).

To measure the contact potential difference, the probe vibrates in the vertical plane, which creates a capacitor with an alternating distance, and an alternating current flows between the probe and the working electrode (Equations 2, 3). The amplitude of this current is proportional to the CPD (Equation 4).

$$\Delta V = (\Phi_w - \Phi_p)/e \quad (1)$$

$$C = \epsilon \epsilon^\circ A / (d + \Delta d \sin \omega t) \quad (2)$$

$$I(t) = I_a \sin(\omega t) \quad (3)$$

$$I_a = \Delta V \epsilon^\circ A \omega / d, \quad (4)$$

where e is the electron charge, C is the capacitance, ϵ and ϵ° are the dielectric constants of the surface coating and vacuum, respectively, d is the distance between the probe and working electrode, $I(t)$ is the AC current, I_a is the amplitude of the current, ω is the frequency of the current, t is the time, and A is the surface area of the probe.

The work function (Φ_w , Equation 1) is a fundamental property of a metal, and it is proportional to the actual potential

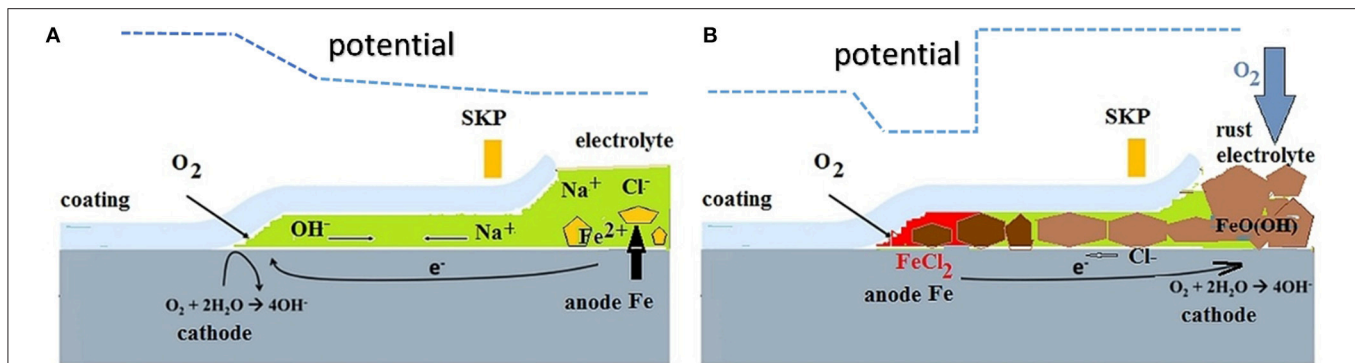


FIGURE 1 | Schematics for corrosion-driven coating de-adhesion. **(A)** Cathodic delamination and **(B)** anodic undermining galvanic cells and potential distributions along the interface.

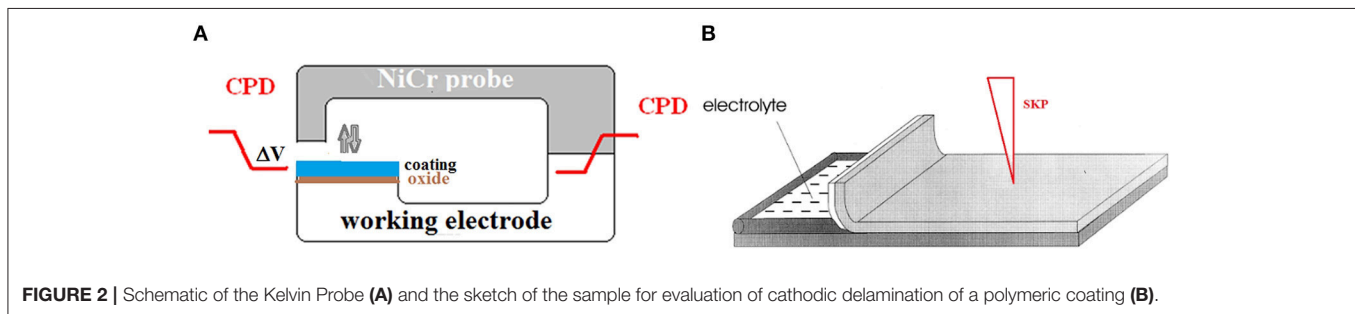


FIGURE 2 | Schematic of the Kelvin Probe **(A)** and the sketch of the sample for evaluation of cathodic delamination of a polymeric coating **(B)**.

of an electron in a metal (Equation 5; Hölzl and Schulte, 1979; Trasatti and Parsons, 1986).

$$\Phi N = -\alpha = -\mu_e + FX_w \quad (5)$$

where α is the electrochemical potential, μ_e is the chemical potential of the electrons, N and F are the Avogadro number and Faraday constant, respectively, and X_w is the potential difference across the metal-air interface (Trasatti and Parsons, 1986).

According to these definitions, the electron work function or electrochemical potential contains bulk and surface contributions. The bulk contribution is determined by the chemical potential of the electrons. The surface contribution (X_w) includes the number of potential drops related to the surface oxide film and dipole layers of adsorbed molecules (Equations 5–7).

$$X_w = \frac{\mu_{ox} - \mu_e}{e} + F_b + \beta_{ox/air} \quad (6)$$

$$X_w = \frac{\mu_{ox} - \mu_e}{e} + F_b + \beta_{ox/coating} + \beta_{coating/air} \quad (7)$$

For a bare metal surface, the potential drop (X_w , Equation 6) includes the contact potential difference between the bulk metal and oxide film relating to the difference in the corresponding chemical potentials of the electrons in the metal (μ_e) and in the oxide (μ_{ox}). The second potential drop (F_b) relates to the adsorption of environmental components (molecules of oxygen, water, etc.) that bend the conductive and valence bands of the

semiconducting oxide film. The electric charges in the oxide are compensated for by the charges of the double electric layer, such as the dipoles of adsorbed species (e.g., O_2^- ions), creating a potential drop ($\beta_{ox/air}$).

For polymer-coated metals, the SKP measured potential has a potential drop (X_w , Equation 7) that includes two additional potential drops $\beta_{ox/coating}$ and $\beta_{coating/air}$. The first corresponds to charge transfer or the formation of a double electric layer of oriented dipoles between the functional groups of the polymer and the oxide that are related to the adhesive bonds (Evans and Ulman, 1990; Taylor, 2000). The second potential drop relates to the dipoles in the organic chains or charged groups of the polymer (e.g., Donnan potential drop) (Samec et al., 1993; Taylor, 2000).

Initially, the Kelvin probe was extensively applied to investigate the kinetics of metal oxidation in the gas phase, leading to the formation of oxide films. In addition, an important area of study was the adsorption of different gases onto the surface of bare metals or those covered by oxide films. These processes change the potential drop across the metal-air interface (Equation 6). Thus, CPD between a platinum probe and an evaporated metal film was monitored during the adsorption of oxygen, nitrogen or water vapor (Hackerman and Lee, 1955). Both reversible and irreversible changes of the Volta potential were found, which corresponded to the formation of either a dipole barrier or an ion barrier that prevented electron transfer. Thus, it was shown that oxygen adsorption increases the electron work function due to electron

transfer from the metal to the adsorbed oxygen molecules (Hackerman and Lee, 1955). An increase in the electron work function due to the formation of an ionic barrier related to the oxide film has also been demonstrated (Hackerman and Lee, 1955).

During measurement, the Volta potential of the probe (Φ_p/e) is kept constant. This makes possible to use CPD measurements (ΔV , Equation 1) to determine the Volta potential of the working electrode (Φ_w/e) relative to a reference electrode or determine the electron work function Φ_w relative to the vacuum level. Finally, SKP measures the surface distribution of the electrochemical potential above the metallic substrate or polymer coated metallic substrate (Grundmeier et al., 2000; Hausbrand et al., 2008). To transform Volta potential to electrochemical potential the probe has to be calibrated using a reversible reference electrode (e.g., Cu/CuSO₄). Modern SKP instruments measure potential distribution with a spatial resolution in the range 70–100 μm . They are equipped with an environmental chamber that enables measurements *in situ*, in a corrosive environment.

M. Stratmann and H. Streckel introduced SKP to electrochemical corrosion (Stratmann and Streckel, 1990; Frankel et al., 2007). It has been shown that for corroding metals, SKP measures the corrosion potential and can be used for studying the corrosion under very thin electrolytic films (Frankel et al., 2007). In the case of an active surface, the potential drop X_w (Equation 6) related to surface oxide significantly decreases. For metals without corrosion activators, the potential is noble and relates to the potential of the metal under passive conditions (Hausbrand et al., 2008). In this case, the redox properties of an oxide film can influence the measured potential (Grundmeier and Stratmann, 1999). According Nernst equation (Equation 8), the potential of Fe is a function of the activities of the different iron species, Fe^{3+} and Fe^{2+} , in the surface oxide:

$$\Delta E = \text{const.} + \frac{RT}{F} \ln \frac{a(\text{Fe}^{3+})}{a(\text{Fe}^{2+})} \quad (8)$$

A potential drop in a semiconducting oxide film that does not change the oxidation state, such as in zinc, also significantly contributes to the potential measured by the SKP. An increase in the oxide thickness of a Zn/ZnO electrode increases the potential measured in air (Nazarov et al., 2015). This can be the result of an increase in the thickness of the space-charge layer in thicker oxide films. The adsorption of environmental components onto the oxide film surface also plays a role (Equations 6, 7). Replacing air with nitrogen decreased the potential of passive zinc by 100–150 mV. Thus, the formation of an oxide/ O^{2-} dipole layer increased, and oxygen desorption decreased the Zn potential (Nazarov and Thierry, 2007; Nazarov et al., 2015).

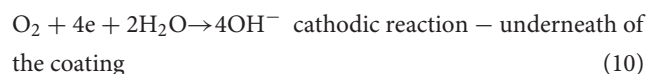
Well-oxidized and uniform oxide films create stable adhesive bonds with coatings (Funke, 1979; Kendig and Mills, 2017; Mills and Jamali, 2017). The application of SKP to studies on metal surfaces are based on measuring the conditions of the surface oxide, which are characterized by a potential drop X_w (Equations 6, 7). Intermetallics, contaminations or defects in oxide locally change the potential that can be visualized by SKP (Nazarov and Thierry, 2007). Thus, SKP inspection of an oxide surface before

application of polymeric coatings can detect surface defects and areas with non-uniform potential distributions, which can later lead to the formation of galvanic corrosion elements working underneath the coating and accelerating coating deadhesion.

RESULTS

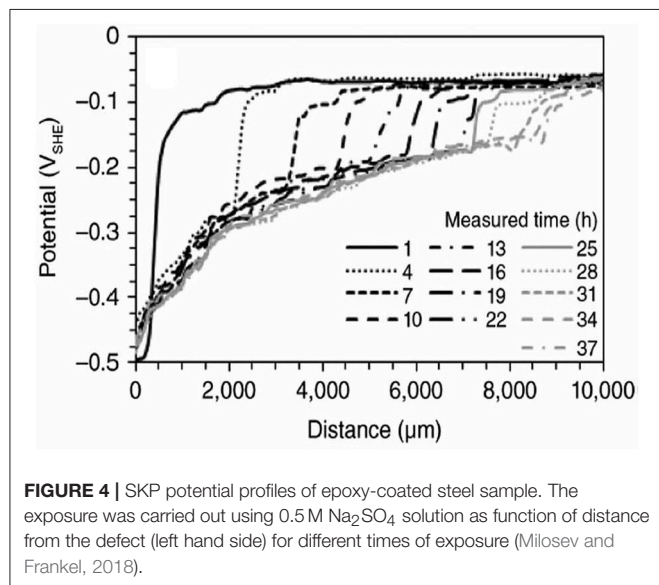
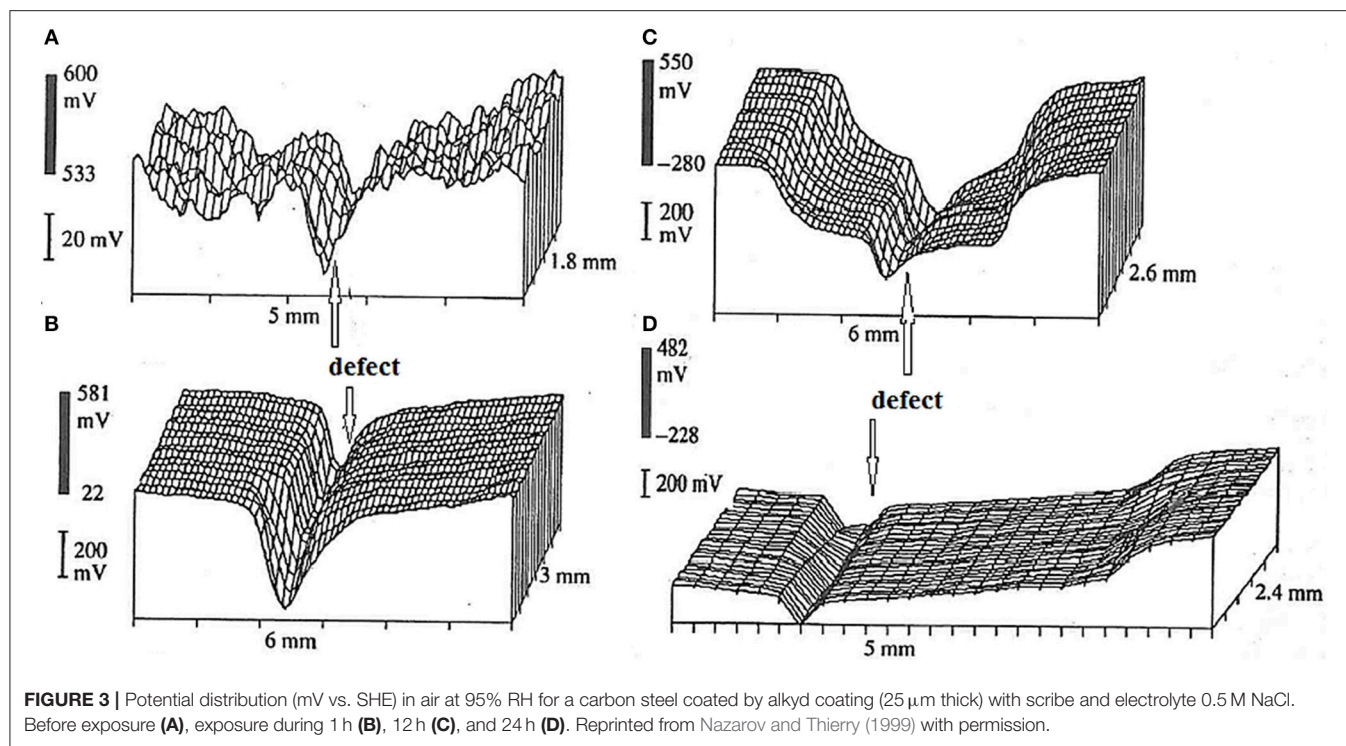
SKP Assessment of Cathodic Delamination of Polymeric Coatings From Carbon and Galvanized Steels

Corrosion-driven coating de-adhesion (Figure 1A) is the result of a non-uniform distribution of the electrochemical potential across the metal-metal oxide-paint interface and the work of macro galvanic couples. SKP mapping of the potential makes possible to determine the galvanic elements (Figure 1A).



Using SKP, M. Stratmann et al determined the electrochemical mechanism for the cathodic delamination of polymeric coatings from steel surfaces (Stratmann et al., 1991; Leng et al., 1999a,b). SKP has the main advantage of being able to measure the potential of a metal underneath a highly resistive, intact and delaminated coating *in situ* (Figure 1). For measurements, an artificial defect in a coating containing a NaCl solution was prepared (Figure 2B). A linear relation between the coordinates for the displacement of the delamination front vs. the square root of the time of exposure was found (Leng et al., 1999a,b). These results showed that ion migration (Na^+) from the defect along the interface is the rate-controlling process for the cathodic delamination of thin model coatings (Figure 1A). The de-adhesion rate is determined by the mobility of the cations, but the mobility along the metal-polymer interface is much slower than the mobility of ions in the bulk electrolyte (Leng et al., 1999b). The results of SKP investigations related to cathodic delamination of the different polymeric coatings from iron, steel and galvanized steel substrates have been published in Stratmann and Hoffmann (1989), Stratmann et al. (1991), Nazarov and Thierry (1999, 2004a, 2010), Nazarov et al. (2012), Leng et al. (1999a,b), Furbeth and Stratmann (2001a,b,c), Williams and McMurray (2003), Reddy et al. (2004), Reddy and Sykes (2005), de la Fuente and Rohwerder (2008), Nazarov et al. (2012a, 2018a), and Khun and Frankel (2013).

For example, Figure 3 shows SKP maps for alkyd coating containing TiO_2 pigment deposited on mild steel surface. The delamination starts from the scribe contaminated by NaCl aqueous electrolyte (Nazarov and Thierry, 1999). The potential of the intact interface relates to the steel in the passive state (cathode, 0.5 V vs. SHE), and at the defect site the steel has a low potential of active corrosion (anode, −0.3 to −0.2 V vs. SHE, Figure 3). The potential difference of 0.7 V is the electromotive force of the galvanic element leading to cathodic delamination of the coating from the defect. Figure 4 shows typical SKP profiles



for steel—epoxy system as function of distance for different times of exposure in neutral 0.5 M Na_2SO_4 solution.

Other factors, such as the roughness of the steel surface and the texture of the surface, influence the cathodic delamination rate of epoxy coatings (Khun and Frankel, 2013). SKP measurements showed that an increase in the steel roughness decreased the rate of delamination. The surface features of the underlying steel substrate also influenced the cathodic delamination of the epoxy coatings. The textured lines (due to

abrasion) parallel to the direction of delamination accelerated the failure compared with texture lines perpendicular to the direction of delamination. In this study, a linear dependence of the creep of coating deadhesion vs. the time of exposure was found (Khun and Frankel, 2013).

It is important to note that strong spatial separation of cathodic and anodic reactions with spreading of the cathodic reaction to the surrounding surface occurs also without a coating, due to atmospheric corrosion of steel or zinc locally contaminated by NaCl (Nazarov and Thierry, 2004a; Nazarov et al., 2015). The formation of galvanic couples consisting of anode in the region of the NaCl deposit and cathode on the bare steel surface has been observed by SKP (Figure 5). The distance of the cathodic spreading also had a dependence on the square root of time, and the spreading across the bare metal surface was faster compared with that of coated steel (see Table 1; Nazarov et al., 2018a). The electromotive force of the galvanic element that is equal to the potential difference between the low-potential anode and the noble potential of the passive steel surface was approximately 0.6 V (Figure 5A). This is the thermodynamic reason for galvanic corrosion. On the other hand, the rate of galvanic corrosion is a function of the rates (polarization resistances) of the partial corrosion reactions and the ionic conductivity along the interface (Nazarov and Thierry, 2004a). The area of cathodic spreading increased with increasing NaCl concentrations in the local deposits. The efficiency of the cathodic reaction on the bare steel surface governs the cathodic spreading that can be visualized by SKP (Figure 5). The rates of electron transfer from the substrate to oxygen molecules (Equation 10) and the migration of cations along the surface can be function of the surface chemistry. Metal surface pretreatments

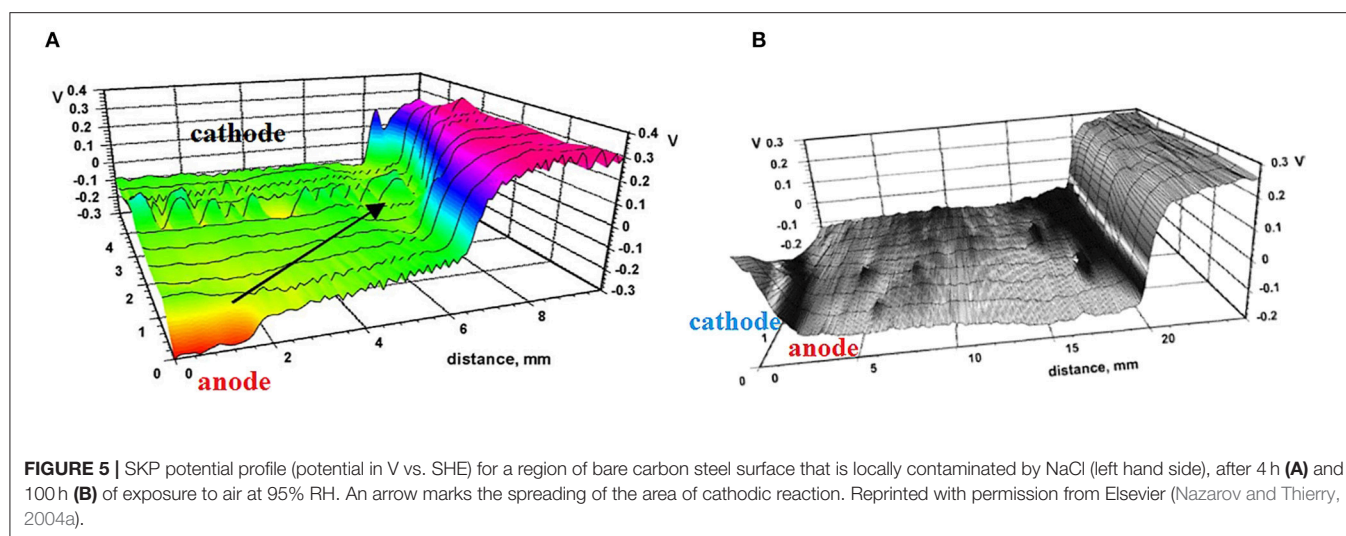


TABLE 1 | Rates of cathodic deadhesion (spreading) for square root or linear kinetics during exposure in aqueous electrolytes, type of coating, and pigment, exposure conditions, coating thickness.

Coating	Exposure	Rate	Rate	Dry film thickness, μm	References
		$\text{mm/h}^{1/2}$	mm/h		
Bare steel, atmospheric corrosion	Droplet of 0.5 M NaCl	2.4		0	Nazarov et al., 2018a
Epoxy model	Aqueous electrolyte 0.5 M NaCl	1.95		40–47	Leidheiser et al., 1983
Epoxy-ester clear model	Aqueous electrolyte 0.5 M NaCl	1.2		50–60	Leng et al., 1999b
Amide-epoxy clear	Aqueous electrolyte 0.5M KCl	0.6		300	Sørensen et al., 2010
Amide epoxy pigmented flake-shaped micaceous iron oxide		0.3			
Epoxy unpigmented model	Aqueous electrolyte 3% NaCl	0.64		40	Bi and Sykes, 2011
Two layers epoxy pigmented	Aqueous electrolyte 3.5% NaCl		0.59	120–200	Bi and Sykes, 2016
Pigmented epoxy marine paint (35°C)	Aqueous electrolyte 3% NaCl		0.38	300–320	Nazarov et al., 2018a
Pigmented epoxy marine paint (22°C)	Aqueous electrolyte 3% NaCl		0.17	300–320	Nazarov et al., 2018a
Waterborne epoxy clear	Aqueous electrolyte 0.85 M NaCl	0.96		53–63	Hernández et al., 2004
Waterborne epoxy, 8.3% zinc phosphate pigment	Aqueous electrolyte 0.85 M NaCl	0.2		53–63	Hernández et al., 2004

(conversion coatings) can be ranked according to their effect on cathodic spreading. Thus, SKP measurements of bare metal surfaces can be useful for choosing the appropriate pretreatment before painting.

SKP is an ideal tool for *in situ* monitoring of the degradation processes at the buried interface contaminated by soluble salts. The study of stability of the steel/coating interfaces to initial stages of blistering and underfilm corrosion has been carried out (de la Fuente and Rohwerder, 2008; Nazarov et al., 2012a). SKP mapping gives the exact locations of the corrosion of the steel underneath a 150 μm thick layer of epoxy-diamine/polyamide paint (**Figure 6A**). This SKP study was carried out to determine the critical amount of NaCl at the interface that can prevent the

development of corrosion beneath the paint. For a particular paint system, 5 $\mu\text{g}/\text{cm}^2$ was the threshold level of NaCl contamination for the paint to inhibit corrosion in humid air at 95% RH. Thus, SKP can quickly assess paints that can withstand corrosion due to NaCl contamination of the interface (de la Fuente and Rohwerder, 2008; Nazarov et al., 2012a). Corroding locations show low (active corrosion) potentials relatively surrounding intact interface (**Figure 6B**). Cathodic delamination of the coating around these active locations can be expected as the exposure time increases.

Cathodic delamination of the polymeric coating can occur on a metallic substrate that has sufficient electronic conductivity and catalytic activity to support the oxygen reduction reaction under

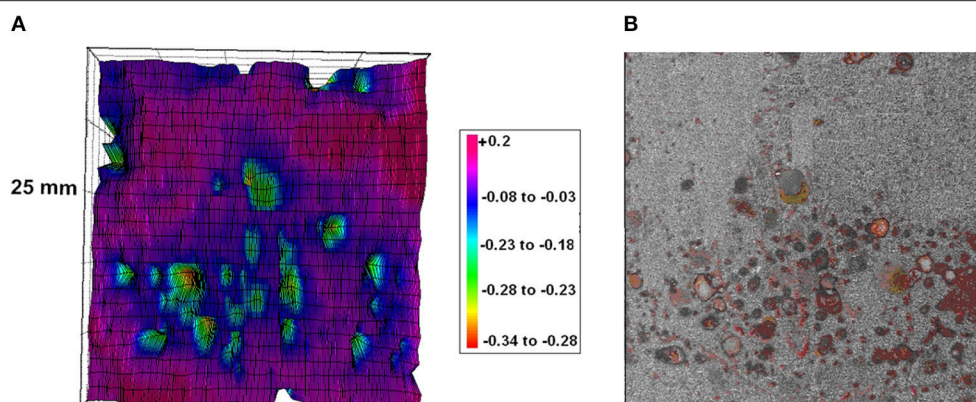


FIGURE 6 | (A) SKP map (V vs. SHE) and **(B)** the photograph of the steel surface after coating removing. The substrate was contaminated by NaCl ($20 \mu\text{g}/\text{cm}^2$). Epoxy-vinyl coating thickness $100 \mu\text{m}$. The measurement was carried out in air at 95% RH. Reprinted with permission from NACE International (Nazarov et al., 2012a).

the coating (Leidheiser et al., 1983). Corrosion of galvanized steel in the defect down to the zinc layer leads to cathodic delamination of polymeric coatings (Furbeth and Stratmann, 2001a,b,c). The propagation kinetics of the cathodic front from the defect is proportional to the square root of the exposure time. In contrast to steel, zinc is an amphoteric metal, and the formation of alkali in cathodic region leads to the growth of an oxide layer at the zinc–polymer interface (Furbeth and Stratmann, 2001a). The cathodic reaction decreases the adhesion of a coating on a steel surface, but it completely delaminates the coating from a zinc surface.

If a defect in the organic coating is prepared through zinc layer down to the steel substrate, the polarity changes, and the defect can serve as a cathode that drives anodic coating de-adhesion from the defect. As a result, the kinetics are a complex combination of cathodic and anodic processes that occur at the metal–polymer interface (Furbeth and Stratmann, 2001b).

SKP Assessment of the Mode of Paint Corrosion Driven De-adhesion

It has been observed that the galvanic elements leading to the cathodic delamination of the coating can reverse their polarity during exposure (Figures 1A,B). SKP and scanning acoustic microscopy were applied to study the corrosion underneath a $120 \mu\text{m}$ thick epoxy amide resin coating (Reddy et al., 2004; Reddy and Sykes, 2005). It has been demonstrated that in some instances, the formation of iron rust at the sites of local coating degradation can reverse the potential distribution and the electrochemical activity, with rust serving as a cathodic reactant and new anodes being formed.

Thus, delamination of a thin polyvinyl butyral (PVB) coating ($20 \mu\text{m}$ thick) from iron starting at a defect site containing NaCl initially showed cathodic disbondment (Williams and McMurray, 2003). Spreading of the low-potential region corresponding to delamination of the PVB coating during exposure was found. In the second phase, the formation of rust at the defect site switches the cathodic mode of de-adhesion to an anodic mode. Filaments grow from the rust locations. The

rust formed on the iron underneath the coating is an effective cathodic component (Stratmann and Hoffmann, 1989). The filaments spreading either under the cathodically delaminated film or under the intact film contain low-potential active heads, where anodic iron oxidation occurs (Williams and McMurray, 2003). The heads mainly contain iron (II) chloride (Figure 1B). The tails of the filaments contain hydrolyzed iron-corrosion products, have a positive potential, and can serve as the cathodes in filament galvanic cells.

Contamination of the defect site in the coating by iron chloride instead of NaCl results in only anodic undermining of the coating occurring (filiform corrosion). Iron is not a mobile cation due to hydrolysis, oxidation, and rust deposition. Thus, this contaminant cannot support spreading of the cathodic region underneath the coating (Williams and McMurray, 2003).

Using steel coated by pigmented epoxy-vinyl coating ($100 \mu\text{m}$ thick), it was found that the polarity of the galvanic couple and the mode of delamination were functions of the thickness of the electrolyte in the defect (Nazarov and Thierry, 2010). Under a thick electrolyte film, the defect site was anodic that polarizes the surrounding interface leading to cathodic delamination (Figure 7A). Under thin films, in atmospheric corrosion conditions, the defect in the same electrode showed a positive (cathodic) potential that anodically polarized the surrounding steel-coating interface and facilitated anodic undermining (Figure 7B). In this system, the delamination (anodic undermining) was uniform without the formation of filaments (Nazarov and Thierry, 2010). The defect and the steel underneath of the coating developed the rust with different compositions and degrees of oxidation. The anodic front (Figure 1B and area of low potential in Figure 7B) is enriched with chloride and contains FeCl_2 . The $\text{Fe}^{2+}/\text{Fe}^{3+}$ redox couple in the rust near the defect site provided effective cathodic oxygen reduction (Stratmann and Hoffmann, 1989).

Changes in the polarity of the galvanic elements were found for bare iron surfaces with local NaCl contaminants (Nazarov and Thierry, 2004a). Atmospheric corrosion and rust formation increased the potential of the contamination, and the potential

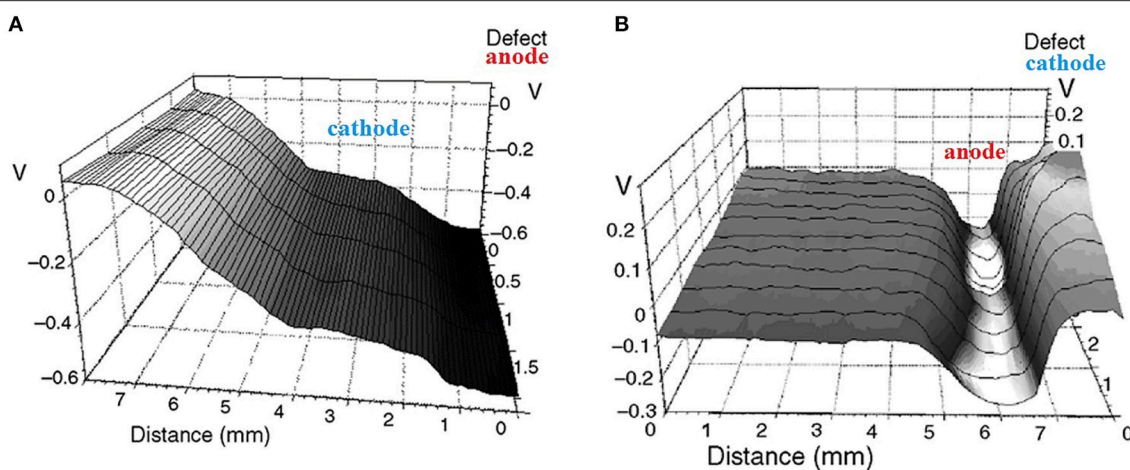


FIGURE 7 | Potential distribution (V vs. SHE) of a coated steel with a linear defect (right-hand side) in the epoxy vinyl coating (100 μm thick). **(A)** Measurement with a thick layer of aqueous electrolyte in the defect. **(B)** Measurement of the same area with a thin electrolyte layer during atmospheric corrosion at 95% RH. Reprinted with permission from NACE International (Nazarov and Thierry, 2010).

became more positive (left hand side in **Figure 5B**). However, significant anodic spreading was observed only for the coated samples. The coating additionally separates the partial reactions, creating a galvanic couple of different aeration, for which the cathode is in a well-aerated defect site and the anode is underneath the polymeric coating. For different systems, it was found that peeling out and removing the paint from anodic region transforms it into a cathodic surface (Nazarov and Thierry, 2010; Nazarov et al., 2012).

During corrosion exposures, the conditions of the defect site can periodically change, accelerating the cathodic or anodic modes of coating de-adhesion. Depending on the thickness of the electrolytic layer at the defect site, switching of the polarity of the galvanic couple was found for a polymer-coated zinc surface on a galvanized steel substrate (Nazarov et al., 2012). Using a cathaphoretic epoxy coating (a system is used in the automotive industry), it was demonstrated that the potential distribution corresponded to cathodic delamination for a thick electrolytic film (**Figure 8A**) and to the anodic undermining (**Figure 8B**) in the case of atmospheric corrosion (Nazarov et al., 2012).

Only anodic de-adhesion mode, with spreading of the chloride ions and formation of anodic blisters contained ZnCl_2 , was observed by SKP for de-adhesion of the coating from galvanized steel (Zn) from the defect down to the steel surface (Nazarov et al., 2012). A more positive steel substrate serves as a cathode, and a more negative zinc-coating interface serves as an anode. This galvanic couple governs the cut-edge corrosion of polymer coated galvanized steel (coil-coated materials) either under atmospheric or immersed in an electrolyte conditions (Nazarov et al., 2012).

Due to its low electronic conductivity, cathodic de-adhesion is strongly inhibited by substrates with dielectric oxide films, such as aluminum and magnesium alloys. However, anodic (filiform) coating de-adhesion in humid atmospheric conditions can be significant (Williams et al., 2001; Le Bozec et al., 2002; Leblanc and Frankel, 2004; Romano et al., 2009; McMurray et al., 2010).

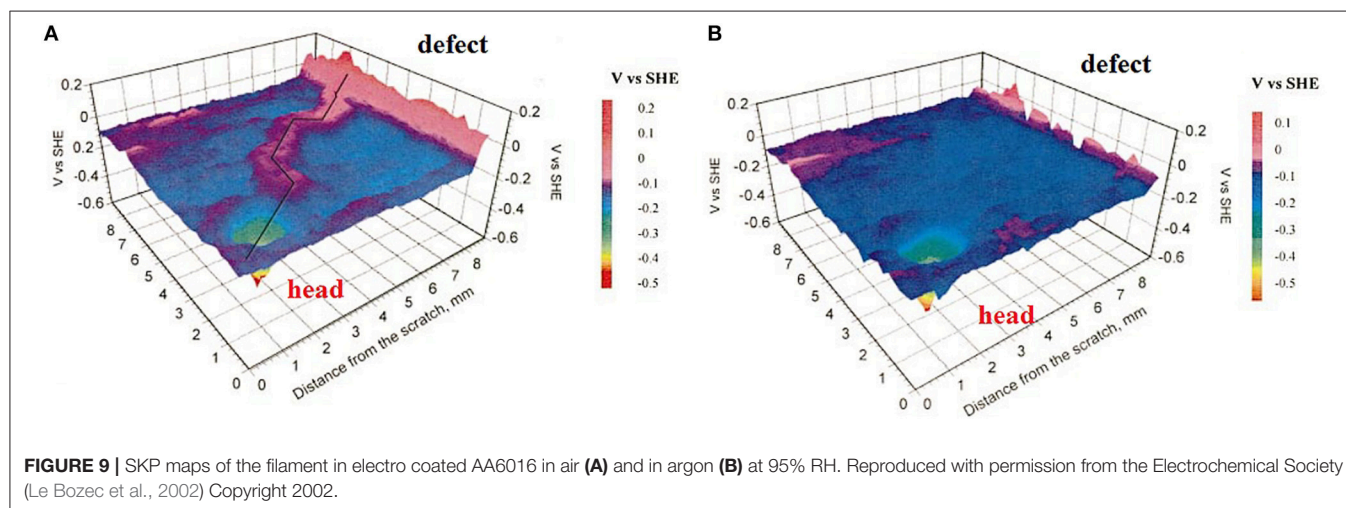
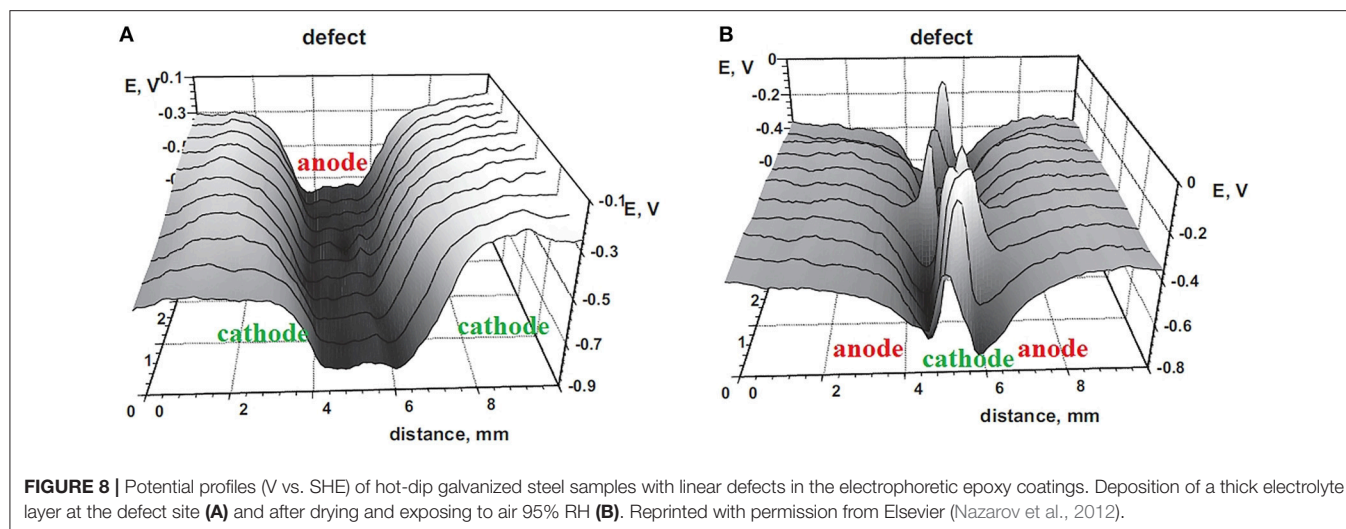
Figure 9 shows the potential distribution over an Al alloy coated with an electrophoretic epoxy coating after 6 weeks of exposure to air at 85% RH. These systems are applied in the automotive industry. The measurements of Le Bozec et al. (2002) performed in air and argon at 95% RH showed that the exchange of the atmosphere decreased the potentials of the tail and the linear defect (**Figure 9**). Thus, pre-corroded areas of Al are a source of cathodic activity (Equation 10) directed to the anodic location in the filament head. The filament head has the potential to be more active at -0.5 V (SHE).

The stress generated during cross-linking and curing of an electrophoretic coating influences the adhesion and spreading of the filiform corrosion of an aluminum AA6016 (Romano et al., 2009). It was found that an increase in the amount of cross-linking in the epoxy cathaphoretic coating increased the adhesion and the uniform front of spreading transforms to more narrow filaments.

Finally, it is possible to point out that the mechanism of deadhesion is mainly determined by electrochemical conditions of the metal in the defect (Nazarov and Thierry, 2010). However many factors such as the electronic conductivity of the oxide film and the corrosion products, amount of water, degree of aeration, the type and concentration of pollutants are influencing and consequently only careful SKP evaluation can inform about the type of coating deadhesion and predict the coating stability under particular conditions.

SKP Assessment of Paint Stability to Delamination. Influence of Loading Pigments and Corrosion Inhibitors Into the Paints

The effects of the thickness of a polymeric film and the addition of pigments on the stability of the interface to de-adhesion have been studied using SKP. As was discussed above, the



delamination rate of unpigmented coatings was controlled by cations mobility and delamination was dependent on the square root of the exposure time (Leng et al., 1999a,b; Furbeth and Stratmann, 2001c; Reddy and Sykes, 2005; Bi and Sykes, 2016). The kinetic was only slightly slower for thicker coatings (Bi and Sykes, 2016). However, the pigments can decrease the cathodic delamination rate significantly (see **Table 1**). A linear dependence of the delamination vs. time was detected for pigmented systems (Hernández et al., 2004; Grundmeier et al., 2006; Bi and Sykes, 2011, 2016; Nazarov et al., 2018a). The rate of delamination also depends from mobility of cations along the interface (Bi and Sykes, 2016). The rate of deadhesion of pigmented epoxy coatings decreased in the sequence $\text{KCl} > \text{CsCl} > \text{NaCl} > \text{LiCl}$ (Bi and Sykes, 2016). Important parameter for pigmented coatings is number of interaction points (hydroxyl groups) between the coating and the substrate that is controlling interfacial interaction (Sørensen et al., 2010). Thus, oxygen diffusion rate, mobility of cations and adhesion are factors, which control the stability.

SKP was used to study the stability of iron with coatings contained advanced pigments based on graphene nanoplatelets and carbon nanotubes (Khun and Frankel, 2016; Glover et al., 2017, 2018). The delamination rates correlated strongly with a decrease in oxygen permeation through the coating as a function of increasing pigment volume fraction in a polyurethane/multiwalled carbon-nanotube coating (Khun and Frankel, 2016). The SKP technique was used to measure the propagation of the delamination front underneath the PVB coating. Incorporation of high-density graphene nano-platelet pigment blocked the oxygen and water pathways to the coating-steel interface, which significantly decreased the rate of cathodic delamination by 98.6% (Glover et al., 2018).

In opposite to oxygen accelerating corrosion, another air component such as carbon dioxide can decrease the corrosion rate of galvanized steel. CO_2 creates carbonates at the interface with galvanized steel during atmospheric exposure that decrease the cathodic coating delamination (Furbeth and Stratmann, 2001c). Polymeric coatings selective to CO_2 were studied. The

important work of Shkrirskiy et al. (2019) investigated the relative ability of a polymeric coating to absorb a carbon dioxide. SKP inspections showed that increased permeation of carbon dioxide through coating and access the interface is favorable for stability of coated galvanized steel (Shkrirskiy et al., 2019).

SKP was applied to study the effect chromate inhibitors that could leach from the coating (Williams and McMurray, 2001). On the other hand, in many countries, legislation does not permit the application of chromates. Less hazardous phenyl phosphonic acid was investigated as an inhibitor of corrosion-driven organic coating disbondment from iron surfaces (Glover and Williams, 2017). SKP assessment of corrosion underneath the paint was carried out *in situ* under corrosive atmospheric conditions. Increasing the loading of phosphonic acid progressively decreased the delamination rate up to 55% (Glover and Williams, 2017). From the delamination kinetics, it was concluded that the species interacting with substrate form an interfacial salt layer that inhibits oxygen reduction beneath the film and cathodic de-adhesion.

SKP was employed by the group of G. Williams and H. N. McMurray to evaluate coating delamination from Al, Fe, Zn substrates after loading of an ion-exchanger, bentonite clay (Williams and McMurray, 2004, 2017; Dodds et al., 2017). Ion exchanger supplies the interface with divalent alkali-earth and trivalent rare-earth metal cations with the subsequent precipitation of sparingly soluble hydroxides. The deposit reduced the ionic conductivity of the electrolyte underneath the polymeric coating and correspondingly decreased the current in galvanic cell. For the best performing divalent cation-exchange pigments, the inhibitory effect was comparable to or provided better protection than that of a conventional strontium chromate pigment (Williams and McMurray, 2004, 2017). Pigments containing Mg^{2+} prevented delamination of the coating from hot-dipped galvanized steel (HDG). *In situ* SKP demonstrated that the high level of inhibition of cathodic delamination could be attributed to the deposition of $Mg(OH)_2$ precipitate (Dodds et al., 2017).

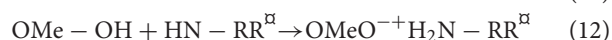
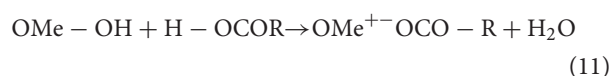
SKP was applied to monitor the cathodic delamination of a 300 μm thick-pigmented epoxy coating from steel, starting from the defect site after immersion of the sample in an aqueous electrolyte (Nazarov et al., 2018a). Due to high barrier properties, this coating is applied in offshore or marine environments. It was found that at ambient temperatures, the cathodic delamination was very slow and the paint partially retained its adhesion (see Table 1). However, under atmospheric corrosive conditions the reduction of oxygen on the rust surface at the defect site led to rapid coating de-adhesion following the anodic undermining mechanism. Thus, anodic de-adhesion under atmospheric weathering conditions is harder to prevent compared with cathodic de-adhesion when metal-polymer joint is immersed in an electrolyte (Nazarov et al., 2018a).

Zinc-rich primers (ZRP) are components of polymeric coatings that provide active corrosion protection to steel structures in heavily corrosive environments, such as offshore. In general, a paint contains different polymeric layers with a total thickness of >400 μm that significantly delays the degradation of the paint and decreases the observation of corrosion failures. *In*

situ SKP measurements of a complete paint system showed the efficiency of cathodic protection of a steel substrate by ZRP with different compositions and from different producers (Nazarov et al., 2018b). The electrolyte ingress to the interface from the defect site and activation of the Zn particles in the primer determine the ability of the primer to polarize the substrate and provided sacrificial protection under either immersed or atmospheric conditions. Thus, SKP mapping can determine the activity of the zinc particles at the interface as a function of the distance from the defect sites (scribe and cut-edge). Monitoring the interfacial potential during exposure provided information about the consumption of the zinc particles and the lifetime over which the primer could provide cathodic protection to the substrate. Thus, SKP provides a quick means of assessing the sacrificial steel protection provided by industrial marine paints containing zinc-rich primers under atmospheric or immersed conditions (Nazarov et al., 2018b).

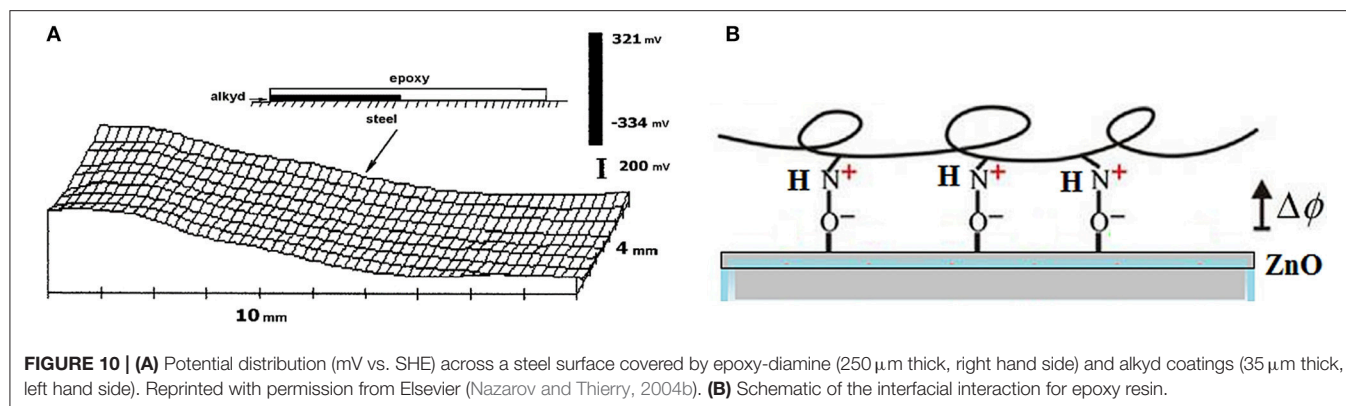
SKP Assessment of the Metal-Metal Oxide-Coating Interface to Determine the Nature of Adhesive Bonds and Their Stability

Achieving durable corrosion protection with polymeric coatings requires an understanding of the chemical interactions at the hybrid polymer/metal oxide/metal interfaces. It is important obtain information *in situ* directly from the solid/solid interface. This section shows the possibility of SKP assessment of the metal-coating interface to determine the nature and the stability of the metal-coating bonds (Nazarov and Thierry, 2004b, 2005; Nazarov et al., 2008, 2011). Metal-polymer interactions include hydrogen bonding, ionic polar or acid-base interactions (Brönsted and Lewis kinds of interaction), and van der Waals secondary forces. Formation of the interfacial dipoles are illustrated by Equations (11) and (12) and in Figure 10 (Nazarov and Thierry, 2004b).



Depending on the ionic groups distributed throughout the coating, the charges in the metal and coating layers can be different. These charges can be determined by scanning across different metal-polymer joints (Figure 10A).

Figure 10A shows the potential distribution for steel substrate sequentially coated by alkyd and epoxy coatings. It is clear that different coatings interact with the steel surface differently. The epoxy coating significantly decreased the potentials of steel or zinc (500 mV), and the alkyd coating increased the potential (100–150 mV) (Nazarov and Thierry, 2004b, 2005). This can be explained by the formation of dipoles according to Equations (11) and (12). Alkyds contain acidic groups, and their interactions with the surface hydroxide OH-Me result in a negative charge in the coating layer and a positive charge on the metal oxide surface. Protonation of the amino groups of the epoxy coating by the OH-Me groups of the surface hydroxides creates a positive



charge in the coating and a negative charge on the metal surface (Equation 12). The potential change across the interface due to the formation of metal oxide-polymer dipoles can be illustrated by the following equation:

$$\Delta\varphi = -4\pi\alpha\mu N_S, \quad (13)$$

where $\Delta\varphi$ is the potential drop across the interface, N_S is the surface coverage, μ is the effective dipole moments of the adsorbed complexes, and α is polarizability (Nazarov and Thierry, 2004b, 2005; Nazarov et al., 2008).

Ingression of the water separates the interface, decreased the dipole moment and the potential drop (Equation 13), and coated surface exhibits the potential close to the values of bare metal surface (Nazarov and Thierry, 2005; Nazarov et al., 2008). However, this process is reversible, and drying the sample restores the dipoles and the initial high potential drop of coated metals with adhesive bonds (Nazarov et al., 2008). The potential changes that occur during water ingress are related to the formation of a thin aqueous film at the interface, which can lead to hydrolysis. On the other hand, a small amount of water at the interface is beneficial for increasing the degree of hydroxylation of the surface oxide (O-Me-OH) and creating anchoring hydrogen bonds that improve the interfacial durability (Nazarov et al., 2008). Aging of the samples decreased variation of the potential during wet-dry cycles and irreversibly decreased the potential drop $\Delta\varphi$ (Equation 13). Thus, the chemistry and the strength of interactions at the interface can be monitored during exposure of the adhesive joints.

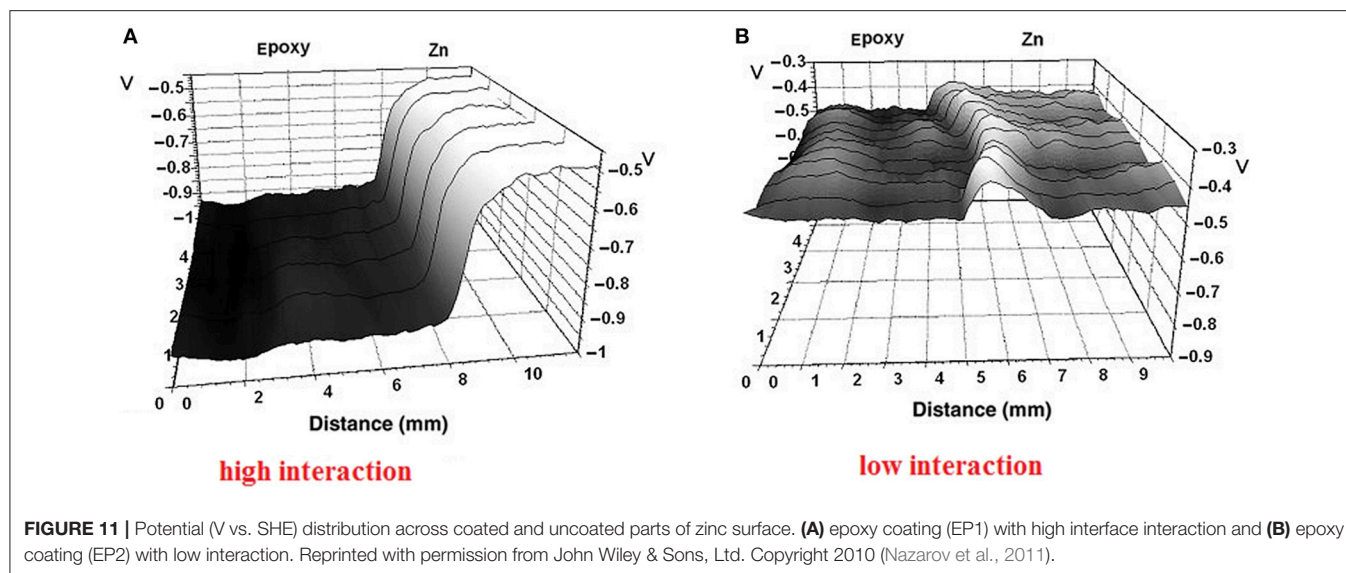
Different epoxy coatings interact differently with the metal surface and create dipoles with different coverage that can be used for SKP ranking according to the adhesive force and interfacial interactions (Nazarov et al., 2011). It has been found that epoxy hardeners containing diamino groups, which are used in two-component epoxy coatings (EP1), could dissolve surface oxides (ZnO), creating stable complexes and an interphase with a mixed organic-inorganic nature. This interaction created a large potential drop across the interface and provided the highest adhesion and water stability to the metal-epoxy polymer (EP1) joint (Figure 11A; Nazarov et al., 2011). In contrast, another

epoxy coating (EP2), which has a low adhesion to metal, showed a low potential drop (Figure 11B; Nazarov et al., 2011).

These points are in agreement with SKP measurements of the potential shifts of iron surfaces with adsorbed carboxylic acids, amines and amides (Wielant et al., 2008, 2010; Nazarov et al., 2011). The adsorption of amines can simulate the epoxy/amine coating systems described above. The adsorption of carboxylic acids shifted the potential in the positive direction (Equation 11), whereas adsorption of amines and amides induced a negative potential shift of 400–500 mV (Equation 12). Brønsted acid–base interactions change the overall dipole moment. The potential shift increased with the degree of protonation on the surface and increased with the amount of surface hydroxide groups (Wielant et al., 2008, 2010). These results are in line with the SKP study on the adsorption of amines and an epoxy coating on Al hydroxylated surfaces (Salgin et al., 2013b). It has been shown that the interaction of N-methyldiethanolamine in the epoxy coating with hydroxide groups on the Al surface decreased the potential of the epoxy-coated Al. The value of the potential drop could be controlled by the amount of hydroxyl groups in the oxide. In addition, the amount of interfacial dipoles can be increased by modifying the chain of an adsorbed amine with hydroxide groups (Wielant et al., 2007). Thus, the application of SKP enables new possibilities for controlling the metal-coating interface with the aim of increasing the adhesion and stability to hydrolyze of the metal-polymer bonds.

SKP Assessment of Metal Surface Pretreatments and Improvement of the Stability of the Interface to Corrosive De-adhesion

The surface energies of metallic substrates are much higher than the surface energies of polymers. This difference decreases the energy of the interfacial interactions and the stability of the contacts. Thus, we have to modify metal surfaces and create the interphases with intermediate properties to obtain good interactions with the polymer. The role of these pretreatments is to increase metal-polymer adhesion under dry and wet conditions, obtain an interface with high dielectric properties that inhibit oxygen reduction, and provide correspondingly high stability against corrosion driven delamination. In addition, the



interface has to decelerate the migration of ions along the interface, which circulate in the galvanic cells.

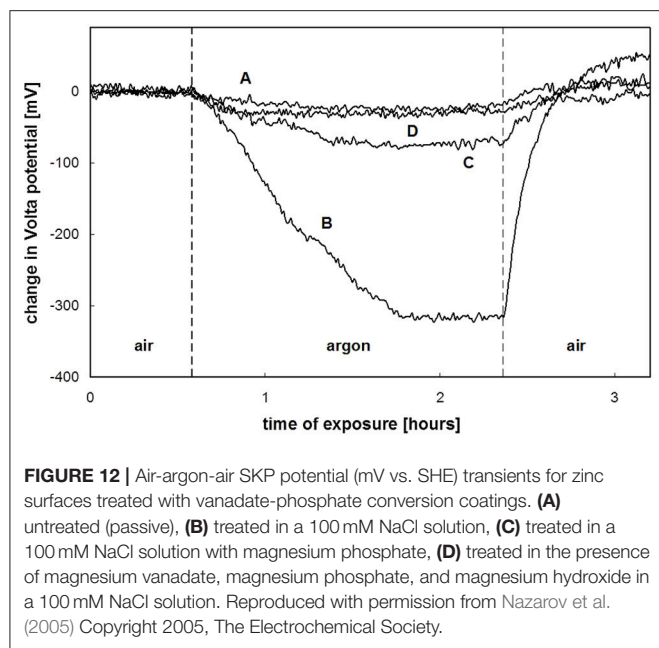
The correlations between the oxide surface energy of the substrate, the adhesion force of the polymer film in corrosive environments and the delamination rate from the defect site as a function of the pretreatment was shown (Wielant et al., 2009). The SKP technique has normally been used to detect the displacement of the de-adhesion front under the polymeric coating from the defect site, as discussed above. Steel surfaces were pretreated in different ways, creating surface hydroxides with different surface energies and polar components (Wielant et al., 2009). It was shown that cathodic delamination decelerates with increase of polar oxide surface energy and the adhesion interactions at the oxide-coating interface.

Additionally to adhesion, interfacial ion mobility is a key parameter in the work of surface galvanic elements on coated galvanized steel and aluminum alloy (Klimow et al., 2007; Posner et al., 2009, 2013, 2014; Salgin et al., 2013a). Cations move during the spreading of the cathodic reactions, and anions migrate across the interface during anodic undermining (Figure 1). The fixed surface charges (ion-exchange groups) determine the ion mobility that can be determined using SKP. Thus, controlled modification of the surface chemistry could selectively hinder or activate the mobility of the desired charge carriers to better control the electrochemical processes occurring on the oxide surface (Posner et al., 2009; Salgin et al., 2013a).

SKP can be used to study the properties of thin conversion films on steel, aluminum or galvanized steel surfaces without the deposition of a top coat. SKP was applied to phosphated zinc surfaces (galvanized steel) to study their ability to reduce oxygen in a humid atmosphere (Nazarov and Thierry, 1998). It was shown that the phosphated surfaces contaminated with carbon microparticles increased the transients of potential during exchange air to argon atmosphere. The cathodic particles were localized in the SKP maps as locations with more positive

potentials relatively to the background level of phosphated zinc. Complete phosphating and replacing of the surface zinc oxide by phosphate decreased the surface potential. Thus, the potential measurements can be used for determination of the quality of phosphatation and the presence of cathodic contaminants (Nazarov and Thierry, 1998).

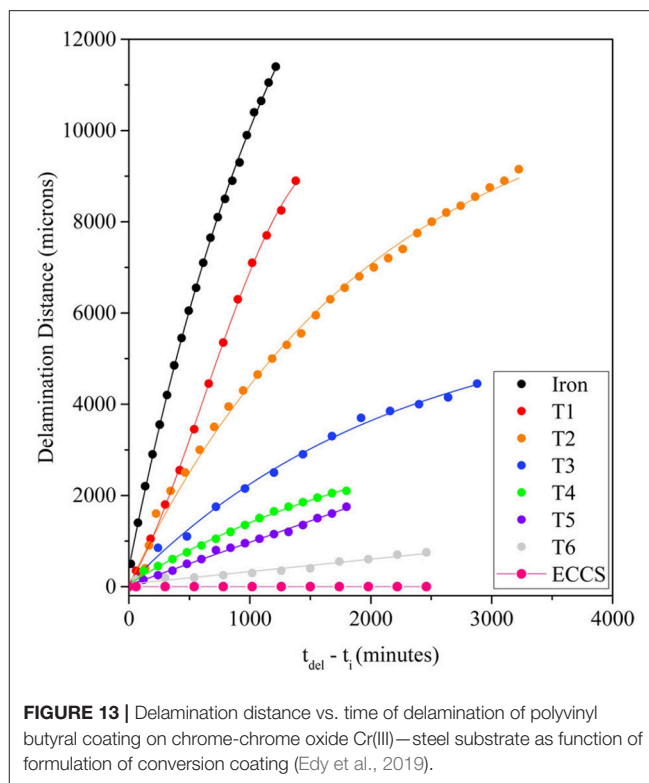
Investigation of the Zn/ZnO electrode using SKP (Nazarov et al., 2015) showed that cathodic spreading is effect of the semiconducting ZnO film participating in the oxygen reduction reaction. A decrease in the ZnO thickness decreased the potential of Zn and inhibited cathodic spreading. From these results, was concluded that effective pretreatment has to decrease the potential of Zn due to the formation of more dielectric and less catalytic deposits (Nazarov et al., 2005). Chromate conversion coatings have shown excellent inhibition of the corrosion. Normally, chromating creates Zn surfaces with extremely negative potentials (-0.7 V vs. SHE) (Nazarov et al., 2005). To replace chromates, different compositions have been developed, and SKP has been useful for selecting the right compositions on the base of vanadate and magnesium phosphates (Nazarov et al., 2005; Gao et al., 2018). Figure 12 shows SKP potential transients as a result of exchanging the air atmosphere for an argon atmosphere. The magnitudes of the potential variations are proportional to the inhibition ability of the pretreated surface to adsorb and reduce oxygen. Thus, the lowest potential deviations during exchange of the atmosphere were seen in compositions containing magnesium vanadate and magnesium phosphate that were comparable with the effect of SrCrO_4 species (Nazarov et al., 2005). The results showed that the addition of magnesium ions was important for inhibition of oxygen reduction on the zinc surface that is in line with the studies of ion-exchange pigments leaching magnesium cations (Dodds et al., 2017; Williams and McMurray, 2017). Additionally, using SKP and XPS, V(IV) species were seen to be cathodic inhibitors of zinc corrosion. The protection was related to the formation and enrichment



of the coating by V(IV) species over increasing exposure times (Gao et al., 2018).

Currently, Zr- and Ti-containing compositions were formulated to achieve better corrosion protection of zinc alloys and steels (Khun and Frankel, 2015; Lostak et al., 2016; Sababi et al., 2017; Milosev and Frankel, 2018). SKP measured the potential distribution and delamination kinetics in the vicinity of artificial defects (Milosev and Frankel, 2018). It was shown that a Zr-based treatment could decrease the electromotive force in cathodic galvanic elements and correspondingly the delamination rates of different coatings (Khun and Frankel, 2015; Lostak et al., 2016). Another silane-Zr-based conversion layers decelerated the electron transfer rate and coating delamination from galvanized steel due to the electron insulating properties of the ZrO_2 conversion coating (Lostak et al., 2016).

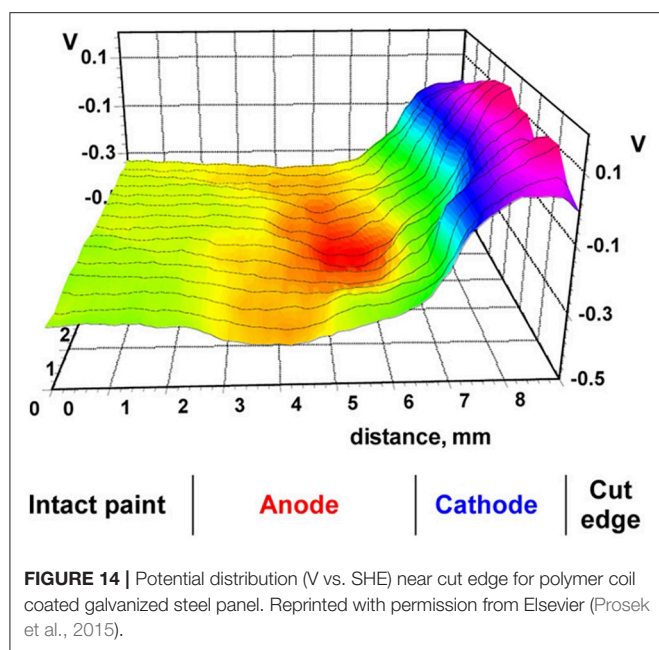
Important SKP works investigated the stability of polymer coated and pre-treated steels, which are applying to packaging materials (Wint et al., 2015, 2016; Edy et al., 2019). Thus, this technique was used *in situ* to compare the stability of a polyvinyl butyral coating deposited on steel substrate that was pre-coated by chromium/chromium oxide layers deposited from bath containing Cr(VI) or Cr(III) species (Wint et al., 2016). It was found that the system containing Cr(VI) species was fully resistant to all kinds of deadhesion. The conversion coating deposited from electrolyte contained Cr(III) species showed cathodic and anodic disbonding. However, cathodic delamination rate of polymeric coating pretreated by Cr(III) compositions significantly decreased after developing of the coatings (Edy et al., 2019). **Figure 13** shows the cathodic delamination rates as a function of the formulations. It was found that the conversion coating diminished electrocatalytic activity for cathodic oxygen reduction process that correlate with a decrease in the delamination rate (Edy et al., 2019). Similar SKP study of



delamination of organic lacquer from tin-iron packing materials was carried out (Wint et al., 2015). It was found that tin and iron-tin intermetallics decrease the rate of cathodic oxygen reduction that also improved the coating stability to cathodic disbonding.

Surface modification of aluminum alloys is important for creating stable metal-polymer interfaces. Normally, deadhesion of the epoxy coating from an untreated Al substrate starts immediately after the ingress of water to the interface (Nazarov and Thierry, 2004b, 2005). This is the result of a low surface density of hydroxide groups in Al_2O_3 , which cannot sufficiently bond with the functional groups of the coating (Salgin et al., 2013b). To solve this problem, SKP was successfully applied to find the correlations between type of Al surface modification, the density of the surface hydroxide groups and the Volta potential (Özkanat et al., 2012).

To have high stability of electrophoretic epoxy coatings on Al alloys substrates is an important issue for the automotive industry. SKP study (Nazarov et al., 2012b) compared the development of filiform corrosion as function of different sol-gel pretreatments (amino-silanes, silane- ZrO_2 (Oxsilan), and sol-gel nanoclays). It was found that some amino-silanes can accelerate anodic undermining of electrophoretic coating. Amines have a positive charge due to their protonation, which decreases the potential of the interface. After exposure, SKP found extended interfacial area that was activated by migration of the chloride ions from the defect site along the interface. Fast corrosive deadhesion of the coating can be an effect of the positive amino groups, which accelerate



the migration of negative chloride ions according to the ion-exchange mechanism. Other compositions decreased the area of activation and the rate of filaments spreading from the defect site (Nazarov et al., 2012b).

SKP Assessment of the Corrosion Stability of Coil Coated Hot Deep Galvanized Steels

Highly stable interface for polymer coated galvanized steel is important issue for automotive and building industries. SKP was successfully applied to study these novel Zn-Mg and Zn-Mg-Al alloys for galvanized steel with polymeric coatings (Hausbrand et al., 2003, 2009; Prosek et al., 2008, 2015; Vimalanandan et al., 2014; Davies et al., 2015). Due to the selective oxidation, the oxide film in the alloys consists of MgO, which is a perfect dielectric material and has poor electrocatalytic properties for reducing of oxygen (Prosek et al., 2008). In addition, due to the enrichment of the oxide film by MgO, the material obtains a low potential and small electromotive force for galvanic cells driving cathodic coating deadhesion (Hausbrand et al., 2009; Vimalanandan et al., 2014). Thus, alloying of zinc by Mg inhibits the cathodic delamination of polymeric coating significantly (Hausbrand et al., 2003, 2009). The strong inhibition of spreading of cathodic reaction was observed for Zn-Mg alloys with small additions of Cr, Zr, and Ti (Nazarov et al., 2017). However, Mg is remaining main component in the alloy inhibiting work of cathodic galvanic element.

Cut-edge corrosion is kind of degradation of coil coated galvanized steels. It is anodic undermining mode of coating deadhesion that is result of work galvanic element consisting from steel substrate (cathode) and the interface Zn/ZnO/polymeric coating (anode) (Figure 14).

The electromotive force (0.4–0.5 V) between anode and cathode governs coating anodic deadhesion. Different industrial coil coatings were studied using SKP to find the effective pigments, pretreatments, composition of alloys, which decrease the rate of cut edge corrosion (Prosek et al., 2012, 2015, 2016a,b; Nazarov et al., 2017). Thus, these SKP studies were important for developing of new more corrosion stable coil coated products.

CONCLUSIONS

1. A review of the literature shows that scanning Kelvin probe is a highly effective technique for assessment of corrosion of metals underneath of dielectric polymeric coatings. Non-uniform distribution of electrochemical potential leads to work of galvanic elements and to coating deadhesion. SKP measures the potential distribution along the interface that helps to predict the coatings failure. Cathodic delamination and anodic undermining modes of corrosion driven de-adhesion can be distinguished.

2. The rate of propagation of the de-adhesion front from the defect site can be determined. The pigments in coatings decrease the rate of oxygen diffusion and inhibit cathodic disbondment. Conversion coatings, adhesion promoters and corrosion inhibitors increased the stability of an interface to anodic undermining. SKP can be used to find the effect of pretreatment on ionic conductivity along the interface controlling acceleration/deceleration effect of galvanic elements.

3. SKP is perspective technique that can determine *in situ* the nature of adhesive bonds and their stabilities. It can be used for engineering of the developed coatings and interfaces.

4. SKP technique helps quickly select most promising and long lasting protective industrial paints. The technique analyses the interface underneath the multilayer coatings *in situ*. Typically, only short-term corrosion exposure has to be employed to predict coating stability.

Thick marine paints and compositions containing zinc rich primers for marine and offshore application can be quickly ranked. Electrophoretic paints on galvanized steel or aluminum substrates used in automotive industry can be evaluated as function of curing or pretreatment chemistry. Coil coated materials used in automotive and architecture industries can be investigated in order to choose effective pretreatment, pigment and alloy composition.

AUTHOR CONTRIBUTIONS

AN was expert in application of electrochemical techniques to study corrosion and degradation of metal-polymer joints. DT was expert in theory of corrosion and electrochemistry, corrosion testing, corrosion protection by polymeric, and metallic coatings. The article was written in close collaboration.

REFERENCES

- Bi, H., and Sykes, J. (2016). Cathodic delamination of unpigmented and pigmented epoxy coatings from mild steel. *Prog. Org. Coat.* 90, 114–125. doi: 10.1016/j.porgcoat.2015.10.002
- Bi, H., and Sykes, J. M. (2011). Cathodic disbonding of an unpigmented epoxy coating on mild steel under semi- and full-immersion conditions. *Corros. Sci.* 53, 3416–3425. doi: 10.1016/j.corsci.2011.06.021
- Davies, J. L., Glover, C. F., Van de Langkruis, J., Zoestbergen, E., and Williams, G. (2015). The effect of Mg concentration on the resistance of PVD Zn-Mg coatings to corrosion driven organic coating delamination. *Corros. Sci.* 100, 607–618. doi: 10.1016/j.corsci.2015.08.036
- de la Fuente, D., and Rohwerder, M. (2008). Fundamental investigation on the stability of the steel/coating interfaces contaminated by submicroscopic salt particles. *Prog. Org. Coat.* 61, 233–239. doi: 10.1016/j.porgcoat.2007.07.035
- Dodds, P. C., Williams, G., and Radcliffe, J. (2017). Chromate-free smart release corrosion inhibitive pigments containing cations. *Prog. Org. Coat.* 102, 107–114. doi: 10.1016/j.porgcoat.2016.05.005
- Edy, J. E., McMurray, H. N., Lammers, K. R., and de Vooys, A. C. A. (2019). Kinetics of corrosion-driven cathodic disbondment on organic coated trivalent chromium metal-oxide-carbide coatings on steel. *Corros. Sci.* 157, 51–61. doi: 10.1016/j.corsci.2019.04.037
- Evans, S. D., and Ulman, A. (1990). Surface potential studies of alkyl-thiol monolayers adsorbed on gold. *Chem. Phys. Lett.* 170, 462–466. doi: 10.1016/S0009-2614(90)87085-6
- Frankel, G. S., Stratmann, M., Rohwerder, M., Michalik, A., Maier, B., Dora, J., et al. (2007). Potential control under thin aqueous layers using a Kelvin Probe. *Corros. Sci.* 49, 2021–2036. doi: 10.1016/j.corsci.2006.10.017
- Funke, W. (1979). The role of adhesion in corrosion protection by organic coatings. *J. Oil Col. Chem. Assoc.* 70, 63–75.
- Funke, W. (1981). Blistering of paint films and filiform corrosion. *Prog. Org. Coat.* 9, 29–46. doi: 10.1016/0033-0655(81)80014-3
- Furbeth, W., and Stratmann, M. (2001a). The delamination of polymeric coatings from electrogalvanized steel – a mechanistic approach. – Part 1: delamination from a defect with intact zinc layer. *Corros. Sci.* 43, 207–227. doi: 10.1016/S0010-938X(00)00047-0
- Furbeth, W., and Stratmann, M. (2001b). The delamination of polymeric coatings from electrogalvanized steel – a mechanistic approach. Part 2: delamination from a defect down to steel. *Corros. Sci.* 43, 229–241. doi: 10.1016/S0010-938X(00)00048-2
- Furbeth, W., and Stratmann, M. (2001c). The delamination of polymeric coatings from electrogalvanized steel – a mechanistic approach. Part 3: delamination kinetics and influence of CO₂. *Corros. Sci.* 43, 243–254. doi: 10.1016/S0010-938X(00)00049-4
- Gao, Z., Zhang, D., Jiang, S., Zhang, Q., and Lia, X. (2018). XPS investigations on the corrosion mechanism of V (IV) conversion coatings on hot-dip galvanized steel. *Corros. Sci.* 139, 163–171. doi: 10.1016/j.corsci.2018.04.030
- Glover, C. F., Richards, C., Baker, J., Williams, G., and McMurray, H. N. (2017). In-coating graphene nano-platelets for environmentally friendly corrosion protection of iron. *Corros. Sci.* 114, 169–172. doi: 10.1016/j.corsci.2016.11.009
- Glover, C. F., Richards, C. A. J., Williams, G., and McMurray, H. N. (2018). Evaluation of multi-layered graphene nano-platelet composite coatings for corrosion control part II – Cathodic delamination kinetics. *Corros. Sci.* 136, 304–310. doi: 10.1016/j.corsci.2018.03.014
- Glover, C. F., and Williams, G. (2017). Inhibition of corrosion-driven organic coating delamination and filiform corrosion on iron by phenyl phosphonic acid. *Prog. Org. Coat.* 102, 44–52. doi: 10.1016/j.porgcoat.2016.03.006
- Grundmeier, G., Rossenbeck, B., Roschmann, K. J., Ebbinghaus, P., and Stratmann, M. (2006). Corrosion protection of Zn-phosphate containing water borne dispersion coatings Part 2: Investigations of the corrosive de-adhesion of model latex coatings on iron. *Corros. Sci.* 48, 3716–3730. doi: 10.1016/j.corsci.2006.01.007
- Grundmeier, G., Schmidt, W., and Stratmann, M. (2000). Corrosion protection by organic coatings: electrochemical mechanism and novel methods of investigation. *Electrochim. Acta* 45, 2515–2533. doi: 10.1016/S0013-4686(00)00348-0
- Grundmeier, G., and Stratmann, M. (1999). Influence of oxygen and argon plasma treatments on the chemical structure and redox state of oxide covered iron. *J. Appl. Surf. Sci.* 141, 43–56. doi: 10.1016/S0169-4332(98)00617-5
- Hackerman, N., and Lee, E. H. (1955). The effect of gases on the contact potential of evaporated metal films. *J. Phys. Chem.* 59, 900–906. doi: 10.1021/j150531a023
- Hamade, R. F., and Dillard, D. A. (2005). Assessing the effects of shear, compression, and peel on the cathodic degradation of elastomer-to-metal adhesive bonds. *Int. J. Adhes. Adhes.* 25, 147–163. doi: 10.1016/j.ijadhadh.2004.06.002
- Hausbrand, R., Stratmann, M., and Rohwerder, M. (2003). Delamination resistant zinc alloys: simple concept and results on the system zinc–magnesium. *Steel Res. Int.* 74, 453–458. doi: 10.1002/srin.200300212
- Hausbrand, R., Stratmann, M., and Rohwerder, M. (2008). The physical meaning of electrode potentials at metal surfaces and polymer/metal interfaces: consequences for delamination. *J. Electrochem. Soc.* 155, C369–C379. doi: 10.1149/1.2926589
- Hausbrand, R., Stratmann, M., and Rohwerder, M. (2009). Corrosion of zinc–magnesium coatings: mechanism of paint delamination. *Corros. Sci.* 51, 2107–2114. doi: 10.1016/j.corsci.2009.05.042
- Hernández, M. A., Galliano, F., and Landolt, D. (2004). Mechanism of cathodic delamination control of zinc–aluminum phosphate pigment in waterborne coatings. *Corros. Sci.* 46, 2281–2300. doi: 10.1016/j.corsci.2004.01.009
- Hölzl, J., and Schulte, F. K. (1979). “Work function of metals,” in *Solid Surface Physics*, eds J. Hölzl, F. K. Schulte, and H. Wagner (Berlin; Heidelberg; New York, NY: Springer–Verlag), 9.
- Huang, V. M., Wu, S. L., Orazem, M. E., Pebere, N., Tribollet, B., and Vivier, V. (2011). Local electrochemical impedance spectroscopy: a review and some recent developments. *Electrochim. Acta* 56, 8048–8057. doi: 10.1016/j.electacta.2011.03.018
- Kendig, M., and Mills, D. J. (2017). An historical perspective on the corrosion protection by paints. *Prog. Org. Coat.* 102, 53–59. doi: 10.1016/j.porgcoat.2016.04.044
- Khun, N. W., and Frankel, G. S. (2013). Effects of surface roughness, texture and polymer degradation on cathodic delamination of epoxy coated steel samples. *Corros. Sci.* 67, 152–160. doi: 10.1016/j.corsci.2012.10.014
- Khun, N. W., and Frankel, G. S. (2015). Effect of hexafluorozirconic acid pretreatment on cathodic delamination of epoxy coating from steel substrates. *Corrosion* 71, 277–284. doi: 10.5006/1407
- Khun, N. W., and Frankel, G. S. (2016). Cathodic delamination of polyurethane/multiwalled carbon nanotube composite coatings from steel substrates. *Prog. Org. Coat.* 99, 55–60. doi: 10.1016/j.porgcoat.2016.05.002
- Kinsella, E. M., and Mayne, J. E. O. (1969). Ionic conduction in polymer films I. influence of electrolyte on resistance. *Br. Polym. J.* 1, 173–176. doi: 10.1002/pi.4980010405
- Klimow, G., Fink, N., and Grundmeier, G. (2007). Electrochemical studies of the inhibition of the cathodic delamination of organically coated galvanized steel by thin conversion films. *Electrochim. Acta* 53, 1291–1300. doi: 10.1016/j.electacta.2007.05.045
- Le Bozec, N., Persson, D., Nazarov, A., and Thierry, D. (2002). Investigation of filiform corrosion on coated aluminium alloys by FTIR micro-spectroscopy and scanning Kelvin probe. *J. Electrochem. Soc.* 149, B403–B408. doi: 10.1149/1.1497172
- Leblanc, P. P., and Frankel, G. S. (2004). Investigation of filiform corrosion of epoxy-coated. 1045 carbon steel by scanning Kelvin probe force microscopy. *J. Electrochem. Soc.* 151, B105–B113. doi: 10.1149/1.1641038
- Leidheiser, H., and Granata, R. D. (1988). Ion transport through protective polymeric coatings exposed to an aqueous phase. *IBM J. Res. Dev.* 32:582. doi: 10.1147/rd.325.0582
- Leidheiser, H., Wang, W., and Igetoft, L. (1983). The mechanism for cathodic delamination of organic coatings from a metal surface. *Prog. Org. Coat.* 11, 19–40. doi: 10.1016/0033-0655(83)80002-8
- Leng, A., Streckel, H., and Stratmann, M. (1999a). The delamination of polymeric coatings from steel. Part 1 Calibration of the Kelvin probe and basic delamination mechanism. *Corros. Sci.* 41, 547–578. doi: 10.1016/S0010-938X(98)00166-8
- Leng, A., Streckel, H., and Stratmann, M. (1999b). The delamination of polymeric coatings from steel. Part 2. First stage of delamination effect of type and

- concentration of cations on delamination, chemical analysis of the interface. *Corros. Sci.* 41, 579–597. doi: 10.1016/S0010-938X(98)00167-X
- Lostak, T., Timma, C., Krebs, S., Flock, J., and Schulz, S. (2016). Organosilane modified Zr-based conversion layer on Zn–Al alloy coated steel sheets. *Surf. Coat. Technol.* 305, 223–230. doi: 10.1016/j.surfcoat.2016.08.030
- Mayne, J. E. O., and Scantlebury, J. D. (1970). Ionic conduction in polymer films II. inhomogeneous structure of varnish films. *Br. Polym. J.* 2, 240–243. doi: 10.1002/pi.4980020407
- McMurray, H. N., Holder, A., Williams, G., Scamans, G. M., and Coleman, A. J. (2010). The kinetics and mechanisms of filiform corrosion on aluminium alloy AA6111. *Electrochimica Acta* 55, 7843–7852. doi: 10.1016/j.electacta.2010.04.035
- Mills, D. J., and Jamali, S. S. (2017). The best tests for anti-corrosive paints. And why: a personal viewpoint. *Prog. Org. Coat.* 102, 8–17. doi: 10.1016/j.porgcoat.2016.04.045
- Milosev, I., and Frankel, G. S. (2018). Review. Conversion coatings based on zirconium and/or titanium. *J. Electrochem. Soc.* 165, C127–C144. doi: 10.1149/2.0371803jes
- Nazarov, A., Diler, E., Persson, D., and Thierry, D. (2015). Electrochemical and corrosion properties of ZnO/Zn electrode in atmospheric environments. *J. Electroanal. Chem.* 737, 129–140. doi: 10.1016/j.jelechem.2014.07.029
- Nazarov, A., Le Bozec, N., and Thierry, D. (2018a). Assessment of steel corrosion and deadhesion of epoxy barrier paint by scanning Kelvin probe. *Prog. Org. Coat.* 114, 123–134. doi: 10.1016/j.porgcoat.2017.09.016
- Nazarov, A., Le Bozec, N., and Thierry, D. (2018b). Scanning Kelvin Probe assessment of steel corrosion protection by marine paints containing Zn-rich primer. *Prog. Org. Coat.* 125, 61–72. doi: 10.1016/j.porgcoat.2018.08.024
- Nazarov, A., le Bozec, N., Thierry, D., le Calve, P., and Pautasso, J.-P. (2012a). Scanning Kelvin probe investigation of corrosion under thick marine paint systems applied on carbon steel. *Corrosion* 68, 720–729. doi: 10.5006/0551
- Nazarov, A., Olivier, M.-G., and Thierry, D. (2012). SKP and FT-IR microscopy study of the paint corrosion de-adhesion from the surface of galvanized steel. *Prog. Org. Coat.* 74, 356–364. doi: 10.1016/j.porgcoat.2011.10.009
- Nazarov, A., Prosek, T., and Thierry, D. (2008). Application of EIS and SKP methods for the study of the zinc/polymer interface. *Electrochim. Acta* 53, 7531–7538. doi: 10.1016/j.electacta.2007.11.053
- Nazarov, A., Romano, A.-P., Fedel, M., Deflorian, F., Thierry, D., and Olivier, M.-G. (2012b). Filiform corrosion of electrocoated aluminium alloy: role of the pre-treatment. *Corros. Sci.* 65, 187–198. doi: 10.1016/j.corsci.2012.08.013
- Nazarov, A., and Thierry, D. (1998). Analysis of surface carbon contamination on phosphated zinc surface by scanning Kelvin probe. *J. Electrochem. Soc.* 145, L39–L42. doi: 10.1149/1.1838334
- Nazarov, A., and Thierry, D. (1999). “A scanning Kelvin Probe Study of the delamination processes at the carbon steel /polymer interface,” in *EFC Series, Vol. 28*, eds P. L. Bonora and F. Deflorian (London: IOM Communications), 73–78.
- Nazarov, A., and Thierry, D. (2004a). Rate-determining reactions of atmospheric corrosion. *Electrochim. Acta* 49, 2717–2724. doi: 10.1016/j.electacta.2004.01.066
- Nazarov, A., and Thierry, D. (2007). Application of Volta potential mapping to determine metal surface defects. *Electrochim. Acta* 52, 7689–7696. doi: 10.1016/j.electacta.2007.05.077
- Nazarov, A., and Thierry, D. (2010). Influence of electrochemical conditions in a defect on the mode of paint corrosion delamination from a steel surface. *Corrosion* 66:025004-1/025004-10. doi: 10.5006/1.3319661
- Nazarov, A., Thierry, D., and Prosek, T. (2017). Formation of galvanic cells and localized corrosion of zinc and zinc alloys under atmospheric conditions. *Corrosion* 73, 77–86. doi: 10.5006/2139
- Nazarov, A., Thierry, D., Prosek, T., and Le Bozec, N. (2005). Protective action of vanadate at defected areas of organic coatings on zinc. *J. Electrochem. Soc.* 152, B220–B227. doi: 10.1149/1.1924067
- Nazarov, A., Thierry, D., Volovitch, P., and Ogle, K. (2011). An SKP and EIS investigation of amine adsorption on zinc oxide surfaces. *Surf. Interface Anal.* 43, 1286–1298. doi: 10.1002/sia.3170
- Nazarov, A. P., and Thierry, D. (2004b). Scanning Kelvin probe study of metal/polymer interfaces. *Electrochimica Acta* 49, 2955–2964. doi: 10.1016/j.electacta.2004.01.054
- Nazarov, A. P., and Thierry, D. (2005). Hydrolyze of interfacial bonds in a double electric layer metal-polymer. *Prot. Metals* 41, 105–116. doi: 10.1007/s11124-005-0015-2
- Negele, O., and Funke, W. (1996). Internal stress and wet adhesion of organic coatings. *Prog. Org. Coat.* 28, 285–289. doi: 10.1016/0300-9440(95)00606-0
- Ogle, K., Baudu, V., Garrigues, L., and Philippe, X. (2000). Localized electrochemical methods applied to cut edge corrosion. *J. Electrochem. Soc.* 147, 3654–3660. doi: 10.1149/1.1393954
- Özkanat, Ö., Salgin, B., Rohwerder, M., Mol, J. M. C., de Wit, J. H. W., and Terryn, H. (2012). Scanning Kelvin probe study of (oxyhydr)oxide surface of aluminum alloy. *J. Phys. Chem. C* 116, 1805–1811. doi: 10.1021/jp205585u
- Philippe, L. V. S., Walter, G. W., and Lyon, S. B. (2003). Investigating localized degradation of organic coatings. *J. Electrochem. Soc.* 150, B111–B119. doi: 10.1149/1.1554913
- Posner, R., Fink, N., Giza, G., and Grundmeier, G. (2014). Corrosive delamination and ion transport along stretch-formed thin conversion films on galvanized steel. *Surf. Coat. Technol.* 253, 227–233. doi: 10.1016/j.surfcoat.2014.05.041
- Posner, R., Fink, N., Wolpers, M., and Grundmeier, G. (2013). Electrochemical electrolyte spreading studies of the protective properties of ultra-thin films on zinc galvanized steel. *Surf. Coat. Technol.* 228, 286–295. doi: 10.1016/j.surfcoat.2013.04.042
- Posner, R., Wapner, K., Stratmann, M., and Grundmeier, G. (2009). Transport processes of hydrated ions at polymer/oxide/metal interfaces: Part. 1. Transport at interfaces of polymer-coated oxide covered iron and zinc substrates. *Electrochim. Acta* 54, 891–899. doi: 10.1016/j.electacta.2008.06.074
- Prosek, T., Nazarov, A., Bexell, U., Thierry, D., and Serak, J. (2008). Corrosion mechanism of model zinc-magnesium alloys in atmospheric conditions. *Corros. Sci.* 50, 2216–2231. doi: 10.1016/j.corsci.2008.06.008
- Prosek, T., Nazarov, A., Goodwin, F., and Šerák, J., Thierry, D. (2016a). Improving corrosion stability of Zn–Al–Mg by alloying for protection of car bodies. *Surf. Coat. Technol.* 101, 45–50. doi: 10.1016/j.surfcoat.2016.03.062
- Prosek, T., Nazarov, A., Le Gac, A., and Thierry, D. (2015). Coil-coated Zn–Mg and Zn–Al–Mg: effect of climatic parameters on the corrosion at cut edges. *Prog. Org. Coat.* 83, 26–35. doi: 10.1016/j.porgcoat.2015.01.023
- Prosek, T., Nazarov, A., and Stoullil, T. D. (2012). Evaluation of the tendency of coil-coated materials to blistering: field exposure, accelerated tests and electrochemical measurements. *Corros. Sci.* 61, 92–100. doi: 10.1016/j.corsci.2012.04.026
- Prosek, T., Nazarov, A., Xue, H. B., Lamaka, S., and Thierry, D. (2016b). Role of steel and zinc coating thickness in cut edge corrosion of coil-coated materials in atmospheric weathering conditions; Part. 1: Laboratory study. *Prog. Org. Coat.* 99, 356–364. doi: 10.1016/j.porgcoat.2016.06.013
- Reddy, B., Doherty, M. J., and Sykes, J. M. (2004). Breakdown of organic coatings in corrosive environments examined by scanning kelvin probe and scanning acoustic microscopy. *Electrochim. Acta* 49, 2965–2972. doi: 10.1016/j.electacta.2004.01.055
- Reddy, B., and Sykes, J. M. (2005). Degradation of organic coatings in a corrosive environment: a study by scanning Kelvin probe and scanning acoustic microscope. *Prog. Organ. Coat.* 52, 280–287. doi: 10.1016/j.porgcoat.2004.04.004
- Romano, A.-P., Olivier, M.-G., Nazarov, A., and Thierry, D. (2009). Influence of cross-linking density of a cataphoretic coating on initiation and propagation of filiform corrosion of AA6016. *Prog. Org. Coat.* 66, 173–182. doi: 10.1016/j.porgcoat.2009.06.015
- Rossi, S., Fedel, M., Deflorian, F., and del Carmen Vadillo, M. (2008). Localized electrochemical techniques: theory and practical examples in corrosion studies. *C. R. Chimie* 11, 984–994. doi: 10.1016/j.crci.2008.06.011
- Sababi, M., Terryn, H., and Mol, J. M. C. (2017). The influence of a Zr-based conversion treatment on interfacial bonding strength and stability of epoxy coated carbon steel. *Prog. Org. Coat.* 105, 29–36. doi: 10.1016/j.porgcoat.2016.11.016
- Salgin, B., Faycal Hamou, R., and Rohwerder, M. (2013a). Monitoring surface ion mobility on aluminum oxide: effect of chemical pre-treatments. *Electrochim. Acta* 110, 526–533. doi: 10.1016/j.electacta.2013.03.060
- Salgin, B., Özkanat, Ö., Mol, J. M. C., Terryn, H., and Rohwerder, M. (2013b). Role of surface oxide properties on the aluminum/epoxy interfacial bonding. *J. Phys. Chem. C* 117, 4480–4487. doi: 10.1021/jp310121e

- Samec, Z., Johnson, B. W., Capadonia, M., Jauch, M., and Dobhofer, K. (1993). Kelvin probe measurements for chemical analysis: interfacial structure of electrodes exposed to the gas phase containing water vapor. *Sens. Actuators B*. 13–14, 741–742. doi: 10.1016/0925-4005(93)85166-8
- Sharman, C. F. (1944). Filiform underfilm corrosion of lacquered steel surfaces. *Nature* 153, 621–622. doi: 10.1038/153621a0
- Shkrirskiy, V., Uebel, M., Maltseva, A., Lefevre, G., Volovich, P., and Rohwerder, M. (2019). Cathodic driven coating delamination suppressed by inhibition of cation migration along Zn|polymer interface in atmospheric CO₂. *npj Mater. Degrad.* 2, 2–10. doi: 10.1038/s41529-018-0064-z
- Sørensen, P. A., Dam-Johansen, K., Weinle, C. E., and Kiil, S. (2010). Cathodic delamination of seawater-immersed anticorrosive coatings: mapping of parameters affecting the rate. *Prog. Org. Coat.* 68, 283–292. doi: 10.1016/j.porgcoat.2010.03.012
- Stratmann, M. (2005). 2005 W.R. Whitney Award Lecture: corrosion stability of Polymer coated metals- new concepts based on fundamental understanding. *Corrosion* 61, 1115–1126. doi: 10.5006/1.3278148
- Stratmann, M., and Hoffmann, K. (1989). *In situ* Mößbauer spectroscopic study of reactions within rust layers. *Corros. Sci.* 29, 1329–1352. doi: 10.1016/0010-938X(89)90123-6
- Stratmann, M., and Streckel, H. (1990). On the atmospheric corrosion of metals which are covered with thin electrolyte layers. I. verification of electrochemical technique. *Corros. Sci.* 30, 681–686. doi: 10.1016/0010-938X(90)90032-Z
- Stratmann, M., Streckel, H., and Feser, R. (1991). A new technique able to measure directly the delamination of organic polymer films. *Corros. Sci.* 32, 467–470. doi: 10.1016/0010-938X(91)90126-A
- Sykes, J. M., Whyte, E. P., Yu, X., and Shaher Sahir, Z. (2017). Does “coating resistance” control corrosion? *Prog. Org. Coat.* 102, 82–87. doi: 10.1016/j.porgcoat.2016.04.015
- Taylor, D. M. (2000). Developments in the theoretical modelling and experimental measurements of the surface potential of condensed monolayers. *Adv. Colloid Interface Sci.* 87, 183–203. doi: 10.1016/S0001-8686(99)00044-5
- Thomas, N. L. (1991). The barrier properties of paint coatings. *Prog. Org. Coat.* 19, 101–121. doi: 10.1016/0033-0655(91)80001-Y
- Trasatti, S., and Parsons, R. (1986). Interphases in systems of conducting phases. *Pure Appl. Chem.* 58, 437–454. doi: 10.1351/pac198658030437
- Upadhyay, V., and Battocchi, D. (2016). Localized electrochemical characterization of organic coatings: a brief review. *Prog. Org. Coat.* 99, 365–377. doi: 10.1016/j.porgcoat.2016.06.012
- Vimalanandan, A., Bashir, M., and Rohwerder, M. (2014). Zn–Mg and Zn–Mg–Al alloys for improved corrosion protection of steel: some new aspects. *Mater. Corros.* 65, 392–400. doi: 10.1002/maco.201307586
- Wielant, J., Hauffman, T., Blajiev, O., Hausbrand, R., and Terryn, H. (2007). Influence of the iron oxide acid–base properties on the chemisorption of model epoxy compounds studied by XPS. *J. Phys. Chem. C* 111, 13177–13184. doi: 10.1021/jp072354j
- Wielant, J., Posner, R., Grundmeier, G., and Terryn, H. (2008). Interface dipoles observed after adsorption of model compounds on iron oxide films: effect of organic functionality and oxide surface chemistry. *J. Phys. Chem. C* 112, 12951–12957. doi: 10.1021/jp802703v
- Wielant, J., Posner, R., Hausbrand, R., Grundmeier, G., Terryn, H. (2009). Cathodic delamination of polyurethane films on oxide covered steel. Combined adhesion and interface electrochemical studies. *Corros. Sci.* 51, 1664–1670. doi: 10.1016/j.corsci.2009.04.014
- Wielant, J., Posner, R., Hausbrand, R., Grundmeier, G., and Terryn, H. (2010). SKP as a tool to study the physicochemical interaction at buried metal-coating interfaces. *Surf. Interface Anal.* 42, 1005–10009. doi: 10.1002/sia.3512
- Williams, G., and McMurray, H. N. (2001). Chromate inhibition of corrosion-driven organic coating delamination studied using a scanning Kelvin probe technique. *J. Electrochem. Soc.* 148, B377–B385. doi: 10.1149/1.1396336
- Williams, G., and McMurray, H. N. (2003). The mechanism of group (I) chloride initiated filiform corrosion on iron. *Electrochem. Commun.* 5, 871–877. doi: 10.1016/j.elecom.2003.08.008
- Williams, G., and McMurray, H. N. (2004). Inhibition of filiform corrosion on organic-coated AA2024-T3 by smart-release cation and anion-exchange pigments. *Corrosion.* 60, 219–228. doi: 10.5006/1.3287724
- Williams, G., and McMurray, H. N. (2017). Inhibition of corrosion driven delamination on iron by smart-release bentonite cation-exchange pigments studied using a scanning Kelvin probe technique. *Prog. Org. Coat.* 102, 18–28. doi: 10.1016/j.porgcoat.2016.03.004
- Williams, G., McMurray, H. N., Hayman, D., and Morgan, P. C. (2001). Time-lapse potentiometric imaging of active filiform corrosion using a scanning Kelvin probe technique. *Phys. Chem. Com.* 4, 26–31. doi: 10.1039/b100835h
- Wint, N., de Vooy, A. C. A., and McMurray, H. N. (2016). The corrosion of chromium based coatings for packaging steel. *Electrochim. Acta* 203, 326–336. doi: 10.1016/j.electacta.2016.01.100
- Wint, W., Geary, S., McMurray, H. N., Williams, G., de Vooy, A. C. A. (2015). The kinetics and mechanism of atmospheric corrosion occurring on tin and iron-tin intermetallic coated steels. I. cathodic delamination. *J. Electrochem. Soc.* 162, C775–C784. doi: 10.1149/2.0681514jes

Conflict of Interest Statement: The authors declare that the research was conducted in the absence of any commercial or financial relationships that could be construed as a potential conflict of interest.

Copyright © 2019 Nazarov and Thierry. This is an open-access article distributed under the terms of the Creative Commons Attribution License (CC BY). The use, distribution or reproduction in other forums is permitted, provided the original author(s) and the copyright owner(s) are credited and that the original publication in this journal is cited, in accordance with accepted academic practice. No use, distribution or reproduction is permitted which does not comply with these terms.



Recent Development of Corrosion Protection Strategy Based on Mussel Adhesive Protein

Fan Zhang* and Jinshan Pan

Division of Surface and Corrosion Science, Department of Chemistry, KTH Royal Institute of Technology, Stockholm, Sweden

Many of traditional anti-corrosion approaches using chromate are effective but hazardous to natural environment and human health, so development of green and effective alternatives is desirable. One of the mussel adhesive proteins derived from mussel byssus presents extraordinary adhesion to steel surface and exhibits film-forming and corrosion inhibition properties. Novel strategies for enhancing the corrosion inhibition of steel by the protein have been demonstrated recently. The protein together with ceria nanoparticles presents a great potential for the development of new corrosion inhibitors and thin films that are “green” and “effective,” and have “smart” protection properties.

Keywords: mussel adhesive protein, film-forming corrosion inhibitor, corrosion inhibition, self-healing (self-repairing), Mefp-1

OPEN ACCESS

Edited by:

Flavio Defforian,
University of Trento, Italy

Reviewed by:

Benjamin Salas Valdez,
Universidad Autónoma de Baja
California, Mexico
Changdong Gu,
Zhejiang University, China
Isolda Costa,
Instituto de Pesquisas Energéticas e
Nucleares (CNEN), Brazil

*Correspondence:

Fan Zhang
fanzhang@kth.se

Specialty section:

This article was submitted to
Environmental Materials,
a section of the journal
Frontiers in Materials

Received: 28 June 2019

Accepted: 12 August 2019

Published: 27 August 2019

Citation:

Zhang F and Pan J (2019) Recent
Development of Corrosion Protection
Strategy Based on Mussel Adhesive
Protein. *Front. Mater.* 6:207.
doi: 10.3389/fmats.2019.00207

INTRODUCTION

Metal corrosion is a serious material degradation problem from both economic and structural integrity standpoints. Carbon steel is the most widely used metal material, and corrosion of carbon steel occurs in almost all practical environments, but it can be largely controlled by suitable strategies. Because of hazardous nature of traditional corrosion inhibitors, development of green and effective alternatives is desirable.

Mussel adhesive proteins (MAPs), derived from *Mytilus* foot, have been suggested as a basis for environmentally friendly adhesives. Chemical characterization of MAPs started in early eighties (Waite, 1983a). So far at least six adhesive proteins have been extracted and identified from several species of mussel, and named as *Mytilus* foot proteins (*Mfp*, plus a number indicating the chronological order of identification; Zhao et al., 2006). These proteins present a basic isoelectric point due to the high content of posttranslational modified amino acid residues (Waite and Tanzer, 1980; Waite, 1983b). They are classified into three groups according to their function in the mussel foot: *cuticle protein*, *adhesive protein*, and *structural protein*. The 3, 4-dihydroxyphenylalanine (DOPA) has been recognized as the primary residue response for both adhesion and cohesion properties of the proteins.

DIFFERENT MUSSEL ADHESIVE PROTEINS

Cuticle Protein

Mfp-1 is the only protein associated with the protective outer cuticle of byssal threads including plaques (Sun and Waite, 2005). It is the largest foot protein that has a molecular weight of about 108 kDa (Filpula et al., 1990; Holten-Andersen et al., 2009). Its molecule structure is open and extended in the acidic solution with minimized secondary structure (Williams et al., 1989), and consists of 75–80 repetitive decapeptide units with about 15 mol% of DOPA in the sequence (Waite, 2002).

Structural Protein

Mfp-2, *4*, *6* serve as structural proteins in mussel foot. *Mfp-2* is the structural component of the plaque matrix. It has a molecule weight about 42–47 kDa and rich in disulfide containing cysteine of about 6 mol% in repetitive sequence (Rzepecki et al., 1992). Pure *Mfp-2* is prone to form aggregates upon prolonged storage (Rzepecki et al., 1992). *Mfp-4* is the junction between byssal plaque and thread. It has a mass of about 93 kDa and contains an N-terminal histidine-rich domain and a C-terminal domain, which can bound strongly to Cu^{2+} , and calcium-binding plaque proteins, respectively (Zhao and Waite, 2006). *Mfp-6* acts as a conjunction of the interfacial proteins and the plaque matrix protein, and antioxidant of the interfacial proteins to maintain adhesive property of the mussel plaques in oxidative environment (Nicklisch et al., 2016). It has a mass of 11.6 kDa, and contains a high level of tyrosine (20 mol%) and cysteine (11 mol%). All these structural proteins contain limited amount of DOPA about 2–3 mol% (Nicklisch et al., 2016).

Adhesive Protein

Mfp-3, *5* are identified as interfacial proteins present at the plaque-substrate interface. They form a primer-like layer at the plaque-substrate interface providing adhesion to the substrate. *Mfp-3* is the smallest one with a mass of about 6 kDa (Papov et al., 1995; Warner and Waite, 1999). Most polymorphic mussel foot protein analogous to *Mefp-3* have been identified from mussel species (Floriolli et al., 2000). The variants contain high level of DOPA (20 mol%) and rich in lysine and glycine. *Mfp-5* is also a small protein with a molecular mass of 9 kDa (Waite and Qin, 2001). It has a homogeneous primary sequence that contains the highest content of DOPA (about 30 mol%) amongst all foot proteins, is also rich in lysine (20 mol%) and glycine (15 mol%), and has a significant number of phosphoserine residues in the sequence. It is found that over 75% of the DOPA in *Mfp-5* is adjacent to lysine, which can remove hydrated cations from the adhesion interface and promote the approaching of catechol of DOPA to the mineral substrate (Maier et al., 2015). The phosphoserine residues contribute to an enhanced mineral-binding property of *Mfp-5* to calcareous surfaces (Long et al., 1998; Silverman and Roberto, 2007). Therefore, *Mfp-5* shows the greatest adhesion than other reported foot proteins. *Mfp-3* and *Mfp-5* present in a small amount in the mussel plaque (Lee et al., 2011).

Mefp-1, *3*, and *5* extracted from *Mytilus edulis* have shown corrosion inhibition properties for metallic materials. Most studies were conducted with *Mefp-1* as corrosion inhibitors in different forms. Only two works have been reported on *Mefp-3* and *Mefp-5*, which were evaluated as dissolved inhibitor against flash rust (Nelson and Hansen, 2016; Hansen et al., 2019). *Mefp-3* and *Mefp-5* show high auto-oxidation rate in bulk solution due to the short chain (Haemers et al., 2003). These factors make them unfavorable materials for development of corrosion inhibitors. On the other hand, *Mefp-1*, the best-characterized mussel adhesive protein, naturally functions as a protective cuticle of byssus. It is abundant in mussels and contains high level of DOPA, which provides the molecule controllable adhesive and cohesive properties. The oxidation rate is low at acidic condition

(Haemers et al., 2003, 2005). All these facts make *Mefp-1* the most promising candidate for the development of bio-based corrosion protective strategies, and a range of *Mefp-1* inhibitors have been developed in recent years. Therefore, this review will be focused on *Mefp-1*.

SURFACE CHEMISTRY OF MEFP-1

Adsorption

Mefp-1 can adsorb strongly on metal and metal oxides and form films on the surface. Mechanisms of the strong adhesion are attributed to displacement of surface-bound water molecules from the target surfaces, and simultaneously formation of catechol-metal coordination and hydrogen bond between the catechol of DOPA and metal atoms of the substrate (Wei et al., 2016). It shows a saturated adsorption of *Mefp-1* due to the electrostatic interactions, the maximum adsorption amount is almost independent to the protein concentration, but determined by the aggregation degree (Haemers et al., 2001). The adsorption rate of the protein is highly related to the hydrodynamic radius (Krivosheeva et al., 2012). Therefore, non-aggregate *Mefp-1* adsorbs faster than *Mefp-1* aggregates. For anticorrosion property, multilayer adsorption and film compaction are desired, which may occur on aggregated *Mefp-1*. This occurs only when the adsorbed layer has undergone a conformational change (Haemers et al., 2002). The adsorption amount of aggregated protein is higher, and the formed film is thicker as compared with the non-aggregated one (Krivosheeva et al., 2013).

Oxidation

DOPA undergoes auto-oxidation in presence of oxygen (Haemers et al., 2003), or can be oxidized by addition of chemical oxidants or enzyme. Oxidation of DOPA results in formation of oxidative conversions of DOPA-quinone, leading to intermolecular crosslinking (Yu et al., 1999). The quinone reversely dismutates to aryloxy free radicals, which then couple and re-oxidize to form coupled diphenols (Burzio and Waite, 2000). The coupling of diphenols results in polymerization of the protein. The polymerization property of DOPA enables the development of highly effective anticorrosion adhesives (Hansen et al., 1998), which can be achieved by adjusting pH, and adding catechol oxidase chemical or enzyme.

Film-forming corrosion inhibitors require both strong affinity to the substrate and low permeation of the corrosive media. Since adhesion and cohesion properties of *Mefp-1* are dependent on DOPA in reduction and oxidation states, respectively, the enhancement of the cohesion property is obtained on the expense of the adhesion property, therefore, a too extensive oxidation of *Mefp-1* film may lead to interfacial failure (Waite, 2002). The crosslinking level of *Mefp-1* must be controlled optimally to ensure a good balance between the adhesion and cohesion properties of the inhibitor film.

pH-induced Oxidation

The pH of the buffer solution has a strong influence on the aggregation degree of *Mefp-1* molecules and the film formation rate on surfaces (Haemers et al., 2001). At higher pH the

auto-oxidation rate of *Mefp-1* is higher, which results in a higher aggregation rate (Haemers et al., 2005). Moreover, at higher pH the formed protein film appears to be more compact (Zhang, 2013), which can be explained by the enhanced oxidative crosslinking of the DOPA segments in the film. The near-neutral pH has been demonstrated as the optimal pH for *Mefp-1* film deposition.

Chemical- or Enzyme-Induced Oxidation

NaIO_4 is suggested to be a suitable oxidant to induce crosslinking of *Mefp-1* (Hedlund et al., 2009). Treatment of the *Mefp-1* film in 10 mM NaIO_4 solution for 10 min leads to oxidative conversion from DOPA to DOPA-quinone, followed by diphenols coupling (Höök et al., 2001). Therefore, the film becomes a thinner, denser and more uniform (Zhang et al., 2012). Enzyme catalyzes crosslinking of DOPA functional groups in the same oxidative mechanism as the chemical oxidants (Fant et al., 2000). Mushroom tyrosinase has been used to treat the adsorbed *Mefp-1*, giving an increased corrosion resistance (Nelson and Hansen, 2016).

Complexation

DOPA can chelate Fe^{3+} to form complexes (Zeng et al., 2010). *In situ* observations of *Mefp-1* on carbon steel indicate an enhanced adsorption of *Mefp-1* at local corroding sites (Zhang et al., 2011). The enrichment of *Mefp-1* is related to the interaction between DOPA and Fe ions released from the substrate. DOPA is a bidentate through which *Mefp-1* can form strong complexes with Fe^{3+} in mono-, bis-, and tris-catecholate- Fe^{3+} forms, depending on the pH and catechol/ Fe^{3+} molar ratios.

The tri-DOPA/ Fe^{3+} complex formation causes a compaction of and removal of the coupled water from the *Mefp-1* film. Different types of metal ions can induce metal-ligand-complexation, whereas Fe^{3+} is the most investigated, especially with aspect to corrosion inhibition. Since Fe^{3+} ions can be released from the corroding steel substrate, the complexation with *Mefp-1* offers the promise of the protein film with the intrinsic self-healing property (Holten-Andersen et al., 2011).

Electrochemical Tuning

Mefp-1 adsorption and the film conformation can be reversibly controlled by applying an electrochemical potential (Zhang et al., 2017). The study with Pt substrate has shown that *Mefp-1* adsorbs to metal via electrostatic and non-electrostatic interactions. At low potential (hydrogen adsorption-desorption region), *Mefp-1* adsorption increases with the increasing potential, leading to higher protein coverage of the surface. At medium potential, the pre-adsorbed *Mefp-1* film becomes less compact with increasing of potential, forming a thicker layer with higher water content. At high potential (Pt oxidation region), the pre-adsorbed *Mefp-1* undergoes oxidative crosslinking, resulting in a film compaction. Moreover, the adsorbed protein film presents a blocking effect on hydrogen adsorption/desorption and Pt oxidation/reduction. The reversible electrochemical reactions of *Mefp-1* provide strategies to control corrosion inhibition properties of the protein film.

Combination With Ceria Nanoparticles

The thin film of ceria (CeO_2) has shown an enhanced corrosion resistance to metallic substrates (Zhong et al., 2008). Nanoparticles of ceria present more special properties, such as oxygen storage and oxidation power due to the redox reaction (Preda et al., 2011). In the regard of the impact to human health, ceria nanoparticles are not cytotoxic but instead protect cells from oxidative insult (Xia et al., 2008). Moreover, negatively charged ceria nanoparticle can facilitate the multilayer deposition of the positively charged *Mefp-1*.

Density Function Theory calculations show that catechol is energetically favored to bind strongly to ceria nanoparticles (Zhang et al., 2013). Therefore, ceria nanoparticles can be irreversibly incorporated into the *Mefp-1* film, to facilitate a continuous build-up of the multilayer of *Mefp-1*/ceria composites (Sababi et al., 2012). *Mefp-1* adsorbs in an extended conformation that allows significant hydrodynamic coupling to the solvent, whereas the incorporation of ceria nanoparticles induces the compaction of the protein layer. As shown in **Figure 1**, the deposited composite film on carbon steel is heterogeneous with some micro-domains showing coherent enrichment of Ce (from ceria) and C (from *Mefp-1*), as well as existence of tri- Fe^{3+} /DOPA complex.

MUSSEL ADHESIVE PROTEIN INSPIRED CORROSION PROTECTION

Mefp-1 as Dissolved Corrosion Inhibitor

Mefp-1 has been demonstrated as an effective corrosion inhibitor to carbon steel when dissolved in corrosive solutions (Zhang et al., 2011). The corrosion inhibition mechanism varies depending on the exposure condition. Under acidic condition, the initial corrosion inhibition efficiency is higher in the solution with higher NaCl concentration. In this situation, the auto-oxidation of *Mefp-1* is retarded or proceeds very slowly; therefore, the oxidative crosslinking is negligible. The higher inhibition efficiency is mainly attributed to the enhanced DOPA- Fe^{3+} complexation, due to a higher amount of released Fe^{3+} in the solution with higher NaCl concentration. The longer-term corrosion inhibition of *Mefp-1*, e.g., 7 days, increases with increasing pH, and the efficiency is higher in the solution with less concentrated NaCl (Zhang, 2013). Clearly, the higher auto-oxidation level of *Mefp-1* at higher pH is the dominant factor for the enhanced corrosion inhibition. At near-neutral pH, the inhibition efficiency increases with exposure time (Zhang et al., 2011). Both the oxidation level of *Mefp-1* and the amount of Fe^{3+} released from the substrate increase with time. Therefore, both the oxidative crosslinking and the DOPA- Fe^{3+} complexation processes enhance the corrosion inhibition.

Furthermore, *Mefp-1* has also been reported to provide a certain corrosion inhibition to 304L stainless steel and Al, retarding the metal dissolution and pitting corrosion (Hansen et al., 1995; Hansen and McCafferty, 1996).

Pre-formed *Mefp-1* Film

Owing to the good film-forming capacity, *Mefp-1* has also been investigated as a pre-formed corrosion inhibition film (Zhang

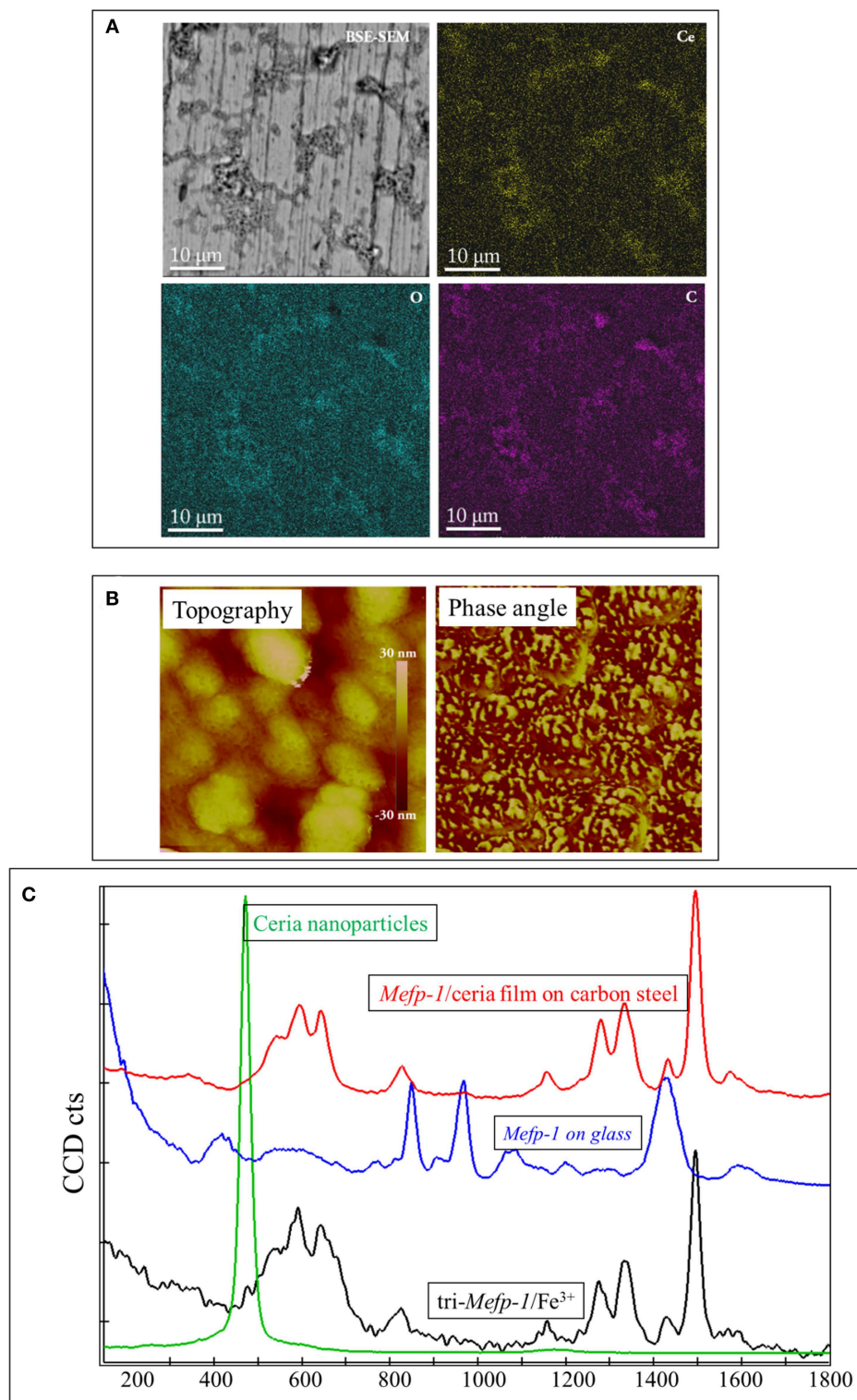


FIGURE 1 | Characterization of the Mefp-1/ceria composite film deposited on the carbon steel. **(A)** BSE-SEM image and corresponding elemental distribution of Ce, C, and O. **(B)** AFM topographic image of a compact area (with a size of 500 nm) of the composite film, and the corresponding phase image showing two distinct phases. **(C)** Raman spectrum of the Mefp-1/ceria composite film on the carbon steel, and the reference spectra of the pure Mefp-1 deposited on glass, ceria nanoparticle deposited on glass, and the complex of Mefp-1 with Fe^{3+} .

et al., 2012). The pre-formed *Mefp-1* film provides a certain corrosion protection for short-term exposure, and the corrosion protection can be significantly enhanced by proper oxidation treatment due to the increased compactness. However, the long-term exposure results indicate that the pre-formed *Mefp-1* film may degrade with time under the exposure condition. Therefore, for long-term applications, it is desirable to develop other types of *Mefp-1* films that are more protective and stable during long exposure.

***Mefp-1*/Ceria Nanocomposite Film**

Nanocomposite films of sub-micron thickness composed of *Mefp-1* and ceria nanoparticles have been deposited on carbon steel using alternative immersions and one-step-dipping methods (Sababi et al., 2012; Chen et al., 2016). The nanocomposite films provide excellent corrosion protection for carbon steel for long-term exposure, and the inhibition efficiency increases with exposure time. The increase of the inhibition effect is mainly due to the integration of the corrosion products into the film, as well as enhanced complexation between *Mefp-1* in the film and Fe ions released from the steel surface. Moreover, the *Mefp-1*/ceria nanocomposite film possesses a certain self-healing ability on carbon steel (Chen et al., 2016). The self-healing ability is attributed to the DOPA of *Mefp-1*, and the healing process is explained by the fact that Fe^{3+} released from the surface defects promote the formation of DOPA- Fe^{3+} complexes in the nanocomposite film, which retards further dissolution and thus the localized corrosion.

Synergistic Effect of Phosphate and *Mefp-1*/Ceria Composite Film

Addition of a small amount of Na_2HPO_4 into the NaCl solution results in an enhance corrosion inhibition effect of the *Mefp-1*/ceria composite film in both short-term and long-term exposures (Zhang et al., 2013). In the phosphate containing solution, the composite film deposited on carbon steel sample presents a two-layer like structure, with the composite film as the inner-layer and a vivianite deposit layer as the outer-layer.

The addition of the phosphate results in ca. one order of magnitude increase of the short-term corrosion resistance of composite film. Moreover, the corrosion resistance of the composite film further increases drastically upon the formation of a continuous phosphate deposit layer that fully covers the surface. In this case the Fe ions released from the steel surface are mostly trapped inside the film due to blockage by the deposited outer layer, and this leads to enhanced complexation between the protein and Fe^{3+} . This consequently causes the compaction of the film and hence a significant increased corrosion protection. Thus, phosphate ions in the solution and the *Mefp-1*/ceria composite film on the surface have a synergistic effect on the corrosion protection for the steel.

Based on the above-mentioned observations, a nanocomposite film composed of *Mefp-1*, ceria nanoparticles and phosphate has been developed (Chen et al., 2017), which provides a self-healing effect against pitting corrosion of carbon steel. Moreover, it is found that the inhibition efficiency can be further enhanced by thermal treatment, which leads to an enhanced oxidative crosslinking of *Mefp-1* in the composite

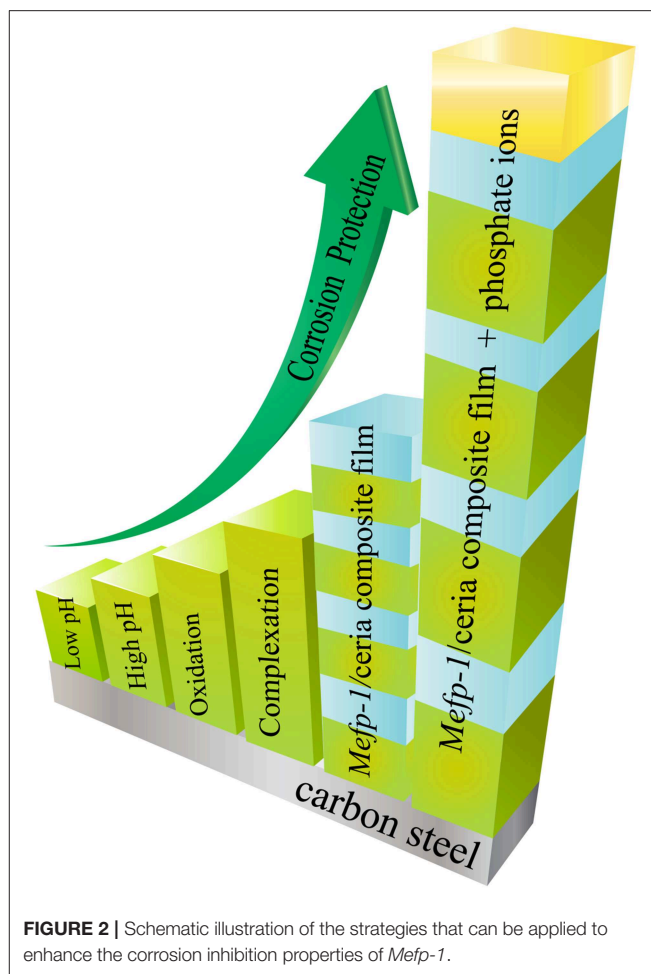


FIGURE 2 | Schematic illustration of the strategies that can be applied to enhance the corrosion inhibition properties of *Mefp-1*.

film. As a result, the film presents a highly compact structure. Furthermore, industrial applications of the nanocomposite films in reinforced concrete structure has been demonstrated (Zhang et al., 2019).

CONCLUSION

The unique adhesive and cohesive properties of the mussel adhesive protein have inspired scientific research efforts of investigation and development of a range of new “green” corrosion inhibitors and protective thin films for carbon steel. As summarized in **Figure 2**, the corrosion inhibition efficiency of the *Mefp-1* can be enhanced by means of adjusting pH, ion-induced complexation, and oxidative crosslinking. The adhesion and cohesion properties of the *Mefp-1* film can be reversibly tuned via electrochemical potential. Moreover, *Mefp-1* can be combined with ceria nanoparticles to form a composite film on steel surface, showing higher corrosion protection efficiency and self-healing properties. Incorporation of phosphate and thermal treatment of the composite film result in a further enhancement of the corrosion inhibition properties.

Based on the fundamental understanding of the chemistry and the obtained corrosion inhibition properties, the mussel adhesive

protein presents a great potential for the development of new environmentally friendly and sustainable corrosion inhibitors and thin protective films.

AUTHOR CONTRIBUTIONS

FZ contributed with the writing of the draft. JP revised it critically for important intellectual content.

REFERENCES

- Burzio, L. A., and Waite, J. H. (2000). Cross-linking in adhesive quinoproteins: studies with model decapeptides. *Biochemistry* 39, 11147–11153. doi: 10.1021/bi0002434
- Chen, C., Hou, R., Zhang, F., Dong, S., Claesson, P. M., Lin, C., et al. (2017). Heating-induced enhancement of corrosion protection of carbon steel by a nanocomposite film containing mussel adhesive protein. *J. Electrochem. Soc.* 164, C188–C193. doi: 10.1149/2.0071706jes
- Chen, C., Zhang, F., Lin, C., and Pan, J. (2016). Corrosion protection and self-healing of a nanocomposite film of mussel adhesive protein and CeO₂ nanoparticles on carbon steel. *J. Electrochem. Soc.* 163, C545–C552. doi: 10.1149/2.0521609jes
- Fant, C., Sott, K., Elwing, H., and Hook, F. (2000). Adsorption behavior and enzymatically or chemically induced cross-linking of a mussel adhesive protein. *Biofouling* 16, 119–132. doi: 10.1080/08927010009378437
- Filpula, D. R., Lee, S.-M., Link, R. P., Strausberg, S. L., and Strausberg, R. L. (1990). Structural and functional repetition in a marine mussel adhesive protein. *Biotechnol. Prog.* 6, 171–177. doi: 10.1021/bp00003a001
- Florioli, R. Y., von Langen, J., and Waite, J. H. (2000). Marine surfaces and the expression of specific byssal adhesive protein variants in *Mytilus*. *Mar. Biotechnol.* 2, 352–363. doi: 10.1007/s101269900032
- Haemers, S., Koper, G. J., and Frens, G. (2003). Effect of oxidation rate on cross-linking of mussel adhesive proteins. *Biomacromolecules* 4, 632–640. doi: 10.1021/bm025707n
- Haemers, S., van der Leeden, M., Nijman, E., and Frens, G. (2001). The degree of aggregation in solution controls the adsorbed amount of mussel adhesive proteins on a hydrophilic surface. *Colloids Surf. A* 190, 193–203. doi: 10.1016/S0927-7757(01)00679-3
- Haemers, S., van der Leeden, M. C., and Frens, G. (2005). Coil dimensions of the mussel adhesive protein Mefp-1. *Biomaterials* 26, 1231–1236. doi: 10.1016/j.biomaterials.2004.04.032
- Haemers, S., van der Leeden, M. C., Koper, G. J., and Frens, G. (2002). Cross-linking and multilayer adsorption of mussel adhesive proteins. *Langmuir* 18, 4903–4907. doi: 10.1021/la025626c
- Hansen, D., Dexter, S., and Waite, J. (1995). The inhibition of corrosion of S30403 stainless steel by a naturally occurring catecholic polymer. *Corrosion Sci.* 37, 1423–1441. doi: 10.1016/0010-938X(95)00050-T
- Hansen, D. C., Corcoran, S. G., and Waite, J. H. (1998). Enzymatic tempering of a mussel adhesive protein film. *Langmuir* 14, 1139–1147. doi: 10.1021/la970881w
- Hansen, D. C., and McCafferty, E. (1996). The effect of various naturally occurring metal-binding compounds on the electrochemical behavior of aluminum. *J. Electrochem. Soc.* 143, 114–119. doi: 10.1149/1.1836394
- Hansen, D. C., Zimlich, K. R., and Bennett, B. N. (2019). Inhibition of flash rusting of HY80 by a mussel adhesive protein: characterizing the interaction of MeFP-5 with a high strength low alloy steel. *Electrochim. Acta* 301, 411–420. doi: 10.1016/j.electacta.2019.01.145
- Hedlund, J., Andersson, M., Fant, C., Bitton, R., Bianco-Peled, H., Elwing, H., et al. (2009). Change of colloidal and surface properties of *Mytilus edulis* foot protein 1 in the presence of an oxidation (NaO₄) or a complex-binding (Cu²⁺) agent. *Biomacromolecules* 10, 845–849. doi: 10.1021/bm801325j
- Holten-Andersen, N., Harrington, M. J., Birkedal, H., Lee, B. P., Messersmith, P. B., Lee, K. Y. C., et al. (2011). pH-induced metal-ligand cross-links inspired by mussel yield self-healing polymer networks with near-covalent elastic moduli. *Proc. Natl. Acad. Sci.* 108, 2651–2655. doi: 10.1073/pnas.1015862108

ACKNOWLEDGMENTS

The authors greatly acknowledge the financial supports from the Swedish Foundation for International Cooperation in Research and Higher Education (STINIT project for Swedish-China collaboration, grant no CH2017-7255). Moreover, FZ acknowledge a seed funding from KTH for allowing collaborative research in the field.

- Holten-Andersen, N., Zhao, H., and Waite, J. H. (2009). Stiff coatings on compliant biofibers: the cuticle of *mytilus californianus* byssal threads. *Biochemistry* 48, 2752–2759. doi: 10.1021/bi900018m
- Höök, F., Kasemo, B., Nylander, T., Fant, C., Sott, K., and Elwing, H. (2001). Variations in coupled water, viscoelastic properties, and film thickness of a Mefp-1 protein film during adsorption and cross-linking: a quartz crystal microbalance with dissipation monitoring, ellipsometry, and surface plasmon resonance study. *Anal. Chem.* 73, 5796–5804. doi: 10.1021/ac0106501
- Krivosheeva, O., Dedinaite A., and Claesson, P. M. (2012). Adsorption of Mefp-1: Influence of pH on adsorption kinetics and adsorbed amount. *J. Colloid Interface Sci.* 379, 107–113. doi: 10.1016/j.jcis.2012.04.040
- Krivosheeva, O., Dedinaite, A., and Claesson, P. M. (2013). Salt- and pH-induced desorption: comparison between non-aggregated and aggregated mussel adhesive protein, Mefp-1, and a synthetic cationic polyelectrolyte. *J. Colloid Interface Sci.* 408, 82–86. doi: 10.1016/j.jcis.2013.07.015
- Lee, B. P., Messersmith, P. B., Israelachvili, J. N., and Waite, J. H. (2011). Mussel-inspired adhesives and coatings. *Ann. Rev. Mater. Res.* 41, 99–132. doi: 10.1146/annurev-matsci-062910-100429
- Long, J. R., Dindot, J. L., Zebroski, H., Kihne, S., Clark, R. H., Campbell, A. A., et al. (1998). A peptide that inhibits hydroxyapatite growth is in an extended conformation on the crystal surface. *Proc. Natl. Acad. Sci.* 95, 12083–12087. doi: 10.1073/pnas.95.21.12083
- Maier, G. P., Rapp, M. V., Waite, J. H., Israelachvili, J. N., and Butler, A. (2015). Adaptive synergy between catechol and lysine promotes wet adhesion by surface salt displacement. *Science* 349, 628–632. doi: 10.1126/science.aab0556
- Nelson, W. F., and Hansen, D. C. (2016). Investigations of mussel adhesive proteins as flash rust inhibitors. *J. Electrochem. Soc.* 163, C553–C562. doi: 10.1149/2.0541609jes
- Nicklisch, S. C., Spahn, J. E., Zhou, H., Gruian, C. M., and Waite, J. H. (2016). Redox capacity of an extracellular matrix protein associated with adhesion in *Mytilus californianus*. *Biochemistry* 55, 2022–2030. doi: 10.1021/acs.biochem.6b00044
- Papov, V. V., Diamond, T. V., Biemann, K., and Waite, J. H. (1995). Hydroxyarginine-containing polyphenolic proteins in the adhesive plaques of the marine mussel *mytilus-edulis*. *J. Biol. Chem.* 270, 20183–20192. doi: 10.1074/jbc.270.34.20183
- Preda, G., Migani, A., Neyman, K. M., Bromley, S. T., Illas, F., and Pacchioni, G. (2011). Formation of superoxide anions on ceria nanoparticles by interaction of molecular oxygen with Ce³⁺ sites. *J. Phys. Chem. C* 115, 5817–5822. doi: 10.1021/jp111147y
- Rzepecki, L. M., Hansen, K. M., and Waite, J. H. (1992). Characterization of a cystine-rich polyphenolic protein family from the blue mussel *Mytilus edulis* L. *Biol. Bull.* 183, 123–137. doi: 10.2307/1542413
- Sababi, M., Zhang, F., Krivosheeva, O., Forslund, M., Pan, J., Claesson, P. M., et al. (2012). Thin composite films of mussel adhesive proteins and ceria nanoparticles on carbon steel for corrosion protection. *J. Electrochem. Soc.* 159, C364–C371. doi: 10.1149/2.061208jes
- Silverman, H. G., and Roberto, F. F. (2007). Understanding marine mussel adhesion. *Mar. Biotechnol.* 9, 661–681. doi: 10.1007/s10126-007-9053-x
- Sun, C., and Waite, J. H. (2005). Mapping chemical gradients within and along a fibrous structural tissue, mussel byssal threads. *J. Biol. Chem.* 280, 39332–39336. doi: 10.1074/jbc.M508674200
- Waite, J. H. (1983a). Adhesion in byssally attached bivalves. *Biol. Rev. Cambridge Philos. Soc.* 58, 209–231. doi: 10.1111/j.1469-185X.1983.tb00387.x

- Waite, J. H. (1983b). Evidence for a repeating 3,4-dihydroxyphenylalanine- and hydroxyproline-containing decapeptide in the adhesive protein of the mussel, *Mytilus edulis* L. *J. Biol. Chem.* 258, 2911–2915.
- Waite, J. H. (2002). Adhesion à la moule. *Integr. Compar. Biol.* 42, 1172–1180. doi: 10.1093/icb/42.6.1172
- Waite, J. H., and Qin, X. (2001). Polyphosphoprotein from the adhesive pads of *Mytilus edulis*. *Biochemistry* 40, 2887–2893. doi: 10.1021/bi002718x
- Waite, J. H., and Tanzer, M. L. (1980). The bioadhesive of *Mytilus byssus*: A protein containing L-DOPA. *Biochem. Biophys. Res. Commun.* 96, 1554–1561. doi: 10.1016/0006-291X(80)91351-0
- Warner, S., and Waite, J. (1999). Expression of multiple forms of an adhesive plaque protein in an individual mussel, *Mytilus edulis*. *Mar. Biol.* 134, 729–734. doi: 10.1007/s002270050589
- Wei, W., Petrone, L., Tan, Y., Cai, H., Israelachvili, J. N., Miserez, A., et al. (2016). An underwater surface-drying peptide inspired by a mussel adhesive protein. *Adv. Funct. Mater.* 26, 3496–3507. doi: 10.1002/adfm.201600210
- Williams, T., Marumo, K., Waite, J. H., and Henkens, R. W. (1989). Mussel glue protein has an open conformation. *Arch. Biochem. Biophys.* 269, 415–422. doi: 10.1016/0003-9861(89)90125-2
- Xia, T., Kovochich, M., Liong, M., Mädler, L., Gilbert, B., Shi, H., et al. (2008). Comparison of the mechanism of toxicity of zinc oxide and cerium oxide nanoparticles based on dissolution and oxidative stress properties. *ACS Nano* 2, 2121–2134. doi: 10.1021/nn800511k
- Yu, M., Hwang, J., and Deming, T. J. (1999). Role of L-3, 4-dihydroxyphenylalanine in mussel adhesive proteins. *J. Am. Chem. Soc.* 121, 5825–5826. doi: 10.1021/ja990469y
- Zeng, H., Hwang, D. S., Israelachvili, J. N., and Waite, J. H. (2010). Strong reversible Fe³⁺-mediated bridging between dopa-containing protein films in water. *Proc. Natl. Acad. Sci.* 107, 12850–12853. doi: 10.1073/pnas.1007416107
- Zhang, F. (2013). *The Mussel Adhesive Protein (Mefp-1): A GREEN Corrosion Inhibitor*. KTH Royal Institute of Technology.
- Zhang, F., Brinck, T., Brandner, B. D., Claesson, P. M., Dedinaite, A., and Pan, J. (2013). *In situ* confocal Raman micro-spectroscopy and electrochemical studies of mussel adhesive protein and ceria composite film on carbon steel in salt solutions. *Electrochim. Acta* 107, 276–291. doi: 10.1016/j.electacta.2013.05.078
- Zhang, F., Chen, C., Hou, R., Li, J., Cao, Y., Dong, S., et al. (2019). Investigation and application of mussel adhesive protein nanocomposite film-forming inhibitor for reinforced concrete engineering. *Corrosion Sci.* 153, 333–340. doi: 10.1016/j.corsci.2019.03.023
- Zhang, F., Pan, J., and Claesson, P. M. (2011). Electrochemical and AFM studies of mussel adhesive protein (Mefp-1) as corrosion inhibitor for carbon steel. *Electrochim. Acta* 56, 1636–1645. doi: 10.1016/j.electacta.2010.10.033
- Zhang, F., Pan, J., Claesson, P. M., and Brinck, T. (2012). Electrochemical, Atomic Force Microscopy and Infrared Reflection Absorption Spectroscopy studies of pre-formed mussel adhesive protein films on carbon steel for corrosion protection. *Thin Solid Films* 520, 7136–7143. doi: 10.1016/j.tsf.2012.07.115
- Zhang, F., Xie, G., and Pan, J. (2017). Tunable adsorption and film formation of mussel adhesive protein by potential control. *Langmuir* 33, 8749–8756. doi: 10.1021/acs.langmuir.6b04125
- Zhao, H., Robertson, N. B., Jewhurst, S. A., and Waite, J. H. (2006). Probing the adhesive footprints of *Mytilus californianus* byssus. *J. Biol. Chem.* 281, 11090–11096. doi: 10.1074/jbc.M510792200
- Zhao, H., and Waite, J. H. (2006). Proteins in load-bearing junctions: the histidine-rich metal-binding protein of mussel byssus. *Biochemistry* 45, 14223–14231. doi: 10.1021/bi061677n
- Zhong, X., Li, Q., Hu, J., and Lu, Y. (2008). Characterization and corrosion studies of ceria thin film based on fluorinated AZ91D magnesium alloy. *Corrosion Sci.* 50, 2304–2309. doi: 10.1016/j.corsci.2008.05.016

Conflict of Interest Statement: The authors declare that the research was conducted in the absence of any commercial or financial relationships that could be construed as a potential conflict of interest.

Copyright © 2019 Zhang and Pan. This is an open-access article distributed under the terms of the Creative Commons Attribution License (CC BY). The use, distribution or reproduction in other forums is permitted, provided the original author(s) and the copyright owner(s) are credited and that the original publication in this journal is cited, in accordance with accepted academic practice. No use, distribution or reproduction is permitted which does not comply with these terms.



A Review of Modern Assessment Methods for Metal and Metal-Oxide Based Primers for Substrate Corrosion Protection

Matthew E. McMahon*, Raymond J. Santucci Jr., Carol F. Glover, Balaji Kannan, Zachery R. Walsh and John R. Scully

Department of Materials Science and Engineering, Center for Electrochemical Science and Engineering, University of Virginia, Charlottesville, VA, United States

OPEN ACCESS

Edited by:

Flavio Defforian,
University of Trento, Italy

Reviewed by:

Guido Grundmeier,
University of Paderborn, Germany
Ricardo M. Souto,
Universidad de La Laguna, Spain
Fatima Montemor,
Higher Technical Institute, University of
Lisbon, Portugal

*Correspondence:

Matthew E. McMahon
mm5kn@virginia.edu

Specialty section:

This article was submitted to
Environmental Materials,
a section of the journal
Frontiers in Materials

Received: 26 April 2019

Accepted: 24 July 2019

Published: 06 September 2019

Citation:

McMahon ME, Santucci RJ Jr, Glover CF, Kannan B, Walsh ZR and Scully JR (2019) A Review of Modern Assessment Methods for Metal and Metal-Oxide Based Primers for Substrate Corrosion Protection. *Front. Mater.* 6:190. doi: 10.3389/fmats.2019.00190

Pigmented coatings developed for the corrosion protection of engineering alloys have been successful in the field of corrosion control, and thus are ubiquitous in application. Supporting this success are an array of methods to diagnostically assess these systems and measure their state of degradation. These methods assist the development of next generation coatings, in-service evaluation, and post-mortem analysis of performance. This review comprehensively explores these modern assessment methods, used to screen candidate corrosion prevention pigments, assess pigment protection efficiency, quantify overall pigment effectiveness, and/or predict coating service lifetime. Coating service life assessment is conducted based on the class of coating considered, as categorized by (1) chemical inhibition, (2) galvanic protection, (3) high impedance ion barrier, or a combination of these protection mechanisms. Exciting new *in-situ* and operando methods are growing in use to enable high fidelity measurement of chemical inhibitor release and deposition, such as micro and *in-situ* Raman spectroscopy and inductively coupled plasma atomic emission spectrometry (ICP-AES), to name a few. In the galvanic protection coating class, service life and the state of coating performance are now being quantified through methods such as galvanostatic pulse and accelerated cycle testing. Galvanic throwing power is assessed by scanning vibrating electrode technique (SVET), multi-electrode array (MEA), and scanning kelvin probe (SKP). The performance of high impedance ion barrier coatings has traditionally been understood through use of electrochemical impedance spectroscopy (EIS) and equivalent circuit modeling, which have been applied to all coating classes. Finite element analysis (FEA) models the combined effects of coating resistance, water layer thickness, and pigment potential on galvanic coupling and/or inhibitor species release as well. The development of effective corrosion prevention pigments and the in-service evaluation of their efficiency/effectiveness demands a broad collection of techniques. These methods now include new advances in thermodynamic modeling via chemical stability diagrams to

assess pigment function in specific conditions, *in-situ* pH measurement, as well as energy dispersive (EDS) and x-ray photoelectron spectroscopic (XPS) analyses to determine elemental distribution and corrosion product formation. These techniques and more are explored in this review to document the state-of-the-art in the field.

Keywords: metal-rich primers, zinc, magnesium, chemical inhibition, SVET, chemical stability modeling

INTRODUCTION

The cost of corrosion was estimated to be 3–4% of each nation's gross national product (GDP) in 2013, or a global cost of approximately US\$2.5 trillion per year (Koch, 2017). The global use of effective corrosion control practices (protective coatings, considerate design strategies, regular preventative maintenance, etc.) is estimated to reduce this cost by 15–35%, or as much as US\$875 billion annually (Koch, 2017). One means of achieving this savings is through the effective design and application of protective coatings such as metal-rich primers, which are now ubiquitous across many engineering sectors to prevent corrosion and extend service life. Metallic corrosion requires thermodynamically viable anodic and cathodic reactions, as well as electrical and ionic conduction between anodes and cathodes. Pigmented coatings such as metal-rich primers, which are composed of sacrificial pigments embedded within an adhesive resin, operate through a variety of means, such as chemical inhibition, galvanic protection, and high impedance barrier protection. These coatings can be designed to alter the dominant anodic/cathodic reactions that occur, limit one or more of the corrosion cell requirements, or even to introduce a new sacrificial anodic reaction to afford corrosion protection to the substrate. The means of protection is dependent upon the type of sacrificial pigment present, the connectivity of the pigment, and the resin type/porosity, to name a few factors. These coatings do not necessarily function in exactly the same manner as metallic coatings, which are thin metal/alloy layers often electro- or vapor-deposited on an alloy surface, where the entirety of the layer is barrier and/or sacrificial and no binding resin is present. The same sacrificial metals may be utilized in both coating types, though the metal-rich primer design offers certain benefits, such as the ability to delay primer activation through the resin or topcoat and reduce the self-corrosion rate by isolating a portion of the particles, as well as the versatile ability to be spray-coated on nearly any free surface (though proper adhesion can be elusive). A key aspect of metal-rich primer (MRP) performance is the ability of the primer to protect latent or operational defects such as scratches as well as the substrate under the intact coating. Effective design of metal-rich primers to achieve such performance requires specific tuning for each chosen alloy substrate, and this tuning is informed by a variety of characterization methods (Bierwagen et al., 2007; Yan et al., 2010; King and Scully, 2011; King et al., 2014a, 2015; Bastos et al., 2016; Santucci et al., 2017a, 2018a).

Through purposeful MRP design, the influence of these coatings may substantially improve long-term component integrity and survivability. On near-shore gas pipelines (steel),

for example, inorganic Zn-rich primers have been observed to maintain corrosion protection for over 50 years (Francis, 2013); on offshore steel platforms, similar primers have been demonstrated to delay the onset of red rust for 10 years or more (Feliu et al., 2001). Thus, Zn-rich primers have become especially useful for steel protection. Zn-based primers (ZnRPs) function mainly through galvanic interactions with the substrate to provide sacrificial protection, and with time of exposure the buildup of corrosion products has been demonstrated to offer secondary impedance barrier protection and/or chemical protection as well (Feliu et al., 1993a,b, 2001; Bierwagen et al., 2007; Hammouda et al., 2011; Krieg et al., 2012; Cubides and Castaneda, 2016; McMahon et al., 2019a). Magnesium-based MRPs (MgRPs) have been demonstrated to continue providing substrate protection on aluminum after 4 years' atmospheric exposure even after all sacrificial metallic pigment has been converted to MgO through a combined galvanic and chemical inhibition mechanism (Santucci et al., 2017a,b). The specific mechanisms through which MgRPs operate are not fully understood. Research findings demonstrate synergistic impacts through several chemical mechanisms (i.e., pH buffering upon Mg^{2+} diffusion to the exposed substrate as well as MgO formation, which has been supported through tests on MgO-rich primers) (Santucci et al., 2017a,b, 2018a), galvanic mechanisms (the galvanic couple potential achieved as Mg pigment volume concentration (PVC) is adjusted) (King and Scully, 2011; King et al., 2014a, 2015), as well as possible coating and corrosion product secondary impedance effects (Nanna and Bierwagen, 2004; Krieg et al., 2012; Stoulil et al., 2015). Of course, MRPs may also cause rather than delay substrate degradation if not properly designed. The interactions between MRPs, the surrounding environment, and macro-defects exposing the substrate are complex, as are the specific combinations of mechanisms through which these coatings operate in unique scenarios. For example, ZnRPs on one high strength armor steel accelerated corrosion and hydrogen embrittlement due to the achievement of overly cathodic potentials (severely hydrogen-generating) (Koul et al., 2014), whereas on a pipeline steel similar ZnRPs suppressed corrosion for decades (Francis, 2013). Thus, well-informed and purposeful design of MRP technologies is necessary to maximize the corrosion protection, subsequent reliability, and cost savings possible through use of MRPs. This is possible through thorough MRP testing and performance evaluation in pertinent environmental conditions.

The wide variety of MRP types, functions, and characterization methods will be reviewed herein to inform further design optimization of these corrosion prevention systems. This review will first discuss the modes of MRP

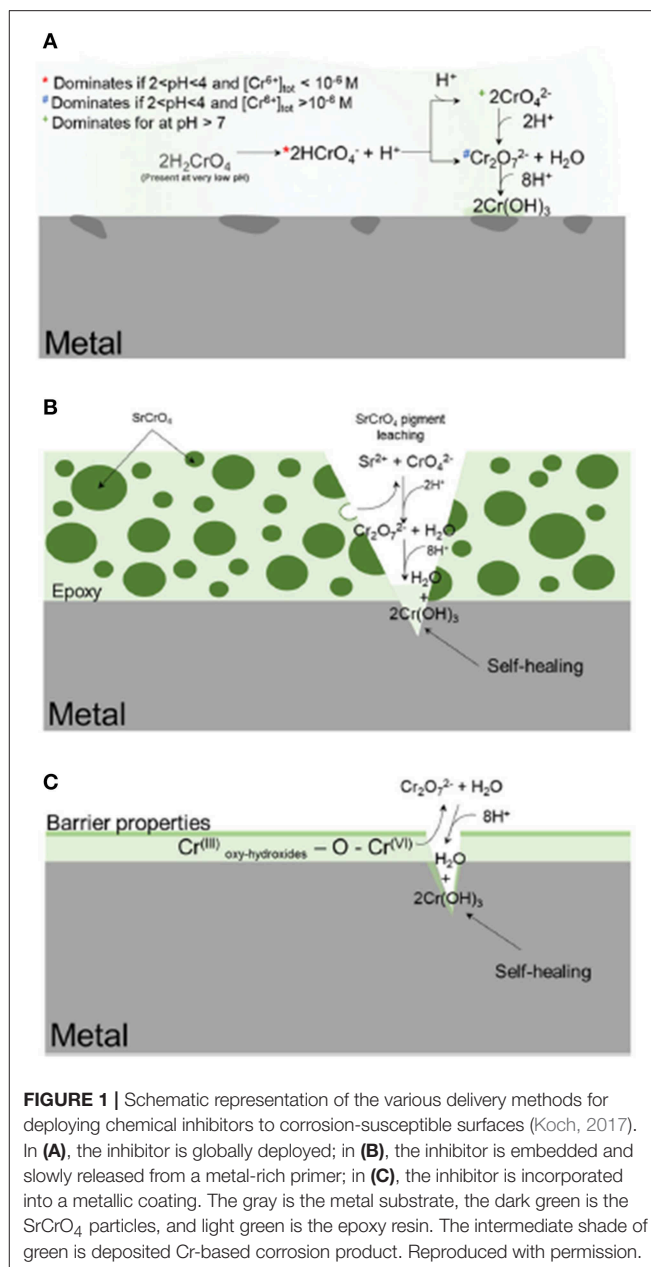
protection, their specific attributes, and the known primer characteristics that may lead to a given type of performance. A key consideration will be mechanisms for “active corrosion inhibition” of a meso- or macro-defect exposing the bare substrate. Following this baseline, the means of characterizing each type of MRP will be reviewed, which will lead into a brief discussion on the future of MRP-based corrosion prevention as well as primer development.

METAL-RICH PRIMER PERFORMANCE ATTRIBUTES

Chemical Inhibition

Metal-rich primers may achieve corrosion prevention via the storage and release of corrosion inhibiting agents, which suppress anodic/cathodic reactions at macro-defects and possibly under the coatings. These inhibitors are often situated in three ways: (1) global deployment of the inhibitor into the solution which comes into contact with the substrate, as with gas/oil/drinking water pipelines, reactors, rinses, etc.; (2) direct application to the substrate either in a conversion coating or a metallic coating; and (3) incorporation into a composite coating where the inhibitor is embedded, such as in a particle, within an organic or inorganic polymer matrix, as with MRPs (Gharbi et al., 2018). These deployment methods and their functions are schematically summarized in **Figure 1** (Gharbi et al., 2018). This review will be primarily concerned with type (3), wherein the chemical inhibitor comprises or is part of the sacrificial particles embedded within a resin, though techniques and strategies for assessment may be applicable throughout.

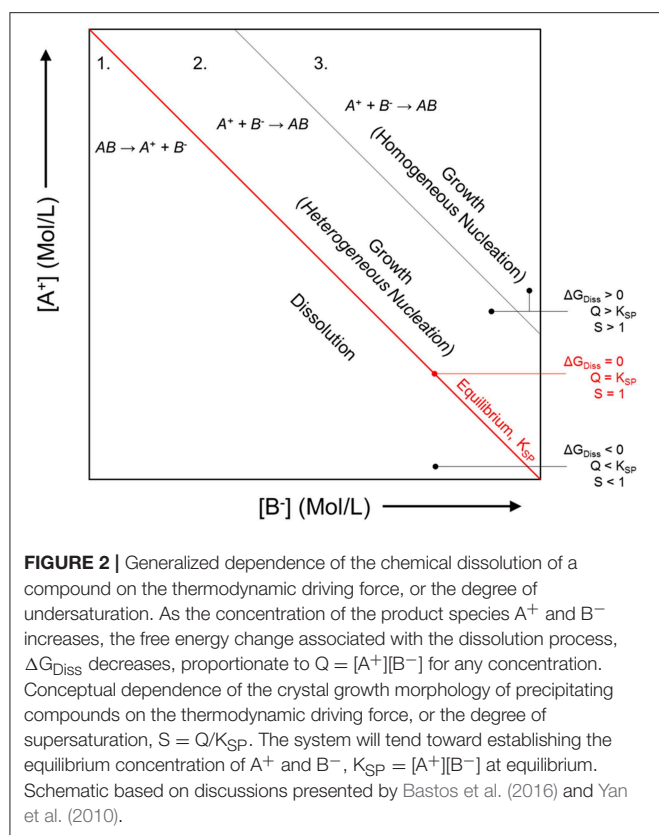
Inhibitor protection is considered an “active protection mode” where inhibitor species can be released from intact portions of coating to chemically protect the exposed substrate after barrier protection has been compromised (Xia et al., 2000; Presuel-Moreno et al., 2005a, 2006, 2008; Ho et al., 2006). The presence of the resin places increased importance on the selective release of inhibitors, which will affect the sensitivity and the service life of these primers. A smart coating is the most desirable because such systems are triggered to selectively release chemical inhibitors by specific changes in pH, O₂ content, ultraviolet light, certain established potentials, and more (Zheludkevich et al., 2012; Montemor, 2014), as demonstrated in **Figure 1**. In this way, the coating may exhibit delayed and purposeful activation only in response to conditions that would otherwise promote corrosion events. In the Al-Co-Ce system, for example, release rates of Co- and Ce-based inhibitors depend on pH and [Cl⁻] (Jakab and Scully, 2008). The release of chromate from chromate conversion coatings has also been demonstrated to occur as a function of pH and ionic strength (Xia et al., 2000). In general, the dissolution process is driven by thermodynamics, or the free energy change achieved by the dissolution of the solid phase inhibitor package into aqueous phase inhibitor species and by-product species. **Figure 2** demonstrates how the driving force for dissolution is dependent on the subsequent change in free energy, which is related to the concentration of species produced according to Equation 1, where Q is the reaction quotient and K_{SP}



is the equilibrium solubility product. There is a decrease in the free energy of the system caused by dissolution when $Q < K_{SP}$. An alternative metric which is sometimes used is the saturation index, S, defined as simply the ratio of Q to K_{SP} (Barker et al., 2018). Similarly, when $S < 1$, dissolution is favorable. When $S > 1$, dissolution is not favorable, and precipitation is likely to occur. When $Q = K_{SP}$, $\Delta G = 0$, $S = 1$, and the system is in equilibrium:

$$\Delta G_{\text{Diss}} = RT \ln \left(\frac{Q}{K_{SP}} \right)$$

Dissolution processes are often activation-controlled in rate (Frankel et al., 2018). This means that the rate is proportionate



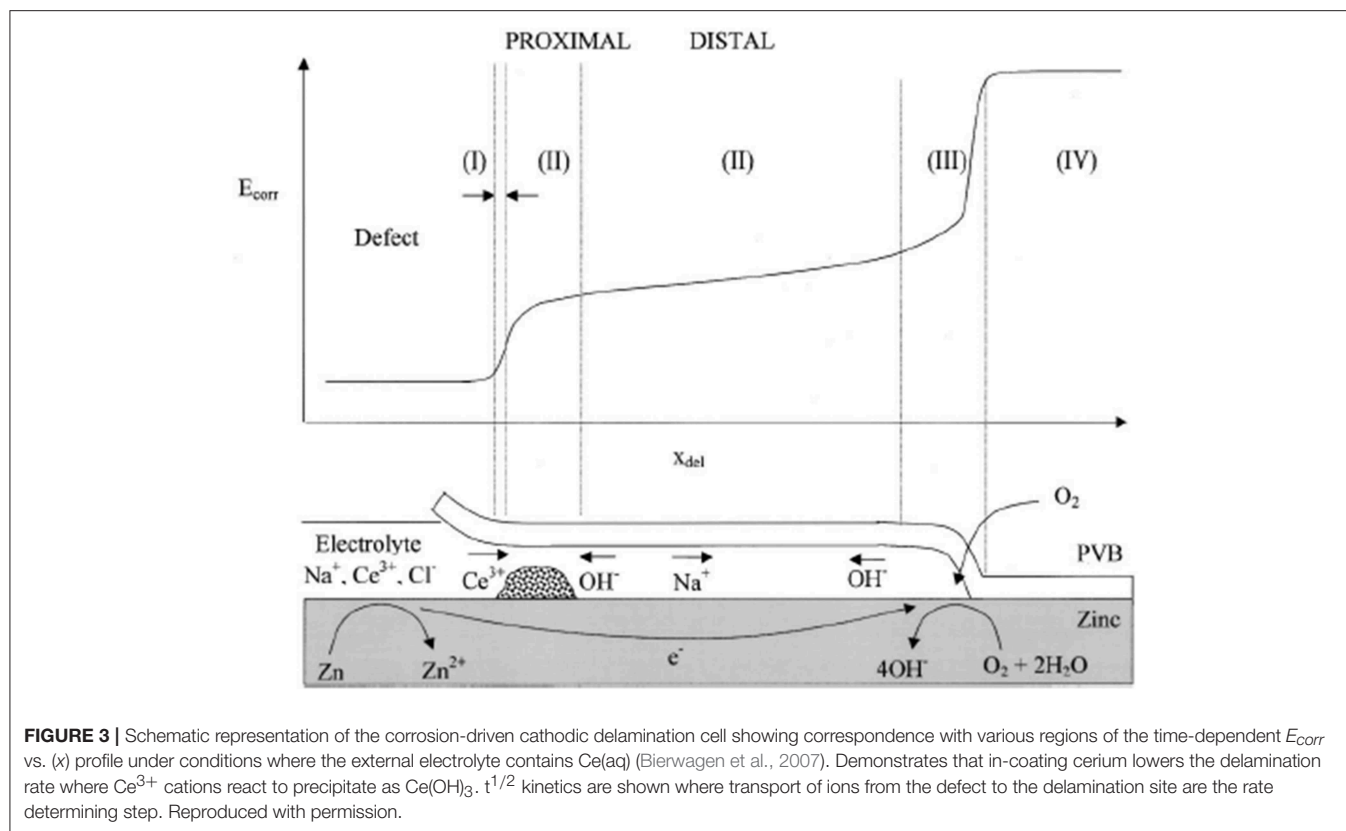
to the thermodynamic driving force. For chemical dissolution processes, this is often described by the Transition State Theory (Frankel et al., 2018). For electrochemical processes, activation-controlled dissolution regulated at the metal-electrolyte interface is described by the Butler-Volmer equation (Frankel et al., 2018). Butler-Volmer kinetics may be utilized to describe the dependency of electrochemical dissolution rates on the chemical inhibitor particle, because these interfacially-controlled processes occur in proportion to the thermodynamic driving force that is present (Hellmann and Tisserand, 2006; Frankel et al., 2018). Since electrons participate in electrochemical reactions as a reacting species, the total rate of dissolution is dependent upon the electrode potential. Other processes can control the interfacial dissolution of inhibitor packages, such as mass transport limitations or the formation of some rate-limiting interfacial film (Frankel et al., 2018).

The transport of the inhibitor from the inhibitor package to the corrosion site is the next critical aspect of the chemical inhibition performance, which can be driven by diffusion/migration (based on activity or potential differences), convection, and other processes. Migration of the Ce^{3+} inhibitor has been successfully modeled to explain the transport of these species into a coating defect, such as a scribe (Akiyama et al., 2003; Presuel-Moreno et al., 2006). Once in contact with the substrate, the inhibitor may affect electrochemical processes in a variety of ways, including but not limited to affecting the charge transfer necessary for important anodic or cathodic reactions,

promoting passive film growth with semiconductive properties, or forming physical diffusion barriers. Numerous works have demonstrated that chemical inhibitors tend to precipitate solid films on the substrate, which may occur chemically (Aldykewicz et al., 1995; Williams et al., 2002; Presuel-Moreno et al., 2005b) or electrochemically (Xia et al., 2000; Presuel-Moreno et al., 2005b). In these cases, the site specificity and morphology of the precipitated films must be understood, which will depend on the thermodynamic driving forces (Figure 2; Lasaga, 2014). The thermodynamic formation conditions for such surface films formed through precipitation and scaling processes may be understood through chemical stability diagram predictions, which will be discussed in an ensuing section.

Inhibitor protection is promoted by high storage capacity in the coating, low threshold concentrations for inhibitor efficacy [$c_{i(crt)}$], and controlled inhibitor release based on intermediate solubility whereby the inhibitor concentration is delivered within a solubility window at which the inhibitor concentration is above $c_{i(crt)}$ but below some high threshold concentration for osmotic blistering (Sinko, 2001). The efficacy of chemical inhibitors is based on the affinity of the inhibitor to affect the rate-limiting anodic or cathodic reactions occurring on the substrate. Thus, the proper selection of chemical inhibitor for storage in a pigment requires that the controlling reaction process be understood for the specific alloy in need of protection. On AA2024-T351, ultramicroelectrode array analysis demonstrated that oxygen reduction reaction (ORR) kinetics occurring on Cu-rich sites were limited either by surface coverage due to Cu replating or the diffusional boundary layer thickness (Presuel-Moreno et al., 2005a). In this well-studied alloy system, the inhibiting species Ce^{3+} , Co^{3+} , and MoO_4^{2-} were evaluated, all of which were shown to affect the cathodic reaction through different means (blocking Cu-rich sites, forming a surface film, etc.) (Scully and Jakab, 2006). Specifically, these inhibitors have been demonstrated to reduce the cathodic kinetics of ORR on pure Cu (Aldykewicz et al., 1995; Presuel-Moreno et al., 2005b; Yasakau et al., 2006). Ce^{3+} and La^{3+} ions have also been demonstrated to act as anodic reaction inhibitors elsewhere (Kaesche, 1985; Aldykewicz et al., 1995; Frankel and McCreery, 2001; Ilevbare and Scully, 2001; Yasakau et al., 2006).

The effect of such ions has been explored using a scanning kelvin probe (SKP) to investigate their effect on under-film cathodic delamination at a defect (Williams et al., 2002). The study of cathodic delamination using SKP was pioneered by Stratmann and the technique is now well-utilized for the assessment of the corrosion protection afforded by organic coatings (Stratmann et al., 1994; Rebhan et al., 2003). This technique has also proven useful to screen inhibitor-containing conductive polymer coatings for their ability to minimize corrosion on the buried metal-coating interface (Rohwerder et al., 2009, 2011). Scanning kelvin probe is a completely non-perturbing technique and allows the temporal and spatial resolution of potential distributions beneath intact organic coatings. This method has been employed in previous studies to gain mechanistic understanding of the delamination corrosion cell on important metal substrates (Williams and McMurray, 2001; Williams et al., 2002). A gold probe, which has an



electrical connection with the specimen via an external circuit, is rastered above the specimen surface at a height of approx. 100 μm . The potential required to null the resultant current flow between probe and specimen is measured. This is the Volta potential difference, which can be converted to corrosion potential (E_{corr}) via application of a conversion factor (Leng et al., 1998; Grundmeier et al., 2000; Williams and McMurray, 2001). Experiments are conducted inside a Faraday cage that also enables control of the humidity, which must be maintained at a consistently high level. In the experiments designed by Stratmann, electrolyte is placed in a large macro-defect created in the polymer. The progression of a cathodic delamination front can then be monitored by profiling the area in the vicinity of the defect with the vibrating gold probe (Figure 3). A full description of the experimental set up can be found elsewhere (Stratmann et al., 1994; Rebhan et al., 2003).

Galvanic Protection

Galvanic protection mechanisms differ from chemical inhibition mechanisms due mostly to the need for galvanic coupling between the sacrificial anodic particles and the substrate, rather than self-corrosion of the particles in response to the surrounding chemistry. In conditions where galvanic coupling is maintained, the overarching goal is to maintain coupled potentials below some critical threshold, such as the substrate breakdown potential (cathodic prevention) (McMahon et al., 2019a), or at a selected magnitude of overpotential to reduce corrosion reaction rates (cathodic protection) (Feliu et al., 2001). These terms, as

well as others which are critical to this review, are defined further in Table 1. According to mixed potential theory, the quantity of exposed sacrificial particles connected to the substrate will affect the coupled potential and the overall corrosion rate in the substrate. This galvanic couple is mediated by the electron transfer kinetics of the anodic pigment, the cathodic substrate, and also the electrical/ionic resistance between the two. The optimal pigment choice requires a specific balance consisting of the achievement of necessary coupled potentials below the open circuit potential (OCP) of the substrate, enduring activity of the pigment to resist passivation/coating deactivation, and fast sacrificial anodic kinetics. Purposeful alloying can assist in reaching this balance, as has been achieved in Mg-based systems for various modes of corrosion protection (Plagemann et al., 2013; Glover et al., 2019).

Cathodic protection is promoted by low coating matrix resistivity, fast pigment anodic kinetics, low pigment corrosion potential, high pigment loading, and low coating polarizability. Increasing the PVC is known to directly impact these performance attributes, since the particle packing dictates the amount of connectivity between the particles to sustain high anodic charge output. This effect has been demonstrated in MgRPs having an epoxy resin on AA2024 up to the critical PVC (CPVC) of 65% (Figure 4; King and Scully, 2011). In ZnRPs, the use of lamellar Zn particles has been demonstrated to be effective in galvanic protection up to 40% CPVC, and when using spherical Zn particles this value increased to 65% CPVC (Kalendová, 2003; Shreepathi et al., 2010). The PVC correlates

TABLE 1 | Glossary of critical terms for the topic of metal-rich primers.

Glossary of terms	
Coating	A layer of material fabricated on the surface of a substrate to provide protection by physical, electrochemical, and/or chemical means.
Conversion coating	A type of coating formed on the surface of a metal via a chemical or electrochemical process to provide corrosion protection. There are three types of common conversion coatings: oxide, phosphate, and chromate. Conversion coatings may be a portion of an overall coating system which may also include a primer and topcoat.
Cathodic protection	A corrosion protection mechanism in which a galvanic couple is used to reduce corrosion rates of the protected substrate according to the magnitude of potential difference between the applied potential and the floating open circuit potential of the substrate.
Cathodic prevention	A corrosion protection mechanism in which potential is maintained below a critical potential such as the breakdown potential above which a passive film formed on the substrate will deteriorate.
Defect	With respect to a coating, a defect is a portion of the coating in which barrier protection has been compromised, and active protection schemes are required. Examples and various names for defects include, but are not limited to: scratch, scribe, scribe creep, delamination, crack, pore, holiday, pin-hole, blister, and void. Defects are usually present even within a freshly applied coating and can develop over time due to environmental degradation (water uptake, UV radiation, temperature, etc.) and service-related factors (mechanical loading, foreign object strikes, application error, etc.).
Electrolyte	Aqueous medium (usually with water as the solvent) which contains ionically charged aqueous species (such as Na ⁺ and Cl ⁻). An electrolyte is necessary for corrosion processes to provide ionic convection between anodes and cathodes by the transport of the charged ions in the aqueous phase. This is necessary to maintain electroneutrality. Electrolytes range in composition and concentration. In atmospheric exposure, thin film electrolyte layers of deliquesced salt films can be quite concentrated depending on the relative humidity.
Chemical inhibition	A corrosion protection mechanism by which electrolyte chemistry is altered to prevent or mitigate corrosion.
Metal-Rich Primer (MRP)	A component of an overall coating system which provides corrosion protection for substrates such as steel or aluminum via physical barrier properties, galvanic protection, and/or chemical inhibition. Metal-rich primers may be used in conjunction with surface pretreatments and topcoats.
Pigment	In the context of metal-rich primers, pigments are metal powders embedded in the resin to provide corrosion protection via cathodic protection, cathodic prevention, or chemical inhibition. The pigment volume concentration of a primer is a critical parameter by which metal-rich primers are designed.
Pigment Volume Concentration (PVC)	The volume fraction of the primer composed of metal pigments. Most primers have a critical PVC value at which coating effectiveness is optimized, which will depend on factors such as the type of resin, metal pigment, pigment geometry, and environment the primer will be exposed to.
Resin	The resin in a metal-rich primer is an organic or inorganic matrix which binds the metal pigments together.

with increasingly negative coupled potential, reduced coating resistivity, and increasing porosity (King and Scully, 2011). A high magnitude of galvanic protection via MRPs also requires high sacrificial particle connectivity within the MRP resin, as well as high ionic connectivity through resin wetting/porosity (King and Scully, 2011). For this reason, limiting ion ingress through use of topcoats, or limiting sacrificial particle connection with the substrate through use of pretreatments, may negatively affect the magnitude of galvanic performance achieved (King and Scully, 2011; Kannan et al., 2015). Corrosion product may also inversely affect galvanic performance through filling pore space or decoupling sacrificial particles, which is commonly observed to occur in ZnRPs (Abreu et al., 1996; Marchebois et al., 2002; Thomas et al., 2013). Thus, the resin porosity, resistivity, and sacrificial particle PVC must be balanced for galvanic protection performance which is long-lasting as well as high in magnitude.

Comparison between ZnRPs has demonstrated that the use of high porosity resins such as ethyl silicate may achieve lower resin resistance than that seen in primers with similar Zn PVC but a less porous, more resistive organic resins (Feliu et al., 1993b; McMahon et al., 2019a). In MgRPs, increasing the resistivity through use of a topcoat or more resistive resin

has been demonstrated to reduce the self-corrosion rate of the sacrificial Mg, although the galvanic performance is suppressed also, meaning that a lower degree of galvanic control is achieved for a longer duration (Figure 5; King et al., 2014a). The effect of the resin for a similar Zn PVC may be balanced with the sacrificial particle size distribution, which influences the particle packing and overall connectivity (Vilche et al., 2002; Kalendová, 2003). The use of lamellar sacrificial particles has been demonstrated to achieve more effective packing and interconnectivity (Vilche et al., 2002; Kalendová, 2003), which directly affects overall primer conductivity (Wang, 2012). When utilizing spherical sacrificial particles, wider size distribution has a similar effect, which was demonstrated utilizing a combination of nanoscale-Zn and macroscale-Zn particles to increase interconnectivity and galvanic longevity on steel (Schaefer and Miszczyk, 2013). Of course, a combination of sacrificial particle types may also be utilized to fine-tune galvanic protection performance. Alloyed sacrificial particles such as Zn-Mg or Al-Zn have been evaluated to determine the exact compositions which achieve the optimal galvanic performance, with attention to the magnitude of galvanic couple potential achieved for the specific substrate as well as the subsequent corrosion product formation that occurs

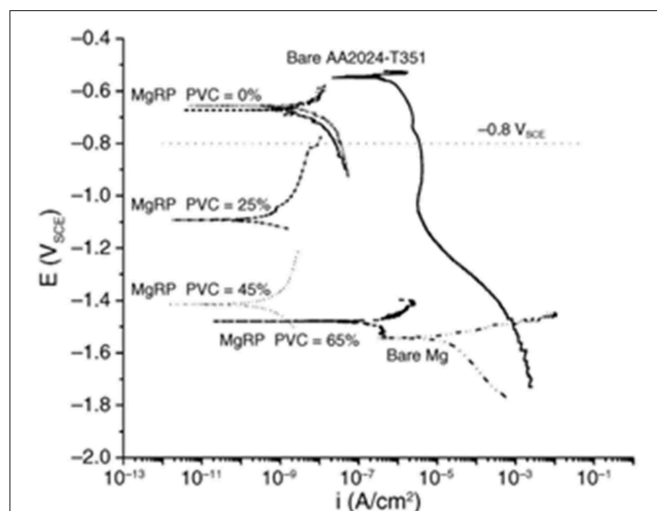


FIGURE 4 | The effect to Mg flake pigment concentration on the global galvanic potential of the MgRP/AA2024 system in 0.6 M NaCl (King et al., 2014a). Reproduced with permission.

to form a secondary barrier (Prosek et al., 2008; Plagemann et al., 2013; Wang et al., 2013; Salgueiro Azevedo et al., 2015; Stoullil et al., 2015). Additives have also been considered within the adhesive resin to increase conductivity, such as polyaniline emeraldine salt, silicone acrylate, and carbon nanotubes, among others (Armelin et al., 2010; Zhang et al., 2012; Cubides and Castaneda, 2016). Additionally, and important toward substrate protection, is the galvanic throwing power of the coating, whereby potential and current distributions are established by the galvanic coupling of a remote, exposed macro-defect to the MRP-coated substrate. In this way, the macro-defect is cathodically polarized by the coated substrate, achieving the desired potential control for protection of the susceptible substrate at the scribe for longer and longer scribe widths.

Metal-rich primers have also been considered for environmental fracture mitigation in the substrate material, which requires a high degree of galvanic protection to maintain effective coupled potentials at crack tips in the presence of tortuous crack paths with considerable IR drop. In short, environmental cracking has distinct critical thresholds (i.e., E_{crit} , T_{crit} , $[Cl^-]$) beyond which this phenomenon occurs, and these thresholds must be avoided. In the case of a primer, $E < E_{crit}$ is a criterion for protection. The ability of ZnRPs to maintain such potentials following aggressive simulated galvanic coupling in 0.6 M NaCl has been demonstrated to depend strongly on the aforementioned primer design characteristics such as sacrificial particle connectivity, porosity, resin resistivity, and more (McMahon et al., 2019a). The performance attribute that is most critical to the ability of an MRP to mitigate crack propagation via a galvanic mechanism besides the corrosion or galvanic couple potential is the pigment/primer polarizability, or the ability of the primer to maintain a cathodic electrode potential despite increasingly large exposed cathode areas (such as during crack growth) (McMahon et al., 2019a,c). This performance

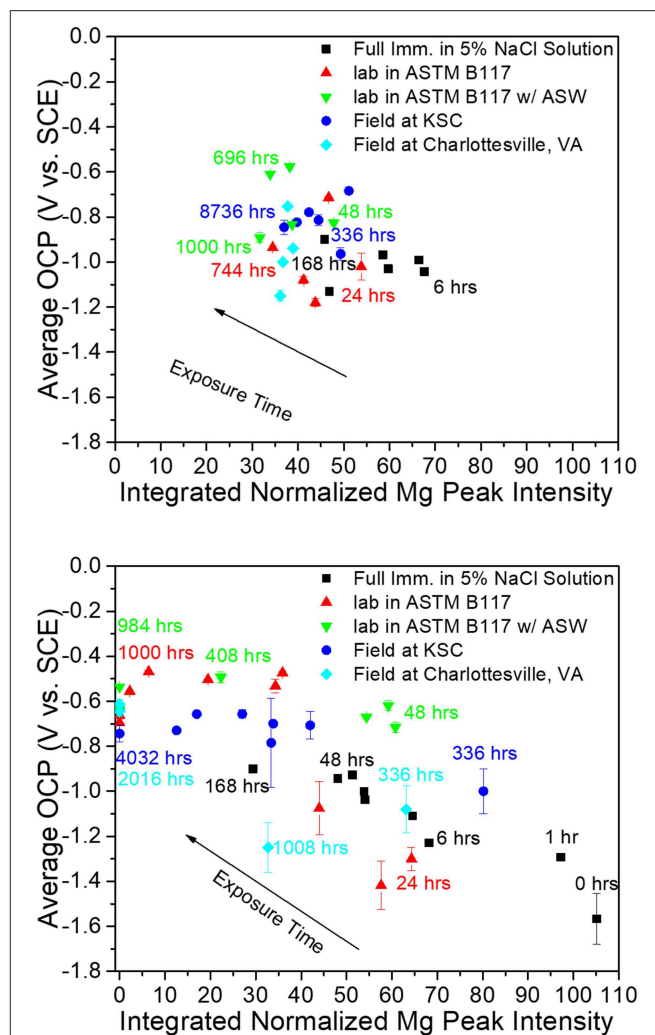


FIGURE 5 | Correlation between integrated Mg peak ($Mg < 200 > 2\theta = 36.6170$ degrees) intensity obtained from pigment vs. galvanic protection potential of AA2024-T351 coated with MgRP (initial MgPVC = 45%) (top) and MgRP + topcoat (bottom) in ambiently aerated 5% NaCl solution after exposure in various environments (King et al., 2015). Reproduced with permission.

attribute is complex, and depends on nearly the entirety of the previously discussed primer attributes and design characteristics: sacrificial particle type, loading, interconnectivity, and the resin (resistivity and porosity) (McMahon et al., 2019a). Optimally low polarizability is achieved through maximized anodic charge output in response to increasing cathodic surface area, with fast anodic response time maintained despite sacrificial particle oxidation and corrosion product formation. This level of performance may conceivably lead to a shorter MRP service life compared to those with higher impedance and lower anodic charge output. Thus, in environmental fracture scenarios, some of the desired MRP attributes for optimal mitigation performance may differ with respect to those desired for typical corrosion prevention situations.

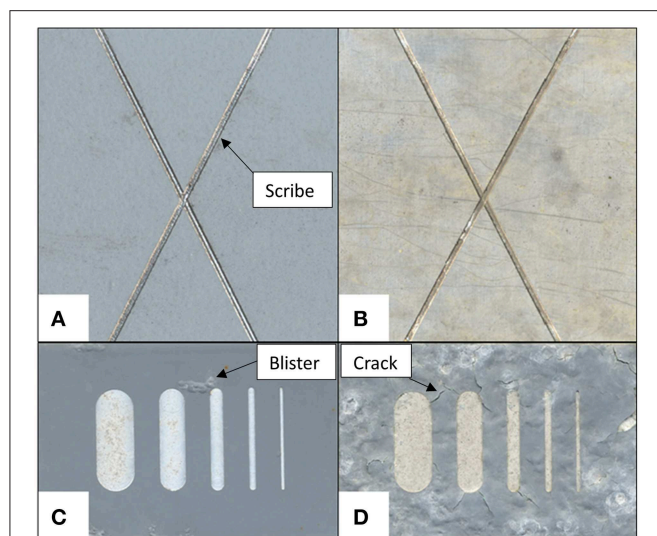


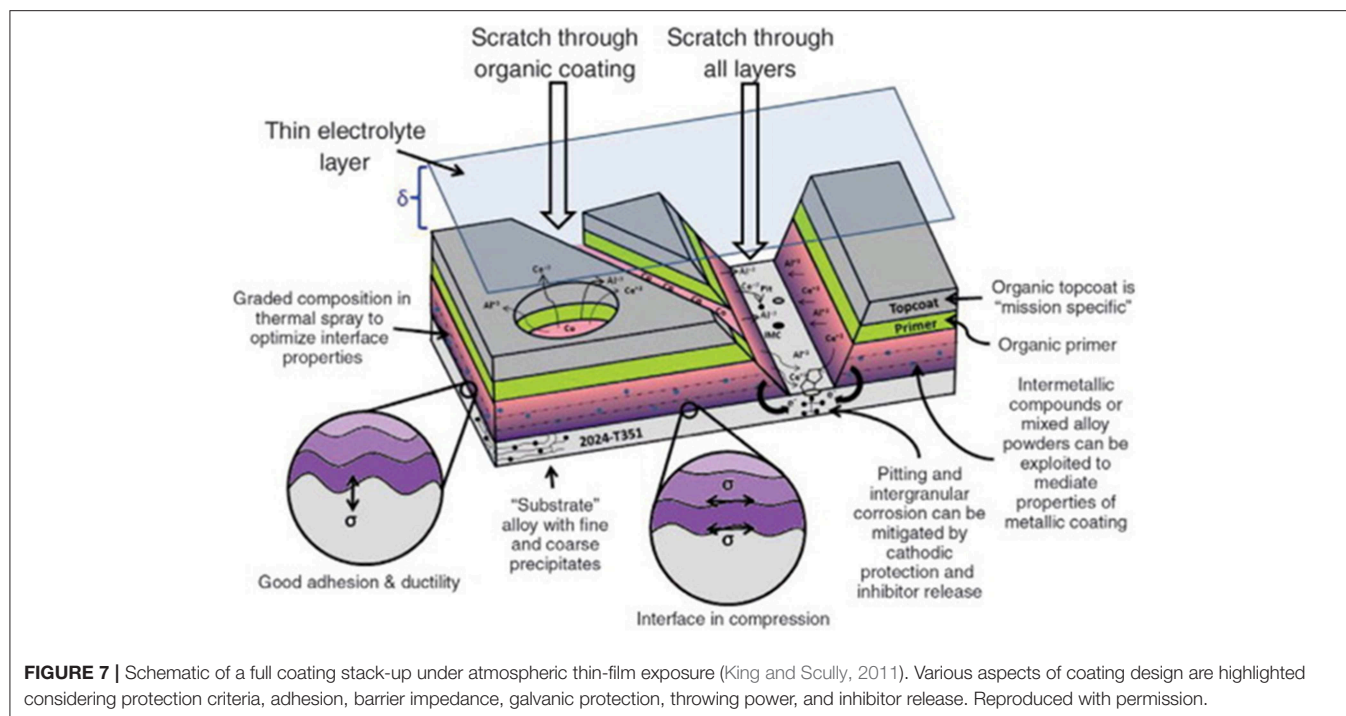
FIGURE 6 | Optical images exemplifying different types of coating defects, some of which are labeled. All coatings were deployed in field exposure testing with a machined scribe defect. In **(A)** a topcoated MgORP is shown after 2.5 years of exposure to Charlottesville, Va Birdwood golf course, and in **(B)** the same MgORP without a topcoat after being deployed in the same exposure conditions, resulting in the primer being completely degraded down to bare substrate. In **(C)**, one type of chromated primer is shown following exposure to Daytona, FL coastal marine environment for 3.2 years, exhibiting blistering in the coating, and in **(D)** a different chromate pigmented primer is shown following exposure to the same coastal environment, in which the coating exhibited severe cracking.

High Impedance Barrier

Coatings can function as a high impedance barrier to prevent high ionic conductivity enabled by electrolyte ingress to the substrate. Metal-rich primers maintaining high impedance act to impede the fast penetration of ions to drive corrosion reactions, and serve as a physical barrier (Leidheiser, 1982; Bellucci and Nicodemo, 1993). By preventing electrolyte contact with the substrate surface, the formation of a corrosion cell is prohibited and attack is circumvented. Barrier protection is promoted by good coating-substrate adhesion, resistive coating thickness, low defect density (as with pores), coating hydrophobicity, and slow coating degradation during exposure. A good barrier coating would allow no transport of species (ions, O_2 , solvent, etc.) to or from the substrate surface. An imperfect coating can still mitigate corrosion damage by severely limiting the transport of current carrying species to and from the surface and between anodes and cathodes. The resin properties dictate such protection, specifically the crosslink density, since the restriction on chain mobility increases barrier properties (Leidheiser, 1982; Bierwagen, 1996; Sørensen et al., 2009). Recent works have also considered intrinsically conductive polymer-based coatings and their ability to maintain adequate barrier properties (Paliwoda-Porebska et al., 2005; Rohwerder et al., 2009, 2011). These findings have demonstrated that conductive polymer separation from the metal surface and macroscale percolation pathway formation must be avoided in order to mitigate a phenomenon

known as buried interface corrosion, wherein the metal-coating interface oxidizes as the coating promotes fast cation mobility to the metal surface (even in the absence of delamination) (Paliwoda-Porebska et al., 2005; Rohwerder et al., 2009, 2011). Over the course of an exposure, the barrier properties of both conductive and non-conductive coatings can degrade, most commonly by degradation of the polymer matrix (through dissolution into the electrolyte or UV radiation decomposition) or formation of transport pathways such as cracks, pores, etc. Field exposures tend to be very severe on organic coating matrices due to the effect of solar UV radiation on polymer decomposition, some examples of which are shown in **Figure 6**. This motivates the application of UV-resistant topcoats to be applied over the primer, which may reduce polymer degradation to extend the lifetime of the barrier properties. Even with a topcoat, however, electrolyte will inevitably penetrate the polymer network, which will reduce the primer impedance with time (Hack and Scully, 1991). For the purposes of reducing the ability of the ions to fully penetrate, the incorporation of inert inorganic or metallic particles may be beneficial when below the CPVC (Thomas, 1991; Koulombi et al., 1997). Above the CPVC, there is insufficient binder to fill the void between pigment particles, and/or there is a connected path along the particle interface and therefore the coating will be porous and have poor barrier properties (Thomas, 1991). Pigment or mineral filler particles such as titanium dioxide, micaceous iron oxide, glass flakes, lamellar aluminum, clay, silica etc. may be utilized to improve barrier properties of the coating. As far as the pigment shape is concerned, lamellar or flake particles are more effective compared to spherical pigments as they increase the tortuosity of the diffusion path prior to reaching the substrate when aligned perpendicular to the diffusion path (Moggridge et al., 2003; Yang et al., 2004). Stronger chemical bonding at the filler particle/resin interface also retards the electrolyte diffusion through the coating, which restrains electrochemical reactions on the underlying substrate. Furthermore, effective barrier coatings may also restrict the ingress of oxygen, which may slow cathodic reactions and thus the overall corrosion rate on the substrate (Walter, 1986; Sørensen et al., 2009; Glover et al., 2017). Restriction of the electrolyte and oxygen ingress may be achieved by a variety of primer formulations in various degrees, and will depend on the environmental exposure conditions (**Figure 5**; King et al., 2014a).

Without proper resin adhesion to the substrate, however, high impedance barrier properties are largely lost as the electrolyte can readily ingress. Proper substrate cleaning may promote proper primer adhesion (Marsh et al., 2001; Vakili et al., 2015). Commonly used pretreatment approaches include silanization, phosphating, application of conversion coatings, abrasive blasting, and anodization. The specific environment to which the primer will be exposed must also be considered. Temperature, pH, ultraviolet radiation, relative humidity, chloride content, as well as the presence of atmospheric pollutants such as nitrates and sulfates may all have deleterious effects on coating formulations, especially concerning the degradation of the barrier and adhesion properties (Mansfeld et al., 1982; Hack and Scully, 1991; Mansfeld and Tsai,



1991; Tayler et al., 2015a,b). The complex combinations of influences that these environmental factors may have on barrier performance are often understood for specific primer formulation types through use of laboratory-based accelerated life cycle testing (LALT) methods and field exposure, which will be discussed in an ensuing section.

Optimization and Effectiveness

Metal-rich primers typically operate through a combination of the previously discussed protection mechanisms. Optimization of MRP effectiveness is possible only through thoroughly understanding the environment to which the MRP will be subjected, the properties of the underlying substrate, resin properties, and the requirements for degradation mitigation. The array of these potential considerations on a substrate such as AA2024-T351 are demonstrated in **Figure 7** for a complex coating system (Presuel-Moreno et al., 2008). The resin properties such as ionic resistance and permeability to different detrimental species such as chloride, oxygen, water, anions, and cations will dictate the primer activation time as the sacrificial particles become increasingly connected with the external environment (Maier and Frankel, 2011). This was demonstrated by Maier et al. using an SKP to profile the interface between a bare substrate and an MRP (Maier and Frankel, 2011). Through a series of line scans across a thin aqueous electrolyte layer, it was shown that electrolyte must first penetrate the polymer network and the oxide layer on the embedded metal pigment before a galvanic couple was established and the metal pigment could function as a sacrificial anode. Once this galvanic couple was established, the magnitude of the established galvanic couple potential must be balanced so as not to be overly negative.

Inducing overly cathodic polarization may cause, rather than mitigate, hydrogen embrittlement phenomena in the substrate, as has been seen when utilizing ZnRPs on high strength steels (**Figure 8A**; Koul et al., 2014). When the potentials are in a passive polarization regime, the magnitude of coupled potential achieved on the substrate may drastically affect the rate of the prevailing degradation phenomena such as stress corrosion cracking, as has been demonstrated with ZnRPs on an Al-Mg alloy (**Figure 8B**; McMahon et al., 2019c). On amphoteric alloys such as Al, there is concern for the initiation of alkaline corrosion as well (Aballe et al., 2001; Tran et al., 2016). Alkaline corrosion phenomena may be especially severe when constituent particles intersect the alloy surface to act as fast cathodic reaction sites, which will form local alkaline regions that aggravate amphoteric substrate dissolution (Aballe et al., 2001, 2003; Huang and Frankel, 2007; Zhu et al., 2018; McMahon et al., in review). Thus, the barrier and galvanic properties of the MRP must be properly balanced to optimize performance for specific substrates, with particular attention to reducing the risk for exacerbation of degradation. As was discussed previously (and demonstrated in **Figure 4**), for a given resin resistivity, this may be achieved by tuning the PVC, or by adding a topcoat (which also provides UV weathering resistance) to increase overall resistivity (King and Scully, 2011; Kannan et al., 2015). The sacrificial particle composition may also be adjusted; for example, Plagemann et al. demonstrated on aluminum substrate that sacrificial particles composed of 74% Zn, 26% Mg achieved the optimal combination of galvanic coupling and self-corrosion rate (Plagemann et al., 2013). The variety of primer attributes which may affect overall performance through simple or complex relationships based on chemical inhibition, galvanic protection,

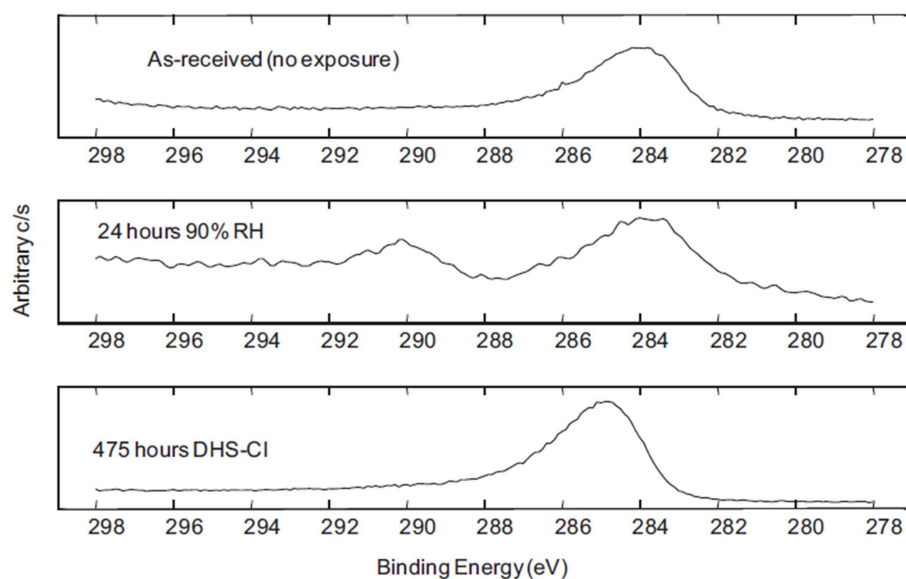


FIGURE 9 | X-Ray Spectroscopic analysis results demonstrating the development of C(1s) peaks over time of exposure in different simulated atmospheric conditions on the surface of a MgRP (Francis, 2013). Reproduced with permission.

this technique may indicate breakdown of primary and secondary amines resulting in degradation of polyurea and polyurethane functional groups. This technique allows for the direct comparison between outdoor exposures and LALT to determine if similar breakdown in primer resins or topcoats is achieved (Pathak et al., 2012; Petry and Hansen, 2016). X-ray diffraction provides evidence to understand the reduction in sacrificial anode (i.e., metal pigment) capacity (i.e., moles of metallic pigment remaining within the primer), which directly relates to subsequent galvanic performance often observed with time of outdoor or simulated outdoor exposure through comparison of sacrificial particle crystalline peak intensity (King and Scully, 2011; King et al., 2014a). Concerning MgRP systems having no topcoat or pretreatment, XRD has demonstrated that a complete loss of Mg content occurs following roughly 1,000 h exposure in ASTM B-117, and after roughly 24 weeks of exposure in marine/rural outdoor environments (King and Scully, 2011; King et al., 2014a). This disparity in achieved performance points out a current gap in the state-of-the-art, which is the lack of correlation between laboratory-based test methods and atmospheric exposure. Despite the complete loss of Mg peak intensity in XRD, studies have shown that MgRPs continue to protect an underlying Al substrate during outdoor exposure, which motivates more detailed assessment into corrosion product formation and alternative chemical protection effects (Santucci et al., 2017a).

Crystalline corrosion product may be effectively evaluated through a combination of bulk and surface-sensitive methods such as Raman spectroscopy, FTIR, XRD, and x-ray photoelectron spectroscopy (XPS), all of which provide either compositional or crystallographic details on the nature of

the precipitates (Pathak et al., 2010; Kannan and Scully, 2016; Santucci et al., 2017a). X-ray photoelectron spectroscopy and Raman spectroscopy are both especially useful for the sensitive detection of corrosion products and/or chemical modification on sacrificial pigment surfaces due to their penetration depth of as little as 5 nm, an example of which is shown in **Figure 9** for a MgRP surface (Park et al., 2012; Gergely et al., 2013; Jalili et al., 2015). The spatial resolution of XPS today, which can be on the order of 10 μm or less, may also aid the detection of corrosion product distribution into scribes and/or inhibitor coverages on remote alloy surfaces (Plagemann et al., 2013). Certain compounds may not have a Raman signature or may be difficult to detect, in which case the XPS precision and/or ability to deconvolute peaks is useful. Critical aspects of these techniques, as well as others essential to the characterization of coating performance, are provided in **Table 2**. Scanning electron microscopy (SEM) may also provide detail on the morphology and location of the precipitates, regardless of crystallinity, although chemical information by related methods such as energy dispersive spectroscopy (EDS) is spatially limited, and penetration depth is typically 1 μm or greater. For the MgRP system, this combination of methods demonstrated that Mg is converted into hydroxides during LALT, and becomes hydroxides as well as carbonates following outdoor exposure due to differences in the atmospheric conditions such as presence of more carbon dioxide (Pathak et al., 2010; Kannan and Scully, 2016; Santucci et al., 2017a). Due to the surface sensitivity of Raman and FTIR (Pathak et al., 2010, 2012; King et al., 2014a; Kannan et al., 2018a) and the identification of hydroxides via XRD (a method with considerably greater signal penetration depth) after long term field exposure (Santucci et al., 2018b), it can be concluded that Mg becomes converted

TABLE 2 | Table summarizing the various techniques discussed, as organized by principles of operation, detailing important characteristic of each.

Principle of operation	Technique	Typical probe	Samples of interest	Interaction	Approximate energy difference	Typical signal	Diagnostic
Bohr Spectral Condition	FTIR	Infrared photon spectrum	Solid and aqueous	Vibrational and bending excitation	4–400 meV	Infrared photons	Molecular structure and bonding
	Raman	Single frequency visible and near-visible photons	Solid and aqueous	Inelastic Raman Scattering	1.5–3 eV	Frequency-shifted visible and near- visible photons	Molecular structure and bonding
	AES	Thermal Energy from Plasma or Arc	Aqueous	Electronic Excitation (Between Atomic Orbitals)	1–3 eV	Visible and near- visible photons	Inner shell atomic identification
	UV-Vis	Ultraviolet and Visible Photon Spectrum	Aqueous	Electronic Excitation (Between Molecular Orbitals)	1–100 eV	Ultraviolet and visible photons	Molecular structure and bonding
	EDS	Energized Electron Beam	Solid	Electronic Excitation (Between Atomic Orbitals)	0.1–100 keV	X-ray photons	Inner shell atomic identification
	XPS	Single Frequency X-ray photons	Solid	Electronic Excitation (Between Atomic Orbitals)	0.1–100 keV	X-ray photons	Inner and outer shell atomic identification
Bragg Diffraction Condition	XRD	Single frequency X-ray photons	Solid	Diffraction from Equivalent Lattice and X-ray Periodicity	NA	Single frequency X ray photons	Crystal structure and interplanar spacing
	P-EIS	Voltage perturbation spectrum	Electrochemical interface	Faradaic and Non-Faradaic Current Emission	$E = \frac{1}{2} CV^2$ where	Frequency-shifted current perturbation	Physical analogs to equivalent circuit elements (Corrosion Rate, Oxide Thickenss, Coating Integrity, etc)
	G-EIS	Current perturbation spectrum			$C = I \div \frac{dV}{dt}$	Frequency-shifted voltage perturbation	

into magnesium hydroxide with a thermodynamically more stable magnesium carbonate surface layer (Santucci et al., 2018a). The combination of SEM and EDS has been utilized to evaluate pigment depletion and redeposition in coating scribes, which has been evidenced to increase with increasing exposure time during both LALT and outdoor exposure tests on MgRP/AA2024 (King et al., 2014a; Kannan and Scully, 2016; Santucci et al., 2017a). In acidified ASTM B-117 LALT, such Mg redeposition and corrosion product formation in the scribe was limited compared to more neutral exposure conditions. The Mg corrosion products are simply more soluble in the acidified environment as indicated a variety of ways, notably chemical stability diagrams (Santucci et al., 2018a). In fact, chemical mapping of the redeposition zone by EDS¹ yields valuable insight into the throwing power and the extent of chemical protection achieved by MgRP as a function of environment (Kannan and Scully, 2016).

Once the scribe is cleaned of corrosion products and redeposited species, corrosion volume loss analysis in the scribe may further identify differences in primer performance as a function of environmental conditions. Classical techniques such as optical profilometry and confocal laser microscopy enable quantification of volume loss due to pitting in the scribe,

through which Kannan et al. demonstrated that the presence of the MgRP achieves corrosion protection on AA2024 more effectively in outdoor exposure than in neutral or acidified LALT (Kannan and Scully, 2016; Kannan et al., 2018b). More advanced evaluations in the laboratory may then further verify the differences in exposure conditions and MRP protection. For example, Nazarov et al. utilized scanning kelvin probe (SKP) on a scribed ZnRP to quantify location-specific potential changes that could be used for cross-evaluation with the corrosion volume loss results after as much as 23 days' immersion, which also directly demonstrated the suppression of pitting events and the MRP throwing power with time (**Figure 10**; Kannan et al., 2018b; Nazarov et al., 2018). Analyses utilizing SKP and complementary techniques such as EIS, scanning electrochemical microscopy (SECM), and more may also utilize SEM to visually confirm results, as has been demonstrated previously (Ogle et al., 2000; Volovitch et al., 2009, 2011; Marques and Simões, 2014). Electrochemical evaluation may offer further insight into the mechanisms driving long-term MRP performance. Embedded counter/reference electrodes may be placed between the primer and the topcoat, or between the primer and a pretreatment, to intermittently evaluate the state of the primer via EIS or measurement of the OCP during LALT, as long as these electrodes are resistant to chemical and environmental changes, do not alter the coating performance, and remain effective over extended periods of exposure (Prosek et al., 2008; King et al., 2014a; Merten et al., 2015). Embedded Ag/AgCl electrodes could be explored for this purpose (Rafla et al., 2018). Intermittent EIS has

¹It should be recognized that the EDS method is not surface sensitive and often has a depth of penetration of several micrometers, but the corrosion products deposited by homogeneous chemical precipitation are often several micrometers thick.

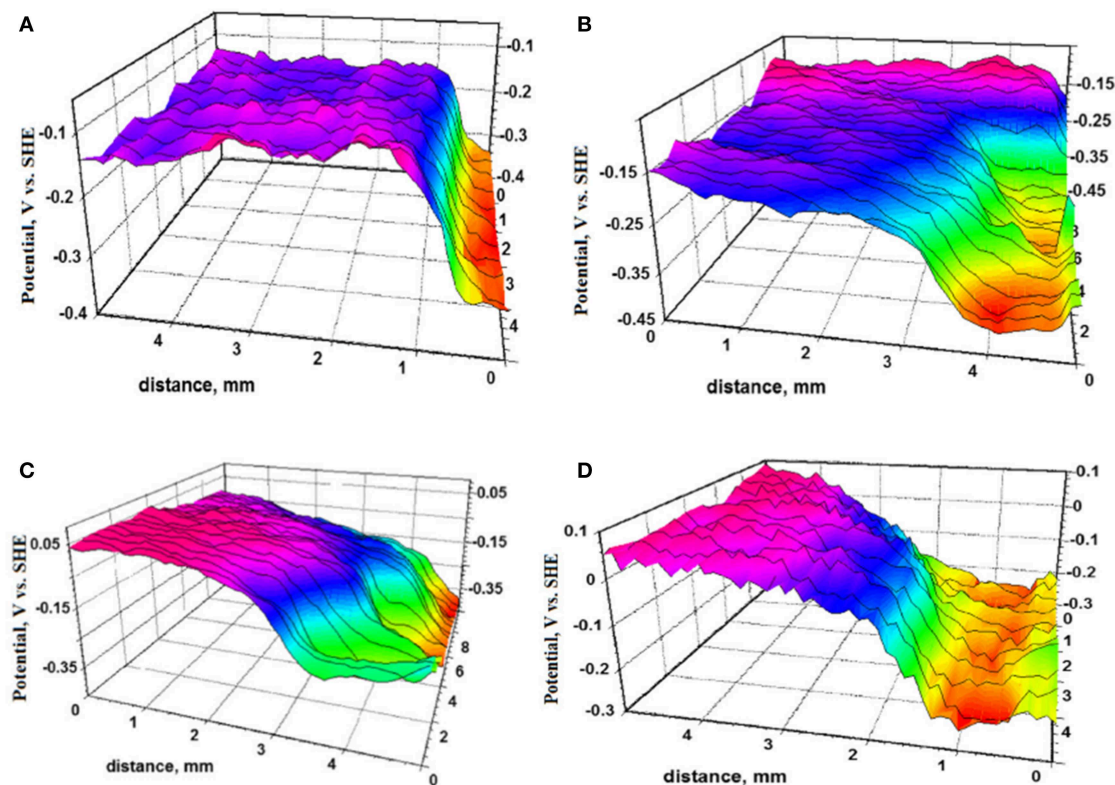


FIGURE 10 | Substrate: structural steel S355MC; Primer pigment: Zinc, with topcoat. Samples were exposed to accelerated testing in 3 wt.% NaCl at 95% relative humidity and were removed to characterize the potential profile of the scribe/coating interface via SKP after (A) 2 days, (B) 8 days, (C) 13 days, and (D) 23 days of exposure (Feliu et al., 2001). Reproduced with permission.

proven especially useful to understand changes in MRP porosity during long-term exposure when conducted at low frequency (0.01 Hz), and through evaluating the breakpoint frequency when conducted across a range of frequencies (Hack and Scully, 1991; Tsai and Mansfeld, 1993; King et al., 2014a).

Electrochemical Evaluation: Chemical Inhibition

Understanding chemical inhibition mechanisms often requires the quantification of the storage, dissolution, release, and transport of inhibitor species to a coating defect, such as a scribe. The delamination kinetics determined by the SKP technique via the measurement of changes in Volta potential difference underneath a scribed, coated sample provide an indirect indication of the effect of in-coating inhibitor species. The protection mechanism against underfilm cathodic delamination can be elucidated, such as: (1) chemical leaching from the coating; (2) the formation of permeation layers to block electron transfer to the cathodic site at the metal/coating interface; and (3) the formation of interfacial layers that increase the pathway for ionic mass-transport (Grundmeier et al., 2000). The SKP technique has been extensively utilized in the study of cation exchange within coatings, through which Williams et al. demonstrated that soluble chromate species are more effective when released from in-coating particulates such as SrCrO_4 because this enables

diffusion of CrO_4^{2-} directly into the under-film electrolyte layer (Williams et al., 2002, 2012). Scanning kelvin probe analysis has also demonstrated that cerium-based particles achieve more effective protection against delamination than simply adding Ce^{3+} to the bulk solution (Williams et al., 2002). To track the release of inhibitor species in solution, techniques such as ultraviolet-visible spectroscopy (UV-vis) may be utilized, which quantifies species concentrations and identifies species based on a characteristic absorption signature. The equilibrium fraction of soluble species will vary based on pH, as will the peak signal frequency and absorbance, as has been shown for Cr^{4+} (Xia et al., 2000). Moreover, identification of the isosbestic point, where absorbance is independent of pH, enables direct tracking of species concentration throughout exposure, which is a powerful capability. For cations that are not active in the UV-vis spectrum, active chelating agents may be added that selectively bind to certain cation types, even with sensitivity to the oxidation state (Shtoyko et al., 2007; Place, 2019). However, when adding chelators, the change of the resulting complex concentration as a function of cation concentration or pH must be understood.

Increasingly complex characterization methods are required to more fully understand the nature of chemical inhibitor-containing primer performance as a function of environment. Atomic emission spectroscopy (AES), which evaluates atomic concentration through exciting atoms contained within a

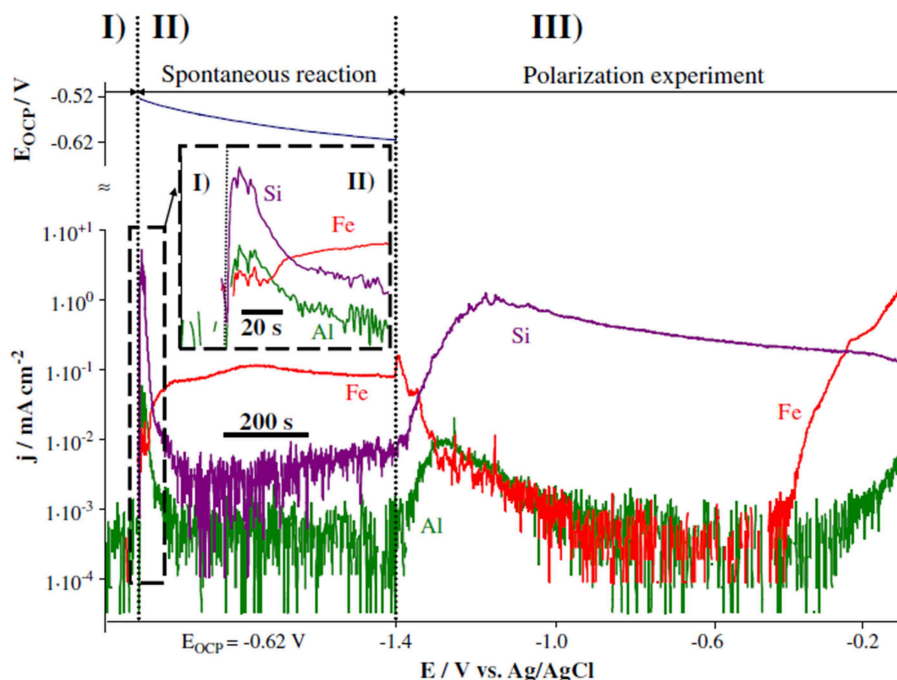


FIGURE 11 | Dissolution rates of Fe, Si, and Al measured through AESEC during both open circuit and applied polarization experiments to evaluate the mechanism of degradation in a silicone-based galvanic coating in 30 g/L NaCl environment (Feliu et al., 1993a). Reproduced with permission.

liquid medium and measuring the resulting photon emission during decay, has been adapted for this purpose (Hieftje, 2000). Inductively coupled plasma (ICP) atomic emission spectroelectrochemistry (ICP-AES) combines the atomic quantification of AES with the ability to control electrochemical conditions via potentiostatic or galvanostatic means, which has been utilized to understand conversion coating stability and substrate dissolution as a function of electrolyte composition (Ogle, 2004; Gharbi et al., 2016). An example of the results obtained on a silicone-based galvanic coating through ICP-AES analysis is shown in **Figure 11** (Ogle, 2004). This method may be coupled with SEM/EDS and Raman spectroscopy to characterize the deposition and/or precipitation of species of interest on the substrate surface, delivering a wholistic idea of the fate of chemical inhibitors from the initial dissolution within the primer. When small inhibitor concentrations are released from the primer, surface-enhanced Raman scattering (SERS) may also be utilized to identify precipitates if they exhibit a Raman signature (Zou et al., 1998; Oblonsky, 2006).

The release, transport, and redeposition of chemical inhibition species has been discussed thus far. The efficacy of these species toward reducing the corrosion rate of a given substrate must also be considered. One simple assessment commonly used is to monitor the mass loss of a known area of substrate exposed to an electrolyte with and without the inhibiting species. After exposure the substrate is subjected to a cleaning step in a process that is tailored to remove the corrosion product without further corroding the intact substrate (ASTM International, 1999). By correlating the mass loss of the substrate to corrosion damage,

a comparison can be made to determine if the inhibitor reduced the extent of damage, on the assumption that corrosion attack is uniform (i.e., not localized in morphology). This assessment is simple to conduct but cannot glean mechanistic understanding and cannot monitor the corrosion process during exposure. Potentiodynamic polarization testing is another well-utilized assessment. The measured current is related to the rate of oxidation and reduction according to Faraday's law and mixed potential theory. In the presence of an efficacious inhibitor, the measured currents should be lower than in the absence of the inhibitor. Alternating current assessments can be made with EIS as well. This measurement technique will be discussed in depth in the Theory and Modeling of Performance section of the review. For now, it is sufficient to note that the polarization resistance, which can be quantified via EIS, and which is related to the corrosion rate of the substrate by the Stern-Geary relationship, should increase in the presence of an effective inhibitor.

Galvanic Protection

The most basic means of directly measuring the magnitude of achieved galvanic protection is via the OCP² (Pereira et al., 1990; Feliu et al., 1993a, 2001; Danford et al., 1995; Hammouda et al., 2011; Santucci et al., 2017b; McMahon et al., 2019a). Feliu et al. have demonstrated, through intermittent OCP measurement, that ZnRPs can maintain galvanic protection on steels for 10

²Also referred to as the global galvanic couple potential to avoid confusion, the achievement of this value is rooted in mixed potential theory, which will be discussed in a section to follow pertaining to electrochemical modeling.

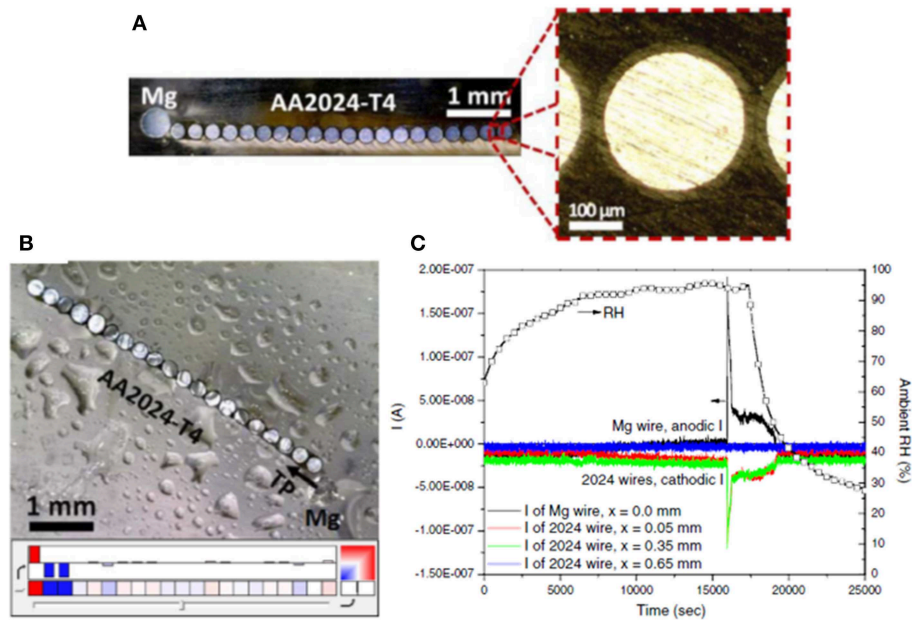


FIGURE 12 | (A) Optical images of a bare Mg/AA2024-T4 microelectrode array used to diagnostically assess the throwing power of Mg over a representative bare AA2024-T4 scratch in an RH controlled cabinet (Feliu et al., 1993b). The Mg electrode is 500 μm in diameter. The AA2024-T4 electrodes are 254 μm in diameter insulated by a 25 μm thick polyimide coating with a mean electrode spacing of 50 μm . The total width of all of the AA2024-T4 microelectrodes is approximately 5750 μm and the total area ratio of AA2024:Mg is 5:1. **(B)** optical image of the bare-Mg/bare AA2024-T4 microelectrode array with 1,000 $\mu\text{g}/\text{cm}^2$ NaCl deposited by salt spray and allowed to equilibrate at 94% RH for at least 3 h. In the color map dark red indicates an anodic current $\geq 1 \times 10^{-5}$ A/cm 2 and dark blue indicates a cathodic current of $\leq -1 \times 10^{-5}$ A/cm 2 . White color indicates a net current of zero. **(C)** Measured current and RH. Reproduced with permission.

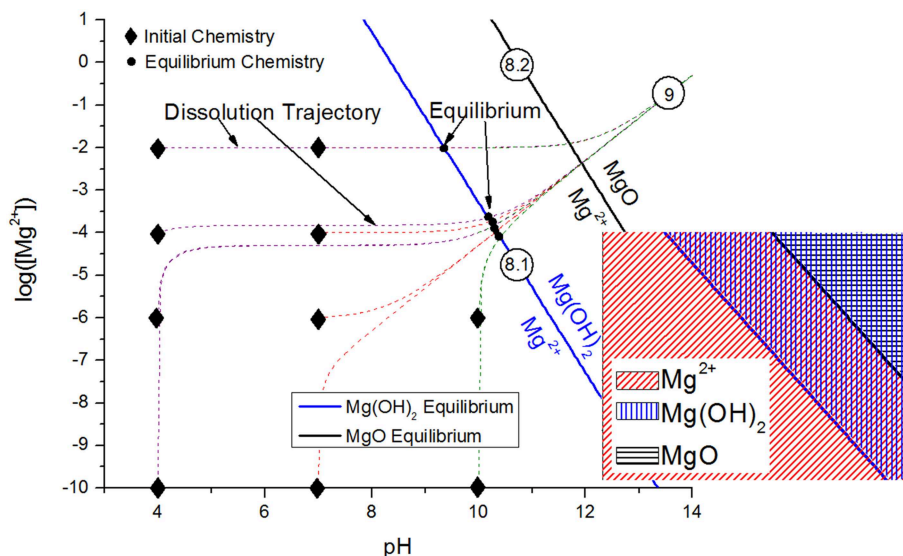


FIGURE 13 | Chemical stability diagrams detailing the ability of these thermodynamic derivations to predict corrosion product stability and conditions for formation in the Mg system (McMahon et al., 2019a). Reproduced with permission.

years in marine outdoor exposure, and the increase in the OCP past a critical threshold accurately predicts the onset of red rust due to known potential dependence (Feliu et al., 2001). When evaluating MRP-based galvanic protection for environmental

fracture mitigation, measurement of the galvanic couple potential on the exposed substrate surface with a nearby primer provides a rough estimate of the degree of protection achieved at a remote location such as the crack tip (McMahon et al., 2019c). In these

more aggressive scenarios, there may be a distance dependence to the galvanic couple potential, achieved due to the finite throwing power achievable via MRPs. Throwing power has been evaluated for several geometries and simulated conditions through use of multi-electrode arrays (MEAs) (King et al., 2015; Rafla and Scully, 2019). An example of an MEA consisting of pure Mg and AA2024-T351 electrodes (in this case, flush mounted wires were used to simulate a planar electrode) is shown in **Figure 12**, as well as an example dataset of currents achieved on various electrodes in salt spray (King et al., 2015). These custom setups enable the simulation of an exposed substrate area with embedded electrodes spaced throughout the exposed dimension, enabling localized current measurement to indicate where net anodic (if throwing power is ineffective at reaching such a distance) or net cathodic reactions are supported (when the throwing power is sufficient to distribute current to the electrode). The design of the electrode size and spacing is important where the dimension should enable potential and current field changes and/or consider anode-cathode microgalvanic couple sizes³.

These experimental evaluations are readily complemented by finite element analysis (FEA), which provides considerable insight on the effect of variables such as solution thickness and resin resistivity on the throwing power phenomenon (King et al., 2016). King et al. utilized FEA to demonstrate means through which MgRP throwing power may be improved on AA2024-T351 based on Mg polarization characteristics, solution thickness and resin resistance (King et al., 2016). The results of this analysis will be detailed further in an ensuing section. The scanning vibrating electrode technique (SVET) is another means of measuring throwing power. The use of SVET to make *in situ* localized corrosion current density distribution measurements in saline immersion was pioneered by H. Isaacs (Isaacs, 1988). The SVET enables the mapping of localized corrosion features occurring on metallic surfaces when fully immersed in aqueous media to discern physical size, shape, and spatial distribution. As such, quantitative anodic and cathodic current density data can be extracted via the numerical integration of SVET-derived current density (j_z) distributions and corrosion rates can be measured (Williams et al., 2010, 2013, 2014; Upadhyay and Battocchi, 2016; Fajardo et al., 2017). A wealth of literature exists documenting the use of SVET to monitor localized corrosion of bare metals and their alloys to elucidate fundamental corrosion mechanisms (Isaacs, 1988; Franklin et al., 1992; Williams et al., 2015). Furthermore, SVET is a very useful tool for the study of galvanic interactions between dissimilar metals (Deshpande, 2010; Yan et al., 2010; Coelho and Olivier, 2018; Glover et al., 2019) and, hence, for the evaluation of MRPs. An SVET study concerning the throwing power from a MgRP over an exposed AA2024 surface was able to locate the exact reach of sufficient galvanic coupling and the successful suppression of pitting (Kannan et al., 2018b). The SECM method has been similarly applied to study localized corrosion processes caused by galvanic coupling, where

galvanic protection may be assessed with high electrochemical sensitivity on the micrometer scale (Simoes et al., 2008; Izquierdo et al., 2013; Filotás et al., 2017; Xavier and Nishimura, 2017).

Primers having high sacrificial particle loading often have increased conductivity due to high particle interconnectivity, which may be measured through conductive atomic force microscopy (CAFM) (Bierwagen et al., 2007). This method differs from AFM by the application of a voltage from the tip to the sample surface, thus both a topographic map as well as a current map may be produced to identify (1) the distribution of conductivity at the surface (an indirect measure of metal particle proximity) as well as (2) the surface profile. This quantification method enables the researcher to determine the CPVC, the resin resistivity, and the sacrificial pigment connectivity without electrochemically testing the primer in an electrolyte (Bierwagen et al., 2007). Related to the conductivity is the MRP polarizability, which may be quantified through use of the newly developed galvanostatic pulse method (McMahon et al., 2019a). This technique consists of a cyclic repetition of applied anodic current having increasing magnitude, with intermediate OCP steps to assess the MRP's state of degradation/activation (McMahon et al., 2019a). Correlation of the polarizability of several ZnRPs based on a critical current threshold agreed with fracture mechanics-based assessment of these primers' performance in environmental fracture mitigation, showing promise as a fast screening method for the assessment of primers that must be capable of responding to sudden increases in bare substrate area which must be protected (McMahon et al., 2019a).

Theory and Modeling of Performance

Several modeling frameworks exist to predict and assess the performance of MRP systems. Typically, models are organized with respect to one of the three principal protection modes previously discussed: chemical inhibition, cathodic protection/prevention, or high impedance barrier protection. All three of these modes may be present in one coating system, though that is rare. Each modeling paradigm will be discussed by this scheme individually, and then synthesized into a discussion pertaining to all forms of protection.

Modeling of the storage, release, and accumulation of chemical inhibitors from coatings should be generally focused on the kinetics of inhibitor release, the transport, and the accumulation of the inhibitor species in some macro-defect in need of inhibition (such as a scribe or holiday). Inhibitor release kinetics are sensitive to the exposure environment, and proper model inputs need to capture this dependence. For chemical dissolution processes, the rate of dissolution is proportional to the degree of undersaturation of the species in solution with respect to the equilibrium conditions of compound stability (**Figure 2**). In this case, both the initial and final equilibrium inhibitor concentrations established by inhibitor dissolution are needed as model inputs, both to establish an upper bound on inhibitor delivery and also to inform chemical dissolution kinetics (Xia et al., 2000). For electrochemical dissolution processes, the kinetics are governed by electrode potential at the primer interface coping with any concentration gradients along with transport of cathodic species to be reduced on the electrode

³By definition the net array current will be zero at open circuit if all the anodes and cathodes reside on the same electrode. When anodic and cathodes are distributed and when there is a meso current and potential distribution the array provides useful information.

surface. The corrosion rate-determining techniques highlighted previously are useful here for determining electrochemical inhibitor release as a function of factors like pH and $[\text{Cl}^-]$ (Presuel-Moreno et al., 2006). The chemical release of Cr^{6+} from a chromate conversion coating (CCC) has been modeled utilizing a Langmuir adsorption-desorption mechanism (Xia et al., 2000; Akiyama et al., 2003). In this model, the CCC was simulated by a porous network consisting of solid chromate compound network and solution-penetrated pores. A Langmuir-type adsorption-desorption equilibrium was assumed between the solid network and the solution in the pore space to calculate a diffusion model for Cr^{6+} transport through the CCC into bulk solution (Akiyama et al., 2003). This assumed model adequately rationalizes experimental observations of Cr^{6+} release and final bulk Cr^{6+} concentration (Xia et al., 2000; Akiyama et al., 2003). Further considerations can be made to model the transport of inhibitor species from the coating to a defect like a scribe. In addition, achieving a critical inhibitor concentration for a large change in corrosion rate or to avoid a critical threshold potential are sometimes considered. Here the accumulation of the inhibitor such as over a scribe is tracked and a database is created on the change in “corrosion behavior” of the substrate alloy in response to the various inhibitor concentrations (Jakab et al., 2005; Presuel-Moreno et al., 2005a; Scully and Jakab, 2006). When the accumulated concentration over the scribe reaches or exceeds the critical level, the maximum level of protection is achieved.

The computational power of FEA has been utilized to model the long-range transport of Zn^{2+} and $\text{V}_{10}\text{O}_{28}^{6-}$ from an intact hydrotalcite/vanadate coating to a scratch through the coating which exposes bare AA2024-T351 (Wang et al., 2004). Model inputs required experimentally determined, quantitative expressions of the anodic and cathodic kinetics of the AA2024-T351 substrate as a function of potential, and inhibitor concentration as well as the inhibitor release rate as a function of pH. Once developed, the model was able to assess the effect of scribe width, electrolyte film thickness, and pH on the concentration profile of the inhibitor species from the coating into a scribe over time (Wang et al., 2004). Furthermore, the same FEA modeling framework has been applied to protective metallic coatings which are designed to galvanically couple to the substrate both under the coating and within the scribe. The release of Ce^{3+} from an Al-Ce-Co metallic coating and the transport of Ce^{3+} from the coating into a scribe has also been modeled (Presuel-Moreno et al., 2006). In this case, an added migration term to Ce^{3+} transport due to the electric field was considered since the scribe can be negatively polarized by the intact coating. It was found that this migration term was significant enough to cause uphill transport of Ce^{3+} against the concentration gradient (Presuel-Moreno et al., 2006).

Galvanic coupling of the coated substrate to the uncoated substrate not only contributes to the migration of inhibitor species, but also acts to protect the exposed substrate by evoking electrode potential control. The motivation for employing cathodic protection having been discussed already, it is necessary to have computational tools with which to model the cathodic protection behavior of anodically-pigmented coatings. Finite

element techniques have been employed to spatially resolve the electrode potential and current distribution within a galvanically coupled scribe. The potential dictates the electrochemistry of the substrate, and also contributes to the transport of ions in solution, as previously discussed for the Al-Ce-Co coating system (Presuel-Moreno et al., 2006). The potential distribution has also been calculated for a scribed MgRP on AA2024-T351 to determine the galvanic throwing power of the coating, or the distance away from the intact coating over which significant potential control could be established in the exposed scribe (King et al., 2016). The effect of electrolyte composition, electrolyte layer thickness, polymer resistivity, and humidity cycling on the throwing power of MgRP was investigated. In general, it was found that throwing power was more extensive for more conductive electrolytes and polymer matrices and for a thicker or deeper electrolyte layer (King et al., 2016). Finite element model inputs relied heavily on experimental determination of the anodic and cathodic reaction rates (i.e., interface reaction rates) as a function of electrode potential, the thermodynamic dependency of the electrolyte layer concentration and physical thickness on the relative humidity and salt composition, as well as the geometry. A challenge with modeling primers is the resin resistance, which is an extremely important variable that must be contained in such models (even for a resin with the same resistivity at all positions) as a function of primer depth buried within the coating. In one approach, this was handled by assigning a depth beneath the primer surface to the pigment, and in other approaches there could be a distribution of depths.

A more generic framework than FEA exists in the mixed potential theory, which describes the galvanic coupling of two or more electrochemically distinct materials. The net anodic and cathodic current of each electrode is plotted as a function of electrode potential in proportion to the available area of each electrode (current is not area normalized). The contribution of current from each electrode is then summed to give the total net current of the system as a function of electrode potential (King and Scully, 2011; King et al., 2016). The electrode potential established on the surface depends on the anodic and cathodic kinetics of each electrode and also the resistance that exists between them. The resistance is proportional to the resistivity of the solution and the distance between the electrodes, giving rise to a geometric distribution of potential. The ohmic resistance which affects the electrode potential distribution is composed of the sum of all resistances between anodic pigments and the cathodic substrate (King and Scully, 2011). Resistance can arise from the solution, primer, topcoat, etc., with the high resistivity of the polymer coating matrix often contributing the most.

For a coating to function as a good barrier, it must prevent or limit either the ingress of the ionic species in the electrolyte to the coated substrate or the rate of anodic/cathodic reactions at the buried interface. Theoretically, a perfect coating would not accommodate any uptake of water or permeation of water to the substrate or transport of ionic species through the coating to and from the substrate. In reality, all coatings will instead suffer water permeation due to intrinsic coating defects (like pores) or developed defects (like cracks or scratches) (Leidheiser, 1982; Bellucci and Nicodemo, 1993). Current may

flow through the coating once it is sufficiently wetted with ionically conducting electrolyte. These coating defects provide low resistance pathways for current flow once saturated with electrolyte. In this way, the resistance of a coating is related to the tortuosity of the current path between anodes and cathodes, and it decreases with decreasing coating thickness as well as increases with wetting and defect development (Amand et al., 2013). Many techniques exist to assess the resistance (or barrier properties) of protective coatings in full immersion exposure. Electrochemical impedance spectroscopy is a commonly utilized technique, wherein an alternating current (AC) perturbation signal can be applied to a coated interface at a given current or potential amplitude centered at a given current or potential value, respectively (Orazem and Tribollet, 2017). When a potentiostatic EIS technique is deployed, for example, the resulting current response of the coated interface is measured. The AC response of the interface is dominated by the path of least resistance for current flow (or the path which gives rise to the lowest impedance response to the alternating potential). The electrochemical surface is composed of real physical elements which are either resistive, capacitive, or inductive in nature. Together, they give rise to an impedance response under AC conditions. The impedance response is a result of these circuit elements interacting together according to the laws which govern their individual behavior in response to alternating potential (or current) perturbations. Resistive elements which control current flow include solution resistance in the bulk electrolyte from the reference electrode to the coating, solution resistance within the pore space of the coating, and polarization resistance to electron transfer reactions at the electrochemical interface incorporating both the charge transfer and mass transport aspects (Mansfeld et al., 1982; Kendig and Scully, 1990; Mansfeld, 1990; Hack and Scully, 1991; Mansfeld and Tsai, 1991; Tsai and Mansfeld, 1993). Capacitive elements, which arise when charges are separated over a finite distance, affect impedance response as a function of perturbation frequency and include the Helmholtz double layer, coating capacitance, and oxide capacitance. Another example is the use of Warburg impedance elements to model real convective diffusional processes, which have a dual resistive and capacitive response to AC perturbations. A broadly applicable method such as EIS is not a universal means to understand all mechanisms of coating performance, and complementary combinations of techniques should always be considered; however, this method can be utilized in a variety of ways to gain valuable insight. It is worth noting that EIS is a global method biased by low parallel impedance and is not area specific (lacks spatial resolution). Overall, the impedance response of a coated system will depend upon the arrangement and magnitude of various resistors and capacitors, such that the electrochemical system can be modeled as an equivalent circuit (Orazem and Tribollet, 2017).

Equivalent circuit models are theoretical analogs to physical components of the electrochemical interface commonly constructed to simulate the impedance response measured by EIS. A least squares residual analysis is performed to vary the values of the various circuit elements to best fit the experimental data. Care must be taken to appropriately choose a representative equivalent circuit with physically significant parameters, some of

which are independently corroborated with to model a coated interface, as many different models could adequately fit the experimental data. For example, the impedance response of an oxide is more accurately comprised of the individual responses of many capacitors/resistors which sum to give the response of the actual oxide, giving rise to a capacitive dispersion. The oxide is not perfect and homogenous, but really inhomogeneous with respect to oxide thickness, oxide composition, oxide impurity concentration, oxide defect concentration, oxide crystallographic orientation, oxide grain boundaries, etc. In this case, it is too complicated to know or to model how all of these capacitances work together to give the impedance response of the cell. Instead, the sum behavior of the oxide capacitance is typically modeled as a constant phase element. Error analysis and independent verification is needed by complementary techniques to hone in on the values of the various elements (Orazem and Tribollet, 2008). Nested RC circuits utilizing two time constants have successfully been applied to impedance data of MgRP (King and Scully, 2011; King et al., 2014a,b; Kannan et al., 2015). Transmission line models have also successfully modeled MgRPs and ZnRPs (Allahar et al., 2008, 2010). In such cases, EIS can be effectively utilized to differentiate coating vs. buried interface corrosion, as a second time constant is developed upon environmental exposure which can be correlated to substrate corrosion. Equivalent circuit models are not only useful for theoretical fitting of EIS experimental data but also for theoretical fitting of potentiostatic pulse testing (PPT) data (Kang and Frankel, 2005). Since the transient current profile is a function of the time constants associated with the various capacitors in the system, equivalent circuit models can be constructed for PPT current transients to determine the value of various capacitive analogs (Kang and Frankel, 2005). This is of advantage over multi-frequency sweep sine EIS because instrumentation is often much more expensive than what would be required for PPT. However, the analytical power of EIS is much more robust than that of PPT, as EIS is able to probe the system over a very large range of frequencies to access more information about the coating system. Additionally, a scanning local electrochemical impedance spectroscopy (LEIS) apparatus has been used to measure all of the same key parameters as global EIS but on a spatially resolved scale with respect to coating defects like scribes and the progression of scribe creep as a function of exposure (Lillard et al., 1994; Jorcin et al., 2006). This is certainly an improvement over global EIS measurements.

Optimizing the protection performance of metal-based pigmented coatings is difficult due to the sometimes-conflicting characteristics which are desirable for good performance of each protection mechanism. Holistic frameworks have been developed to determine how to best maximize the corrosion protection of pigmented coatings. For example, barrier and inhibition protection must be carefully considered for coatings which contain metal-based inhibitor compounds. A framework has been considered to assess the selection of inhibitor pigments for corrosion protection (Sinko, 2001). For a given anion package, various metal cations can be selected to store the compound in the coating. While some beneficial corrosion inhibition effects have been observed for cations like Zn^{2+} (Krieg et al., 2012;

Liu et al., 2019), Mg^{2+} (Krieg et al., 2012; Liu et al., 2019), and Ce^{3+} (Kaesche, 1985; Jakab and Scully, 2005; Presuel-Moreno et al., 2005a, 2006; Ho et al., 2006; Scully and Jakab, 2006), the cation also influences the solubility of the compound and the subsequent pH of the solution due to hydrolysis (Sinko, 2001). While corrosion inhibition necessitates the release of the inhibiting ion, excessive solubility can be detrimental to coating barrier properties by excessive pore formation in volumes once occupied by pigments and also in blistering caused by the osmotic pressure differential (Sinko, 2001). This pressure differential may be established by electrolyte uptake into the coating, which is thermodynamically driven to dilute the high inhibitor concentration in the pore space (Sinko, 2001). In this way, an optimal pigment solubility (and usually solution pH) is required where inhibition is achieved (inhibitor concentration exceeds the critical concentration for inhibition) but osmotic blistering avoided (inhibitor concentration does not exceed the threshold for onset blistering). The solubility of metal-based compounds as a function of pH, constituent concentration, and chloride concentration is easily represented by the chemical stability diagram (Santucci et al., 2018a; McMahon et al., 2019b). Establishment of these diagrams allows for easy comparison of the equilibrium conditions for the formation and dissolution of compounds. Included in this framework, are calculation for determining how the solution chemistry (in terms of pH and metal ion concentration) progresses from some initial condition to some final, equilibrium condition (Santucci et al., 2018a; McMahon et al., 2019b). Analysis with chemical stability diagrams has proven useful for interpreting the behavior of Mg and Zn-based coating systems (Santucci et al., 2018a; McMahon et al., 2019b). An example of a chemical stability diagram for the Mg system is given in **Figure 13**.

As another example, barrier properties and cathodic protection must be carefully balanced to achieve optimal protection. The barrier protection of a coating is most effective when the coating contains a small fraction of defects which allow for electrolyte uptake in the coating and wetting of the substrate. However, this increases the resistance of the coatings, and in turn, the resistance between the anodic pigments and the cathodic substrate. As barrier properties increase, the efficacy of cathodic protection is mitigated. This has been observed for MgRPs which contain resistive topcoats and pretreatments (King et al., 2014a,b; Kannan et al., 2015; Kannan and Scully, 2016; Santucci et al., 2017a,b) and ZnRP containing various organic and inorganic polymer matrices (Knudsen et al., 2001, 2005; McMahon et al., 2019a). In this way, a balance must be struck between barrier performance and cathodic protection. Due to the difficulty in designing fully optimized coating systems, final formulations are often determined by Edisonian-type trial and error performance analysis in various field or laboratory-accelerated exposures. Even then, it becomes difficult to determine the best formulation for a given application due to the varied nature of service condition exposures and also the different lifetimes at which each type of corrosion protection dominates. For this reason, it is useful to employ mathematical ranking methods and decision-making theories to impartially determine the best formulation for a given application (Athanasopoulos et al., 2009; Ghafari et al.,

2019). When desirable attributes of a corrosion resistant coating are known (as delineated above), and experimental results of exposure analysis collected, they can be used as model inputs with which to rank the various formulations against each other. Numerical ranking methods have been applied to a composite zirconia coating on AA7057 to impartially determine what inhibitor package (null, Ce, or BTA) best protects the AA7057 substrate (Ghafari et al., 2019) according to the corrosion rate, corrosion potential, and impedance response, for example.

SUMMARY AND FUTURE PROSPECTS

Metal-rich primers operate through multiple modes of protection, many times in combination to protect the substrate, which has proven challenging to collectively characterize and thoroughly understand to guide further innovation. It is clear that multi-probe spatially resolved methods must be combined to obtain chemical, materials, electrochemical and physical characteristics. Further complexity lies in the timing, as the activation of sacrificial particles may be delayed by design or accidentally depending on the coating's purpose. In the case of pretreatments, the resistive layer might degrade enabling better contact between the primer particles and the substrate. One dominant mode of protection may transition into another as well, such as when galvanic protection ceases due to corrosion product filling of pore spaces, which then promotes better primer barrier properties. However, pigment passivation could be detrimental, thus these mechanisms often have to be balanced for optimal performance. Coating designers should think in terms of the coating attributes desired and then collectively design for them, rather than selecting coating stack ups piecewise according to surface preparation, pretreatment, primer and topcoat. As MRPs progress in performance and complexity, a thorough understanding of characterization methods ranging across numerous length scales will be increasingly necessary. It is important to note that contemporary coating analysis such as by EIS in isolation is inadequate to assess all aspects of primer performance. For the purposes of this review, many of the previously discussed techniques are summarized in **Table 2** to assist the reader in understanding the role of each method. Unique combinations of experimental methods and characterization techniques must be increasingly utilized together or concurrently to further reveal the mechanisms enabling MRP performance (King et al., 2014a; Santucci et al., 2017a,b). The large datasets created through such work will then be well-suited for computer-aided performance ranking and coating selection models.

The global high performance anti-corrosion coating market, which was valued at US\$11.95 billion in 2014, is anticipated to grow 4.8% per year to reach US\$18.22 billion by 2023 (CNBC, 2016). Research on and development of new-age coatings will increasingly solidify the important position that these systems hold in combatting the significant loss of infrastructure due to corrosion while further reducing their environmental impact. As emission regulations tighten and industrial leaders continually strive to conform while continuing to improve

corrosion protection, modern coatings may be amongst the first products which incorporate new polymer resin formulations, alloys, and additives to meet increasingly stringent performance demands. Trial- and-error type studies and lessons-learned-approaches require too much time to enable rapid insertion of new technologies. The need for new coating solutions, such as will often be driven by changing environmental regulations, new substrates, and harsher environments, requires high fidelity methods in tandem, interactive analysis, and rapid feedback combined with accelerated testing. The issue of accelerated testing accuracy will remain of great importance, innovation will continue to push the envelope of modern understanding on the mechanisms of anti-corrosion coating performance, and increasingly diverse characterization techniques will be required to push further advancement. In addition, it is clear that artificial intelligence will be required such as neural network methods in order to establish relationships between many variables, test metrics, and long-term coating performance.

AUTHOR CONTRIBUTIONS

All authors contributed to the literature review and the structuring of the manuscript. JS oversaw and edited

the development and production of the manuscript. BK and ZW conducted the literature review of accelerated and outdoor exposure test methods. CG conducted the literature review of a variety of modern characterization methods such as scanning kelvin probe for the study of chemical inhibition and cathodic protection. RS conducted the literature review on chemical inhibition and modeling methods, and composed the section on modeling of coatings as well as portions of the manuscript detailing electrochemical impedance spectroscopy. MM conducted the literature review on galvanic protection and drafted the manuscript.

ACKNOWLEDGMENTS

The authors would like to thank the Office of Naval Research (Airan Perez, Award #N000-14-15-1-2491), the Office of the Undersecretary of Defense Corrosion University Pilot Program (Daniel Dunmire, Awards #FA7000-18-2-0006 and #FA7000-14-2-0010), the National Science Foundation under NSF DMR #1309999, and the Army Research Office under agreement #W911NF-14-2-0005 for the financial support enabling this work.

REFERENCES

- Aballe, A., Bethencourt, M., Botana, F. J., Cano, M. J., and Marcos, M. (2001). Localized alkaline corrosion of alloy AA5083 in neutral 3.5% NaCl solution. *Corros. Sci.* 43, 1657–1674. doi: 10.1016/S0010-938X(00)00166-9
- Aballe, A., Bethencourt, M., Botana, F. J., Cano, M. J., and Marcos, M. (2003). Influence of the cathodic intermetallics distribution on the reproducibility of the electrochemical measurements on AA5083 alloy in NaCl solutions. *Corros. Sci.* 45, 161–180. doi: 10.1016/S0010-938X(02)00067-7
- Abreu, C. M., Izquierdo, M., Keddad, M., Nóvoa, X. R., and Takenouti, H. (1996). Electrochemical behaviour of zinc-rich epoxy paints in 3% NaCl solution. *Electrochim. Acta* 41, 2405–2415. doi: 10.1016/0013-4686(96)00021-7
- Akiyama, E., Markworth, A. J., McCoy, J. K., Frankel, G. S., Xia, L., and McCreery, R. L. (2003). Storage and release of soluble hexavalent chromium from chromate conversion coatings on Al Alloys: kinetics of release. *J. Electrochem. Soc.* 150, B83–B91. doi: 10.1149/1.1537755
- Aldykewicz, A. J., Isaacs, H. S., and Davenport, A. J. (1995). The Investigation of cerium as a cathodic inhibitor for aluminum-copper alloys. *J. Electrochem. Soc.* 142, 3342–3350. doi: 10.1149/1.2049985
- Allahar, K. N., Battocchi, D., Bierwagen, G. P., and Tallman, D. E. (2010). Transmission line modeling of EIS data for a Mg-Rich Primer on AA 2024-T3. *J. Electrochem. Soc.* 157:C95. doi: 10.1149/1.3274206
- Allahar, K. N., Hinderliter, B. R., Tallman, D. E., and Bierwagen, G. P. (2008). Water transport in multilayer organic coatings. *J. Electrochem. Soc.* 155:F201. doi: 10.1149/1.2946429
- Amand, S., Musiani, M., Orazem, M. E., Pébère, N., Tribollet, B., and Vivier, V. (2013). Constant-phase-element behavior caused by inhomogeneous water uptake in anti-corrosion coatings. *Electrochim. Acta* 87, 693–700. doi: 10.1016/j.electacta.2012.09.061
- Armelin, E., Marti, M., Liesa, F., Iribarren, J. I., and Aleman, C. (2010). Partial replacement of metallic zinc dust in heavy duty protective coatings by conductive polymer. *Prog. Org. Coatings* 69, 26–30. doi: 10.1016/j.porgcoat.2010.04.023
- ASTM International (1999). *G1-03(2017)e1 Standard Practice for Preparing, Cleaning, and Evaluating Corrosion Test Specimens*. West Conshohocken, PA: ASTM International. doi: 10.1520/G0001-03R17E01
- ASTM International (2018). *B117-18: Standard Practice for Operating Salt Spray (Fog) Apparatus*. West Conshohocken, PA: ASTM International. doi: 10.1520/B0117-18
- Athanasopoulos, G., Riba, C. R., and Athanasopoulou, C. (2009). A decision support system for coating selection based on fuzzy logic and multi-criteria decision making. *Expert Syst. Appl.* 36, 10848–10853. doi: 10.1016/j.eswa.2009.01.016
- Barker, R., Burkle, D., Charpentier, T., Thompson, H., and Neville, A. (2018). A review of iron carbonate (FeCO₃) formation in the oil and gas industry. *Corros. Sci.* 142, 312–341. doi: 10.1016/j.corsci.2018.07.021
- Bastos, A. C., Quevedo, M. C., and Ferreira, M. G. S. (2016). Investigating the separation of anodic and cathodic defects in organic coatings applied on metal substrates. An experimental contribution. *Prog. Org. Coatings* 96, 26–31. doi: 10.1016/j.porgcoat.2015.12.016
- Bellucci, F., and Nicodemo, L. (1993). Water transport in organic coatings. *Corrosion* 49, 235–247. doi: 10.5006/1.3316044
- Bierwagen, G., Allahar, K., Hinderliter, B., and Jung, H. (2007). “Zn-Rich coatings revisited,” in *Tri-Service Corros Conference* (Denver, CO).
- Bierwagen, G. P. (1996). Reflections on corrosion control by organic coatings. *Prog. Org. Coatings* 28, 43–48. doi: 10.1016/0300-9440(95)00588-9
- CNBC (2016). *High Performance Anti-corrosion Coatings Market to reach US\$18.22 bn by 2023; Product Segment, End-User and Global Regional Analysis by Transparency Market Research*. Available online at: <https://www.cnbc.com/2016/04/11/globe-newswire-high-performance-anti-corrosion-coatings-market-to-reach-us1822-bn-by-2023-product-segment-end-user-global-regional.html>
- Coelho, L. B., and Olivier, M. (2018). The inhibition efficiency of different species on AA2024/graphite galvanic coupling models depicted by SVET. *Corros. Sci.* 136, 292–303. doi: 10.1016/j.corsci.2018.03.015
- Cubides, Y., and Castaneda, H. (2016). Corrosion protection mechanisms of carbon nanotube and zinc-rich epoxy primers on carbon steel in simulated concrete pore solutions in the presence of chloride ions. *Corros. Sci.* 109, 145–161. doi: 10.1016/j.corsci.2016.03.023
- Danford, M. D., Walsh, D. W., and Mendrek, M. J. (1995). *The Corrosion Protection of 2219-T87 Aluminum by Organic and Inorganic Zinc-Rich Primers*. Huntsville, AL: NASA Report.

- Deshpande, K. B. (2010). Validated numerical modelling of galvanic corrosion for couples : magnesium alloy (AE44)– mild steel and AE44 – aluminium alloy (AA6063) in brine solution. *Corros. Sci.* 52, 3514–3522. doi: 10.1016/j.corsci.2010.06.031
- Fajardo, S., Glover, C. F., Williams, G., and Frankel, G. S. (2017). The evolution of anodic hydrogen on high purity magnesium in acidic buffer solution. *Corrosion* 73, 482–493. doi: 10.5006/1.3290386
- Feliu, J. S., Morcillo, M., and Feliu, S. (2001). Deterioration of cathodic protection action of zinc-rich paint coatings in atmospheric exposure. *Corrosion* 57, 591–597. doi: 10.5006/1.3290386
- Feliu, S. J., Barajas, R., Bastidas, J. M., Morcillo, M., and Feliu, S. (1993b). Study of protection mechanisms of zinc-rich paints by electrochemical impedance spectroscopy, electrochem. *Impedance Anal. Ans Interpret.* 1188, 438–449. doi: 10.1520/STP18084S
- Feliu, S. J., Morcillo, M., Bastidas, J. M., and Feliu, S. (1993a). Evolution of the protective mechanisms of zinc-rich paints during atmosphere exposure. *J. Coatings Technol.* 65, 43–48.
- Filotás, D., Izquierdo, J., Kiss, A., Nagy, L., Nagy, G., and Souto, R. M. (2017). Improved potentiometric SECM imaging of galvanic corrosion reactions. *Corros. Sci.* 129, 136–145. doi: 10.1016/j.corsci.2017.10.006
- Francis, R. A. (2013). “Inorganic zinc silicate coatings - the early days part II: the morgan whyalla pipeline,” in *Inorg. Zinc Coatings Hist. Chem. Prop. Appl. Altern., 2nd edition*, ed R. A. Francis (Victoria: The Australasian Corrosion Association Incorporated), 18–23.
- Frankel, G. S., and McCreery, R. L. (2001). Inhibition of al alloy corrosion by chromates. *Interface-Electrochemical Soc.* 10, 34–39.
- Frankel, G. S., Vienna, J. D., Lian, J., Scully, J. R., Gin, S., V., et al. (2018). A comparative review of the aqueous corrosion of glasses. Crystalline ceramics, and metals. *Npj Mater. Degrad.* 15, 1–17. doi: 10.1038/s41529-018-0037-2
- Franklin, M. J., White, D. C., and Isaacs, H. S. (1992). A study of carbon steel corrosion inhibition by phosphate ions and by an organic buffer using a scanning vibrating electrode. *Corros. Sci.* 33, 251–260. doi: 10.1016/0010-938X(92)90149-W
- Gergely, A., Bertóti, I., Török, T., Pfeifer, É., and Kálmán, E. (2013). Corrosion protection with zinc-rich epoxy paint coatings embedded with various amounts of highly dispersed polypyrrole-deposited alumina monohydrate particles. *Prog. Org. Coatings* 76, 17–32. doi: 10.1016/j.porgcoat.2012.08.005
- Ghafari, A., Yousefpour, M., and Shanaghi, A. (2019). Corrosion protection determine of ZrO₂ / AA7057 nanocomposite coating with inhibitor using a mathematical ranking methods. *Appl. Surf. Sci.* 465, 427–439. doi: 10.1016/j.apsusc.2018.09.110
- Gharbi, O., Biribilis, N., and Ogle, K. (2016). In-Situ Monitoring of alloy dissolution and residual film formation during the pretreatment of Al-Alloy AA2024-T3. *J. Electrochem. Soc.* 163, C240–C251. doi: 10.1149/2.1121605jes
- Gharbi, O., Thomas, S., Smith, C., and Biribilis, N. (2018). Chromate replacement: what does the future hold? *Npj Mater. Degrad.* 12, 23–25. doi: 10.1038/s41529-018-0034-5
- Glover, C. F., Cain, T. W., and Scully, J. R. (2019). Performance of Mg-Sn surface alloys for the sacrificial cathodic protection of Mg alloy AZ31B-H24. *Corros. Sci.* 149, 195–206. doi: 10.1016/j.corsci.2019.01.015
- Glover, C. F., Richards, C., Baker, J., Williams, G., and McMurray, H. N. (2017). In-coating graphene nano-platelets for environmentally-friendly corrosion protection of iron. *Corros. Sci.* 114, 169–172. doi: 10.1016/j.corsci.2016.11.009
- Grundmeier, G., Schmidt, W., and Stratmann, M. (2000). Corrosion protection by organic coatings : electrochemical mechanism and novel methods of investigation. *Electrochim. Acta.* 45, 2515–2533. doi: 10.1016/S0013-4686(00)00348-0
- Hack, H. P., and Scully, J. R. (1991). Defect area determination of organic coated steels in seawater using the breakpoint frequency method. *J. Electrochem. Soc.* 138, 33–40. doi: 10.1149/1.2085574
- Hammouda, N., Chadli, H., Guillemot, G., and Belmokre, K. (2011). The corrosion protection behaviour of zinc rich epoxy paint in 3% NaCl solution. *Adv. Chem. Eng. Sci.* 01, 51–60. doi: 10.4236/aces.2011.12009
- Hellmann, R., and Tisserand, D. (2006). Dissolution kinetics as a function of the Gibbs free energy of reaction: An experimental study based on albite feldspar. *Geochimica* 70, 364–383. doi: 10.1016/j.gca.2005.10.007
- Hieftje, G. M. (2000). Atomic emission spectroscopy — it lasts and lasts and lasts. *J. Chem. Educ.* 77, 577–583. doi: 10.1021/ed077p577
- Ho, D., Brack, N., Scully, J., Markley, T., Forsyth, M., and Hinton, B. (2006). Cerium dibutylphosphate as a corrosion inhibitor for AA2024-T3 aluminum alloys. *J. Electrochem. Soc.* 153, B392–B401. doi: 10.1149/1.2217260
- Huang, T.-S., and Frankel, G. S. (2007). Effects of temper and potential on localized corrosion kinetics of aluminum alloy 7075. *Corrosion* 63, 731–743. doi: 10.5006/1.3278422
- Ilevbare, G. O., and Scully, J. R. (2001). Mass-transport-limited oxygen reduction reaction on AA2024-T3 and selected intermetallic compounds in chromate-containing solutions. *Corrosion* 57, 134–152. doi: 10.5006/1.3290339
- Isaacs, H. S. (1988). The measurement of the galvanic corrosion of soldered copper using the scanning vibrating electrode technique. *Corros. Sci.* 28, 547–558. doi: 10.1016/0010-938X(88)90023-6
- Izquierdo, J., Nagy, L., González, S., Santana, J. J., Nagy, G., and Souto, R. M. (2013). Resolution of the apparent experimental discrepancies observed between SVET and SECM for the characterization of galvanic corrosion reactions. *Electrochem. Commun.* 27, 50–53. doi: 10.1016/j.elecom.2012.11.002
- Jakab, M. A., Little, D. A., and Scully, J. R. (2005). Experimental and modeling studies of the oxygen reduction reaction on AA2024-T3. *J. Electrochem. Soc.* 152, B311–B320. doi: 10.1149/1.1949047
- Jakab, M. A., and Scully, J. R. (2005). On-demand release of corrosion-inhibiting ions from amorphous Al-Co-Ce alloys. *Nat. Mater.* 4, 667–670. doi: 10.1038/nmat1451
- Jakab, M. A., and Scully, J. R. (2008). Effect of pH and chloride ion concentration on inhibitor storage in amorphous Al-Co-Ce Alloys. *Corrosion* 64, 198–209. doi: 10.5006/1.3278466
- Jalili, M., Rostami, M., and Ramezanzadeh, B. (2015). An investigation of the electrochemical action of the epoxy zinc-rich coatings containing surface modified aluminum nanoparticle. *Appl. Surf. Sci.* 328, 95–108. doi: 10.1016/j.apsusc.2014.12.034
- Jorcin, J. B., Aragon, E., Merlati, C., and Pèbère, N. (2006). Delaminated areas beneath organic coating: a local electrochemical impedance approach. *Corros. Sci.* 48, 1779–1790. doi: 10.1016/j.corsci.2005.05.031
- Kaesche, H. (1985). *Metallic Corrosion: Principles of Physical Chemistry and Current Problems*, 2nd edition. Houston, TX: NACE International.
- Kalendová, A. (2003). Effects of particle sizes and shapes of zinc metal on the properties of anticorrosive coatings. *Prog. Org. Coatings* 46, 324–332. doi: 10.1016/S0300-9440(03)00022-5
- Kang, J., and Frankel, G. S. (2005). Potentiostatic pulse testing for assessment of early coating failure. *Z. Phys. Chem.* 219, 1519–1537. doi: 10.1524/zpch.2005.219.11.1519
- Kannan, B., Glover, C. F., McMurray, H. N., Williams, G., and Scully, J. R. (2018b). Performance of a magnesium-rich primer on pretreated AA2024-T351 in full immersion: a galvanic throwing power investigation using a scanning vibrating electrode technique. *J. Electrochem. Soc.* 165, C27–C41. doi: 10.1149/2.0711802jes
- Kannan, B., King, A. D., and Scully, J. R. (2015). Effect of pretreatments on Alloy 2024-T351 corrosion protection by magnesium-rich. Nonchromium primer (MgRP): laboratory characterization in full immersion. *Corrosion* 71, 1093–1109. doi: 10.5006/1700
- Kannan, B., and Scully, J. R. (2016). Performance of a magnesium-rich primer on pretreated AA2024-T351 in selected laboratory and field environments: Conversion coating pretreatments. *Corrosion* 72, 1363–1384. doi: 10.5006/2187
- Kannan, B., Wolanski, D. M., and Scully, J. R. (2018a). Performance of a magnesium-rich primer on pretreated AA2024-T351 in selected laboratory and field environments : anodization pretreatment. *Corrosion* 74, 654–668. doi: 10.5006/2424
- Kendig, M., and Scully, J. R. (1990). Basic aspects of electrochemical impedance application for the life prediction of organic coatings on metals. *Corrosion* 46, 22–29. doi: 10.5006/1.3585061
- King, A. D., Biribilis, N., and Scully, J. R. (2014b). Accurate electrochemical measurement of magnesium corrosion rates; A combined impedance mass-loss and hydrogen collection study. *Electrochim. Acta* 121, 394–406. doi: 10.1016/j.electacta.2013.12.124
- King, A. D., Kannan, B., and Scully, J. R. (2014a). Environmental degradation of a mg-rich primer in selected field and laboratory environments: part 1-without a topcoat. *Corrosion* 70, 512–535. doi: 10.5006/0988

- King, A. D., Lee, J. S., and Scully, J. R. (2015). Galvanic couple current and potential 892 distribution between a Mg electrode and 2024-T351 under droplets analyzed by 893 microelectrode arrays. *J. Electrochem. Soc.* 162, 12–23. doi: 10.1149/2.0121501jes
- King, A. D., Lee, J. S., and Scully, J. R. (2016). Finite element analysis of the galvanic couple current and potential distribution between Mg and 2024-T351 in a Mg rich primer configuration. *J. Electrochem. Soc.* 163, C342–C356. doi: 10.1149/2.0171607jes
- King, A. D., and Scully, J. R. (2011). Sacrificial anode-based galvanic and barrier corrosion protection of 2024-T351 by a Mg-rich primer and development of test methods for remaining life assessment. *Corrosion* 67, 1–22. doi: 10.5006/1.3590330
- Knudsen, O. Ø., Steinsmo, U., and Bjordal, M. (2005). Zinc-rich primers - Test performance and electrochemical properties. *Prog. Org. Coatings* 54, 224–229. doi: 10.1016/j.porgcoat.2005.06.009
- Knudsen, O. Ø., Steinsmo, U., Bjordal, M., and Nijjer, S. (2001). Accelerated testing: correlation between four accelerated tests and five tears of offshore field testing. *JPCL* 18, 52–56.
- Koch, G. (2017). “Cost of corrosion,” in *Trends Oil Gas Corros. Res. Technol. Prod. Transm.*, ed. A. M. El-Sherik (Cambridge: Woodhead Publishing), 3–30.
- Koul, M. G., Sheetz, A., Ault, P., Repp, J., and Whitfield, A. (2014). The effect of Zn-rich coatings on the corrosion and cracking resistance of high strength armor steel. *Corrosion* 70, 337–350. doi: 10.5006/1027
- Koulombi, N., Tsangaris, G. M., Vourvahi, C., and Molnar, F. (1997). Corrosion resistance and dielectric properties of an iron oxide filled epoxy coating. *J. Coatings Technol.* 69, 53–59. doi: 10.1007/BF02696252
- Krieg, R., Rohwerder, M., Evers, S., Schuhmacher, B., and Schauer-Pass, J. (2012). Cathodic self-healing at cut-edges: The effect of Zn^{2+} and Mg^{2+} ions. *Corros. Sci.* 65, 119–127. doi: 10.1016/j.corsci.2012.08.008
- Lasaga, A. C. (2014). *Kinetic Theory in the Earth Sciences, Ch. 7*. Princeton, NJ: Princeton University Press.
- Leidheiser, H. R. (1982). Corrosion of painted metals — a review. *Corrosion* 38, 374–383. doi: 10.5006/1.3581899
- Leng, A., Streckel, H., and Stratmann, M. (1998). The delamination of polymeric coatings from steel. Part 1: calibration of the Kelvin probe and basic delamination mechanism. *Corros. Sci.* 41, 547–578. doi: 10.1016/S0010-938X(98)00166-8
- Lillard, R. S., Kruger, J., Tait, W. S., and Moran, P. J. (1994). Using local electrochemical impedance spectroscopy to examine coating failure. *Corrosion* 51, 251–259. doi: 10.5006/1.3294331
- Liu, C., Yang, V. A., and Kelly, R. G. (2019). Inhibition of cathodic kinetics by Zn^{2+} and Mg^{2+} on AA7050-T7451. *J. Electrochem. Soc.* 166, C134–C146. doi: 10.1149/2.0551906jes
- Maier, B., and Frankel, G. S. (2011). Behavior of magnesium-rich primers on AA2024-T3. *Corrosion* 67, 1–15. doi: 10.5006/1.3586018
- Mansfeld, F. (1990). Electrochemical impedance spectroscopy (EIS) as a new tool for investigating methods of corrosion protection. *Electrochim. Acta* 35, 1533–1544. doi: 10.1016/0013-4686(90)80007-B
- Mansfeld, F., Kendig, M. W., and Tsai, S. (1982). Evaluation of corrosion behavior of coated metals with ac impedance measurements. *Corrosion* 38, 478–485. doi: 10.5006/1.3577363
- Mansfeld, F., and Tsai, C. H. (1991). Determination of coating deterioration with EIS. I. Basic relationships. *Corrosion* 47, 958–963. doi: 10.5006/1.3585209
- Marchebois, H., Joiret, S., Savall, C., Bernard, J., and Touzain, S. (2002). Characterization of zinc-rich powder coatings by EIS and Raman spectroscopy. *Surf. Coatings Technol.* 157, 151–161. doi: 10.1016/S0257-8972(02)00147-0
- Marques, A. G., and Simões, A. M. (2014). EIS and SVET assessment of corrosion resistance of thin Zn-55% Al-rich primers: Effect of immersion and of controlled deformation. *Electrochim. Acta* 148, 153–163. doi: 10.1016/j.electacta.2014.10.015
- Marsh, J., Scantlebury, J. D., and Lyon, S. B. (2001). The effect of surface/primer treatments on the performance of alkyd coated steel. *Corros. Sci.* 43, 829–852. doi: 10.1016/S0010-938X(00)00070-6
- McMahon, M. E., Burns, J. T., and Scully, J. R. (2019a). New criteria for substrate protection against stress corrosion cracking in Al-Mg alloys based on non-polarizability of Zn-rich primers. *Prog. Org. Coatings* 135, 392–409. doi: 10.1016/j.porgcoat.2019.05.049
- McMahon, M. E., Santucci, R. J. Jr., and Scully, J. R. (2019b). Advanced chemical stability diagrams to predict the formation of complex zinc compounds in chloride environment. *RSC Adv.* 9, 19905–19916. doi: 10.1039/C9RA00228F
- McMahon, M. E., Scully, J. R., and Burns, J. T. (2019c). Mitigation of intergranular cracking in Al-Mg alloys via Zn-based electrode potential control in sodium chloride solution. *Corrosion* 75, 911–928. doi: 10.5006/3185
- Merten, B. J. E., Battocchi, D., and Bierwagen, G. P. (2015). Aluminum alloy 2024-T3 protection by magnesium-rich primer with chromate-free metal salts. *Prog. Org. Coatings* 78, 446–454. doi: 10.1016/j.porgcoat.2014.09.013
- Moggridge, G. D., Lape, N. K., Yang, C., and Cussler, E. L. (2003). Barrier films using flakes and reactive additives. *Prog. Org. Coatings* 46, 231–240. doi: 10.1016/S0300-9440(02)00180-7
- Montemor, M. F. (2014). Functional and smart coatings for corrosion protection : a review of recent advances. *Surf. Coat. Technol.* 258, 17–37. doi: 10.1016/j.surfcoat.2014.06.031
- Nanna, M. E., and Bierwagen, G. P. (2004). Mg-rich coatings: A new paradigm for Cr-free corrosion protection of Al aerospace alloys. *J. Coatings Technol. Res.* 1, 69–80. doi: 10.1007/s11998-004-0001-7
- Nazarov, A., Le Bozec, N., and Thierry, D. (2018). Scanning Kelvin Probe assessment of steel corrosion protection by marine paints containing Zn-rich primer. *Prog. Org. Coatings* 125, 61–72. doi: 10.1016/j.porgcoat.2018.08.024
- Oblonsky, L. J. (2006). Surface-enhanced raman scattering from pyridine adsorbed on thin layers of stainless steel. *J. Electrochem. Soc.* 141:3312. doi: 10.1149/1.2059332
- Ogle, K. (2004). The alkaline stability of phosphate coatings I : ICP atomic emission spectroelectrochemistry. *Corros. Sci.* 46, 979–995. doi: 10.1016/S0010-938X(03)00182-3
- Ogle, K., Baudu, V., Garrigues, L., and Philippe, X. (2000). Localized electrochemical methods applied to cut edge corrosion. *J. Electrochem. Soc.* 147:3654. doi: 10.1149/1.1393954
- Orazem, M. E., and Tribollet, B. (2008). An integrated approach to electrochemical impedance spectroscopy. *Electrochim. Acta* 53, 7360–7366. doi: 10.1016/j.electacta.2007.10.075
- Orazem, M. E., and Tribollet, B. (2017). *Electrochemical Impedance Spectroscopy, 2nd edition*. Hoboken, NJ: Wiley.
- Paliwoda-Porebska, G., Stratmann, M., Rohwerder, M., Potje-Kamloth, K., Lu, Y., Pich, A. Z., et al. (2005). On the development of polypyrrole coatings with self-healing properties for iron corrosion protection. *Corros. Sci.* 47, 3216–3233. doi: 10.1016/j.corsci.2005.05.057
- Park, J. H., Yun, T. H., Kim, K. Y., Song, Y. K., and Park, J. M. (2012). The improvement of anticorrosion properties of zinc-rich organic coating by incorporating surface-modified zinc particle. *Prog. Org. Coatings* 74, 25–35. doi: 10.1016/j.porgcoat.2011.09.012
- Parker, M., Shrivastava, S., and Kelly, R. G. (2015). Developing a framework for accelerated test design by investigating the impact of key testing variables on the exfoliation corrosion of AA2060. *ECS Meet. Abstr.* 14, 694–694.
- Pathak, S. S., Blanton, M. D., Mendon, S. K., and Rawlins, J. W. (2010). Investigation on dual corrosion performance of magnesium-rich primer for aluminum alloys under salt spray test (ASTM B117) and natural exposure. *Corros. Sci.* 52, 1453–1463. doi: 10.1016/j.corsci.2009.11.032
- Pathak, S. S., Mendon, S. K., Blanton, M. D., and Rawlins, J. W. (2012). Magnesium-based sacrificial anode cathodic protection coatings (Mg-Rich Primers) for aluminum alloys. *Metals* 2, 353–376. doi: 10.3390/met2030353
- Pereira, D., Scantlebury, J. D., Ferreira, M. G. S., and Almeida, M. E. (1990). The application of electrochemical measurements to the study and behaviour of zinc-rich coatings. *Corros. Sci.* 30, 1135–1147. doi: 10.1016/0010-938X(90)90061-9
- Petry, L., and Hansen, D. C. (2016). A comparative study of two coating systems exposed for 2 years in the field and in accelerated atmospheric corrosion chamber environments. *Corrosion* 72, 1385–1396. doi: 10.5006/2084
- Place, B. J. (2019). Activity analysis of iron in water using a simple LED spectrophotometer. *J. Chem. Educ.* 96, 714–719. doi: 10.1021/acs.jchemed.8b00515

- Plagemann, P., Weise, J., and Zockoll, A. (2013). Zinc-magnesium-pigment rich coatings for corrosion protection of aluminum alloys. *Prog. Org. Coatings* 76, 616–625. doi: 10.1016/j.porgcoat.2012.12.001
- Presuel-Moreno, F., Jakab, M. A., Tailleart, N., Goldman, M., and Scully, J. R. (2008). Corrosion-resistant metallic coatings. *Mater. Today* 11, 14–23. doi: 10.1016/S1369-7021(08)70203-7
- Presuel-Moreno, F. J., Goldman, M. E., Kelly, R. G., and Scully, J. R. (2005b). Electrochemical sacrificial cathodic prevention provided by an Al-Co-Ce metal coating coupled to AA2024-T3. *J. Electrochem. Soc.* 152, B302–B310. doi: 10.1149/1.1943588
- Presuel-Moreno, F. J., Jakab, M. A., and Scully, J. R. (2005a). Inhibition of the oxygen reduction reaction on copper with cobalt, cerium, and molybdate ions. *J. Electrochem. Soc.* 152, B376–B387. doi: 10.1149/1.1997165
- Presuel-Moreno, F. J., Wang, H., Jakab, M. A., Kelly, R. G., and Scully, J. R. (2006). Computational modeling of active corrosion inhibitor release from an Al-Co-Ce metallic coating protection of exposed AA2024-T3. *J. Electrochem. Soc.* 153, B486–B498. doi: 10.1149/1.2335946
- Prosek, T., Nazarov, A., Bexell, U., Thierry, D., and Serak, J. (2008). Corrosion mechanism of model zinc-magnesium alloys in atmospheric conditions. *Corros. Sci.* 50, 2216–2231. doi: 10.1016/j.corsci.2008.06.008
- Rafla, V. N., Khullar, P., Kelly, R. G., and Scully, J. R. (2018). Coupled multi-electrode array with a sintered Ag/AgCl counter/reference electrode to investigate AA7050-T7451 and Type 316 stainless steel galvanic couple under atmospheric conditions. *J. Electrochem. Soc.* 165, C562–C572. doi: 10.1149/2.1001809jes
- Rafla, V. N., and Scully, J. R. (2019). Galvanic couple behavior between AA7050-T7451 and stainless steel in a fastener arrangement assessed with coupled multi-electrode arrays under atmospheric exposure conditions. *Corrosion* 75, 12–28. doi: 10.5006/2885
- Rebhan, M., Rohwerder, M., and Stratmann, M. (2003). Delamination of polymeric coatings on silidized iron. *Mater. Corros.* 54, 19–22. doi: 10.1002/maco.200390001
- Rohwerder, M., Duc, L. M., and Michalik, A. (2009). *In situ* investigation of corrosion localised at the buried interface between metal and conducting polymer based composite coatings. *Electrochim. Acta* 54, 6075–6081. doi: 10.1016/j.electacta.2009.02.103
- Rohwerder, M., Isik-Uppenkamp, S., and Amarnath, C. A. (2011). Application of the Kelvin Probe method for screening the interfacial reactivity of conducting polymer based coatings for corrosion protection. *Electrochim. Acta* 56, 1889–1893. doi: 10.1016/j.electacta.2010.09.098
- Salgueiro Azevedo, M., Allely, C., Ogle, K., and Volovitch, P. (2015). Corrosion mechanisms of Zn(Mg,Al) coated steel: 2. The effect of Mg and Al alloying on the formation and properties of corrosion products in different electrolytes. *Corros. Sci.* 90, 482–490. doi: 10.1016/j.corsci.2014.07.042
- Santucci, R. J., Kannan, B., Abbott, W., and Scully, J. (2018b). Scientific investigation of the corrosion performance of magnesium and magnesium oxide primers on Al Alloy 2024-T351 in field exposures. *Corrosion* 75, 440–456. doi: 10.5006/2879
- Santucci, R. J., Kannan, B., Abbott, W., and Scully, J. R. (2017a). Magnesium and magnesium oxide primer on AA2024-T351: assessment of field performance. *Corrosion* 73, 1196–1201. doi: 10.5006/2545
- Santucci, R. J., McMahon, M. E., and Scully, J. R. (2018a). Utilization of chemical stability diagrams for improved understanding of electrochemical systems: evolution of solution chemistry towards equilibrium. *Npj Mater. Degrad.* 2, 1–9. doi: 10.1038/s41529-017-0021-2
- Santucci, R. J., Kannan, B., and Scully, J. R. (2017b). Electrochemical diagnostic cycle testing on magnesium and magnesium oxide-pigmented primers on 2024-T351. *Corrosion* 74, 96–111. doi: 10.5006/2547
- Schaefer, K., and Miszczyk, A. (2013). Improvement of electrochemical action of zinc-rich paints by addition of nanoparticulate zinc. *Corros. Sci.* 66, 380–391. doi: 10.1016/j.corsci.2012.10.004
- Scully, J. R., and Jakab, M. A. (2006). Design of cathodic inhibitors for AA2024-T3 guided by understanding heterogeneous cathodic reaction kinetics. *ECS Trans.* 1, 47–63. doi: 10.1149/1.2215578
- Shreepathi, S., Bajaj, P., and Mallik, B. P. (2010). Electrochemical impedance spectroscopy investigations of epoxy zinc rich coatings: Role of Zn content on corrosion protection mechanism. *Electrochim. Acta* 55, 5129–5134. doi: 10.1016/j.electacta.2010.04.018
- Shoyko, T., Stuart, O. D., and Gray, H. N. (2007). Spectroelectrochemical sensing of aqueous iron : an experiment for analytical chemistry. *J. Chem. Educ.* 84, 1467–1470. doi: 10.1021/ed084p1467
- Simoes, A., Battocchi, D., Tallman, D., and Bierwagen, G. (2008). Assessment of the corrosion protection of aluminium substrates by a Mg-rich primer : EIS, SVET and SECM study. *Prog. Org. Coatings* 63, 260–266. doi: 10.1016/j.porgcoat.2008.02.007
- Sinko, J. (2001). Challenges of chromate inhibitor pigments replacement in organic coatings. *Prog. Org. Coatings* 42, 267–282. doi: 10.1016/S0300-9440(01)00202-8
- Sørensen, P. A., Kiil, S., Dam-Johansen, K., and Weinell, C. E. (2009). Anticorrosive coatings : a review. *J. Coatings Technol. Res.* 6, 135–176. doi: 10.1007/s11998-008-9144-2
- Stouil, J., Prosek, T., Nazarov, A., Oswald, J., Kriz, P., and Thierry, D. (2015). Electrochemical properties of corrosion products formed on Zn-Mg, Zn-Al and Zn-Al-Mg coatings in model atmospheric conditions. *Mater. Corros.* 66, 777–782. doi: 10.1002/maco.201408058
- Stratmann, M., Feser, R., and Leng, A. (1994). Corrosion protection by organic films. *Electrochim. Acta* 39, 1207–1214. doi: 10.1016/0013-4686(94)E0038-2
- Taylor, M. L., Blanton, M., Konecki, C., Rawlins, J., and Scully, J. R. (2015a). Scribe creep and underpaint corrosion on ultra high molecular weight epoxy resin coated 1018 steel (UNS G10180) Part I : comparison of field exposures to standard lab accelerated life tests. *Corrosion* 71, 71–91. doi: 10.5006/1348
- Taylor, M. L., Blanton, M., Konecki, C., Rawlins, J., and Scully, J. R. (2015b). Scribe creep and underpaint corrosion on ultra-high molecular weight epoxy resin coated 1018 steel part 2: scribe creep model as a function of environmental severity factors. *Corrosion* 71, 326–342. doi: 10.5006/1349
- Thomas, N. L. (1991). The barrier properties of paint coatings. *Prog. Org. Coatings* 19, 101–121. doi: 10.1016/0033-0655(91)80001-Y
- Thomas, S., Birbilis, N., Venkatraman, M. S., and Cole, I. S. (2013). Self-repairing oxides to protect zinc: review. Discussion and prospects. *Corros. Sci.* 69, 11–22. doi: 10.1016/j.corsci.2013.01.011
- Tran, T. T. M., Tribollet, B., and Sutter, E. M. M. (2016). New insights into the cathodic dissolution of aluminium using electrochemical methods. *Electrochim. Acta* 216, 58–67. doi: 10.1016/j.electacta.2016.09.011
- Tsai, C. H., and Mansfeld, F. (1993). Determination of coating deterioration with EIS: Part II. Development of a method for field testing of protective coatings. *Corrosion* 49, 726–737. doi: 10.5006/1.3316106
- Upadhyay, V., and Battocchi, D. (2016). Localized electrochemical characterization of organic coatings : a brief review. *Prog. Org. Coatings* 99, 365–377. doi: 10.1016/j.porgcoat.2016.06.012
- Vakili, H., Ramezanzadeh, B., and Amini, R. (2015). The corrosion performance and adhesion properties of the epoxy coating applied on the steel substrates treated by cerium-based conversion coatings. *Corros. Sci.* 94, 466–475. doi: 10.1016/j.corsci.2015.02.028
- Vilche, J. R., Bucharsky, E. C., and Giudice, C. A. (2002). Application of EIS and SEM to evaluate the influence of pigment shape and content in ZRP formulations on the corrosion prevention of naval steel. *Corros. Sci.* 44, 1287–1309. doi: 10.1016/S0010-938X(01)00144-5
- Volovitch, P., Allely, C., and Ogle, K. (2009). Understanding corrosion via corrosion product characterization: I. Case study of the role of Mg alloying in Zn-Mg coating on steel. *Corros. Sci.* 51, 1251–1262. doi: 10.1016/j.corsci.2009.03.005
- Volovitch, P., Vu, T. N., Allély, C., Abdel Aal, A., and Ogle, K. (2011). Understanding corrosion via corrosion product characterization: II. Role of alloying elements in improving the corrosion resistance of Zn-Al-Mg coatings on steel. *Corros. Sci.* 53, 2437–2445. doi: 10.1016/j.corsci.2011.03.016
- Walter, G. W. (1986). A critical review of the protection of metals by paints. *Corros. Sci.* 26, 27–38. doi: 10.1016/0010-938X(86)90120-4
- Wang, H., Presuel, F., and Kelly, R. G. (2004). Computational modeling of inhibitor release and transport from multifunctional organic coatings. *Electrochim. Acta* 49, 239–255. doi: 10.1016/j.electacta.2003.08.006
- Wang, J., Zuo, Y., and Tang, Y. (2013). The study on Mg-Al rich epoxy primer for protection of aluminum alloy. *Int. J. Electrochem. Sci.* 8, 10190–10203.

- Wang, Q. (2012). *The Role of Zinc Particle Size and Loading in Cathodic Protection Efficiency*. Richmond, VA: Virginia Commonwealth University.
- Williams, G., Birbilis, N., and McMurray, H. N. (2015). Controlling factors in localised corrosion morphologies observed for magnesium immersed in chloride containing electrolyte. *Faraday Discuss.* 180, 313–330. doi: 10.1039/C4FD00268G
- Williams, G., Coleman, A. J., and McMurray, H. N. (2010). Inhibition of Aluminium Alloy AA2024-T3 pitting corrosion by copper complexing compounds. *Electrochim. Acta* 55, 5947–5958. doi: 10.1016/j.electacta.2010.05.049
- Williams, G., Dafydd, H., and Grace, R. (2013). The localised corrosion of Mg alloy AZ31 in chloride containing electrolyte studied by a scanning vibrating electrode technique. *Electrochim. Acta* 109, 489–501. doi: 10.1016/j.electacta.2013.07.134
- Williams, G., Dafydd, H., and Subramanian, R. (2014). Chloride ion concentration effects on passivity breakdown in magnesium. *ECS Trans.* 58, 23–34. doi: 10.1149/05831.0023ecst
- Williams, G., Geary, S., and McMurray, H. N. (2012). Smart release corrosion inhibitor pigments based on organic ion-exchange resins. *Corros. Sci.* 57, 139–147. doi: 10.1016/j.corsci.2011.12.024
- Williams, G., and McMurray, H. N. (2001). Chromate inhibition of corrosion-driven organic coating delamination studied using a scanning kelvin probe technique. *J. Electrochem. Soc.* 148, B337–B385. doi: 10.1149/1.1396336
- Williams, G., McMurray, H. N., and Worsley, D. A. (2002). Cerium (III) inhibition of corrosion-driven organic coating delamination studied using a scanning kelvin probe technique. *J. Electrochem. Soc.* 149, B154–B162. doi: 10.1149/1.1457983
- Xavier, J. R., and Nishimura, T. (2017). Evaluation of the corrosion protection performance of epoxy coatings containing Mg nanoparticle on carbon steel in 0.1 M NaCl solution by SECM and EIS techniques. *J. Coatings Technol. Res.* 14, 395–406. doi: 10.1007/s11998-016-9856-7
- Xia, L., Akiyama, E., Frankel, G., and McCreery, R. (2000). Storage and release of soluble hexavalent chromium from chromate conversion coatings equilibrium aspects of Cr^{VI} concentration. *J. Electrochem. Soc.* 147, 2556–2562. doi: 10.1149/1.1393568
- Yan, M., Gelling, V. J., Hinderliter, B. R., Battocchi, D., Tallman, D. E., and Bierwagen, G. P. (2010). SVET method for characterizing anti-corrosion performance of metal-rich coatings. *Corros. Sci.* 52, 2636–2642. doi: 10.1016/j.corsci.2010.04.012
- Yang, C., Smyrl, W. H., and Cussler, E. L. (2004). Flake alignment in composite coatings. *J. Memb. Sci.* 231, 1–12. doi: 10.1016/j.memsci.2003.09.022
- Yasakau, K. A., Zheludkevich, M. L., Lamaka, V. S., and Ferreira, M. G. S. (2006). Mechanism of corrosion inhibition of AA2024 by rare-earth compounds. *J. Phys. Chem. B* 110, 5515–5528. doi: 10.1021/jp0560664
- Zhang, L., Ma, A., Jiang, J., Song, D., Chen, J., and Yang, D. (2012). Anti-corrosion performance of waterborne Zn-rich coating with modified silicon-based vehicle and lamellar Zn (Al) pigments. *Prog. Nat. Sci. Mater. Int.* 22, 326–333. doi: 10.1016/j.pnsc.2012.07.001
- Zheludkevich, M. L., Tedim, J., and Ferreira, M. G. S. (2012). “Smart” coatings for active corrosion protection based on multi-functional micro and nanocontainers. *Electrochim. Acta* 82, 314–323. doi: 10.1016/j.electacta.2012.04.095
- Zhu, Y., Sun, K., and Frankel, G. S. (2018). Intermetallic phases in aluminum alloys and their roles in localized corrosion. *J. Electrochem. Soc.* 165, C807–C820. doi: 10.1149/2.0931811jes
- Zou, S., Williams, C. T., Chen, E. K.-Y., and Weaver, M. J. (1998). Surface-enhanced raman scattering as a ubiquitous vibrational probe of transition metal interfaces: benzene and related chemisorbates on palladium and rhodium in aqueous solution. *J. Phys. Chem. B* 102, 9039–9049. doi: 10.1021/jp9824205

Conflict of Interest Statement: The authors declare that the research was conducted in the absence of any commercial or financial relationships that could be construed as a potential conflict of interest.

Copyright © 2019 McMahon, Santucci, Glover, Kannan, Walsh and Scully. This is an open-access article distributed under the terms of the Creative Commons Attribution License (CC BY). The use, distribution or reproduction in other forums is permitted, provided the original author(s) and the copyright owner(s) are credited and that the original publication in this journal is cited, in accordance with accepted academic practice. No use, distribution or reproduction is permitted which does not comply with these terms.



Assessment of Self-Healing Epoxy-Based Coatings Containing Microcapsules Applied on Hot Dipped Galvanized Steel

*Evangelia K. Karaxi, Ioannis A. Kartsonakis and Costas A. Charitidis**

Research Unit of Advanced, Composite, Nanomaterials and Nanotechnology, School of Chemical Engineering, National Technical University of Athens, Athens, Greece

OPEN ACCESS

Edited by:

Flavio Defforian,
University of Trento, Italy

Reviewed by:

Rita Bacelar Figueira,
University of Minho, Portugal
Fatima Montemor,
Instituto Superior Técnico, Portugal

*Correspondence:

Costas A. Charitidis
charitidis@chemeng.ntua.gr

Specialty section:

This article was submitted to
Environmental Materials,
a section of the journal
Frontiers in Materials

Received: 17 June 2019

Accepted: 28 August 2019

Published: 11 September 2019

Citation:

Karaxi EK, Kartsonakis IA and
Charitidis CA (2019) Assessment of
Self-Healing Epoxy-Based Coatings
Containing Microcapsules Applied on
Hot Dipped Galvanized Steel.
Front. Mater. 6:222.
doi: 10.3389/fmats.2019.00222

This study focuses on the design, development, and validation of two coating systems for corrosion protection of hot dip galvanized steel substrates. The coatings consist of epoxy-based resin reinforced with core-shell microcapsules, either cerium oxide or cuprous oxide core and a polymeric shell doped with cerium ions. The effect of the modification of the epoxy resin with a liquid rubber polymer has also been studied. Corrosion studies via electrochemical impedance spectroscopy (EIS) revealed that the coatings have enhanced barrier properties. Moreover, EIS studies on coatings with artificial scribes, demonstrated an autonomous response to damage and a self-healing effect. Heat-induced material re-flow has also been observed after exposure to temperature higher than the T_g of the system, which offered an additional self-healing mechanism, partially inhibiting the underlying corrosion processes when the liquid rubber is present in the system.

Keywords: self-healing (self-repairing), core/shell microcapsules, corrosion protective coatings, hot dip galvanized steel, EIS (electrochemical impedance spectroscopy)

INTRODUCTION

Corrosion phenomena on metallic structures result eventually in the degradation of the metal and the deterioration of its properties. Failure of a metallic operating structure compromises the safety, which is a critical consideration during an equipment design. The degradation of engineering structures such as bridges, automobiles, airplanes, and ships due to their exposure in corrosive environments may contribute to life-threatening situations. Moreover, direct and indirect economic losses are linked to corrosion phenomena such as maintenance or replacement costs, expenses related to industry temporary shutdown, efficiency, and product losses. According to the literature, about 25–30% of this total could be avoided if currently available corrosion technology was effectively applied (Uhlig, 2008).

Eventually, all coatings develop defects which are responsible for the direct access of corrosive agents to the metallic substrate. Chromate-based conversion coatings are the most popular all over the world as a pretreatment strategy for a variety of substrates because they offer re-passivation of the corroded area, so hexavalent chromium remains the most effective corrosion preventive compound to date (Gharbi et al., 2018) which is still used in advanced applications (e.g., aerospace). Unfortunately, chromates are long known as environmentally unfriendly and life-threatening compounds due to their leachability and superior oxidation properties, which render

them responsible for DNA damage and cancer (Levina et al., 2006; OSHA3373-10, 2009). The most widely used alternative corrosion prevention measure, is the application of organic coatings with less toxic organic and inorganic additives that are able to provide a dense barrier against corrosive species (Kartsonakis et al., 2013; Figueira et al., 2014; Upadhyay and Battocchi, 2016; Lyon et al., 2017). The recent research activity in the corrosion protection field is focused on the development of new coatings incorporating self-healing characteristics being able to extend the service-life of the coating. The main desired achievement in self-healing coatings is the restoration of their protective performance with minimal or no external intervention (Zhang et al., 2018). According to the same recent review article, self-healing coatings can be categorized in two broad categories, autonomous and non-autonomous coating systems, depending on the mechanism of the onset of healing action (triggered or not). The most common self-healing mechanisms reported in literature are based on (i) polymerizable healants (Zhu et al., 2015; Balaskas et al., 2017), (ii) encapsulated corrosion inhibitors, (iii) reversible bonds, and (iv) reversible chain conformation (Abdolah Zadeh et al., 2016; Samiee et al., 2019). Thus, protective coatings can be characterized by damage-responsive functionalities which result in defect healing/sealing action and/or active corrosion protection by inhibiting corrosion reactions (Kakaroglou et al., 2016; Snihirova et al., 2016; Ulaeto et al., 2017).

Thus, along with the barrier properties, a corrosion protection mechanism responsive to damage has become a promising strategy in order to deliver a coating system with long-term corrosion protection effect. A more sophisticated system dictates, ideally, the occurrence of multiple self-healing events in an autonomous way based on the intrinsic characteristics of the coating system (Yin et al., 2015; Das et al., 2016). The incorporation of actively responsive sub-micron materials in a corrosion protective system can be considered as a favorable pathway to ensure the recovery of its main function, namely, hindering of the corrosion activity.

However, thermoset epoxy-based networks, which are one of the most widely used in coating applications, have many undesirable features, i.e., they have poor resistance to impact and crack growth, which limits their application to certain technological areas. The fracture energy of an epoxy resin is two and three orders of magnitude smaller than thermoplastic polymers and metals. This suggests the need to strengthen these systems in order to expand their applications (Comstock et al., 1989; Figueira et al., 2014).

Hence, the modification of epoxy resins to enhance their brittleness has received considerable research interest. Many research efforts have been reported since 1970, where the first resin modifications with secondary elastomeric phases was initiated by McGarry (1970) and then extensive research has been focused on the investigation and understanding of the toughening mechanism of rubber-toughened epoxies (Yee and Pearson, 1986; Vázquez et al., 1987; Garg and Mai, 1988; Yamanaka et al., 1989; Verchere et al., 1990; Iijima et al., 1991; Williams et al., 1997; Ratna, 2001; Ratna and Banthia,

2004; Bagheri et al., 2009; Unnikrishnan and Thachil, 2012; Parameswaranpillai et al., 2017).

In addition, another limitation arises from the direct addition of inorganic capsules in self-healing epoxy coatings which is their limited compatibility of the inert inorganic surface with the organic coating. The coating's protective performance and adhesion properties are severely affected due to particle agglomeration and defect formation at the interface of these incompatible materials, which are also a function of the concentration and size of the containers and the coating's thickness, as reported by recent research and review articles (Kartsonakis et al., 2010; Borisova et al., 2013; Zhang et al., 2018). A way through these phenomena is the surface modification and decoration of the inorganic surfaces which gives endless options and possibilities to manufacture an engineered microstructure with the desired functional characteristics and limit compatibility issues in epoxy coatings (Skorb et al., 2009; Kainourgiou et al., 2017; Kongparakul et al., 2017; Li et al., 2017).

The motivation for this work is to develop a new multifunctional smart coating system, with self-healing characteristics which contribute to its protective anticorrosion properties. Thus, the main aim of this study is to evaluate the self-healing responsiveness and corresponding barrier properties of two developed advanced coating systems. Both samples consist of a hybrid organic-inorganic epoxy coating toughened by the addition of an organically modified silicate. Core-shell modified cerium oxide (CeO_2) and cuprous oxide (Cu_2O) microcapsules were incorporated into the epoxy-based matrices. In addition, in one of the studied systems, the incorporation of a liquid rubber modifier in free form was selected to investigate its influence on the electrochemical response of the obtained coating. The hybrid organic-inorganic coatings were applied onto hot dip galvanized (HDG) steel panels.

The core-shell microcapsules were characterized with respect to their morphology and chemical composition through transmission electron microscopy (TEM), Fourier transform infrared spectroscopy (FT-IR), gel permeation chromatography (GPC), X-ray diffraction (XRD), and thermogravimetric analysis (TGA). The protective and self-healing ability of intact and scribed coatings as well as their responsiveness and their ability to restore their anticorrosion properties after thermal treatment were evaluated through electrochemical impedance spectroscopy (EIS) while immersed in selected corrosive electrolytes.

MATERIALS AND METHODS

Acetonitrile (Acros Organics), toluene (Acros Organics), acetone (Acros Organics), absolute ethanol (Acros Organics), methanol (MeOH, Acros Organics), absolute ethanol (Sigma Aldrich), N,N-dimethylformamide (DMF, Sigma Aldrich), copper acetate (Sigma Aldrich), hydrazine hydrate (N_2H_4 , 50–60%, Sigma Aldrich), cerium acetyl acetonate [$\text{Ce}(\text{acac})_3$, Sigma Aldrich], potassium peroxodisulfate (KPS, Sigma Aldrich), α -bromoisobutyl bromide (BIBB, Sigma Aldrich), (3-aminopropyl)triethoxy silane (APTES, Sigma Aldrich), triethylamine (Sigma Aldrich), copper (II) bromide [$\text{Cu}(\text{II})\text{Br}$,

Sigma Aldrich], cerium nitrate [$\text{Ce}(\text{NO}_3)_3$, Sigma Aldrich], ammonium cerium(IV) nitrate [$\text{Ce}(\text{NH}_4)_2(\text{NO}_3)_6$, Sigma Aldrich], trifluoroacetic acid (CF_3COOH , Merck, >99%), dichloromethane (Sigma Aldrich, 99.8%), 2,2'-Bipyridyl (bpy, Sigma Aldrich), diethylenetriamine (Sigma Aldrich), ascorbic acid (Sigma Aldrich), epoxy resin based on phenol 4,4'-(1-methylethylidene) bis- (Ciba-Geigy), sodium hydroxide (Sigma Aldrich), and sodium chloride (Sigma Aldrich) were used as received. The monomers methacrylic acid (MAA) and n-butyl acrylate (nBA) and tert-butyl acrylate (tBA) were double distilled under reduced pressure prior to use.

Synthesis of Cu_2O and CeO_2 Cores

The synthesis of Cu_2O cores was performed by a simple one-pot wet chemical route using copper acetate as the precursor and hydrazine as the reducing agent. The experiment was conducted at room temperature by adding hydrazine hydrate (0.03 mol) in a copper acetate solution (0.042 M). The reaction was left to proceed under vigorous stirring for 10 min, while the solution's color changed from blue to green and finally to bright orange. The products were left to precipitate, the supernatant solution was discarded and the sediments were repeatedly washed through multiple centrifugations. The Cu_2O cores were left to dry in a vacuum desiccator.

For the production of CeO_2 cores a two-step process was followed as reported elsewhere (Kartsonakis et al., 2008, 2010). Briefly, negatively charged polymethacrylic acid (PMAA) nanospheres were synthesized through radical polymerization in acetonitrile using KPS as initiator and then utilized as templates for the formation of an inorganic surface layer composed of cerianite (CeO_2) using $\text{Ce}(\text{acac})_3$ as precursor ($\text{PMAA}@\text{CeO}_2$). Hollow CeO_2 cores were formed through the dispersion of the $\text{PMAA}@\text{CeO}_2$ composites in EtOH/ H_2O mixture (2:1) which resulted in the controlled and selective dissolution of PMAA cores. The final inorganic hollow cores were isolated through multiple centrifugations and were washed with water and ethanol.

Synthesis of Core-Shell Microcapsules

Inorganic-organic core-shell microcapsules were synthesized through surface-initiated activators regenerated by electron transfer atom transfer radical polymerization (ARGET-ATRP) process. The inorganic core materials, CeO_2 or Cu_2O , were selected due to their inherent corrosion protective and antifouling characteristics, respectively. A diblock copolymer, poly(n-butyl acrylate-b-acrylic acid) [$\text{P}(\text{BA}-b\text{-AA})$], was synthesized on the surface of cerium oxide, $\text{CeO}_2@\text{P}(\text{BA}-b\text{-AA})$, or cuprous oxide microcapsules, $\text{Cu}_2\text{O}@\text{P}(\text{BA}-b\text{-AA})$. The addition of a second PAA-based polymer block was decided in order to obtain a carboxyl-terminated block copolymer and enhance the reaction between carboxyl and oxirane groups of the epoxy matrix.

The synthesis of the diblock copolymer onto the surface of either CeO_2 or Cu_2O was performed according to the following procedure (schematic representation in **Supplementary Figure S1**): firstly, an α -bromoester initiator was tethered on the inorganic cores' surface by self-assembly

of APTES followed by amidization with BIBB. The APTES-functionalization ensures the covalent bonding of the initiator molecules with the inorganic surface. Then, surface initiated ARGET ATRP was carried out from the above-mentioned initiator-modified particles.

Either CeO_2 or Cu_2O cores were dispersed in absolute ethanol using ultra sonication in a three-neck flask equipped with a condenser and a magnetic stirrer. After heating to 70°C , APTES was added under N_2 atmosphere and the dispersion was left for 24 h under stirring. The APTES-modified inorganic cores were centrifuged, washed with ethanol and redispersed in DMF. Then BIBB was added drop-wise in the flask using triethylamine as the catalyst and left in an ice bath for 1 h under stirring in N_2 atmosphere and then at room temperature for 24 h. The macroinitiators (initiator-functionalized inorganic particles) were isolated and rinsed through centrifugation. A septum-sealed Schenk flask was used during surface initiated ARGET-ATRP. For each experiment, CeO_2 or Cu_2O cores were dispersed in toluene followed by the complete dissolution of the $\text{Cu}(\text{II})\text{Br}/\text{bpy}$ complex and the addition of the deoxygenated monomer. The nBA was used as monomer and ascorbic acid served as reducing agent for initiating the polymerization process. Then, t-BA was added to the above mixture resulting in a diblock polymer shell comprising of PnBA and PtBA. The AA block resulted from an acidolysis reaction, as reported elsewhere (Colombani et al., 2007). Detailed experimental conditions for the aforementioned synthetic procedure are given in **Table 1**. The final inorganic-organic core-shell microcapsules, $\text{CeO}_2@\text{P}(\text{BA}-b\text{-AA})$ or $\text{Cu}_2\text{O}@\text{P}(\text{BA}-b\text{-AA})$, were isolated and purified through multiple centrifugations and washings with MeOH and remained in dispersed state for further modification. The cerium-doped microcapsules were then developed by adding dropwise a 0.5% w/v cerium ammonium nitrate solution (in MeOH) to the above dispersion. The final composites were isolated again by centrifugation. Additionally, ARGET-ATRP was performed in order poly(n-butyl acrylate; PBA) to be synthesized using KPS (0.5 g), nBA (10.0 ml), and toluene (50.0 ml) as solvent at 60°C for 12 h.

Coating Synthesis and Application

The HDG steel substrates pre-treatment prior to coating application included degreasing and cleaning using acetone

TABLE 1 | The conditions used in the preparation of core/ shell microcapsules.

Material	Quantity
CeO_2 or Cu_2O cores	1.0 (g)
(3-aminopropyl)triethoxy silane	1.0 (ml)
Absolute ethanol	20.0 (ml)
N,N-dimethylformamide	20.0 (ml)
Triethylamine	1.0 (ml)
α -bromoisobutyl bromide	2.0 (ml)
Toluene	20.0 (ml)
Copper (II) bromide	0.1 (g)
2,2'-Bipyridyl	1.0 (g)
N-butyl acrylate	10.0 (ml)
Ascorbic acid	1.0 (g)

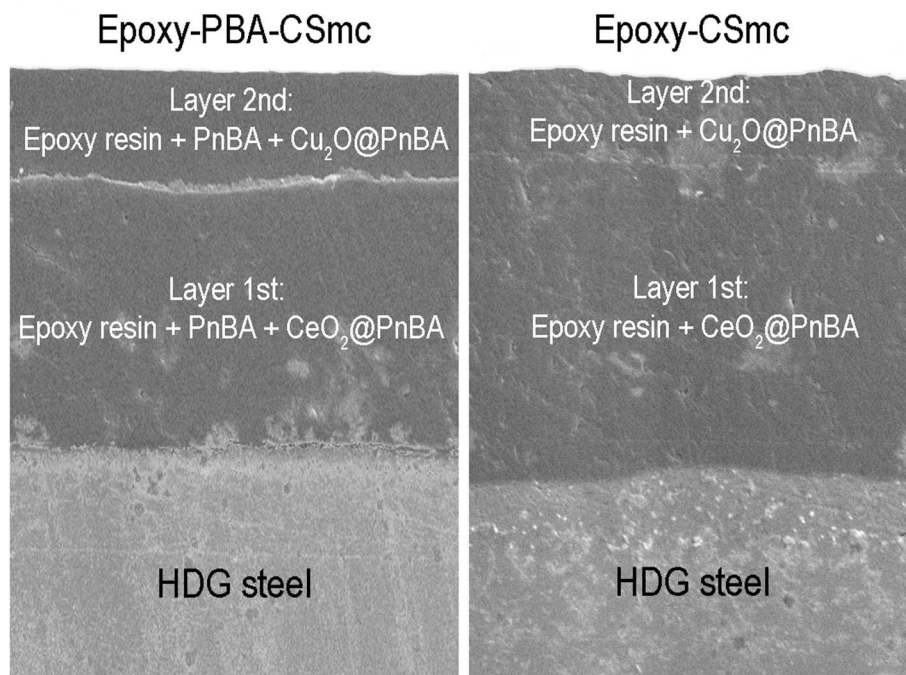


FIGURE 1 | Schematic representation of the produced two-layer coating systems.

TABLE 2 | The conditions used in the preparation of the epoxy solution.

Material	Quantity (wt. %)
(3-aminopropyl)triethoxy silane	2.0
2,2-Bis[4-(glycidyl oxy)phenyl]propane	25.0
Diethylenetriamine	2.0
PnBA	5.0
Absolute ethanol	34.0
Acetone	30.0
CeO ₂ @P(BA-b-AA) or Cu ₂ O@P(BA-b-AA) core-shell microcapsules	2.0

and NaOH solution at pH 11 for 5 min at 50°C, thoroughly washing with distilled water and their storage in a vacuum designator. Two coating systems were prepared; named *Epoxy-PBA-CSmc* and *Epoxy-CSmc* (**Figure 1**). The matrix of each of the two-layered coating system was based on the combination of a cross-linked epoxy polymer with organically modified silicates as described in detail in our previous work (Kartsonakis et al., 2012). The conditions used in the preparation of the epoxy solution are tabulated in **Table 2**. The synthesized core-shell microcapsules were incorporated as reinforcing additives in both epoxy-based hybrid coatings in a concentration of 4 wt.% and were applied with a baker film applicator onto the metallic substrates. The liquid rubber (PBA) was mixed with the epoxy-based solution prior to deposition for the preparation of the second coating system (*Epoxy-PBA-CSmc*). Finally, the as-prepared coated substrates (in triplicates for each system) were

left in a furnace at 90°C for 4 days and deposited in a vacuum designator until use.

Characterization Methods

Transmission electron microscope (TEM; JEM2000 FX, 200 KV, resolution 0.28 nm) and Fourier Transform Infrared Spectroscopy (FT-IR) were utilized for the chemical composition determination of the hybrid composites through Attenuated Total Reflectance (ATR) method with Agilent Cary 630 spectrometer.

The thermal degradation of the synthesized microcapsule materials was analyzed via thermogravimetric analysis (TGA) using a thermal analyzer apparatus (STA 449 F5 Jupiter). The samples were measured under constant nitrogen flow (50 ml/min) plus nitrogen flow as protective gas (20 ml/min) from 25 to 1,000°C at a heating rate of 10°C/min. Prior to the non-isothermal experiments the instrument was calibrated both for temperature and sensitivity. The exported data were manipulated through Proteus 6.1 Software. The polymer content was determined from the total of weight loss the microcapsules. The total organic content was then used to calculate the grafting density (σ_{TGA}) based on the core diameter established by TEM, utilizing the Equation (1) (Benoit et al., 2012):

$$\sigma_{TGA} = \frac{\frac{wt\% \text{ shell}}{wt\% \text{ core}} \times \rho_{core} \times \frac{4}{3}\pi r_{core}^3 \times N_A}{MW \times 4\pi r_{core}^2} \quad (1)$$

where the weight percentages of the shell and core materials were obtained by TGA for the temperature range 300–500°C.

The crystal structure was identified by powder X-ray diffraction (XRD) using X Bruker D8 Advance Twin Twin,

employing Cu-K α radiation ($\lambda = 1.5418 \text{ \AA}$). The thickness of the final coating system was measured with a coating thickness test instrument through the magnetic induction method (ACUTECH LTD, DUALSCOPE MP0R) and through SEM at the coatings' cross-section. In addition, Differential Scanning Calorimetry (DSC) testing was conducted on selected coating sample using Perkin Elmer Pyris 6 DSC apparatus calibrated with indium for temperature and heat capacity. Measurements were carried out in high purity nitrogen atmosphere on samples of $\sim 8 \text{ mg}$ in mass closed in standard aluminum Perkin Elmer pans. Measurement was performed on fresh sample that was heated from 20°C up to 250°C with a heating rate of $20^\circ\text{C}/\text{min}$, stayed there isothermally for 2 min, cooled down to -110°C at $30^\circ\text{C}/\text{min}$ and, finally, heated from -110°C to 350°C at $5^\circ\text{C}/\text{min}$.

The microstructure, thickness and qualitative elemental analysis of the coatings were studied by Scanning Electron Microscopy (SEM) coupled with Energy Dispersive X-Ray Spectroscopy (EDS) using a PHILIPS Quanta Inspect (FEI Company) microscope with 149 W (tungsten) filament 25 KV equipped with EDAX GENESIS (AMETEX PROCESS & 150 ANALYTICAL INSTRUMENTS). Electrochemical Impedance Spectroscopy (EIS) measurements were conducted to assess the anti-corrosive properties of coatings and to verify its corrosion mechanism. A potentiostat/galvanostat connected to a Frequency Response Analyzer (VersaStat 3/FRA, PAR AMETEK) was used with an electrochemical cell of three electrodes (K0235 Flat Cell Kit, AMETEK), consisting of a working electrode ($\sim 1 \text{ cm}^2$ exposed sample surface), a saturated silver/silver chloride electrode [Ag/AgCl, KCl (sat)] as a reference electrode and a platinum mesh electrode as the counting electrode for the measurements. The measurement frequency ranged from 100 kHz to 0.01 Hz and the sinusoidal perturbation applied was 10 mV. The spectra were analyzed through ZView[®] software (Scribner Associates) using the appropriate equivalent electrochemical circuit each time. The study of the anti-corrosion properties of the intact coating systems on galvanized steel samples included exposure to corrosive artificial ocean water prepared in accordance with ASTM D1141-98. The chemical composition of the solution is shown in **Supplementary Table T1**. As stated in the standard, the chlorinity is 19.38 and the pH of the solution (after correction with 0.1N NaOH) is 8.2. Thus, all the measurements were conducted in triplicate in a pH range from 8.2 to 9.

A second set of EIS measurements was performed on artificially scribed coated samples exposed to 5 mM NaCl solution in order to understand the mechanism of corrosion and its inhibition. For the in-depth study of the coatings and the investigation of their potential use as self-healing coating systems, artificial scribes of 1–2 mm length were created so that the metal substrate remains exposed to the electrolyte. This was confirmed for each sample by SEM analysis and the corresponding line elemental EDS analysis of the HDG metal substrate elements, Fe and Zn (**Supplementary Figure S2**). The exposed area of 1 cm^2 was carefully selected in a way that the scribe is located in its center. The interpretation of the EIS results was performed by numerical fitting using equivalent electric circuit models (Zheludkevich et al., 2005; Kartsonakis et al., 2016). Constant

phase elements (CPE) were used to account for the electrode heterogeneity. Generally, as reported in literature the CPE is related with a distribution of the capacitance over a surface or its changes with frequency which are associated with electrode heterogeneity (Montemor et al., 2008; Plawecka et al., 2014). Therefore, in the equivalent circuits worked with in our study, CPE were used instead of pure capacitors. This modification is obligatory when the phase shift of a capacitor is different from -90° (Hsu and Mansfeld, 2001). The impedance of an R-CPE parallel association is given by:

$$Z_{R-CPE} = \frac{R}{1 + RY_0(j\omega)^n} \quad (2)$$

where Y_0 is the admittance of the CPE and n is the CPE exponent. The n equals to 1 when it corresponds to a capacitor, it takes the values $0.5 < n < 1$ when a non-ideal capacitor behavior takes place, n equals to 0.5 when the CPE describes a diffusion process and represents a Warburg impedance, and finally, n equals to 0 when it represents a resistor (Orazem and Tribollet, 2008; Zhu et al., 2016).

Using the Cole-Cole approach together with CPE (Cole and Cole, 1942; Barsoukov and Macdonald, 2018), the capacitance can be calculated by numerical fitting through the Equation (3):

$$C = \sqrt[n]{\frac{RY_0}{R^n}} \quad (3)$$

In addition, the investigation of a thermally-induced self-healing mechanism was conducted. Both the two-layer coating systems were subjected to the formation of a defect in a way that the underlying metal is exposed. Microscopic observation was then performed through SEM along with elemental mapping. The anticorrosion protection performance of each scribed coating was evaluated through EIS immediately after SEM analysis through the exposure to 5 mM NaCl solution. The samples were dried and were thermally treated at 90°C for 30 min and their corrosion behavior via EIS was again measured once. The low frequency impedance values were compared before and after heat treatment in order to evaluate the recovery of the barrier properties, the main function of the coatings studied.

RESULTS AND DISCUSSION

Figures 2, 3 depict the TEM images of the $\text{CeO}_2@P(\text{BA}-b\text{-AA})$ and $\text{Cu}_2\text{O}@P(\text{BA}-b\text{-AA})$ core-shell microcapsules, respectively. Regarding **Figure 2a**, it may be remarked that the $\text{CeO}_2@P(\text{BA}-b\text{-AA})$ sample consists of spherical hybrid microcapsules with a core-shell configuration with average diameter size $600 \pm 150 \text{ nm}$. The shell is amorphous (dark contrast ring) and its average thickness is $30 \pm 10 \text{ nm}$, while the core is nanocrystalline (lighter contrast) comprising of randomly oriented nanocrystals with a diameter range of 2–3 nm (**Figure 2b**), as illustrated by high-resolution TEM (HRTEM). According to HRTEM image that depicts the atomic structure of the core nanocrystals, the 3.12 Å interplanar spacing of the {111} crystal planes of CeO_2 is clearly resolved. The crystal structure of the nanocrystalline core was

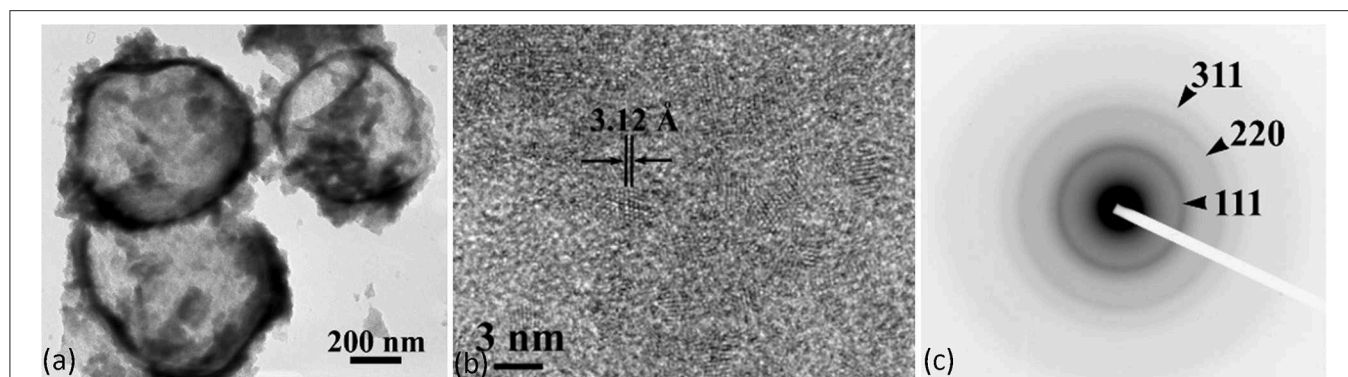


FIGURE 2 | (a) TEM micrographs illustrating the core-shell morphology of the $\text{CeO}_2@P(\text{BA}-b\text{-AA})$ microcapsules, (b) HRTEM images showing the atomic structure of the core nanocrystals; the 3.12 Å interplanar spacing of the {111} crystal planes of CeO_2 is clearly resolved, (c) corresponding SAED from the core region. The diffuse ring pattern is characteristic of a nanocrystalline material. The {111}, {220}, and {311} reflections of CeO_2 are clearly determined.

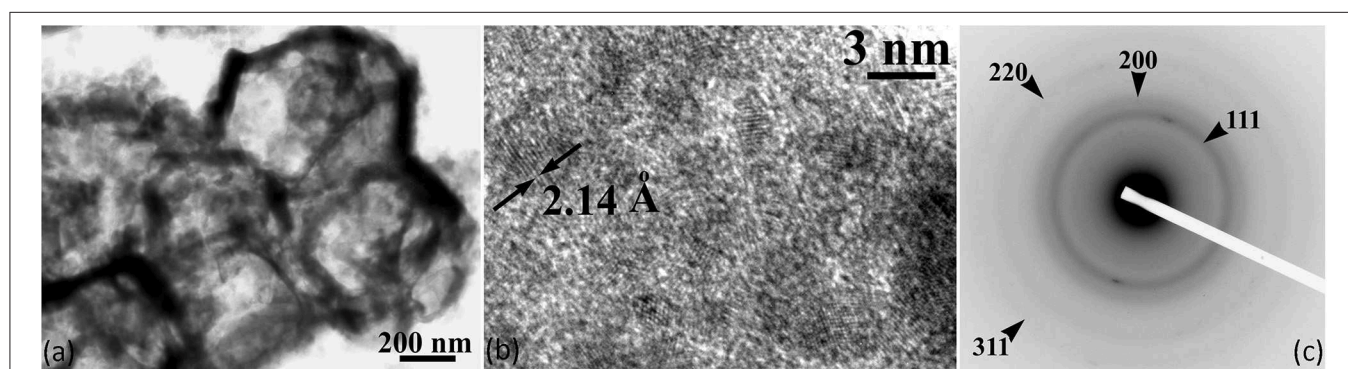


FIGURE 3 | (a) TEM micrographs illustrating the core-shell morphology of the $\text{Cu}_2\text{O}@P(\text{BA}-b\text{-AA})$ microcapsules, (b) HRTEM image of the atomic structure of the core nanocrystalline phase; the 2.14 Å interplanar spacing of the crystal planes of Cu_2O is clearly resolved, (c) the diffuse rings of the corresponding SAED pattern are characteristic of a nanocrystalline material. The {111}, {200}, {220}, and {311} reflections of Cu_2O are clearly determined.

explored by selected area electron diffraction (SAED) patterns (Figure 2c) and powder-XRD (Supplementary Figure S3). It can be seen that the diffuse ring pattern is characteristic of a nanocrystalline material. The {111}, {220}, and {311} reflections of CeO_2 are clearly determined. Taking into consideration Supplementary Figure S3, it was estimated that the core material is Cerianite (CeO_2) (PDF card #34-0394) crystallized in the face centered cubic structure and characterized by a lattice constant of 5.41 Å. The morphological and structural characteristics of the $\text{CeO}_2@P(\text{BA}-b\text{-AA})$ core-shell microcapsules are tabulated in Supplementary Table T2.

According to Figure 3a, spherical shapes of $\text{Cu}_2\text{O}@P(\text{BA}-b\text{-AA})$ microcapsules are observed with a core-shell configuration and average diameter of 670 ± 100 nm. The double shell is amorphous (dark contrast ring) and its average thickness is 70 ± 15 nm. The core comprises of the Cu_2O structure (lighter contrast) and exhibits a nanocrystalline phase with nanocrystals having a diameter range of 3–10 nm (Figures 3b,c), as illustrated by HRTEM and the corresponding SAED pattern. According to the HRTEM image of the atomic structure of the core nanocrystalline phase, the 2.14 Å

interplanar spacing of the crystal planes of Cu_2O is clearly resolved. Moreover, considering the diffuse rings of the corresponding SAED pattern it could be mentioned that they are characteristic of a nanocrystalline material. The {111}, {220}, and {311} reflections of Cu_2O are clearly determined. The core crystal structure is cubic with a lattice parameter equal to 4.27 Å. Supplementary Figure S4 illustrates the Cu_2O core powder-XRD where the {111}, {220}, and {311} diffraction peaks are clearly demonstrated. The morphological and structural characteristics of the $\text{Cu}_2\text{O}@P(\text{BA}-b\text{-AA})$ core-shell microcapsules are tabulated in Supplementary Table T3.

The successful synthesis of the polymer shell was confirmed through FT-IR analysis which revealed the characteristic adsorption peaks of poly(n-butyl acrylate; Figure 4). More specifically, in the region $3,000\text{--}2,800\text{ cm}^{-1}$ the C-H stretching vibrations arise and are more evident in the case of $\text{CeO}_2@P(\text{BA}-b\text{-AA})$ sample. The peaks at $2,970$ and $2,875\text{ cm}^{-1}$ are attributed to the asymmetric and symmetric stretching vibrations of the methyl group of PBA, respectively. A third intermediate peak at $2,930\text{ cm}^{-1}$ can be ascribed to the asymmetric C-H vibration of

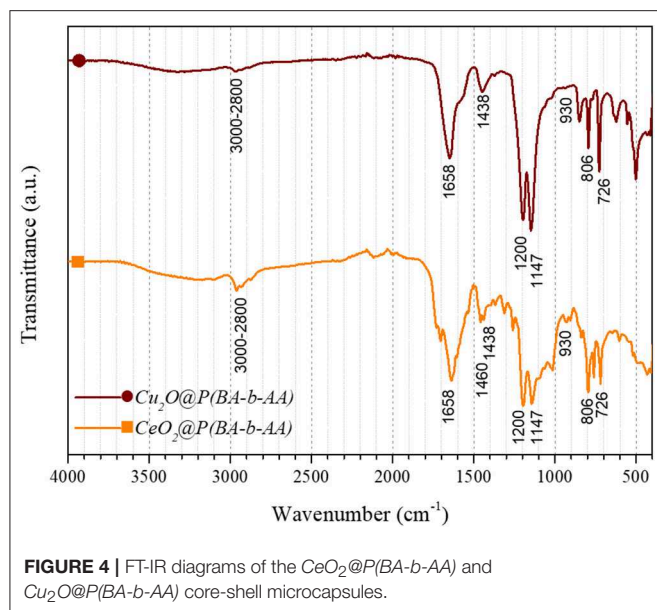


FIGURE 4 | FT-IR diagrams of the $\text{CeO}_2@P(\text{BA-b-AA})$ and $\text{Cu}_2\text{O}@P(\text{BA-b-AA})$ core-shell microcapsules.

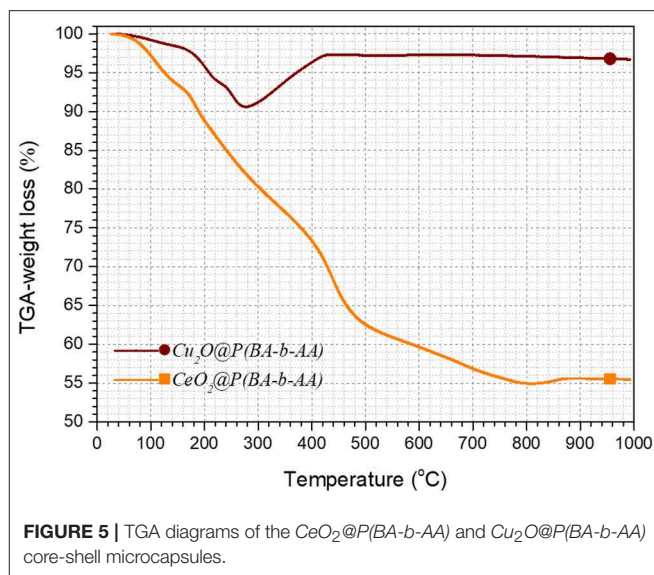


FIGURE 5 | TGA diagrams of the $\text{CeO}_2@P(\text{BA-b-AA})$ and $\text{Cu}_2\text{O}@P(\text{BA-b-AA})$ core-shell microcapsules.

the methylene groups. These peaks are enhanced according to the increment in the polymer's crystallinity.

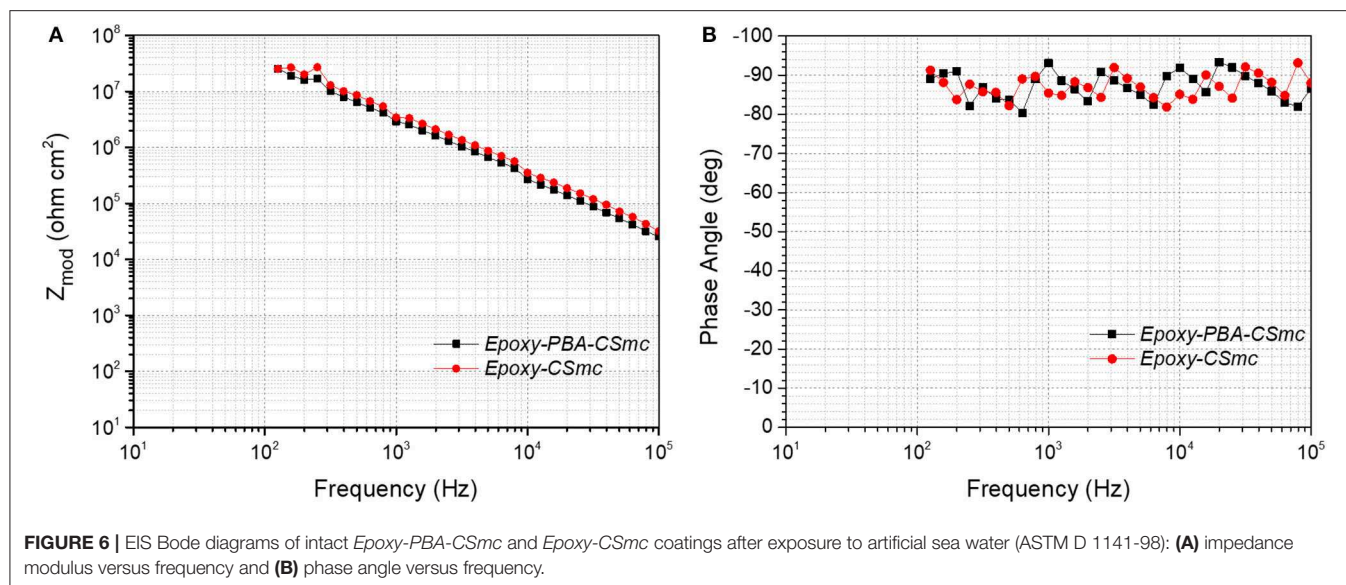
The broad adsorption peak at about $1,658\text{ cm}^{-1}$ refers to the stretching vibration of the carbonyl group ($\text{C}=\text{O}$) of PAA. The methylene bending mode vibration occurs at $1,460\text{ cm}^{-1}$ (main polymer chain), $1,438\text{ cm}^{-1}$, $1,395\text{ cm}^{-1}$ (n-butyl groups) and the CH_2 scissoring vibration at $1,454\text{ cm}^{-1}$ (polyacrylic acid). The two peaks at $1,373$ and $1,320\text{ cm}^{-1}$ correspond to the symmetric methyl bending mode and the C-H bending mode of the tertiary C-H groups, respectively.

The C-O stretching mode shows two strong bands in the region $1,300\text{--}1,000\text{ cm}^{-1}$ in esters. In our case, the first adsorption band appears at $1,200\text{ cm}^{-1}$ and the second one at $1,147\text{ cm}^{-1}$. These bands are mainly attributed to asymmetrical and symmetrical C-O-C stretching modes of the n-butyl ester groups, respectively. Moreover, the doublet near 930 cm^{-1} is ascribed to the vibration corresponding to the n-butyl groups of the polymer and the skeletal stretching mode of the polymer main chain. The sharp band at 806 cm^{-1} also corresponds to the n-butyl groups. Finally, the double peaks at 767 and 726 cm^{-1} is due to the methylene rocking vibration mode (Kawasaki et al., 1961; Moharram et al., 2002; Moharram and Khafagi, 2007).

The thermal behavior of the synthesized polymer shell was investigated through TGA in N_2 atmosphere as illustrated in **Figure 5**. Taking into account the TGA diagram of the $\text{Cu}_2\text{O}@P(\text{BA-b-AA})$ microcapsules, it may be remarked that in the temperature range between 30 and 170°C the diagram demonstrates a weight loss due to the evaporation of adsorbed water and the dehydroxylation process. Above this range, two parallel phenomena take place; the thermal decomposition of the PBA shell and the oxidation of the cuprous oxide core. A mass reduction is observed equal to $\sim 8\%$. On the other hand, a weight gain is observed over 600°C . The gain in weight did not exceed 7% of the initial mass, as seen from the TGA curve. This indicates that it is not stoichiometric with the amount of copper present

in the material. The most possible reaction is the oxidation of the cuprous oxide core to the thermodynamically more stable cupric oxide form (Sierra-Ávila et al., 2015), which overcomes the weight loss due to the polymer shell decomposition between 250 and 500°C (Li et al., 2006, 2015) due to the presence of gaseous contaminants within the N_2 gas as well as residual humidity in the material.

With respect to the $\text{CeO}_2@P(\text{BA-b-AA})$ microcapsules (**Figure 5**) the sharp weight loss of 22% at 500°C is assigned to the polymeric shell decomposition. Over this temperature the thermal decomposition of other acetylacetonate-based metal complexes $[\text{Me}(\text{acac})_z]$ suggest intermediate compound burning $[\text{Ce}(\text{C}_5\text{H}_7\text{O}_2)_2(\text{CH}_3\text{COO})]$, $\text{Ce}(\text{C}_5\text{H}_7\text{O}_2)(\text{CH}_3\text{COO})_2$, $\text{Ce}(\text{OH})(\text{CH}_3\text{COO})_3$, $\text{CeO}(\text{CH}_3\text{COO})$, and CeOCO_3 prior to CeO_2 crystallization at 800°C , as reported in literature. A slight weight gain (0.5%) can be ascribed to the oxidation of Ce^{3+} to Ce^{4+} (Yao et al., 2003; Tania et al., 2008). Additionally, from equation (1) a grafting density of 1.5 chains/nm^2 was calculated. The surface morphology of the produced coating systems was also evaluated. The surface top-viewed SEM images (**Supplementary Figures S5a,b**) reveal no defects or cracks can be spotted on the corrosion protective coating systems, *Epoxy-PBA-CSmc* and *Epoxy-CSmc*, respectively. In **Supplementary Figures S6a,b** the topographic maps of the average coating thicknesses of the *Epoxy-PBA-CSmc* and *Epoxy-CSmc*, respectively, corrosion protective coating systems measured through induction method reveal an increment corresponding on the bottom side of the samples; an observation commonly presented when a baker film applicator is utilized. For consistency reasons, all the electrochemical characterizations were conducted on the middle zone of the coated HDG substrates. The cross-section SEM image of *Epoxy-PBA-CSmc* (**Supplementary Figure S7a**) illustrates the coating thickness measurements which were found equal to $44 \pm 3\text{ }\mu\text{m}$, and $90 \pm 3\text{ }\mu\text{m}$ for the two layers, respectively. Moreover, the cross-section SEM image of *Epoxy-CSmc* is



depicted in **Supplementary Figure S7b** where it can be seen that the thickness of the two layers is $30 \pm 3 \mu\text{m}$ and $114 \pm 3 \mu\text{m}$, respectively.

Electrochemical Studies

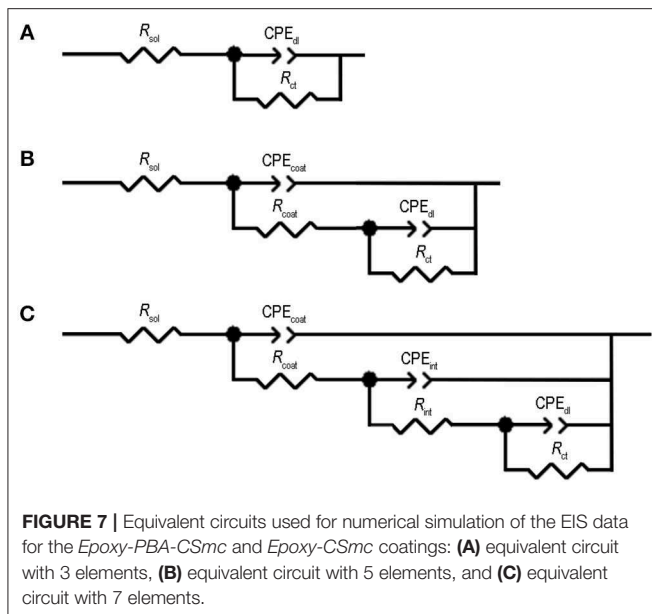
EIS is used as a powerful tool to investigate the barrier properties of the coating systems developed in the current study and to assess the impact of the addition of a liquid rubber polymer either as a container surface modified or as an additive incorporated in free form in the epoxy matrix. As it has been well-documented previously in literature, the magnitude of impedance modulus at low frequency ($|Z|_{0.01}$ Hz) can be used to assess the overall anti-corrosive behavior of an organic coating system, while the charge transfer resistance (R_{ct}) indicates the resistance to a flow of charge, electronic or ionic, which is inversely proportional to the corrosion rate underneath the coating and its enhancement is associated with self-healing effects (Zhang et al., 2004; Zheludkevich, 2009; Borisova et al., 2013; Meng et al., 2015; Njoku et al., 2017; Ubaid et al., 2019).

Figure 6 illustrates the Bode diagrams of (a) the impedance plot vs. frequency and (b) the phase angle diagram vs. the frequency resulting from the exposure of intact coatings to artificial sea water (ASTM D 1141-98) over a period of 223 days. It is observed that in all spectra, both intact coatings are characterized by the presence of a capacitive response during their exposure to the highly corrosive environment for a period of 223 days. The intact coatings reveal a time constant that is at the high frequencies, characteristic of the increased anticorrosive protection they provide to the substrate. In particular, the capacitive behavior of the coatings is shown at high frequencies. The phase angle of the system is between -80° and -90° in the measured frequency range for all immersion time, revealing that the coatings behave as a capacitor. This behavior implies that the coatings are characterized by good barrier properties and behave as an insulator by isolating the metal surface from the corrosive

environment (Cabral et al., 2006; Trabelsi et al., 2006; Foyet et al., 2013; Qiao et al., 2015).

Supplementary Figures S8, S9 show the evolution of impedance spectra of the two artificially scribed coatings after exposure to 5 mM NaCl solution. The impedance spectra evolution of scribed *Epoxy-PBA-CSmc* after exposure to 5 mM NaCl solution are illustrated in **Supplementary Figure S8a**. The coating showed stable impedance values for 1 to 4 h of immersion to the corrosive electrolyte, equal to $470 \text{ k}\Omega \text{ cm}^2$. After 96 h of immersion, the impedance value $|Z|_{0.01}$ Hz increased to $670 \text{ k}\Omega \text{ cm}^2$. The scribed *Epoxy-PBA-CSmc* reveals three time constants from the beginning of immersion (**Supplementary Figure S8b**). The one in the high frequency range can be attributed to the coating due to the fact that the exposed area includes the scribe together with a part of the coating, a second small one in the middle frequency range can be ascribed to the response of processes occurring at the coating/ substrate interface and a third time constant in the low frequency range due to the corrosion process at the metallic surface. EIS Bode plots of scribed *Epoxy-CSmc* are depicted in **Supplementary Figure S9a**. The coating presents a progressively increase of the magnitude of impedance modulus at low frequency ($|Z|_{0.01}$ Hz) from $56 \text{ k}\Omega \text{ cm}^2$ at 7 h to $130 \text{ k}\Omega \text{ cm}^2$ after 96 h of exposure to the electrolyte. The *Epoxy-CSmc* reveals three time constants for all time intervals till 96 h of immersion (**Supplementary Figure S9a**). The overall impedance values revealed that the presence of the liquid rubber addition in free form (*Epoxy-PBA-CSmc*) improves the charge transfer resistance of the epoxy-based coating system including microcapsules with cerium-ions resulting in higher impedance values after defect formation.

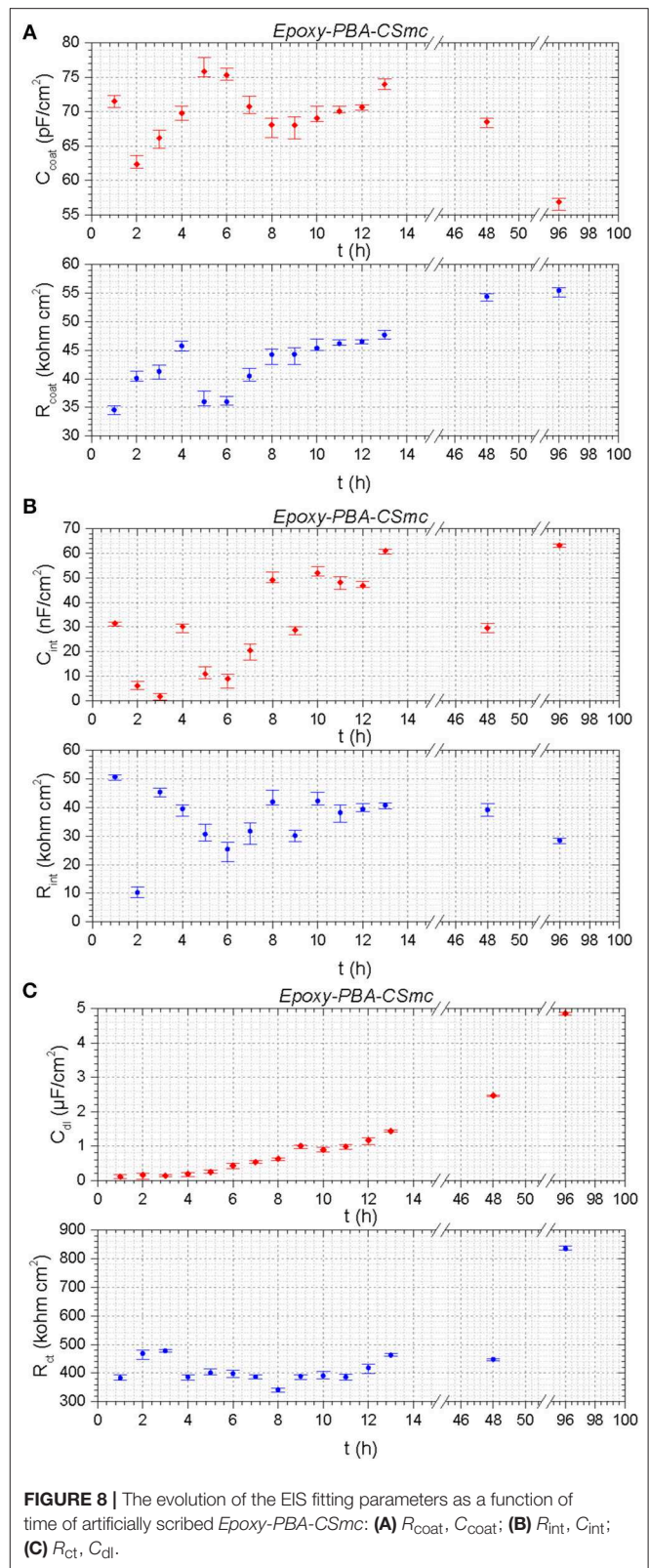
The EIS results of the artificially scribed *Epoxy-PBA-CSmc* and *Epoxy-CSmc* coatings were fitted using the equivalent electric circuit of **Figure 7C**. The equivalent electric circuit of **Figure 7C** includes seven elements and corresponds to an EIS spectrum comprising of three time constants. In particular, it consists of



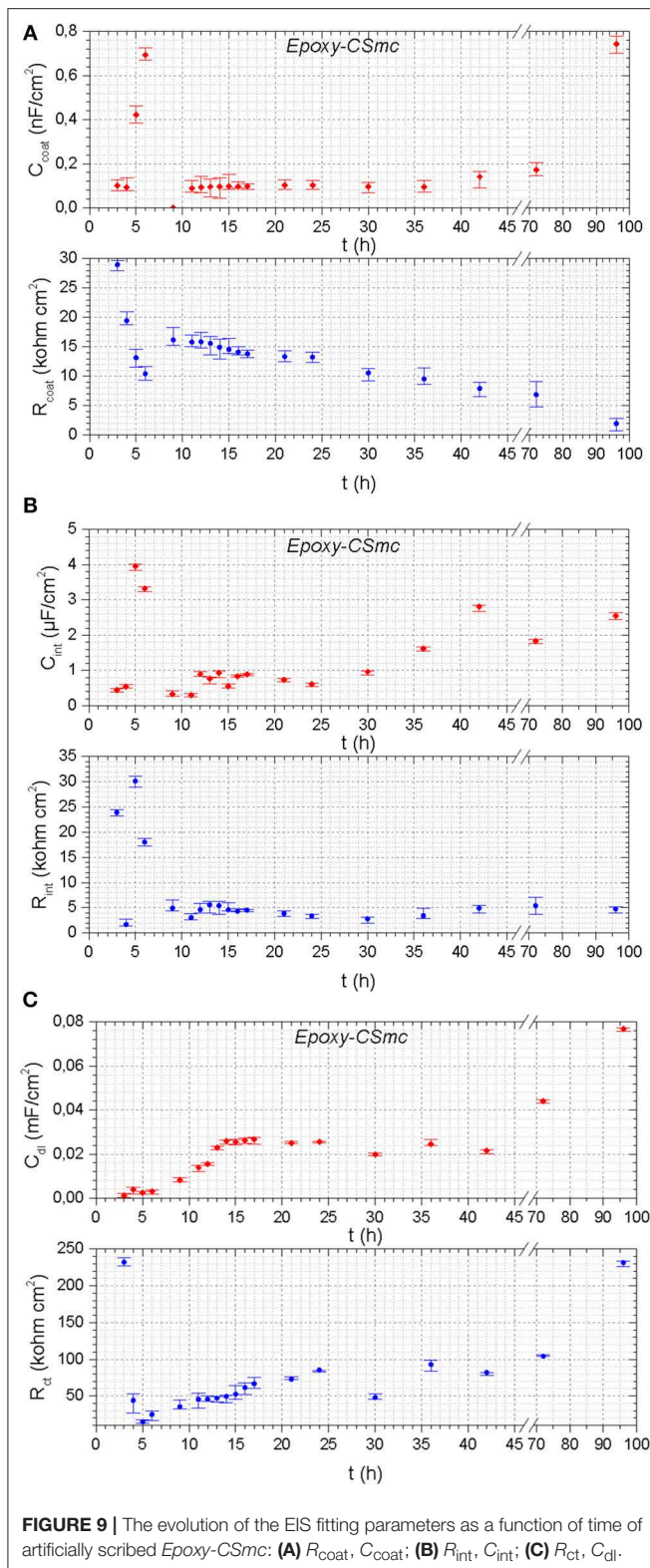
the resistance of the solution (R_{sol}), the pore resistance and the CPE of the coating ($R_{coat} - CPE_{coat}$) in parallel connection that are attributed to the response of the electrolyte inside the pores of the coating, the interface resistance and the interface CPE ($R_{int} - CPE_{int}$) that are assigned to the response of the presence of electrolyte at the oxide layer and finally, the charge transfer resistance and the double-layer CPE ($R_{ct} - CPE_{dl}$) that are due to the presence of corrosion active pits at the oxide-metallic substrate interface.

Taking into account the aforementioned Equation (3), the C_{coat} , C_{int} , C_{dl} parameters were calculated. **Figures 8, 9** illustrate the evolution of C_{coat} , C_{int} , C_{dl} , R_{coat} , R_{int} , R_{ct} as a function of time in 5 mM NaCl for both the artificially scribed *Epoxy-PBA-CSmc* and *Epoxy-CSmc* coatings, respectively (**Supplementary Table T4**).

The fitting results for the scribed *Epoxy-PBA-CSmc* reveal relatively small fluctuations on R_{coat} and C_{coat} , which indicate a stable performance of the coating during immersion in the corrosive environment (**Figure 8A**). In detail, the pore resistance of the coating increases till the 4 h of exposure, while it suffers from a sudden drop at the 5 and 6 h, with a corresponding increment in the coating capacitance values (C_{coat}). After 7 h and till the fourth day of exposure (96 h) the pore resistance shows a continuous enhancement, while the corresponding capacitance is decreased. The values for the pore resistance and capacitance reflect the evolution of the barrier properties of the system and the decreasing number of conductive ways from the electrolyte to the substrate (Montemor et al., 2008; Plawecka et al., 2014). The R_{ct} values present a progressive increment after 8 h of immersion (**Figure 8C**), while at the same time interval the interlayer resistance (R_{int}) is also increased, indicating the formation of a stable protective oxide layer (**Figure 8B**). The overall recovery of R_{ct} value increased 144% from the first till the 96th hour of immersion, from 341.53 to 834.7 kΩ cm², respectively (Ubaid et al., 2019).



The pore resistance (R_{coat}) for the scribed *Epoxy-CSmc* continuously decreases as the immersion time elapses and the corresponding capacitance values (C_{coat}) continue to increase,



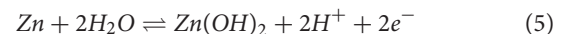
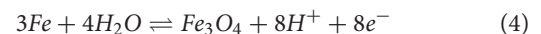
indicating the progressive damage of the coating due to successive electrolyte ingress (Figure 9A). The smallest R_{ct} value is observed at the 5 h after which an improvement follows till the 96 h of exposure (Figure 9C). The recovery of the charge transfer

resistance from the smallest value observed is equal to 1,465% (Ubaid et al., 2019; increased from 14.8 to 231.71 kΩ cm²).

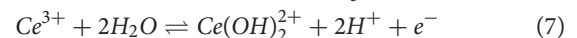
Concluding, in both studied systems, the charge transfer resistance is decreased after the contact with the corrosive environment, yet the values are recovered to some point due to the beneficial effect of cerium-based additives.

In general, the literature agrees that rare earths behave as cathodic corrosion inhibitors for many metal alloys when added to a corrosive electrolyte (de Damborenea et al., 2014; Hughes et al., 2014; O'Keefe et al., 2014; Yasakau et al., 2014). In particular, the process of inhibiting corrosion through the lanthanide salts for various materials is a consequence of the inhibition of cathodic regions by the precipitation of an oxide/hydroxide film. This was first mentioned by Hinton in 1984 and shortly afterwards in his own bibliographic review in 1992 (Hinton, 1992).

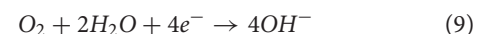
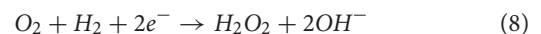
Iron and zinc undergo severe localized dissolution at a number of anodic sites forming hydroxides of limited solubility according to the following equations (Pourbaix and de Zoubov, 1966):



Trivalent ions of rare earths in an aqueous environment undergo gradual hydrolysis and form complexed hydroxylated ions, as shown in Equation (7), and for Ce in Equation (8).



The exact chemical composition of these compounds depends on the type of the lanthanide cation added to the medium and the specific anion of the solution. This complex precipitates and results in the formation of a hydroxide layer as the pH of the solution locally increases at the cathodic areas, where the main reaction is the reduction of oxygen (Equations 9, 10).



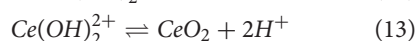
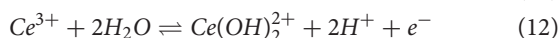
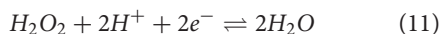
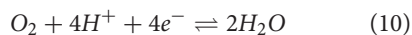
Which of these two reaction pathways predominates, depends on the composition of the metal substrate and the presence, or absence, of any surface oxide film (Bockris and Khan, 1993).

The rare earth hydroxides formed are stable in alkaline solutions and dissolve under acidic conditions. The critical pH values at which the hydroxides precipitate is a function of the concentration of the trivalent ion (Ce^{3+}), which cannot be assumed or calculated in our case (de Damborenea et al., 2014).

Additionally, as shown in related works, in the case of zinc, the gradual dissolution occurring in the early stages of immersion is altered due to the adsorption of cerium ions. According to Aramaki and Arenas and de Damborenea cerium will react with the hydroxylated surface of the metal, thus impeding adsorption of the chlorides. Then, a complex is formed on the metallic surface such as $[\text{Zn}]\text{OCe}(\text{III})\text{OH}_2$ acting as a precursor to form the corrosion inhibiting layer. In addition, the precipitation of $\text{Ce}(\text{OH})_3$ in the cathodic regions is favored due to the lower

solubility compared to zinc hydroxide (1.6×10^{-20} and 7.28×10^{-17} ; Aramaki, 2001; Arenas and de Damborenea, 2006).

A conflicting issue in literature is related with the oxidative state of the cerium ions found in the film. In detail, some claim that both oxygen and hydrogen peroxide (as produced by Equation 9) can act as oxidizing agents producing Ce^{4+} and CeO_2 , as shown by the following reactions (Equations 7–10)



Although in the present study no local pH measurement techniques and electrode potential measurements were utilized, according to literature (Böhm et al., 2000), a pH equal to 8.7 is needed in order Ce^{3+} to be oxidized to Ce^{4+} (giving $Ce(OH)_2^{2+}$) for air-equilibrated water at ambient pressure ($p_{O_2} = 0.2$ atm), but no direct oxidation of $Ce(OH)_3$ to CeO_2 is possible in any pH value. In any case, the pH values needed for the formation of Ce^{4+} by oxidation caused by hydrogen peroxide, are above 10, which is unlikely under our experimental conditions (pH ranging from 6 to 9). In addition, according to Hinton and Wilson (Hinton and Wilson, 1989), it is unlikely that all Ce^{3+} will be oxidized because H_2O_2 is only formed as an intermediate product of the oxygen reduction reaction.

In other related works, it is said that hydrogen peroxide presence contributes to the oxidation of Ce^{3+} to Ce^{4+} , promoting the formation of oxides and hydroxides from both species, under prolonged time exposure conditions (Thierry et al., 1991; Aramaki, 2002a,b). Given the above, it is assumed that the first step in the deposition of a Ce-rich film under our particular experimental conditions is the precipitation of $Ce(OH)_3$ which may subsequently react with CO_2 from the air to form carbonates. The formation of a stable Ce-rich film is confirmed by elemental mapping EDS results on the blocked scribe area with precipitated products after the exposure to the corrosive electrolyte (Figure 10).

It is also reported in literature that the reaction between amine and epoxy groups is catalyzed by increased pH producing a new protective film (Kartsonakis et al., 2012). Another parameter positively affecting the protective performance of the studied systems after scratch formation is the incorporation of the polymer-modified microcapsules which promote the compatibility with the epoxy resin matrix and enhance the consistency of the coating matrix due to the reaction of hydroxyl groups of the PAA block of the polymer shell with the epoxide rings of the epoxy resin (Soares and Livi, 2017).

Effect of Thermally-Induced Defect Closure on Barrier Properties

In the current study, a low T_g liquid rubber elastomer was used in order to add a second self-healing mechanism into the coatings. The polymer which was incorporated either as a surface modification of the microcapsules or as a polymer in free form is expected to modify the T_g of the system. The main aim is to

induce self-healing of an artificial scribe upon heating the film above its T_g , where the polymeric chains have enhanced mobility. In this way, the deformation can be cured, possibly affecting positively and restoring the corrosion protection performance of the under-study film. Thus, the term “self-healing” is related with the recovery of the anti-corrosion protection of a coating system after being damaged due to a non-autonomous self-healing mechanism triggered by temperature. Theoretically, if the ratio between the defect size and the coating thickness is smaller than one, the aforementioned recovery may be complete and repeatable (D'Hollander et al., 2009; Jorcin et al., 2010; Luo and Mather, 2013).

Figures 11, 12 illustrate the morphology of the scribed coatings before and after thermal treatment at $90^\circ C$ for 30 min, along with the line elemental EDS analysis of the main chemical elements of the metallic substrate (Fe, Zn) and the coating (C).

The separated crack surfaces are in spatial proximity after heating for samples *Epoxy-PBA-CSmc* and *Epoxy-CSmc*. The transition from a glassy to a fluid state is based on the onset of molecular motion within the polymer chains. In the region of T_g , and above, the polymer softens and the modulus of elasticity decreases by 3 orders of magnitude and the polymer switches to an elastic state (Souza and Reis, 2013). The potential crack re-bonding cannot be easily visualized due to crack closure. Thus, EIS is again used to assess the functional self-healing, which in the current study is the partial restoration of the barrier properties. **Supplementary Figure S10** represents the EIS Bode results of the scribed *Epoxy-PBA-CSmc* and *Epoxy-CSmc* coatings after their exposure for 1 h into 5 mM NaCl, before and after heat-induced healing. The results were also numerically fitted to quantitatively assess the coatings protective performance after heat treatment (Table 3). One relaxation time is observed for both coatings before their exposure to temperature that is described by the equivalent circuit of Figure 7A. The R_{sol} refers to the electrolyte resistance, CPE_{dl} refers to the CPE of the double layer and R_{ct} is the charge transfer resistance. Both CPE_{dl} and R_{ct} are associated to the corrosion process. On the other hand, two time constants are evident for both coatings after their thermal treatment. In the equivalent circuit (Figure 7B) the pore resistance R_{coat} is combined with a CPE element (CPE_{coat}) to account for the response of the electrolyte inside the pores of the coating and the R_{ct} is associated with the double layer CPE (CPE_{dl}). It should be mentioned that the presence of two time constants indicates that there is no sufficient re-bonding of the two separated surfaces of the artificial defect and an imperfect self-healing action. Additionally, the corrosion process underneath the scratched films has already initiated during immersion in the electrolyte, which explain the presence of two time constants. The corresponding EIS Nyquist plots (Supplementary Figure S11) confirm the aforementioned results. The increment of the charge transfer resistance from 2.04 to 102.9 $k\Omega\ cm^2$ suggests a recovery of 4.944% for *Epoxy-PBA-CSmc* (Table 3). Thus, the polarization resistance or the corrosion reactions at the HDG surface is partially suppressed. Moreover, the fitting results for *Epoxy-CSmc* reveal that the charge transfer resistance is also increased from 4.77 to 234.1 $k\Omega\ cm^2$, clearly denoting a recovery of 4.807%

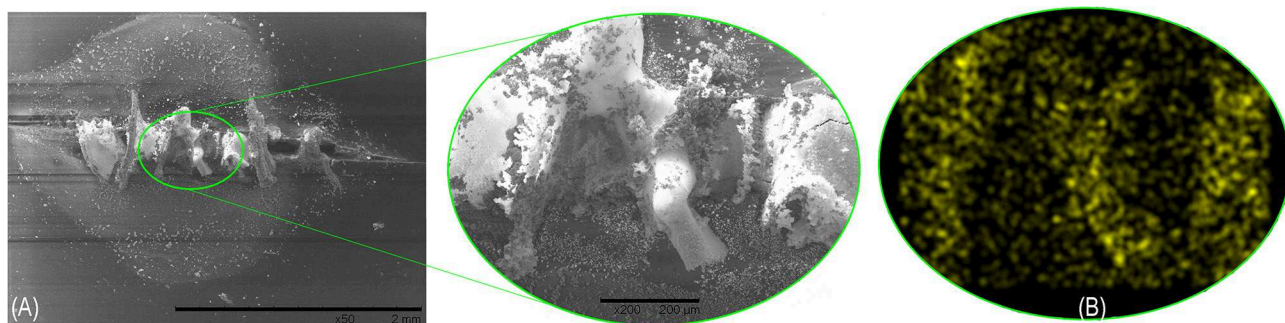


FIGURE 10 | (A) SEM and **(B)** elemental mapping EDS analysis of the formatted stable Ce-rich film on the blocked scribe area with precipitated products after the exposure to the corrosive electrolyte.

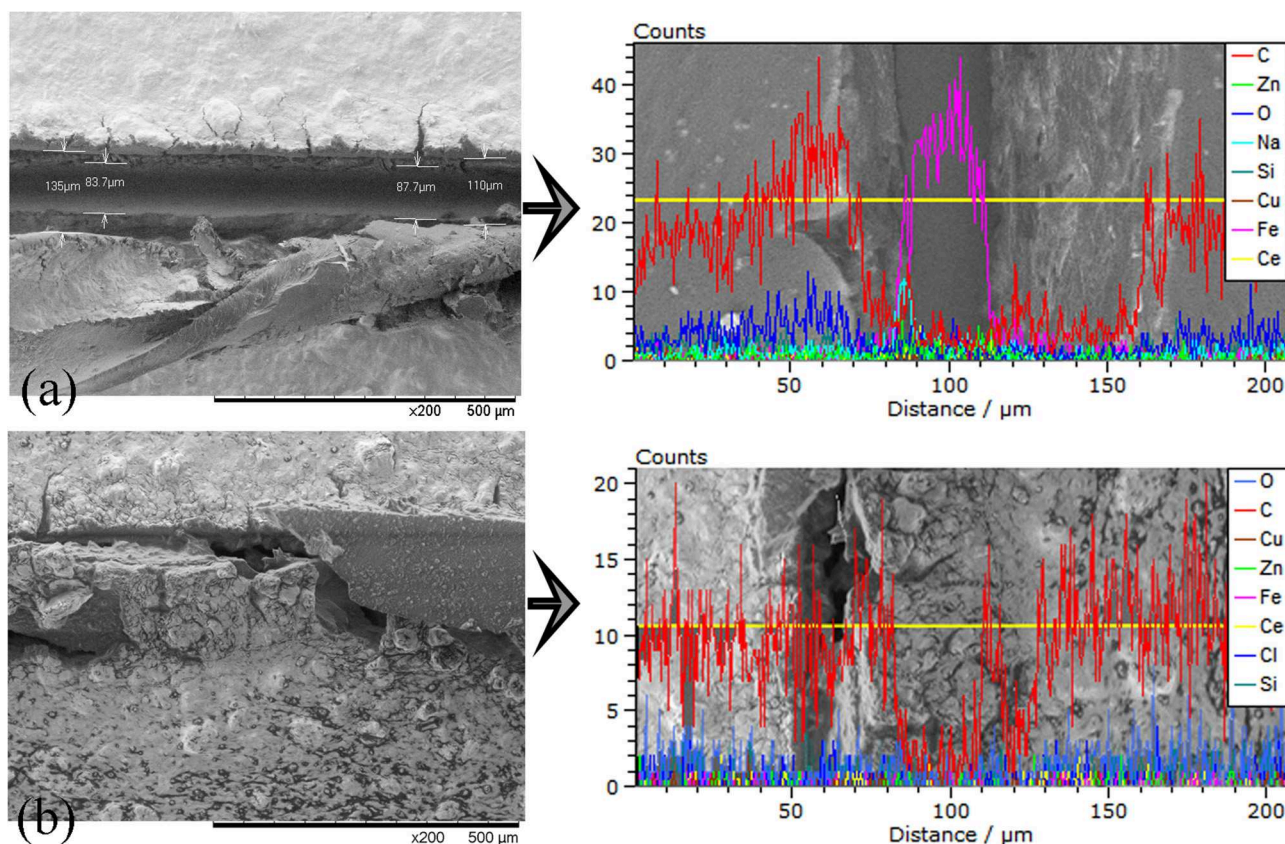


FIGURE 11 | SEM surface images and line elemental analysis of the scribed *Epoxy-PBA-CSmc* coatings **(a)** before and **(b)** after thermal treatment at 90°C for 30 min along with the line elemental EDS analysis of the main chemical elements of the metallic substrate (Fe, Zn) and the coating.

(Table 3). The results for *Epoxy-CSmc* further confirm the observation through SEM that there is also a material reflow in the defect's area where the metallic substrate was exposed, indicating re-bonding between the HDG steel and the liquid rubber polymer.

To conclude, the EIS measurements showed that the liquid rubber addition either in free form (*Epoxy-PBA-CSmc*) or in the presence of the core-shell microcapsules, improved the charge transfer resistance of the coating systems,

indicating a partial inhibition of the corrosion process on HDG substrate, after thermal exposure above its T_g . This is also supported by the DSC measurements conducted on *Epoxy-PBA-CSmc* coating (Supplementary Figure S12), which revealed a reduction of the T_g of the system ($T_g = 79^\circ\text{C}$) due to the elastomer addition, in comparison to the theoretical T_g values of its main epoxy-based component (122°C for bisphenol A diglycidyl ether—diethylenetriamine cured; Bryan Ellis, 2000).

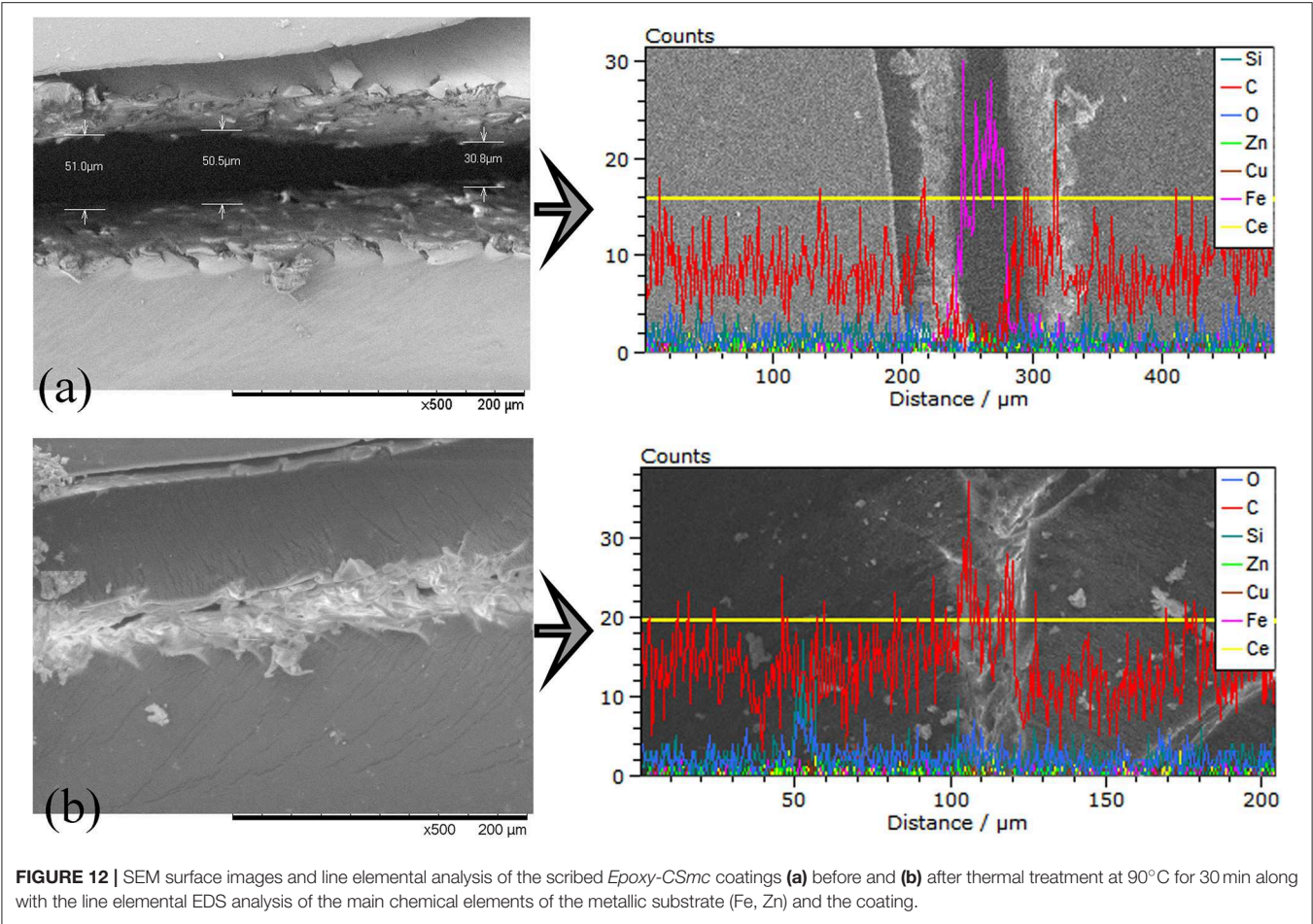


TABLE 3 | Fitting parameters according to equivalent circuits of **Figures 7A,B** of the scribed *Epoxy-PBA-CSmc* and *Epoxy-CSmc* coatings after their exposure for 1 h into 5 mM NaCl, before and after heat-induced healing.

	<i>Epoxy-PBA-CSmc</i> before	<i>Epoxy-PBA-CSmc</i> after	<i>Epoxy-CSmc</i> before	<i>Epoxy-CSmc</i> after
CPE_{coat-T} (nF cm ⁻² s ⁻ⁿ)	–	0.13	–	1.79
Error (%)	–	15.7	–	50.0
CPE_{coat-P}	–	0.97422	–	0.75727
Error (%)	–	1.36	–	5.46
R_{coat} (kohm cm ²)	–	37.3	–	36.4
Error (%)	–	0.85	–	5.99
C_{coat} (nF cm ⁻²)	–	903.3	–	814.1
CPE_{dl-T} (μF cm ⁻² s ⁻ⁿ)	25.5	1.27	1.52	0.13
Error (%)	2.56	4.91	6.69	8.92
CPE_{dl-P}	0.68035	0.63769	0.73103	0.76513
Error (%)	0.57	1.76	1.18	2.06
R_{ct} (kohm cm ²)	2.04	102.9	4.77	234.1
Error (%)	0.71	1.68	0.85	2.07
C_{dl} (μF cm ⁻²)	6.36	0.40	0.24	0.05
Chi-squared	0.00237	0.00299	0.00833	0.01198

CONCLUSION

Two advanced coating systems have been presented in this work incorporating a type of core-shell cerium-based microcapsules which were compared with an epoxy-based coating including cerium microcapsules. The main aim was to investigate the influence of a liquid rubber polymer addition either as a surface-modifier or as an additive in free form on the anti-corrosion protection offered and their potentially heat-triggered material re-flow/self-healing ability.

The first autonomous self-healing mechanism refers to the well-known and studied anti-corrosion effect of cerium-based containers that contribute to the formation of stable chelating complexes on the surface of galvanized steel. On the other hand, their polymer-based surface modification enhanced the interaction of the microcapsules' surface with the epoxy matrix and the overall EIS response upon defect formation.

With the addition of a liquid rubber polymer in free form it is possible to incorporate a second, non-autonomous mechanism which was studied and presented in this work based on activation by increasing the temperature to values higher than the T_g of the coating system. In this case, except from the material re-flow ability of the system also shown in the coating incorporating the core-shell microcapsules, the protection performance of the coating is increased, offering a partial suppression of the underlying corrosion process.

Future plans of the current work include localized impedance spectroscopy measurements for the assessment of the local electrochemical corrosion reaction under the artificially scribed coating, along with complementary antifouling performance evaluation.

DATA AVAILABILITY

The datasets generated for this study are available on request to the corresponding author.

AUTHOR CONTRIBUTIONS

EK and IK conceived, designed and performed the analysis. EK collected the data and wrote the paper. IK performed the Scanning Electron Microscopy Analysis and also contributed during the experiments and the data analysis. CC had the overall responsibility for the final manuscript and contributed with critical comments and suggestions during the experimental process.

REFERENCES

- Abdolah Zadeh, M., van der Zwaag, S., and García, S. J. (2016). Assessment of healed scratches in intrinsic healing coatings by AC/DC/AC accelerated electrochemical procedure. *Surf. Coat. Technol.* 303, 396–405. doi: 10.1016/j.surfcoat.2015.11.001
- Aramaki, K. (2001). The inhibition effects of cation inhibitors on corrosion of zinc in aerated 0.5 M NaCl. *Corros. Sci.* 43, 1573–1588. doi: 10.1016/S0010-938X(00)00144-X

SUPPLEMENTARY MATERIAL

The Supplementary Material for this article can be found online at: <https://www.frontiersin.org/articles/10.3389/fmats.2019.00222/full#supplementary-material>

Supplementary Figure S1 | Schematic representation of the synthesis of the diblock copolymer onto the surface of either CeO_2 or Cu_2O .

Supplementary Figure S2 | SEM surface images and line elemental EDS analysis of the artificially scribed: (a) *Epoxy-PBA-CSmc* and (b) *Epoxy-CSmc* coating systems.

Supplementary Figure S3 | XRD pattern of the $\text{CeO}_2@P(\text{BA-b-AA})$ core-shell microcapsules.

Supplementary Figure S4 | XRD pattern of the $\text{Cu}_2\text{O}@P(\text{BA-b-AA})$ core-shell microcapsules.

Supplementary Figure S5 | SEM surface images of the: (a) *Epoxy-PBA-CSmc* and (b) *Epoxy-CSmc* corrosion protective coating systems.

Supplementary Figure S6 | Topographic maps with the average coating thicknesses of the: (a) *Epoxy-PBA-CSmc* and (b) *Epoxy-CSmc* corrosion protective coating systems.

Supplementary Figure S7 | SEM cross-section images of the coating thicknesses of the: (a) *Epoxy-PBA-CSmc* and (b) *Epoxy-CSmc* corrosion protective coating systems.

Supplementary Figure S8 | EIS Bode diagrams of artificially scribed *Epoxy-PBA-CSmc* after exposure to 5 mM NaCl solution: (a) Impedance modulus versus frequency and (b) Phase angle versus frequency.

Supplementary Figure S9 | EIS Bode diagrams of artificially scribed *Epoxy-CSmc* after exposure to 5 mM NaCl solution: (a) Impedance modulus versus frequency and (b) Phase angle versus frequency.

Supplementary Figure S10 | EIS Bode diagrams of artificially scribed *Epoxy-PBA-CSmc* and *Epoxy-CSmc* coatings, before and after heat-induced healing after exposure to 5 mM NaCl solution: (a) Impedance modulus versus frequency and (b) Phase angle versus frequency.

Supplementary Figure S11 | EIS Nyquist diagrams of artificially scribed *Epoxy-PBA-CSmc* and *Epoxy-CSmc* coatings, before and after heat-induced healing after exposure to 5 mM NaCl solution.

Supplementary Figure S12 | The DSC measurements conducted on the scribed *Epoxy-PBA-CSmc* coating after thermal treatment at 90°C for 30 min.

Supplementary Table T1 | Chemical Composition of Substitute Ocean Water (according to ASTM D1141-98).

Supplementary Table T2 | The morphological and structural characteristics of the $\text{CeO}_2@P(\text{BA-b-AA})$ core-shell microcapsules.

Supplementary Table T3 | The morphological and structural characteristics of $\text{Cu}_2\text{O}@P(\text{BA-b-AA})$ core-shell microcapsules.

Supplementary Table T4 | Fitting parameters according to equivalent circuit of Figure 7C after samples exposure to 5 mM NaCl solution.

- Aramaki, K. (2002a). Preparation of chromate-free, self-healing polymer films containing sodium silicate on zinc pretreated in a cerium(III) nitrate solution for preventing zinc corrosion at scratches in 0.5 M NaCl. *Corros. Sci.* 44, 1375–1389. doi: 10.1016/S0010-938X(01)00138-X
- Aramaki, K. (2002b). Self-healing mechanism of an organosiloxane polymer film containing sodium silicate and cerium(III) nitrate for corrosion of scratched zinc surface in 0.5 M NaCl. *Corros. Sci.* 44, 1621–1632. doi: 10.1016/S0010-938X(01)00171-8

- Arenas, M. A., and de Damborenea, J. (2006). Interference by cerium cations during the multi-step zinc dissolution process in a chloride-containing electrolyte. *Corros. Sci.* 48, 3196–3207. doi: 10.1016/j.corsci.2005.10.015
- Bagheri, R., Marouf, B. T., and Pearson, R. A. (2009). Rubber-toughened epoxies: a critical review. *Polym. Rev.* 49, 201–225. doi: 10.1080/15583720903048227
- Balaskas, A. C., Hashimoto, T., Curioni, M., and Thompson, G. E. (2017). Two-shell structured PMAA@CeO₂ nanocontainers loaded with 2-mercaptobenzothiazole for corrosion protection of damaged epoxy coated AA 2024-T3. *Nanoscale* 9, 5499–5508. doi: 10.1039/c7nr00858a
- Barsoukov, E., and Macdonald, R. J. (2018). *Impedance Spectroscopy Theory Experiment and Applications*. Hoboken, NJ: John Wiley and Sons Inc., Publication, 13–20.
- Benoit, D. N., Zhu, H., Lilierose, M. H., Verm, R. A., Ali, N., Morrison, A. N., et al. (2012). Measuring the grafting density of nanoparticles in solution by analytical ultracentrifugation and total organic carbon analysis. *Anal. Chem.* 84, 9238–9245. doi: 10.1021/ac301980a
- Bockris, J. O. M., and Khan, S. U. M. (eds.). (1993). "Surface electrochemistry," in *A Molecular Level Approach*, eds J. O'M. Bockris and S. U. M. Khan (Boston, MA: Springer), 764–770.
- Böhm, S., Greef, R., McMurray, H. N., Powell, S. M., and Worsley, D. A. (2000). Kinetic and mechanistic studies of rare earth-rich protective film formation using *in situ* ellipsometry. *J. Electrochem. Soc.* 147, 3286. doi: 10.1149/1.1393897
- Borisova, D., Akçakayran, D., Schenderlein, M., Möhwald, H., and Shchukin, D. G. (2013). Nanocontainer-based anticorrosive coatings: effect of the container size on the self-healing performance. *Adv. Funct. Mater.* 23, 3799–3812. doi: 10.1002/adfm.201203715
- Bryan Ellis, R. S. (2000). *Polymers - A Property Database*. Boca Raton, FL: CRC Press.
- Cabral, A. M., Trabelsi, W., Serra, R., Montemor, M. F., Zheludkevich, M. L., and Ferreira, M. G. S. (2006). The corrosion resistance of hot dip galvanized steel and AA2024-T3 pre-treated with bis-[triethoxysilylpropyl] tetrasulfide solutions doped with Ce(NO₃)₃. *Corros. Sci.* 48, 3740–3758. doi: 10.1016/j.corsci.2006.01.010
- Cole, K. S., and Cole, R. H. (1942). Dispersion and absorption in dielectrics II. Direct current characteristics. *J. Chem. Phys.* 10, 98–105. doi: 10.1063/1.1723677
- Colombani, O., Ruppel, M., Schubert, F., Zettl, H., Pergushov, D. V., and Müller, A. H. E. (2007). Synthesis of Poly(n-butyl acrylate)-block-poly(acrylic acid) diblock copolymers by ATRP and their micellization in water. *Macromolecules* 40, 4338–4350. doi: 10.1021/ma0609578
- Comstock, M. J., Hertzberg, R. W., and Riew, C. K. (1989). Rubber-toughened plastics, copyright, advances in chemistry series, FOREWORD, ABOUT THE EDITOR, Dedication. *Adv. Chem.* 222, i–x. doi: 10.1021/ba-1989-0222.fw001
- Das, R., Melchior, C., and Karumbaiah, K. M. (2016). Chapter 11: Self-healing composites for aerospace applications. *Adv. Compos. Mater. Aerospace Eng.* 333–364. doi: 10.1016/b978-0-08-100037-3.00011-0
- de Damborenea, J., Conde, A., and Arenas, M. A. (2014). "3 - Corrosion inhibition with rare earth metal compounds in aqueous solutions," in *Rare Earth-Based Corrosion Inhibitors*, eds M. Forsyth and B. Hinton (Cambridge, UK: Woodhead Publishing), 84–116.
- D'Hollander, S., Van Assche, G., Van Mele, B., and Du Prez, F. (2009). Novel synthetic strategy toward shape memory polyurethanes with a well-defined switching temperature. *Polymer* 50, 4447–4454. doi: 10.1016/j.polymer.2009.07.021
- Figueira, R. B., Silva, C. J. R., and Pereira, E. V. (2014). Organic-inorganic hybrid sol-gel coatings for metal corrosion protection: a review of recent progress. *J. Coat. Technol. Res.* 12, 1–35. doi: 10.1007/s11998-014-9595-6
- Foyet, A., Wu, T. H., Kodentsov, A., van der Ven, L. G. J., de With, G., and van Benthem, R. A. T. M. (2013). Corrosion protection and delamination mechanism of epoxy/carbon black nanocomposite coating on AA2024-T3. *J. Electrochem. Soc.* 160, C159–C167. doi: 10.1149/2.086304jes
- Garg, A., and Mai, Y. W. (1988). Failure mechanisms in toughened epoxy resins—A review. *Compos. Sci. Technol.* 31, 179–223. doi: 10.1016/0266-3538(88)90009-7
- Gharbi, O., Thomas, S., Smith, C., and Biribilis, N. (2018). Chromate replacement: what does the future hold? *npj Mater. Degrad.* 2, 1–2. doi: 10.1038/s41529-018-0034-5
- Hinton, B. R. W. (1992). Corrosion inhibition with rare earth metal salts. *J. Alloys Compd.* 180, 15–25. doi: 10.1016/0925-8388(92)90359-H
- Hinton, B. R. W., and Wilson, L. (1989). The corrosion inhibition of zinc with cerous chloride. *Corros. Sci.* 29, 967–985. doi: 10.1016/0010-938X(89)90087-5
- Hsu, C. H., and Mansfeld, F. (2001). Technical note: concerning the conversion of the constant phase element parameter Y₀ into a capacitance. *Corrosion* 57, 747–748. doi: 10.5006/1.3280607
- Hughes, A. E., Harvey, T. G., Biribilis, N., Kumar, A., and Buchheit, R. G. (2014). "7 - Coatings for corrosion prevention based on rare earths," in *Rare Earth-Based Corrosion Inhibitors*, eds M. Forsyth and B. Hinton (Cambridge, UK: Woodhead Publishing), 186–232.
- Iijima, T., Horiba, T., and Tomoi, M. (1991). Toughening of epoxy resins by modification with reactive elastomers composed of butyl acrylate, glycidyl methacrylate and acrylonitrile or styrene. *Eur. Polym. J.* 27, 1231–1238. doi: 10.1016/0014-3057(91)90060-2
- Jorcin, J.-B., Scheltjens, G., Van Ingelgem, Y., Tourwé, E., Van Assche, G., De Graeve, I., et al. (2010). Investigation of the self-healing properties of shape memory polyurethane coatings with the 'odd random phase multisine' electrochemical impedance spectroscopy. *Electrochim. Acta* 55, 6195–6203. doi: 10.1016/j.electacta.2010.01.027
- Kainourgios, P., Kartsonakis, I. A., Dragatogiannis, D. A., Koumoulos, E. P., Goulis, P., and Charitidis, C. A. (2017). Electrochemical surface functionalization of carbon fibers for chemical affinity improvement with epoxy resins. *Appl. Surf. Sci.* 416, 593–604. doi: 10.1016/j.apsusc.2017.04.214
- Kakaroglou, A., Domini, M., and De Graeve, I. (2016). Encapsulation and incorporation of sodium molybdate in polyurethane coatings and study of its corrosion inhibition on mild steel. *Surf. Coat. Technol.* 303, 330–341. doi: 10.1016/j.surfcoat.2016.02.007
- Kartsonakis, I. A., Balaskas, A. C., Koumoulos, E. P., Charitidis, C. A., and Kordas, G. (2013). ORMOSIL-epoxy coatings with ceramic containers for corrosion protection of magnesium alloys ZK10. *Prog. Organic Coat.* 76, 459–470. doi: 10.1016/j.porgcoat.2012.10.028
- Kartsonakis, I. A., Balaskas, A. C., Koumoulos, E. P., Charitidis, C. A., and Kordas, G. C. (2012). Incorporation of ceramic nanocontainers into epoxy coatings for the corrosion protection of hot dip galvanized steel. *Corros. Sci.* 57, 30–41. doi: 10.1016/j.corsci.2011.12.037
- Kartsonakis, I. A., Danilidis, I. L., Pappas, G. S., and Kordas, G. C. (2010). Encapsulation and release of corrosion inhibitors into titania nanocontainers. *J. Nanosci. Nanotechnol.* 10, 5912–5920. doi: 10.1166/jnn.2010.2571
- Kartsonakis, I. A., Liatsi, P., Daniilidis, I., and Kordas, G. (2008). Synthesis, characterization, and antibacterial action of hollow ceria nanospheres with/without a conductive polymer coating. *J. Am. Ceramic Soc.* 91, 372–378. doi: 10.1111/j.1551-2916.2007.02088.x
- Kartsonakis, I. A., Stanciu, S. G., Matei, A. A., Hristu, R., Karantonis, A., and Charitidis, C. A. (2016). A comparative study of corrosion inhibitors on hot-dip galvanized steel. *Corros. Sci.* 112, 289–307. doi: 10.1016/j.corsci.2016.07.030
- Kawasaki, A., Furukawa, J., Tsuruta, T., Wasai, G., and Makimoto, T. (1961). Infrared Spectra of Poly(butyl acrylates). *Die Makromolekulare Chemie* 49, 76–111. doi: 10.1002/macp.1961.020490108
- Kongparakul, S., Kornprasert, S., Suriya, P., Le, D., Samart, C., Chantarasiri, N., et al. (2017). Self-healing hybrid nanocomposite anticorrosive coating from epoxy/modified nanosilica/perfluorooctyl triethoxysilane. *Prog. Org. Coat.* 104, 173–179. doi: 10.1016/j.porgcoat.2016.12.020
- Levina, A., Harris, H. H., and Lay, P. A. (2006). Binding of chromium(VI) to histones: implications for chromium(VI)-induced genotoxicity. *J. Biol. Inorg. Chem.* 11, 225–234. doi: 10.1007/s00775-005-0068-3
- Li, G. L., Hu, J., Wang, H., Pilz-Allen, C., Wang, J., Qi, T., et al. (2017). Polymer-decorated anisotropic silica nanotubes with combined shape and surface properties for guest delivery. *Polymer* 109, 332–338. doi: 10.1016/j.polymer.2016.12.048
- Li, H., Wang, W., Tan, J., Li, C., and Zhang, Q. (2015). Synthesis and characterization of graft copolymers PnBA-g-PS by miniemulsion polymerization. *RSC Adv.* 5, 45459–45466. doi: 10.1039/C5RA06502J

- Li, Q., Wu, G., Zhang, X., and Wu, C. (2006). Preparation of Poly (n-butyl acrylates) encapsulated carbon black via ultrasonic irradiation initiating emulsion polymerization. *Polym. J.* 38, 1245–1250. doi: 10.1295/polymj.PJ2006053
- Luo, X., and Mather, P. T. (2013). Shape memory assisted self-healing coating. *ACS Macro Lett.* 2, 152–156. doi: 10.1021/mz400017x
- Lyon, S. B., Bingham, R., and Mills, D. J. (2017). Advances in corrosion protection by organic coatings: what we know and what we would like to know. *Prog. Org. Coat.* 102, 2–7. doi: 10.1016/j.porgcoat.2016.04.030
- McGarry, F. J. (1970). Building design with fibre reinforced materials. *Proc. R. Soc. A Math. Phys. Eng. Sci.* 319, 59–68. doi: 10.1098/rspa.1970.0165
- Meng, F., Liu, L., Tian, W., Wu, H., Li, Y., Zhang, T., et al. (2015). The influence of the chemically bonded interface between fillers and binder on the failure behaviour of an epoxy coating under marine alternating hydrostatic pressure. *Corros. Sci.* 101, 139–154. doi: 10.1016/j.corsci.2015.09.011
- Moharram, M. A., and Khafagi, M. G. (2007). Application of FTIR spectroscopy for structural characterization of ternary poly(acrylic acid)–metal–poly(vinyl pyrrolidone) complexes. *J. Appl. Polym. Sci.* 105, 1888–1893. doi: 10.1002/app.25703
- Moharram, M. A., Rabie, S. M., and El-Gendy, H. M. (2002). Infrared spectra of γ -irradiated poly(acrylic acid)–polyacrylamide complex. *J. Appl. Polym. Sci.* 85, 1619–1623. doi: 10.1002/app.10702
- Montemor, M. F., Trabelsi, W., Lamaka, S. V., Yasakau, K. A., Zheludkevich, M. L., Bastos, A. C., et al. (2008). The synergistic combination of bisilane and CeO₂-ZrO₂ nanoparticles on the electrochemical behaviour of galvanised steel in NaCl solutions. *Electrochim. Acta* 53, 5913–5922. doi: 10.1016/j.electacta.2008.03.069
- Njoku, D. I., Cui, M., Xiao, H., Shang, B., and Li, Y. (2017). Understanding the anticorrosive protective mechanisms of modified epoxy coatings with improved barrier, active and self-healing functionalities: EIS and spectroscopic techniques. *Sci. Rep.* 7:15597. doi: 10.1038/s41598-017-15845-0
- O'Keefe, M. J., Fahrenholtz, W. G., Stoffer, J. O., and Morris, E. L. (2014). “6 - Corrosion-resistant polymer coatings containing rare earth compounds,” in *Rare Earth-Based Corrosion Inhibitors*, eds M. Forsyth and B. Hinton (Cambridge, UK: Woodhead Publishing), 163–185.
- Orazem, M. E., and Tribollet, B. (eds.). (2008). “Time-constant dispersion 13.1 constant phase elements,” in *Electrochemical Impedance Spectroscopy* (Hoboken, NJ: Wiley), 233–237.
- OSHA3373-10 (2009). *Hexavalent Chromium*. Hoboken, NJ: Occupational Safety and Health Administration; U.S. Department of Labor.
- Parameswaranpillai, J., Hameed, N., Pionteck, J., and Woo, E. M. (2017). *Handbook of Epoxy Blends*. Cham: Springer International Publishing.
- Plawecka, M., Snihirova, D., Martins, B., Szczepanowicz, K., Warszynski, P., and Montemor, M. F. (2014). Self healing ability of inhibitor-containing nanocapsules loaded in epoxy coatings applied on aluminium 5083 and galvanneal substrates. *Electrochim. Acta* 140, 282–293. doi: 10.1016/j.electacta.2014.04.035
- Pourbaix, M., and de Zoubov, N. (1966). *Atlas of Electrochemical Equilibria in Aqueous Solutions*. New York, NY: Pergamon Press, 307.
- Qiao, Y., Li, W., Wang, G., Zhang, X., and Cao, N. (2015). Application of ordered mesoporous silica nanocontainers in an anticorrosive epoxy coating on a magnesium alloy surface. *RSC Adv.* 5, 47778–47787. doi: 10.1039/c5ra05266a
- Ratna, D. (2001). Phase separation in liquid rubber modified epoxy mixture. Relationship between curing conditions, morphology and ultimate behavior. *Polymer* 42, 4209–4218. doi: 10.1016/s0032-3861(00)00798-9
- Ratna, D., and Banthia, A. K. (2004). Rubber toughened epoxy. *Macromol. Res.* 12, 11–21. doi: 10.1007/bf03218989
- Samiee, R., Ramezanzadeh, B., Mahdavian, M., and Alibakhshi, E. (2019). Assessment of the smart self-healing corrosion protection properties of a water-base hybrid organo-silane film combined with non-toxic organic/inorganic environmentally friendly corrosion inhibitors on mild steel. *J. Clean. Prod.* 220, 340–356. doi: 10.1016/j.jclepro.2019.02.149
- Sierra-Ávila, R., Pérez-Alvarez, M., Cadenas-Pliego, G., Comparán Padilla, V., Ávila-Orta, C., Pérez Camacho, O., et al. (2015). Synthesis of copper nanoparticles using mixture of allylamine and polyallylamine. *J. Nanomater.* 2015, 1–9. doi: 10.1155/2015/367341
- Skorb, E. V., Fix, D., Andreeva, D. V., Möhwald, H., and Shchukin, D. G. (2009). Surface-modified mesoporous SiO₂ containers for corrosion protection. *Adv. Funct. Mater.* 19, 2373–2379. doi: 10.1002/adfm.200801804
- Snihirova, D., Lamaka, S. V., and Montemor, M. F. (2016). Part II: Smart composite coatings for corrosion protection of aluminium alloys in aerospace applications. *Smart Compos. Coat. Membr.* Part II, 85–121. doi: 10.1016/b978-1-78242-283-9.00004-x
- Soares, B. G., and Livi, S. (2017). “Novel techniques for the preparation of different epoxy/rubber blends,” in *Handbook of Epoxy Blends*, eds J. Parameswaranpillai, N. Hameed, J. Pionteck and E. M. Woo (Cham: Springer International Publishing), 29–67.
- Souza, J. P. B., and Reis, J. M. L. (2013). Thermal behavior of DGEBA (Diglycidyl Ether of Bisphenol A) adhesives and its influence on the strength of joints. *Appl. Adhes. Sci.* 1:6. doi: 10.1186/2196-4351-1-6
- Tania, R., Ciontea, L., Suciu, R.-C., Petrisor, T. Jr., Gabor, M., Thalmayer, G., et al. (2008). Thermal decomposition study by DTA-TG-MS of cerium[III] acetylacetonate used as ceria thin film precursor. *J. Optoelectron. Adv. Mater.* 10, 2223–2227. Available online at: <https://www.tib.eu/en/search/id/BLSE%3ARN237661951/Thermal-decomposition-study-by-DTA-TG-MS-of-cerium/>
- Thierry, D., Massinon, D., and Hugot-Le-Goff, A. (1991). *In situ* determination of corrosion products formed on painted galvanized steel by raman spectroscopy. *J. Electrochem. Soc.* 138, 879–880. doi: 10.1149/1.2085702
- Trabelsi, W., Triki, E., Dhoubi, L., Ferreira, M. G. S., Zheludkevich, M. L., and Montemor, M. F. (2006). The use of pre-treatments based on doped silane solutions for improved corrosion resistance of galvanised steel substrates. *Surf. Coat. Technol.* 200, 4240–4250. doi: 10.1016/j.surfcoat.2005.01.044
- Ubaid, F., Radwan, A. B., Naem, N., Shakoob, R. A., Ahmed, Z., Montemor, M. F., et al. (2019). Multifunctional self-healing polymeric nanocomposite coatings for corrosion inhibition of steel. *Surf. Coat. Technol.* 372, 121–133. doi: 10.1016/j.surfcoat.2019.05.017
- Uhlig, H. R. (2008). *Corrosion and Corrosion Control: An Introduction to Corrosion Science and Engineering*. ed W. Revie Hoboken, NJ: John Wiley and Sons, Inc.
- Ulaeto, S. B., Rajan, R., Pancracious, J. K., Rajan, T. P. D., and Pai, B. C. (2017). Developments in smart anticorrosive coatings with multifunctional characteristics. *Prog. Org. Coat.* 111, 294–314. doi: 10.1016/j.porgcoat.2017.06.013
- Unnikrishnan, K. P., and Thachil, E. T. (2012). Toughening of epoxy resins. *Design. Monom. Polym.* 9, 129–152. doi: 10.1163/156855506776382664
- Upadhyay, V., and Battocchi, D. (2016). Localized electrochemical characterization of organic coatings: a brief review. *Prog. Org. Coat.* 99, 365–377. doi: 10.1016/j.porgcoat.2016.06.012
- Vázquez, A., Rojas, A. J., Adabbo, H. E., Borrajo, J., and Williams, R. J. J. (1987). Rubber-modified thermosets: Prediction of the particle size distribution of dispersed domains. *Polymer* 28, 1156–1164. doi: 10.1016/0032-3861(87)90259-x
- Verchere, D., Sautereau, H., Pascault, J. P., Moschiar, S. M., Riccardi, C. C., and Williams, R. J. J. (1990). Rubber-modified epoxies. I. Influence of carboxyl-terminated butadiene-acrylonitrile random copolymers (CTBN) on the polymerization and phase separation processes. *J. Appl. Polym. Sci.* 41, 467–485. doi: 10.1002/app.1990.070410303
- Williams, R. J. J., Rozenberg, B. A., and Pascault, J.-P. (1997). “Reaction-induced phase separation in modified thermosetting polymers,” in *Polymer Analysis Polymer Physics*. Berlin; Heidelberg: Springer, 95–156. Available online at: <https://link.springer.com/content/pdf/bfm%3A978-3-540-68374-2%2F1.pdf>
- Yamanaka, K., Takagi, Y., and Inoue, T. (1989). Reaction-induced phase separation in rubber-modified epoxy resins. *Polymer* 30, 1839–1844. doi: 10.1016/0032-3861(89)90355-8
- Yao, Z., Braid, N., Botton, G. A., and Adronov, A. (2003). Polymerization from the surface of single-walled carbon nanotubes - preparation and characterization of nanocomposites. *J. Am. Chem. Soc.* 125, 16015–16024. doi: 10.1021/ja037564y
- Yasakau, K. A., Ferreira, M. G. S., Zheludkevich, M. L., Terryn, H., Mol, J. M. C., and Gonzalez-Garcia, Y. (2014). “8 - Novel and self-healing anticorrosion coatings using rare earth compounds,” in *Rare Earth-Based Corrosion Inhibitors*, eds M. Forsyth and B. Hinton (Cambridge, UK: Woodhead Publishing), 233–266.

- Yee, A. F., and Pearson, R. A. (1986). Toughening mechanisms in elastomer-modified epoxies. *J. Mater. Sci.* 21, 2462–2474. doi: 10.1007/bf01114293
- Yin, X., Liu, Z., Wang, D., Pei, X., Yu, B., and Zhou, F. (2015). Bioinspired self-healing organic materials: chemical mechanisms and fabrications. *J. Bionic Eng.* 12, 1–16. doi: 10.1016/s1672-6529(14)60095-0
- Zhang, F., Ju, P., Pan, M., Zhang, D., Huang, Y., Li, G., et al. (2018). Self-healing mechanisms in smart protective coatings: a review. *Corros. Sci.* 144, 74–88. doi: 10.1016/j.corsci.2018.08.005
- Zhang, J.-T., Hu, J.-M., Zhang, J.-Q., and Cao, C.-N. (2004). Studies of water transport behavior and impedance models of epoxy-coated metals in NaCl solution by EIS. *Prog. Org. Coat.* 51, 145–151. doi: 10.1016/j.porgcoat.2004.08.001
- Zheludkevich, M. (2009). “Self-healing anticorrosion coatings,” in *Self-Healing Materials*, ed S. K. Ghosh (Weinheim: WILEY-VCH Verlag GmbH & Co. KGaA), 101–139.
- Zheludkevich, M. L., Serra, R., Montemor, M. F., Yasakau, K. A., Salvado, I. M. M., and Ferreira, M. G. S. (2005). Nanostructured sol–gel coatings doped with cerium nitrate as pre-treatments for AA2024-T3. *Electrochim. Acta* 51, 208–217. doi: 10.1016/j.electacta.2005.04.021
- Zhu, D. Y., Rong, M. Z., and Zhang, M. Q. (2015). Self-healing polymeric materials based on microencapsulated healing agents: from design to preparation. *Prog. Polym. Sci.* 49–50, 175–220. doi: 10.1016/j.progpolymsci.2015.07.002
- Zhu, Y., Free, M. L., and Yi, G. (2016). The effects of surfactant concentration, adsorption, aggregation, and solution conditions on steel corrosion inhibition and associated modeling in aqueous media. *Corros. Sci.* 102, 233–250. doi: 10.1016/j.corsci.2015.10.012

Conflict of Interest Statement: The authors declare that the research was conducted in the absence of any commercial or financial relationships that could be construed as a potential conflict of interest.

Copyright © 2019 Karaxi, Kartsonakis and Charitidis. This is an open-access article distributed under the terms of the Creative Commons Attribution License (CC BY). The use, distribution or reproduction in other forums is permitted, provided the original author(s) and the copyright owner(s) are credited and that the original publication in this journal is cited, in accordance with accepted academic practice. No use, distribution or reproduction is permitted which does not comply with these terms.



Corrosion Assessment of Zn-Rich Epoxy Primers With Carbon Nanotube Additions in an Electrolyte With a Bacteria Consortium

Homero Castaneda^{1*} and Monica Galicia²

¹ Department of Materials Science and Engineering, Texas A&M University, College Station, TX, United States,

² Departamento de Ciencias Químico Biológicas, Instituto de Ciencias Biomédicas, Universidad Autónoma de Ciudad Juárez, Ciudad Juárez, Mexico

OPEN ACCESS

Edited by:

Michele Fedel,
University of Trento, Italy

Reviewed by:

Farhad Sharif,
Amirkabir University of
Technology, Iran
Idalina Vieira Aoki,
University of São Paulo, Brazil

*Correspondence:

Homero Castaneda
hcastaneda@tamu.edu

Specialty section:

This article was submitted to
Environmental Materials,
a section of the journal
Frontiers in Materials

Received: 09 July 2019

Accepted: 14 November 2019

Published: 03 December 2019

Citation:

Castaneda H and Galicia M (2019)
Corrosion Assessment of Zn-Rich
Epoxy Primers With Carbon Nanotube
Additions in an Electrolyte With a
Bacteria Consortium.
Front. Mater. 6:307.
doi: 10.3389/fmats.2019.00307

Multifunctional coatings for corrosive environments have been developed to include two basic principle protection mechanisms: a barrier mechanism acting as a mass transfer process blocker, and cathodic protection mechanism acting as a charge transfer process promoter. Both mechanisms were assessed for Zinc-Rich Epoxy (ZRE) coatings in the presence of Carbon Nanotubes (CNTs) and exposure to a bioelectrolyte in order to study the evolution process during microbial corrosion conditions. The purpose of this study is to characterize in a comprehensive experimental platform the electrochemical response of a dual-protection zinc epoxy coating with different ratios of additive carbon nanotubes to active zinc particles upon exposure to a sulfate reducing consortium. Carbon nanotubes addition was found to affect both the prevailing mechanism at the coating interfaces and the formation of a biofilm at the coating surface that influenced the relatively dominance of the barrier protection mechanism. These multifunctional coatings with active particles could help to balance the charge transfer efficiency in terms of the sacrificial of zinc and barrier mechanisms, which influence biofilm formation and have potential consequences for biocorrosion on carbon steel.

Keywords: zinc rich epoxy coatings, carbon nanotubes, biocorrosion, biofilm, EIS

INTRODUCTION

Most coatings used for microbiologically induced corrosion (MIC) in industry are designed to provide an effective barrier to inhibit corrosion processes and/or provide a biocidal effect. These coatings are synthesized using organic, inorganic, and hybrid approaches. Organic coatings have been demonstrated to provide an effective physical barrier in a variety of aggressive conditions (Deflorian et al., 2005; Abdolahi et al., 2014; Fedel et al., 2019). However, when exposed to anoxic conditions such as those prevailing in seawater or oil and gas pipelines, some of these coatings degrade faster upon exposure to either a bacterial consortium or a specific strain of microbial attack (Enning and Garrelfs, 2014).

Unfortunately, inorganic and hybrid protective coatings on steel have also been proven to degrade when exposed to MIC in such anoxic conditions (Abdolahi et al., 2014; Enning and Garrelfs, 2014; Ciubotariu et al., 2015). Environmentally friendly coatings are being developed to improve their physicochemical properties to resist microbiological attack, either in aerobic or anaerobic conditions, while avoiding toxicity to the environment from the inherently toxic formulations of some coatings.

Recent coating research has investigated nano-architected sacrificial coatings as a new technology with dual protection mechanisms. The first is galvanic or cathodic protection, which is achieved by integrating electrochemically active particles into the organic coating matrix. The second protection mechanism is the classical barrier effect offered by a polymeric matrix. The addition of nanostructures such as carbon nanotubes (CNTs) can enhance both properties by influencing the interconnectivity of active particles and filling the voids created during synthesis of the coating in the polymeric matrix, as noted by Cubides and Castaneda (2016).

Zn-rich epoxy primers have shown excellent results and have been used by the industry since the 60's and 70's (Weinell and Rasmussen, 2007). The mechanisms of corrosion protection in the Zn-rich epoxy primers include a galvanic effect due to metallic zinc dissolution, as well as a barrier effect resulting not only from the epoxy resin but also via the formation of Zn and Fe products (Deflorian et al., 2005; Weinell and Rasmussen, 2007). However, a balance must be considered in the formulation in order to assure cathodic protection for an extended time. A load of 90 wt.% of Zn particles may be beneficial for the charge transfer process (Park and Shon, 2015). However, that amount can reduce substrate adhesion and cause problems with the spraying application related to the high viscosity and poor dispersion of zinc particles (Park and Shon, 2015). Hence, research has sought to decrease the percentage of Zn load while retaining the connection among the particles and maintaining or increasing mechanical coating properties (Weinell and Rasmussen, 2007; Jeon et al., 2013; Park and Shon, 2015).

Weinell and Rasmussen (Weinell and Rasmussen, 2007) noted that different pigments, such as thixotropic agents, can be added to the epoxy matrix of coatings to prevent zinc precipitation. The authors incorporated colored pigments to differentiate between steel substrate and the grayish Zn primer, adding oil-absorbing pigments to decrease the Zn load while maintaining the same level of cathodic protection. Park and Shon suggested the addition of multi-walled carbon nanotubes (MWCNTs) to a maximum load of 0.6 wt.%, which resulted in improved conductivity, adhesion strength, and corrosion protectiveness as the MWCNTs increased from 0 to 0.25 wt.% (Park and Shon, 2015). Similarly, the addition of MWCNTs in an epoxy coating provided greater adhesion strength, transport behavior, and hydrophobicity as the MWCNT concentration increased from 0 to 0.5 wt.% (Jeon et al., 2013).

The microbiological environment and underlying mechanisms have not been extensively explored in coating studies of Zn-rich epoxy primers. A few studies have evaluated Zn-rich epoxy primers in media containing sulfate reducing bacteria (Liu et al., 2007; Wang et al., 2012), but to the best of our knowledge no studies have investigated Zn-rich primers with MWCNTs added to their matrix in an environment including a sulfate reducing consortium.

This work aims to determine the electrochemical behavior of a Zn-rich primer with MWCNTs additions in an electrolyte containing an SRM consortium. Electrochemical techniques were used to elucidate the interfacial mechanisms. We used electrochemical impedance spectroscopy as a primer technique

TABLE 1 | Specifications of the different coating systems.

Coating	Zinc (wt.%)	(CNTs) (~wt.%)
ZnR	70	0
Zn-1CNT	70	1.0
Zn-2CNT	70	2.0

to characterize the mechanisms presented at different interfaces formed in the system, and the results were analyzed using electrical analog element coupled with high-resolution surface techniques. Different CNTs compositions were used to support the influence of the mechanism's dominance based on the corrosion control method.

MATERIALS AND METHODS

Microbial Culture

The consortium of sulfate reducing bacteria (sulfate reducing microorganisms) used in this study was collected with an in-line inspection tool used for internal inspection in pipelines (the so-called smart 'PIGS'). The sample consortium was inoculated in ATCC1250 modified Baar's medium for Sulfate Reducers with NaCl (2.5 wt.%) [ATTC®]. The pH value was adjusted to 7.2 under de-aeration by applying nitrogen to the electrolyte. The medium was autoclaved at 120°C for 15 min. The SRM consortium was incubated at 37°C.

Multifunctional Coatings

The Zn-rich epoxy primers and multi-walled carbon nanotubes were supplied by Tesla NanoCoatings company. The epoxy resin (Tesla P1150ASAS) was mixed with CNTs at 1 and 2 wt.%. After the CNTs were completely dispersed in the epoxy resin through mechanical stirring according to a previously method (Cubides and Castaneda, 2016), Zn particles at 70 wt.% were slowly added while stirring the solution, and a hardener (Tesla P1150BSAS) was then poured in to a final weight ratio of 2:1 (epoxy resin-hardener). The 70 wt. % was used based on the previous work (Cubides and Castaneda, 2016) where is was demonstrated the Zn content was the most balanced for cathodic protection or sacrificial conditions. In addition, Zn-rich epoxy primer without CNTs was also used in this study. The coatings were air-sprayed onto UNS1008 steel plates. This procedure was performed previously (Cubides and Castaneda, 2016). **Table 1** shows the different sample characteristics.

Electrochemical Characterization

A three-electrode electrochemical cell was used for the experimental characterization. The electrochemical cells were autoclaved. The working electrode was the multifunctional coating sample. The counter electrode was a platinum mesh, and the reference electrode was a saturated calomel electrode (SCE). The working electrodes and the reference and auxiliary electrode were sterilized with 70% ethanol and acetone and set under UV light and laminar flow. They were placed on a 25 mL electrochemical cell containing culture medium under N₂ gas injection before each experiment. It was conducted

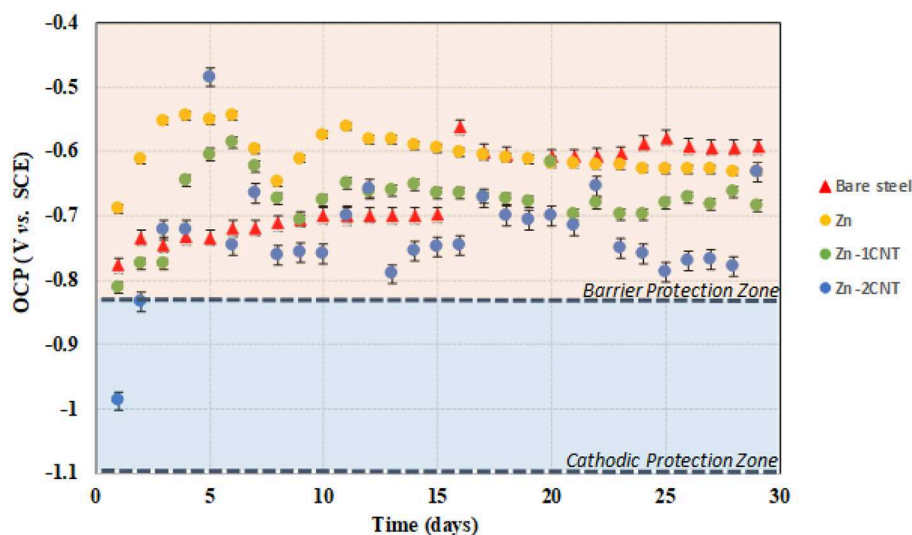


FIGURE 1 | OCP for bare steel and the three different multifunctional coatings under bioelectrolyte conditions.

at 25°C. OCP was performed on prior EIS measurements during a period of 10 min. EIS was performed in a frequency range of 100 KHz to 10 mHz with a ± 10 mV peak-to-peak amplitude vs. the open circuit potential (OCP). All the tests were carried out in a potentiostat/galvanostat (VSP-300; Bio-Logic Science Instruments), using the software EC-Lab[®] V.10.32. All electrochemical experiments were performed in duplicate to ensure reproducibility of the electrochemical behavior.

SEM Sample Preparation

Once the electrochemical test was completed, the samples were rinsed with PBS 1X (8.0 g of NaCl, 0.2 g of KCl, 1.4 g of $\text{Na}_2\text{HPO}_4 \cdot 2\text{H}_2\text{O}$, and 0.2 g of KH_2PO_4 per liter, pH = 7.2). Subsequently, the samples were fixed with glutaraldehyde 2.5% w/v in PBS for 2 h, with washing every 30 min. All fixation was conducted at room temperature. After fixation, the cells were washed twice in PBS and then re-suspended in sterilized ultrapure water to avoid salt crystallization during the drying process. The samples were dried for 24 h in a LABCONO Freezone 6 lyophilizer. Finally, the samples were sputtered with silver particles and observed under a JSM-7000F/JOEL microscope through energy-dispersive spectroscopy (EDS).

RESULTS AND DISCUSSION

Open Circuit Potential

The ZnR coating system shows the potential evolution influenced by different conditions and interfacial configurations such as the epoxy physical barrier, the galvanic phenomenon between zinc and steel, the physicochemical barrier of corrosion products, the concentration of Fe and Zn near the particle/coating or substrate/coating interfaces and inside the coating, amongst other factors, as described by Cubides (Cubides and Castaneda, 2016). The cathodic protection of steel has been established at ≤ -0.90 V vs. Cu/CuSO₄ (-0.826 vs. SCE) under anaerobic

conditions (Schwerdtfeger, 1958; Guan et al., 2016; Liu and Cheng, 2017). This level is drawn as a dash line in **Figure 1**. At higher (more positive) potentials, barrier protection tends to be the dominant control mechanism, which may be associated with the epoxy-polymer and the corrosion products of Zn and/or Fe. The OCP monitoring of the AISI/SAE 1008 steel substrate and the multifunctional coatings under biotic conditions is shown in **Figure 1**. The OCP for the bare steel is more positive (passive region or protective layer region based on thermodynamics) than the cathodic potential criteria because the galvanic effect results in a negative potential value, in which the steel faces immune thermodynamic conditions. The OCP for the bare steel 1008 was determined in a test where the sample was kept in the culture medium in bacterial consortium conditions, and the steel potential was found to be influenced by the biofilm and corrosion products formed at the surface of the substrate. Classic work by Castaneda (Castaneda and Benetton, 2008) characterized mild steel in seawater in the presence of SRB, which resulted in positive potentials due to the combination of corrosion products and biofilm. **Figure 1** shows the initiation and growth stages for the biofilm formation. At this respect, Castaneda marked 14 days for the initiation to biofilm growth transition, similar to this condition, where the OCP increases the magnitude following 2 weeks of exposure.

The Zn-rich primer (70 wt.% Zn) exposed to the bacteria consortium shows a potential oscillating within the barrier protection zone over the exposure time. This means that the Zn particles are randomly distributed in the epoxy matrix with a connectivity between them that is insufficient to trigger the galvanic effect formation. There is a transient state during the first 10 days of exposure, and during this time, the potential values are in the barrier zone. This behavior is associated with water uptake in the coating and the formation of Zn products during the initial days of exposure. Finally, the potential is around the OCP of 1008 carbon steel in biotic conditions, but both experimental

results are above the corrosion protection located in the barrier protection zone, and barrier zone dominance can result from the Zn-Fe corrosion products and/or biofilm formation to produce a blocking effect for the water uptake process.

At the early stage, the Zn-1CNT potential is located close to the cathodic protection zone for the first day. Following the negative potentials, a transient stage occurs during the next 10 days within the barrier protection area. The initial conditions could be the response of the bioelectrolyte wetting over the Zn particles and due to the interconnectivity among Zn particles and steel arising from the influence of MWCNTs or the cathodic protection effect; the potential between 4 and 10 days may be the result of Zn and/or Fe corrosion products acting as a barrier or passive particle state, which switches the system to prevail in more positive potentials. These latter compounds fill the porous surfaces within the coating structure, and the potential subsequently increases at day 2. The interaction between consortium/coating subsequently changes the quantity and morphology of the products, and the potential decreases at day 10. Eventually, the potentials reach $\sim -0.680\text{V}$ vs. SCE in the barrier zone, 100 mV more negative than the ZnR sample. Subsequently, the potential remains stable at close to -0.680V vs. SCE. This latter effect could be due to the influence of the biofilm at the surface, in which the zinc ions inhibit the formation of the biofilm layer at initial conditions (Babich and Stotzky, 1978; Bong et al., 2010; Billanger et al., 2015; Tong et al., 2015), but the ions are depleted and the biofilm starts to grow over time to become more homogeneous and distributed compared with the 2CNT, and the magnitude of the potential becomes more negative than the ZnR sample to produce a less dominant barrier effect with the addition of 1CNT.

OCP for the Zn-2CNT sample are more negative than the threshold for the cathodic protection magnitude during the first 2 days. This behavior is associated with a greater MWCNTs concentration, resulting in better interconnection between the Zn/Zn electrical connection particles due to the CNT/Zn/CNT interconnectivity. This latter finding is confirmed in the cross-section SEM images. These potentials are more negative than the Zn-1CNT results. A transient potential state exists between days 3 and 10 of exposure. After 10 days, there are two transient states during the barrier protection zone and close to the cathodic protection threshold, one between 10 and 15 days and the other between 16 and 24 days. Finally, the potential keeps fluctuating in the barrier protection zone and reaches lower values than the OCP of carbon steel in biotic conditions. The potentials reveal the dominance of cathodic protection for this sample in different stages. Particle activation was promoted by the distribution of CNTs within the coating, and the products formed in the coating are not sufficiently compact to stop bioelectrolyte uptake within the coating, with the unstable biofilm leading to lower potential magnitudes. This may result from greater electrochemical activity among particle/coating interface. This latter result is evidence of a certain grade of galvanic effect, i.e., the system is at a lower potential than the value found for steel without coating due to reaction with the Zn particles. The presence of two increments may be due to the creation of products that fill the pores in the coating, with the decrease resulting from the particle layer and

an interaction forming with an incipient heterogeneous biofilm. That is, zinc ion formation inhibits biofilm growth and leads to various areas of biofilm depletion, thus affecting the morphology of these compounds over time and altering the distribution of the biofilm at the surface of the coating.

Qualitative Analysis of Impedance

Figure 2 shows the complex and phase angle diagrams for Bare steel and Zinc Rich Epoxy multifunctional coatings in SRM consortium environment.

The Nyquist representation for the AISI 1008 bare steel sample exposed to the biotic electrolyte is shown in **Figure 2A**. The results show a loop with a large diameter characteristic of a capacitance and charge transfer process. The phase angle representation is illustrated in **Figure 2B**. The medium frequency response is associated with capacitance (double layer) at the surface, whereas the response at low frequency is associated with the electrochemical reactions at the steel/electrolyte interface. On day 5, this system represents biofilm formation, and the corrosion products form an inorganic and organic mixing layer. At low frequencies, the magnitude of the semicircle's diameter is associated with the substrate/mixing layer/electrolyte interface. The magnitude for the biotic conditions results in a loop intercepting the locus point on the order of $12,000\ \Omega\ \text{cm}^2$, whereas at 10 days, an increase in the loop diameter occurs, which may be associated with the accumulation of a mixing layer formed at the surface. At the surface, the number of active sites decreases, and the R_{ct} increases, as previously described by Castaneda and Benetton (2008), with mild steel exposed to an SRM electrolyte during the first 2 weeks. At day 15, the impedance magnitudes begin to decrease, reflecting an activation mechanism, and an increase in the number of active sites occurs at the metallic substrate/mixing layer interface. On day 20, the impedance lowers the magnitude for this sample, an effect associated with the active sites, owing to the charge transfer process. After 25 days, the contribution of two potential interfaces is revealed by two maximum points in the phase angle representation. At days 25, and 29, the active sites remain constant, owing to the maintenance of the impedance at low magnitudes and the formation of two separate contributions at the interface layers, owing to the stability and physical presence of a mixing layer on the surface, as a result of precipitation of corrosion products and presumed biofilm formation. This finding corroborates the OCP biofilm transition from initiation to growth stage. The EC representation for this system can be described by **Figures 3A,B**; the first days include an activation capacitance RC analog, and after 25 days, two time constants are represented by two constant phase elements.

Zinc Rich Epoxy

The EIS results for the ZnR sample are shown in **Figures 2C,D**. Two loops are observed: one at medium-high frequency and another at low frequency in the complex representation. In the phase angle representation, two time constants are observed, representing the interfaces due to the presence of a mixed layer (biofilm, epoxy coating) and the zinc particle/coating interface. **Figure 3B** represents the equivalent circuit used for the ZnR

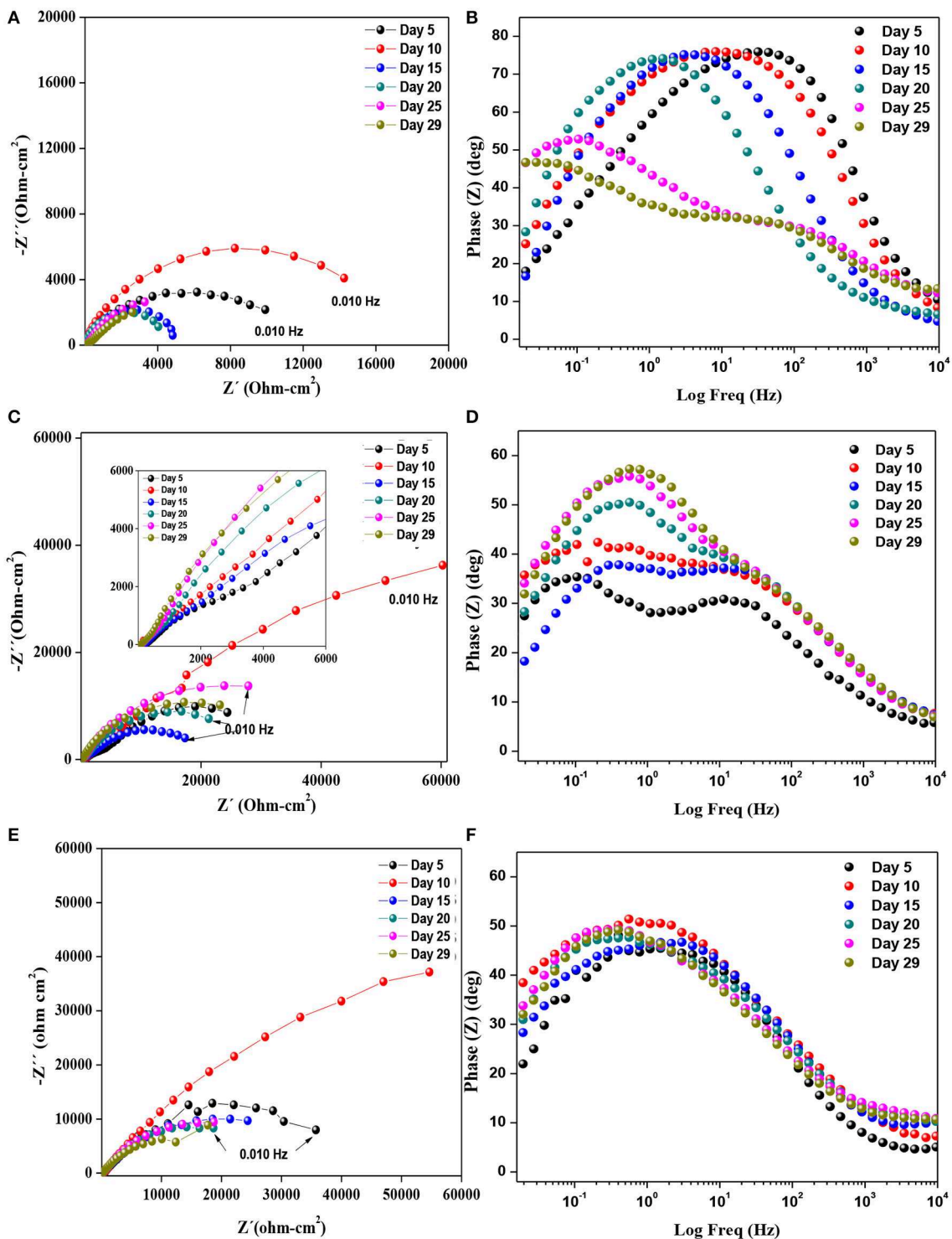


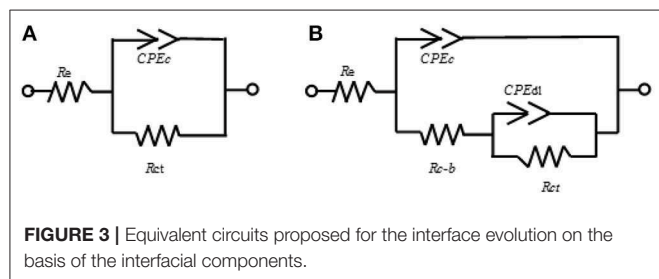
FIGURE 2 | Diagrams of Nyquist and phase angle in the SRM consortium for (A,B) 1008 bare steel, (C,D) for ZnR coating, and (E,F) for Zn-1CNT coating.

epoxy/steel interface in the early stage. Part of this circuit has been proposed by Cubides to represent the ZnR on a metallic substrate system when the zinc particles are active after being

exposed to an electrolyte, where R_s is the electrolyte resistance, R_p is the porous layer resistance formed by the coating, CPE_1 is the constant element for medium frequencies, R_{ct} is the

charge transfer resistance due to the active particle/coating interface, CPE_2 is the constant phase element associated with the double layer capacitance, and n is the roughness factor (Cubides and Castaneda, 2016). In general, all the impedances are higher than those of the bare steel samples, as can be seen in **Table 2**. This is due to conductivity of the Zn-rich epoxy influenced by the polymer coating matrix. In addition, the impedance signal is influenced by several factors such as electrolyte uptake within the coating, the galvanic effect of the Zn particles, the relation between Fe/Zn areas exposed to electrolyte, product formation, and biofilm formation (Abreu et al., 1999; Galicia et al., 2017). The R_{ct} impedances in this case are within an order of magnitude at around 50,000–100,000 $\Omega\cdot\text{cm}^2$ as illustrated in **Table 2**. This is in concordance with the OCP results in which the behavior of the systems is maintained at a specific potential zone. The semicircle acquired at the higher-medium frequency is associated with presumable coating-biofilm mixed layer, and the semicircle recorded at low frequency is the response of Zn/Epoxy interfacial reactions. The equivalent circuits describing the early stage of the system are illustrated in **Figure 3B**. The EC shows two time constant phase elements in parallel with two resistances representing early and continued evolution for 20 days. The time constants associated with the medium and low frequencies are consistent with the evolution of each element in the system. During the initial days, the electrolyte uptakes the coating and wetting of Zn particles, even though the galvanic effect prevailing at the particle/coating interface the overall OCP shows positive magnitudes away from the cathodic protection potential for anaerobic conditions, this latter can be attributed to the poor particles interconnection within the epoxy, resulting in a small area for the electrochemical reaction. The zinc particles react to produce ionic species and corrosion products; the zinc ionic species preserve the surface of the coating with no biofilm formation, likely due to a cytotoxic

mechanism against microorganisms (Babich and Stotzky, 1978; Billanger et al., 2015; Tong et al., 2015). Two time constants are maintained for the phase angle representation while the R_p and R_{ct} impedance in the complex representation increases up to 20 days. The wetting of the zinc particles following the charge transfer reactions no longer predominates, owing to the formation of corrosion products such as ZnO and $\text{Zn}(\text{OH})_2$ at the zinc particle/coating interface, as reported previously (Cubides and Castaneda, 2016). The production of extracellular polymeric substances (EPSs) apparently begins to influence the high impedance values revealed at high-medium frequencies. Subsequently, a mature biofilm forms a heterogeneous layer as illustrated in **Figure 4a** obtained by scanning electronic microscopy, SEM. After 20 days, the complex signature reaches a higher impedance magnitude, resulting in the capacitance EIS signature representation. This latter result is consistent with the phase angle representation with the formation of only one time constant at medium-low frequencies. The final layer is a mixture of EPS/biofilm, corrosion products, and precipitates, which allows the capture of the influence of this layer in the frequency interval range. The phase angle identifies one time constant in the system with a magnitude of 60 degrees, closer to the ideal capacitor effect of 90 degrees. This latter is attributed to a semi compact (heterogeneous) layer formed by mixture of organic epoxy, organic EPS/biofilm and corrosion products. The sample was evaluated at 29 days of bioelectrolyte exposure conditions. The Zn-rich epoxy illustrated in **Figure 4a** shows that the morphology is modified after exposure and demonstrates the underlying mechanisms; the sample shows the presence of a heterogeneous Extracellular Polymeric substances on the electrode as a biofilm. The balance between the Zn presence and the biofilm formation produce a biolayer of 12.5 μm in thickness.



Zinc Rich Epoxy With 1CNT

The Nyquist diagram of the Zn-1CNT is displayed in **Figure 2E** for the complex representation and **Figure 2F** for the phase angle. There is one loop with a finite locus point in the real axis, owing to the capacitance behavior and charge transfer reaction step control process at the zinc/coating interface. At day 5, the R_{ct} impedance magnitudes in the EIS signature are similar in magnitude to those of the ZnR epoxy samples (see **Tables 2** and **3**, respectively). The electrical interconnection between Zn particles is increased with the addition of CNTs, which in turn favors the formation of products within the coating through favoring the charge transfer reaction at the Zn/coating interface, and the level

TABLE 2 | Fitting parameters from an equivalent circuit simulation for AISI 1008 bare steel.

Circuit element → Time (day) ↓	R_e ($\Omega\cdot\text{cm}^2$)	CPE_1 (F cm^{-2})	α	R_{c-b} ($\Omega\cdot\text{cm}^2$)	CPE_2 (F cm^{-2})	R_{ct} ($\Omega\cdot\text{cm}^2$)
5	4.7	1.5E-04	0.8	-	-	11,987
10	5.0	1.7E-04	0.8	-	-	15,090
15	5.7	4.2E-04	0.8	-	-	5,254
20	7.1	8.6E-04	0.8	-	-	5,137
25	9	7.1E-04	0.5	315	4.1E-04	16,554
29	22	1.7E-05	0.5	977	8.7E-04	12,352

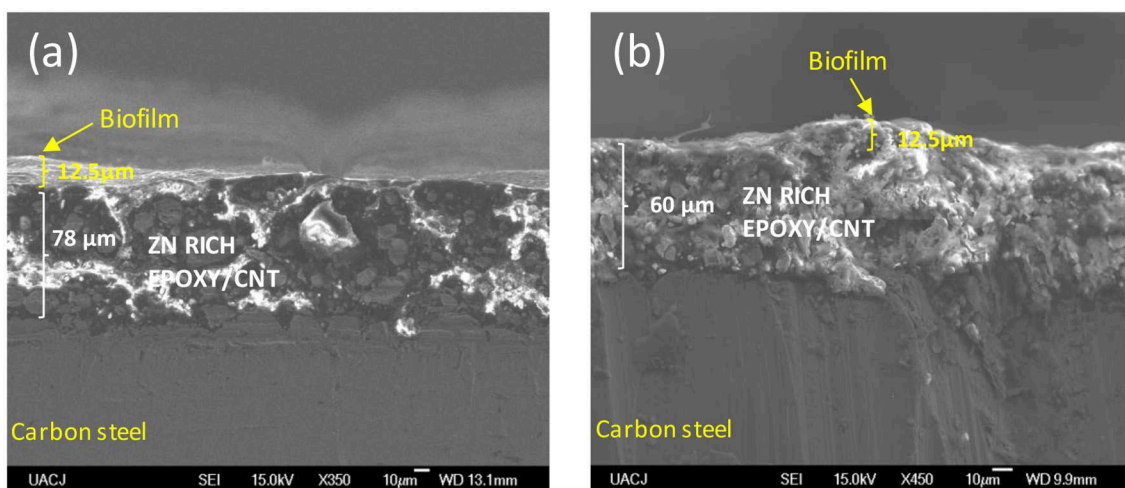


FIGURE 4 | Cross-section SEM images of the coatings immersed in an electrolyte with the SRM consortium. **(a)** Zn rich-primer, **(b)** Zn-rich primer with 1 wt.% CNTs.

TABLE 3 | Fitting parameters from an equivalent circuit simulation for multifunctional coatings.

Circuit element → Time (day) ↓	R_e ($\Omega \cdot \text{cm}^2$)	CPE_1 (F cm^{-2})	α	R_{c-b} ($\Omega \cdot \text{cm}^2$)	CPE_2 (F cm^{-2})	R_{ct} ($\Omega \cdot \text{cm}^2$)
ZnR						
5	502	8.5E-07	0.5	21204	5.7E-07	39,143
10	400	4.6E-07	0.5	175716	6.8E-07	53,761
15	205	9.8E-07	0.5	23631	1.3E-06	1,203
20	171	1.2E-04	0.6	29509	5.8E-07	5,654
25	138	1.1E-04	0.7	-	-	29,245
29	85	2.1E-04	0.7	-	-	26,936
Zn-1CNT						
5	400	8.9E-07	0.6	-	-	39,001
10	426	5.4 E-07	0.6	-	-	50,038
15	183	1.0E-02	0.6	-	-	37,817
20	139	1.4 E-02	0.6	-	-	33,855
25	132	1.6 E-02	0.6	-	-	39,595
29	109	2.2 E-02	0.6	-	-	39,516
Zn-2CNT						
5	290	5.0E-07	0.6	-	-	77,908
10	157	1.0E-05	0.6	-	-	35,247
15	125	6.7E-05	0.6	-	-	43,741
20	123	7.2E-05	0.6	-	-	42,736
25	138	9.2E-05	0.6	-	-	43,580
29	49	3.1E-04	0.6	-	-	13,532

of protection subsequently improves, as corroborated by the OCP in early stages. The presence of the CNTs promoted zinc particle area/substrate or particle/particle interactions; initially, charge transfer process kinetics are favored due to the area available for galvanic reactions. The initial presence and distribution of extracellular polymeric substances was influenced by Zn leaching and precipitation within the coating as well as precipitation at the surface of the corrosion products. EPS formation and subsequent biofilm stability was influenced by the amount of reacted zinc at the particle/coating interface. Following system

evolution, changes in the corrosion products and growth of the biofilm shifted the charge transfer magnitude. Competition between formation of the biofilm on the surface and the corrosion products within the coating is balanced by the formation of zinc ions and influenced by the amount of CNTs. The SEM image in **Figure 4b** shows a smaller biofilm thickness on the coating surface after 29 days of exposure when the concentration of CNTs stayed at 1CNT. The impedance gain could mark a transition moment of the system, which does not follow the EIS application principle of stability (Bosch et al., 2001) because the

OCP for the sample decreased significantly at 10 days. However, the subsequent exposure times at 15, 20, and 25 days exhibit an increase in charge transfer resistance (see **Table 3**), or R_{ct} , which agrees with the OCP results. The 1CNT concentration influences the EPS, biofilm formation and mix layer, by dissolution or inhibition mediated by the Zn ions and the kinetics of the corrosion products formed at the Zn particle interface. This latter result is due to the decrease in Zn ionic formation caused by surface de-activation of particles and their depletion resulting from their usage in the formation of corrosion products, with the decrease also due to biofilm inhibition (Babich and Stotzky, 1978; Bong et al., 2010). The presence of one time constant in the phase angle representation for Zn-1CNT reflects the influence of capacitive behavior resulting from a mixture of the organic coating, inorganic corrosion products and biofilm. This indicates that a mix layer was formed on top of the coating, as evidenced by the impedance signature of **Figure 2F** and SEM image of **Figure 4b**. The morphology of the biofilm is very different from that of with zinc-rich sample. The Zn products were obtained with a higher density, the corrosion products expanded the ZnR coating in some locations, and the biofilm was no continuous compared with ZnR. For Zn-1CNT, the phase angle shows one-time constant appearance at early stage. The early stage at OCP correlates interconnectivity of the CNTs, with active zinc particles reacting faster compared to without the CNTs.

Zinc Rich Epoxy With 2 CNT

The impedance signature of the Zn-2CNT sample is exhibited in **Figures 5A,B**. There is one loop for the complex representation and one time constant for the phase angle signature. The electrical connection among the Zn particles is evident in the OCP results, and this is associated with a Zn area that is much greater than the Fe iron exposed to the electrolyte, which is due to the increased CNTs content. The EIS signature corroborates the formation/initiation of EPS and the biofilm as well as the charge transfer dominance due to Zn particle activation, resulting in corrosion products within the coating. The formation of corrosion products at the particle/coating interface should be favored due to the higher electronic interconnectivity. However, the biofilm does not form homogeneously due to the presence of Zn products formed from bulk zinc ion generation from the coating and their transport to the coating surface. The substantial CNT content surpasses the ionic Zn content that inhibits biofilm formation. After 10 days, the impedance magnitude decreases, owing to the activation of Zn particles. At day 29, the system evolves to the lowest charge transfer resistance, R_{ct} magnitude. The CNT increases the Zn particle kinetics and avoids continuous formation of a mixed layer that does not appear at this concentration.

The impedance analysis gave insight into the competition among anodic dissolution of zinc particles, EPS/biofilm formation, and the formation of zinc-rich corrosion products. Phase angle representation shows one time constant. The signature is characteristic of capacitive process and controlled by charge transfer resistance. The time constant at medium frequencies may represent the influence of a capacitance of

a unified (mixed) layer forming at the surface, and the low frequency characterizes the particle/coating interface. With time, anodic dissolution of Zn and the formation of Zn corrosion products become less prevalent, and thus do not provide sufficient protection to the metal substrate. From the Nyquist plot, the impedance of the ZnR coating increased with time. Great influence in resistance is attributed to the EPS/biofilm formation noted above in combination with inorganic semiconductor ZnO and $Zn(OH)_2$ corrosion products following Zn dissolution, which provides added barrier. EIS analysis agrees with the OCP measurement findings in that the addition of CNTs to the polymeric matrix structure improves the electrical connectivity between zinc particles and the metallic steel substrate through electron transport. In early stages, both the Zn-1CNT and Zn-2CNT coated samples showed potential below the CP threshold potential. SEM images after 28 days of immersion in **Figure 7**, suggest that the biofilm forms at the early days of immersion and subsequently grows/inhibits based on the Zn content generated by the more efficient galvanic system. The limited presence of an exopolysaccharide matrix, along with the limited population of bacteria and other organisms, accounts for the possibility that biofilm limited formation at the surface occurred, in part due to the presence of carbon nanotubes for Zn-1CNT and Zn-2CNT.

The SEM image of a Zn-2CNT sample in **Figure 6** shows several regions with biolayer removal and some residual Zn particles in the epoxy. This Zn-2CNT sample has the thinnest randomly distributed biofilm formed at the top of the coating surface. This latter result, could be attributed to the dissolution of zinc particles, which form $ZnCl_2$ or ZnO that presumably inhibit initial biofilm formation by poisoning certain cellular elements present in microorganisms (Tong et al., 2015). Many investigations have demonstrated that zinc cations, zinc oxides and zinc chlorides are cytotoxic by disturbing gene regulation processes associated with the production of extracellular polymeric substances (EPSs) (Babich and Stotzky, 1978; Billanger et al., 2015; Tong et al., 2015). The above factors prevent construction of the matrix component of the biofilm. OCP and EIS results were able to demonstrate initiation of the biofilm or mixed layer formation due to the transient state revealed by both techniques over time. The shifts in OCP, magnitude and impedance elements associated with the system interfaces accompanied trends including formation of the biofilm is a clear indicator of the influence by the CNT in terms of corrosion control mechanism. Zn ions formed following CNT addition, which are then transported into the coating and inhibit biofilm formation in locations with a higher density of Zn particles, the Zn and CNT content can be balance to establish a critical magnitude or Zn/CNT ratio for the efficiency of the ZRE epoxy coatings.

Surface Evolution (Top and Cross Section) Characterization Before and After Bioelectrolyte Exposure

Figure 7 shows the cross-section SEM images obtained for the multifunctional coatings after 29 days of immersion in the

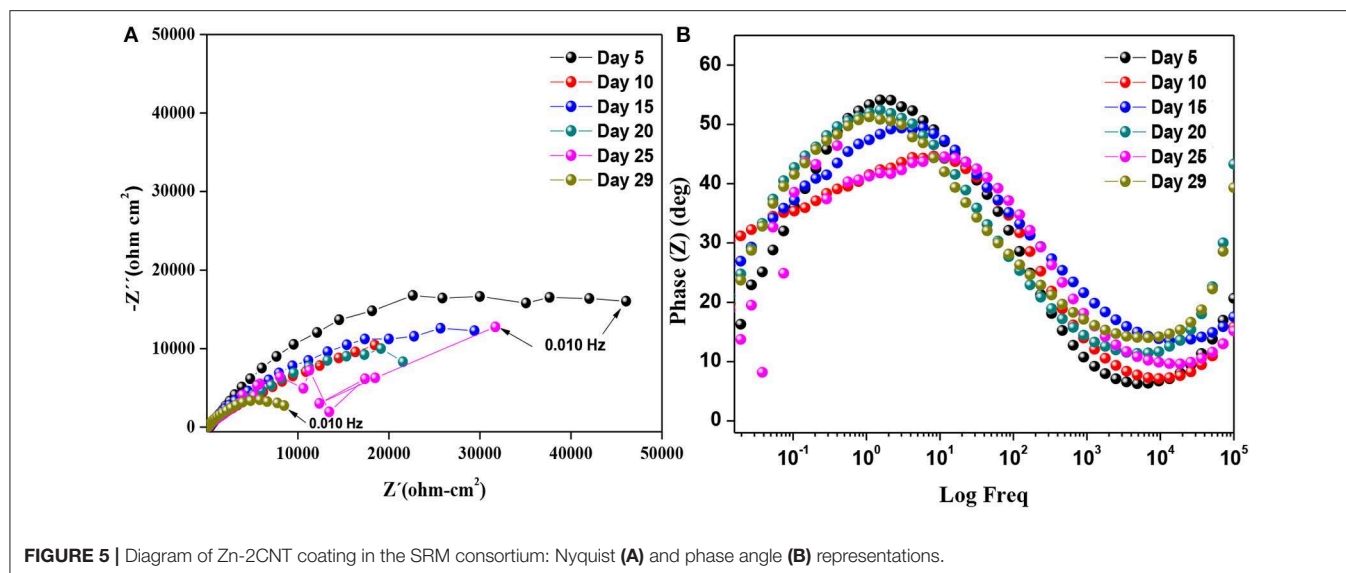


FIGURE 5 | Diagram of Zn-2CNT coating in the SRM consortium: Nyquist (A) and phase angle (B) representations.

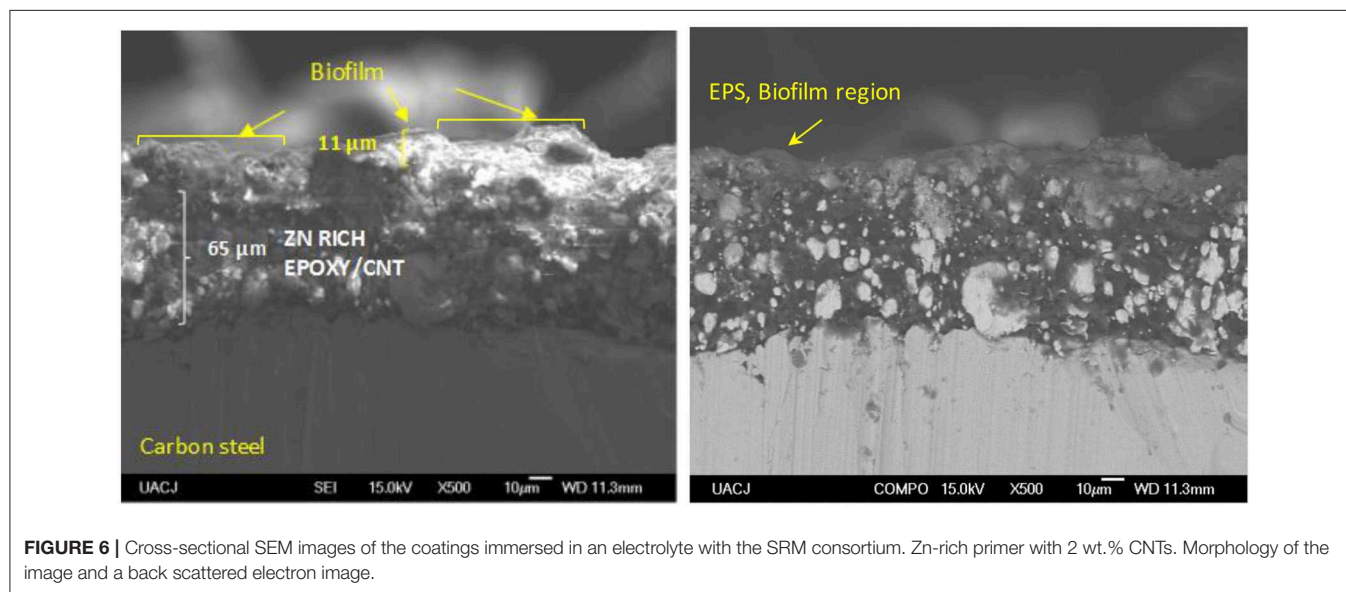


FIGURE 6 | Cross-sectional SEM images of the coatings immersed in an electrolyte with the SRM consortium. Zn-rich primer with 2 wt.% CNTs. Morphology of the image and a back scattered electron image.

SRM bioelectrolyte. These images corroborate the findings from the OCP data and the impedance analysis. For Zn-1CNT and Zn-2CNT coatings, it was possible to detect and demonstrate the presence and interconnectivity of Zn particles with carbon nanotubes at the interface of carbon steel, the coating matrix itself and the EPS/corrosion product layer. The biofilm layer can be considered to provide greater extension for the ZnR coating because, as described above, the CNT content leads to cytotoxicity toward the main bacterial and fungal constituents of the SRM consortium (Upadhyayula and Gadhamshetty, 2010). The increase in CNT content promotes the formation of Zn ions, thus resulting in a cytotoxic environment. The images in Figure 7 reveal biofilm patch formation instead of a continuous layer at the electrode surface. Therefore, the presence of biofilm is not favored when CNTs are present.

The presence of CNTs, as evident in Figure 7, was associated with an excellent influence on conductivity at the inner section of the coating according to the impedance analysis. Lack of uniform layer is ascribable to the dissolution of zinc cations, which are presumably cytotoxic to the microorganisms. In turn, zinc ions could be also responsible for the formation of corrosion products such as ZnO and ZnCl_2 , also the presence of these corrosion products also became evident according to the EDS elemental analysis, this latter illustrated in Figure 8.

Figures 8a–c show top-view SEM images of the three multifunctional coatings after 29 days of immersion in bioelectrolyte. For ZnR in Figure 8a, a continuous layer of extracellular polymeric substances is observed covering the surface, which becomes less evident in the presence of CNT

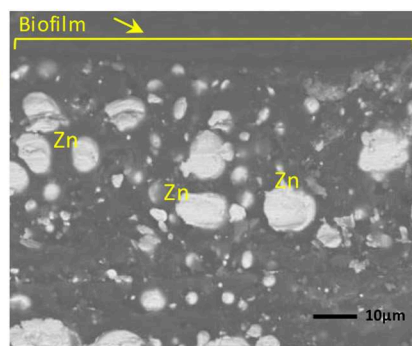
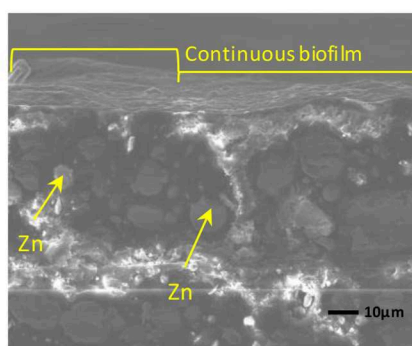
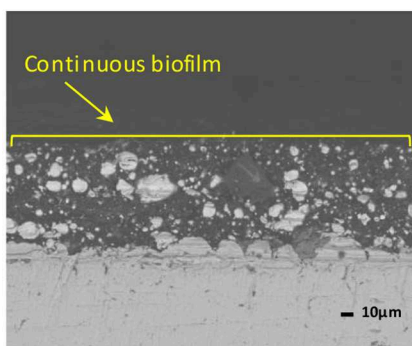
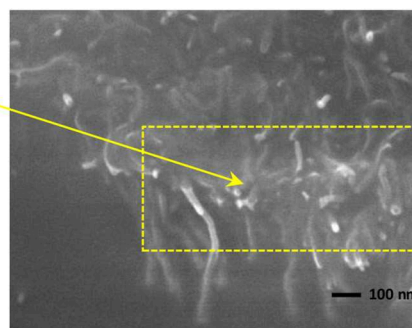
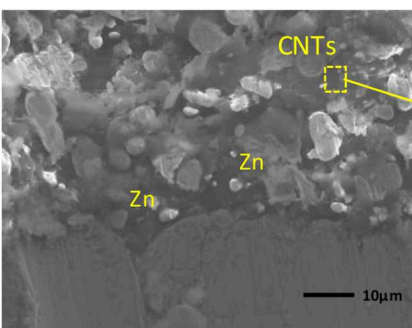
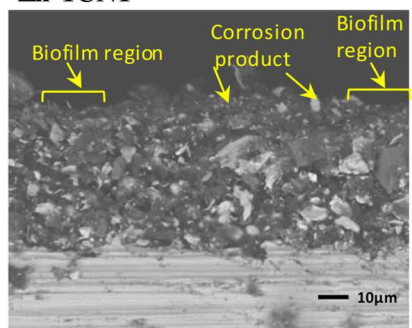
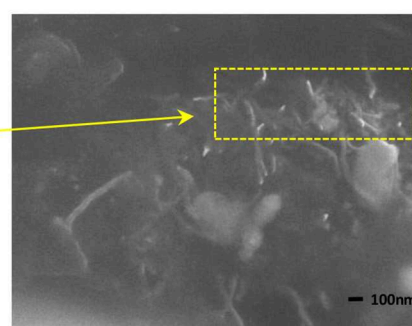
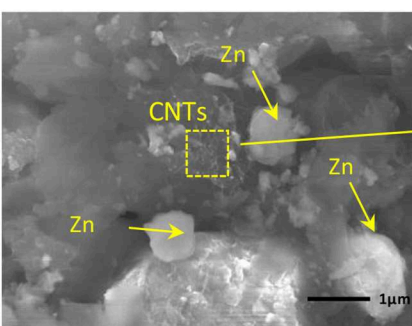
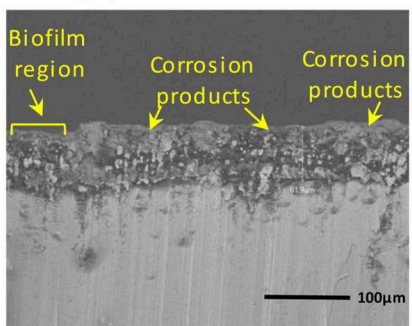
ZnR**Zn-1CNT****Zn-2CNT**

FIGURE 7 | Cross-section SEM images of the multifunctional coatings immersed in an electrolyte solution with the SRM consortium: Zn rich-primer, Zn-rich primer with 1 wt.% CNTs and Zn-rich primer with 2 wt.% CNTs.

particles. **Figure 8b** illustrates the initial formation and lack of persistence of a layer of biofilm that shows some heterogeneous and residual over time. This finding is attributable to the inhibition of mature biofilm formation by the CNTs influence along with a poisoning mechanism by the cytotoxic effect of Zn soluble products (Babich and Stotzky, 1978; Bong et al., 2010). At this respect, CNTs are considered to have adverse effects on biofilm growth at some levels according to the investigations of Upadhyayula and Gadhamshetty (2010). When a double content of CNTs is present, a greater porosity can be appreciated as shown in **Figure 8c**, which is mainly attributed to the lack of continuous biofilm layer caused by an increased level of zinc corrosion products and the double content of

carbon nanotubes that alter the development and formation of a mature biofilm.

Also, **Figures 8a–c** show the EDS analysis demonstrating that the ZnR coating has a higher content of organic compounds, such as carbon, sulfur, nitrogen, and phosphorous (C, S, N, and P) due to presence of a more mature biofilm, which supports the OCP data and impedance results. For the Zn-1CNT and Zn-2CNT coatings, a higher content of Zn and O is evident, and a lower level of organic compounds is found. Higher Zn levels indicate the formation of zinc corrosion products over the coating surface. In addition, the Zn-1CNT and Zn-2CNT coatings exhibit higher Zn and O content, thus further indicating that these coatings inhibit the formation of extracellular polymeric substances

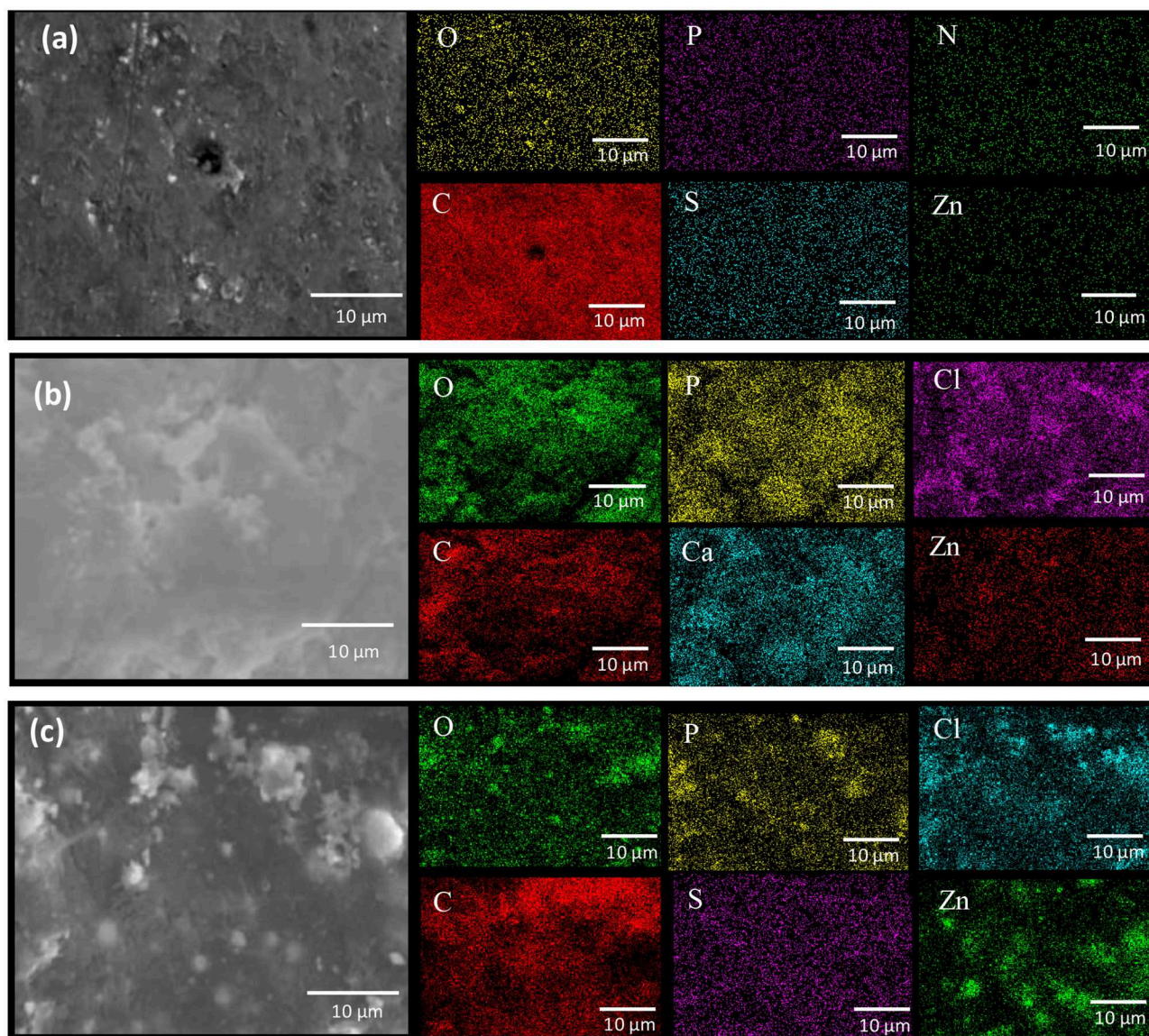


FIGURE 8 | Top views and EDS mapping analysis showing coatings samples after 29 days of exposure to the SRM consortium, **(a)** ZnR, **(b)** Zn-1CNT, and **(c)** Zn-2CNT. ZnR coating has a high content of organic compounds, such as carbon, sulfur, nitrogen and phosphorous (C, S, N, and P) due to biofilm formation.

(Babich and Stotzky, 1978; Bong et al., 2010; Billanger et al., 2015; Tong et al., 2015), and therefore disturb biofilm growth to a greater extent due to the toxicity of the high levels of CNTs (Upadhyayula and Gadhamshetty, 2010).

CONCLUSIONS

This investigation determined that for these multifunctional coatings, the anodic dissolution of zinc particles, the formation of an extra biolayer and the formation of zinc-rich corrosion products represent competing processes. The contribution of an extra layer formed on the coating surface can be attributed to the formation of EPSs and a biofilm by the SRM consortium.

The CNTs content enhances the anodic reactions of the zinc particles in the coatings, promoting cathodic protection and the formation of more corrosion products in the form of solid oxide/hydroxide compounds. However, doubling the CNT content results in more interaction with the zinc particles and impairment of biofilm growth. This represented a qualitative influence of CNTs concentration as evidenced by reduced levels of corrosion products. The ZnR coating exhibits galvanic protection, as evidenced by the formation of corrosion products and secretion of extracellular polymeric substances to produce a more homogeneous biolayer. The Zn-1CNT coating exhibits partial cytotoxicity toward microorganisms, thereby controlling biofilm initiation and growing processes. The Zn-2CNT ratio

represents the saturated concentration of carbon nanotubes leading to less-optimal conditions for biofilm formation. Finally, we considered to be a CNTs content that could be used to balance biofilm formation and zinc anodic dissolution to influence microbiologically induced corrosion mechanisms.

DATA AVAILABILITY STATEMENT

All datasets generated for this study are included in the article/supplementary material.

AUTHOR CONTRIBUTIONS

HC: substantial contributions to the interpretation of data for the work, drafting the work content, final approval of the version to be published, and agreement to be accountable for all aspects of

the work in ensuring that questions related to the accuracy or integrity of any part of the work are appropriately investigated and resolved. MG: substantial contributions to the design and set up conditions of the work and data acquisition (responsible of the laboratory where the work was made), participating in drafting the work and revising it critically for content, final approval of the version to be published, and agreement to be accountable for all aspects of the work.

ACKNOWLEDGMENTS

MG would like to thank Ivan Salcido for assistance with SEM images. Also, the authors would like to thank QBP Graciela García for a culture donation and Violeta Valencia for the electrochemical set up design.

REFERENCES

- Abdolahi, A., Hamzah, E., Ibrahim, Z., and Hashim, S. (2014). Application of environmentally-friendly coatings toward inhibiting the microbially influenced corrosion (MIC) of steel: a review. *Polym. Rev.* 54, 702–745. doi: 10.1080/15583724.2014.946188
- Abreu, C. M., Izquierdo, M., Perino, P., Novoa, X. R., and Pérez, C. (1999). A new approach to the determination of the cathodic protection period in Zinc-rich paints. *Corrosion* 55, 1173–1181. doi: 10.5006/1.3283955
- Babich, H., and Stotzy, G. (1978). Toxicity of Zinc to fungi, bacteria, and coliphages: influence of chloride ions. *Appl. Environ. Microbiol.* 36, 906–914.
- Billanger, X., Billard, P., Schneider, R., Balan, L., and Merlin, C. (2015). Stability and toxicity of ZnO quantumdots: Interplay between, nanoparticles and bacteria. *J. Hazard Mater.* 283, 110–116. doi: 10.1016/j.jhazmat.2014.09.017
- Bong, C. W., Malfatti, F., Azam, F., Obayashi, Y., and Suzuki, S. (2010). *The Effect of Zinc Exposure on the Bacteria Abundance and Proteolytic Activity in Seawater, Interdisciplinary Studies on Environmental Chemistry — Biological Responses to Contaminants* (Tokyo: Terrapub), 57–63.
- Bosch, R. W., Moons, F., Zheng, J. H., and Bogaerts, W. F. (2001). Application of electrochemical impedance spectroscopy for monitoring stress corrosion cracking. *Corrosion* 57, 532–539. doi: 10.5006/1.3290379
- Castaneda, H., and Benetton, X. (2008). SRB-biofilm influence in active corrosion sites formed at the steel-electrolyte interface when exposed to artificial seawater conditions. *Corr. Sci.* 50, 1169–1183. doi: 10.1016/j.corsci.2007.11.032
- Ciubotariu, A., Benea, L., and Sand, W. (2015). “Effects of sulphate reducing bacteria on thermosetting polymer-Zn composite coatings” in *Mircea cel Batran Naval Academy Scientific Bulletin*, Vol. XVIII – 2015 (Constanta: “Mircea cel Batran” Naval Academy Press) (//PROQUEST SciTech Journals, PROQUEST Engineering Journals, Technology Journals, PROQUEST Military Collection PROQUEST Advanced Technologies and Aerospace).
- Cubides, Y., and Castaneda, H. (2016). Corrosion protection mechanisms of carbon nanotube and zinc-rich epoxy primers on carbon steel in simulated concrete pore solutions in the presence of chloride ions. *Corr. Sci.* 109, 145–161. doi: 10.1016/j.corsci.2016.03.023
- Deflorian, F., Rossi, S., Fedrizzi, L., and Bonora, P. L. (2005). EIS study of organic coating on zinc surface pretreated with environmentally friendly products. *Progress in Organic Coatings* 52, 271–279. doi: 10.1016/j.porgcoat.2004.04.005
- Enning, D., and Garrelfs, J. (2014). Corrosion of iron by sulfate-reducing bacteria: new views of an old problem. *Appl. Environ. Microbiol.* 80, 1226–1236. doi: 10.1128/AEM.02848-13
- Fedel, M., Rodríguez Gómez, F. J., Rossi, S., and Deflorian, F. (2019). Characterization of polyorganosilazane-derived hybrid coatings for the corrosion protection of mild steel in chloride solution. *Coatings* 9:680. doi: 10.3390/coatings9100680
- Galicia, M., Valencia, V. G., and Aguirre-Ramírez, M., Castaneda, H. (2017). “Interfacial and Corrosion Characterization of Zinc Rich-Epoxy Primers with Carbon Nanotubes Exposed to Marine Bacteria,” in *CORROSION 2017*. New Orleans, LA: NACE International.
- Guan, F., Zhai, X., Duan, J., and Zhang, M., Hou, B. (2016). Influence of sulfate-reducing bacteria on the corrosion behavior of high strength steel EQ70 under cathodic polarization. *PLoS ONE* 11:e0162315. doi: 10.1371/journal.pone.0162315
- Jeon, H., Park, J., and Shon, M. (2013). Corrosion protection by epoxy coating containing multi-walled carbon nanotubes. *J. Indus. Eng. Chem.* 19, 849–853. doi: 10.1016/j.jiec.2012.10.030
- Liu, D., Fe Lin, Q., Hui Li, C., and Li Xue, L. (2007). Improvement of MIC behavior of low alloy steel with Zn-rich epoxy coating. *Key Eng. Mater.* 348–349, 509–512. doi: 10.4028/www.scientific.net/KEM.348-349.509
- Liu, T., and Cheng, Y. F. (2017). The influence of cathodic protection potential on the biofilm formation and corrosion behaviour of an X70 steel pipeline in sulfate reducing bacteria media. *J. Alloys Compounds* 729, 180–188. doi: 10.1016/j.jallcom.2017.09.181
- Park, S. M., and Shon, M. Y. (2015). Effects of multi-walled carbon nanotubes on corrosion protection of zinc rich epoxy resin coating. *J. Indus. Eng. Chem.* 21, 1258–1264. doi: 10.1016/j.jiec.2014.05.042
- Schwerdtfeger, W. J. (1958). Current and potential relation for the cathodic protection of steel in salt water. *J. Res. Natl. Bureau Stand.* 60, 153–159. doi: 10.6028/jres.060.019
- Tong, T., Wilke, C. M., Wu, J., Binh, C. T., Kelly, J. J., and Gaillard, J. F. (2015). Combined toxicity of Nano-ZnO and Nano-TiO₂: from single- to multinanomaterial systems. *Environ. Sci. Technol.* 49, 8113–8123. doi: 10.1021/acs.est.5b02148
- Upadhyayula, V., and Gadhamshetty, V. (2010). Appreciating the role of carbon nanotube composites in preventing biofouling and promoting biofilms on material surfaces in environmental engineering: a review. *Biotechnol. Adv.* 28, 802–816. doi: 10.1016/j.biotechadv.2010.06.006
- Wang, J., Li, Q. F., Fu, Y. D., and Li, C. H. (2012). MIC behdltfavior of the low alloy steel with different Zn-epoxy coating in SRB solution. *Key. Eng. Mater.* 488–489, 262–265. doi: 10.4028/www.scientific.net/KEM.488-489.262
- Weinell, C. E., and Rasmussen, S. N. (2007). *Advancement in Zinc Rich Epoxy Primers for Corrosion Protection*, in *CORROSION 2007*. Nashville, TN: NACE International.

Conflict of Interest: The authors declare that the research was conducted in the absence of any commercial or financial relationships that could be construed as a potential conflict of interest.

Copyright © 2019 Castaneda and Galicia. This is an open-access article distributed under the terms of the Creative Commons Attribution License (CC BY). The use, distribution or reproduction in other forums is permitted, provided the original author(s) and the copyright owner(s) are credited and that the original publication in this journal is cited, in accordance with accepted academic practice. No use, distribution or reproduction is permitted which does not comply with these terms.



Epoxy Self-Healing Coating by Encapsulated Epoxy Ester Resin in Poly (Urea-Formaldehyde-Melamine) Microcapsules

Fernando Cotting^{1*}, André Koebsch² and Idalina Vieira Aoki³

¹ Corrosion and Surface Engineering Laboratory, Chemical Engineering Department, Federal University of Minas Gerais, Belo Horizonte, Brazil, ² Petrobras-Cenpes, Rio de Janeiro, Brazil, ³ Polytechnic School of the University of São Paulo, São Paulo, Brazil

OPEN ACCESS

Edited by:

Flavio Defforian,
University of Trento, Italy

Reviewed by:

Ioannis A. Kartsonakis,
National Technical University of
Athens, Greece

Mario G. S. Ferreira,
University of Aveiro, Portugal

*Correspondence:

Fernando Cotting
fernando@deq.ufmg.br

Specialty section:

This article was submitted to
Environmental Materials,
a section of the journal
Frontiers in Materials

Received: 17 March 2019

Accepted: 20 November 2019

Published: 05 December 2019

Citation:

Cotting F, Koebsch A and Aoki IV
(2019) Epoxy Self-Healing Coating by
Encapsulated Epoxy Ester Resin in
Poly (Urea-Formaldehyde-Melamine)
Microcapsules. *Front. Mater.* 6:314.
doi: 10.3389/fmats.2019.00314

In this work, poly (urea-formaldehyde-melamine) (PUFM) microcapsules containing a commercial epoxy ester resin were synthesized by *in-situ* polymerization technique. The microcapsules size distribution was analyzed by laser diffraction, and the obtained microcapsules were evaluated by the Fourier-transform infrared spectroscopy (FTIR-ATR) to prove the ester epoxy resin microencapsulation. The filled microcapsules were incorporated into an epoxy three-layer coating system, varying the microcapsules concentration (10 and 15%) and the microcapsules incorporation on the different layers—first, second, or both. The coatings electrochemical behavior was evaluated by electrochemical impedance spectroscopy (EIS) technique and localized scanning vibrating electrode technique (SVET). Pull-off adhesion tests were performed in the coatings systems, to verify if the microcapsules presence affect the adhesion and/or cohesion coating properties. The EIS results showed that microcapsules change the coating electrochemical response, but the samples visual aspect suggests that the microcapsules improve the barrier properties of the microcapsules systems. The coating system containing the microcapsules showed a significant self-healing effect when stressed by a mechanical defect and the higher concentration (15 wt. %) of microcapsules provided a better self-healing protection, with better anticorrosive performance. Additionally, the microcapsules did not disturb the adhesion/cohesion properties of the coating system.

Keywords: self-healing, epoxy ester resin, polymeric microcapsules, pull-off adhesion, SVET, EIS

INTRODUCTION

The use of coatings is the most popular corrosion protection method, to protect metallic surfaces against aggressive species. Corrosion process implies significant costs mainly due to the need for a protection method to be applied (NACE International, 2016). Even employing the best protective technology, maintenance is mandatory to extend the useful life of metallic structures in all industrial practices. If some technology can diminish the frequency of repairing interferences, the economic gains would be substantial.

In this way, in the last 20 years, there are a growing number of researches in the self-healing coatings theme. Among the different strategy to develop a self-healing coating, the directly incorporation of polymeric microcapsules in the coating matrix is the best one. The polymeric

microcapsules are synthesized to entrap in their core a film former or a corrosion inhibitor, so when they are incorporated in the coating they act as recovery material storage. Therefore, after a mechanical defect the microcapsules are broken and release the content of their core in the defect site, providing the formation of a polymeric film or allowing the released corrosion inhibitor to act in the damaged area (Montemor, 2014; Bekas et al., 2016; Cotting and Aoki, 2016).

Among many possible film formers like cyclopentadiene (White et al., 2001), linseed oil (Adamczak et al., 2013; Siva and Sathiyarayanan, 2015; Vakhitov et al., 2017), Tung oil (Cailleux and Pollet, 2009; Samadzadeh et al., 2011; Fayyad et al., 2015; Singh et al., 2015), silanes (Montemor et al., 2009; Cotting and Aoki, 2016), and epoxy bi-component (Liu et al., 2015; Ebrahimiya et al., 2018), or polyurethane (Huang and Yang, 2011). The alkyd healing systems are more advantageous than other systems; because they do not need catalysis for the polymerization reaction, making them autonomous systems. Otherwise, the alkyd coatings have low anti-corrosive and barrier properties than epoxy systems (Tracton, 2007; Singh et al., 2015).

The epoxy ester resin is a hybrid resin, which is synthesized from epoxy resins and fatty acids. Epoxy ester resins are synthesized from the esterification reaction between an epoxy resin and a fatty acid in the presence of p-toluene sulfonic acid (p-TSA). The epoxy resin used is the resin synthesized from Bisphenol A and the fatty acid used comes from vegetable oils. The most commonly used vegetable oils for the synthesis of epoxy ester resins are linseed oil, soybean oil, castor oil and Tung oil. This approach makes these resins have hybrid characteristics because they have a more crosslinked polymer network due to the epoxy groups and the curing is done at room temperature due to the oxidative polymerization of the unsaturation's present in the epoxy ester resin (Singh et al., 2015). Also, the epoxy ester self-healing systems have not been explored (Zhang et al., 2018).

Therefore, the main goal of this paper is to present the encapsulation of an epoxy ester resin in poly (urea-formaldehyde-melamine) walled microcapsules and their effective incorporation in an epoxy coating system, obtaining a self-healing coating. Scanning electron microscopy (SEM) and FTIR-ATR techniques were employed to morphological and chemical characterization. Electrochemical methods, such as EIS (electrochemical impedance spectroscopy) and SVET (scanning vibrating electrode technique) were used for self-healing effect evaluation. Pull-off strength test was also provided to verify the microcapsules influence on the cohesion and adhesion properties.

EXPERIMENTAL

Surface Treatment

The carbon steel specimens were blasted with carbon steel grit G-25 till a roughness profile of 60–70 μm and after blast step; the samples were cleaned with dry airflow. Before coating application, the carbon steel samples were cleaned with acetone, ethanol and finally dried with hot airflow.

Microcapsules Synthesis

Microcapsules were obtained by the *in situ* polymerization method. The procedure adopted was similar to Patent WO2014032130A1 (Petrobras et al., 2012). Therefore, 250 g of water, 20 g of an epoxy ester resin, 2.5 g of urea, 3.5 g of sodium chloride, 0.25 g of ammonium chloride, 0.25 g of resorcinol, 2 g of Arabic gum and 0.25 of melamine were added into a 350 ml Becker. The agitation was added to the system with Ika® Ultra-turrax T-25 disperser, adjusting the rotation in 5,000 RPM. After 60 min, the pH was adjusted with a 10% HCl solution to 3.5 and 6.4 g formaldehyde was added to the reaction vessel. So, the agitation was slowed to 250 RPM to avoid the evaporation of the ester epoxy resin solvents during the wall of microcapsules formation, the reaction temperature was controlled in three steps 1 h at 45°C, 2 h at 50°C, and finally 1 h at 55°C. Vacuum filtration permits the separation of the microcapsules that are allowed to dry at room conditions for 12 h. A free-flowing powder was obtained.

The following methodology was performed to determine the amount of encapsulated resin in the microcapsules. A 1.0 g sample of microcapsules was macerated in a mortar, in the presence of 5 ml dichloromethane. After the maceration process, the material was subjected to an ultrasonic bath for 5 min and then vacuum filtered. The material retained on the filter paper was again washed with the organic solvent, macerated and filtered again to ensure full extraction of the encapsulated material from the sample.

The filtered solution—solvent and encapsulated material—and the material retained on the filter paper—polymer—were placed in an oven at 60°C for 48 h. After this step, the filtered material and the retained material were weighed so that the fraction of encapsulated material and the polymer fraction in each sample could be determined. The percentage of encapsulated material present in the sample was determined by Equation (1).

$$\% \text{ encapsulated material} = (\text{mass of filtered material}) / (\text{total mass of sample}) \times 100 \quad (1)$$

This procedure was performed in triplicate.

Microcapsules Incorporation in an Epoxy Coating and Application on Carbon Steel Panels

The microcapsules were added to a surface tolerant epoxy coating with 97% of solids in 10 and 15 wt. % ratios. Three-layer coating system was applied, with around 200 μm thick each one. Besides that, different colors were adopted for each coating layer, in order to assist the pull-off test assessment. **Figure 1** shows the coating scheme employed.

Table 1 shows all the conditions and respective codes for the microcapsules samples. Letter E denotes the epoxy ester resin. Three numbers denote the three layers of the coating system and 100/10C means that the microcapsules were added only in the first layer (primer) in 10% ratio; 120/15C denotes that microcapsules were added in the first and also in the second layer in 15 wt. % ratio, and so on. Finally, the layers with microcapsules have the letter C in their code and the layers that do not have

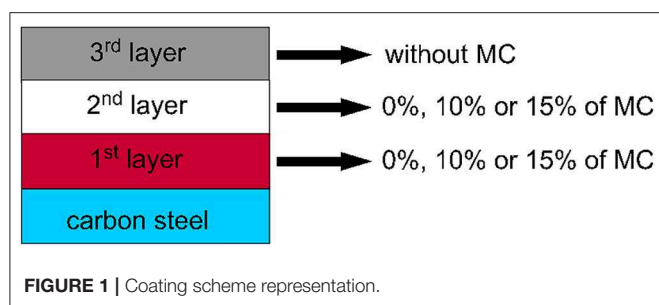


TABLE 1 | Composition of different coating layers, with or without microcapsules, on carbon steel, and their respective codes.

Samples	1st layer	2nd layer	3rd layer	Codes
1	SC	SC	SC	E000
2	SC	10C	SC	E020/10C
3	SC	15C	SC	E020/15C
4	10C	SC	SC	E100/10C
5	10C	10C	SC	E120/10C
6	15C	SC	SC	E100/15C
7	15C	15C	SC	E120/15C

microcapsules have the letters SC, indicating the absence of this pigment.

EIS Measurements

The EIS measurements were performed in a three-electrode electrochemical cell using an Ag/AgCl (sat KCl) reference electrode, a platinum counter electrode with an exposed area of 12 cm² and the working electrode being the coated steel panel with an exposed area of 6.26 cm². The area was delimited by attaching a glass tube, with neutral curing silicone adhesive to the coated specimens. In the EIS measurements, the employed electrolyte was 0.1 mol/L NaCl aqueous solution.

As the real exposed area of the metal to the electrolyte is absolutely significant for the EIS results, it is very critical to perform reproducible defects in order to achieve confident results. In this sense, EIS measurements were performed in coated panels with and without a provoked defect. In the absence of the defect, the objective was to verify if the presence of the microcapsules were disturbing the performance of the painting system. For the conditions with a provoked defect, it was possible to evaluate the self-healing ability of the microcapsule-containing samples. In order to guarantee the reproducibility of the 200 μm diameter defects, these were performed with a manual micro-drill. The immersion tests for the EIS evaluation were performed 14 days after the last layer of coating was applied to the specimens to assure the complete cure of the epoxy coating.

The frequency range analyzed in the samples without defect was 100 kHz to 10 mHz; with a sinusoidal perturbation of 20 mV rms at open circuit potential (OCP) and 10 measurements were acquired per decade of frequency. For damaged samples, the frequency range used was from 50 kHz to 5 mHz, employing a sinusoidal perturbation of 10 mV rms at OCP and 10

measurements were also acquired per frequency decade. The damaged samples were exposed to room air for 48 h after the defect was made to permit there was time to cure and reticulate the epoxy ester resin released from the core of the microcapsule by contact with the oxygen in the air. For the defect samples, EIS measurements were performed after 6, 24, and 48 h of immersion in the electrolyte. The intact samples were evaluated up to 28 days of immersion.

SVET Measurements

The SVET tests were carried out using Applicable Electronics equipment controlled by ASET-Scienceware software. Data were treated by Quikgrid software version 5.4. The vibrating probe was a MicroProbe platinum/iridium microelectrode containing a platinum deposit at the tip whose diameter was ~10 μm. The use of the local technique was intended to assess the activity in a provoked defect region on coated samples, for with microcapsules or without microcapsules conditions. A defect of 3 mm length was made with a blade. After provoking the defects, the samples were allowed to stay in the laboratory atmosphere for 48 h before the SVET measurements have been performed. This time is sufficient to promote the polymerization by air O₂ in order to obtain a protective film in the defect region. For SVET measurements only one layer of 200 μm thickness were applied because for a complete system of about 600 μm thick, it would be impossible to detect ionic currents coming from such long distance in defect area. In such terms, only three conditions have been evaluated: (1) without microcapsules; (2) with 10 wt. % of microcapsules; and (3) with 15 wt. % of microcapsules. A 0.01 mol/L NaCl solution was used during the SVET measurements.

Pull off Adhesion Test of Coated Samples

Pull-off adhesion measurements were performed 21 days after application of the last layer of coating on the specimens to ensure complete cure of coating. Using PATTI Quantum digital equipment, measurements were taken at three points of each panel. The piston used in the tests was the F-8 and the stubs were 2.54 cm in diameter. The adhesive used was the J-B Weld bi-component epoxy adhesive. The tests were performed and discussed according to ASTM D4541-17.

Aspect and Size of Microcapsules

A TESCAN Vega 3 scanning electron microscope (SEM) was used to register the aspect of the obtained microcapsules. The cumulative numeric size distribution of the microcapsules was obtained by laser diffraction using a model 3000 Mastersizer from Malvern.

FTIR-ATR Analysis of the Entire and Crushed Microcapsules

The microcapsules containing the epoxy resin were characterized by the FTIR-ATR technique. FTIR-ATR analyses were performed on a Nicolet brand 6700 model with diamond crystal. Spectra were obtained in the region of 0–4,000 cm⁻¹. Samples of intact microcapsules, ruptured microcapsules and pure epoxy resin were analyzed, thus verifying if microencapsulation was performed successfully.

Salt Spray Chamber Exposition

The salt spray chamber exposition was performed in a fog chamber according to the ASTM standard B-117. The coatings were damaged with a blade with 0.7 mm width, creating a horizontal scribe with ~ 8 cm. Only the original coating—no microcapsules—and the self-healing coating containing 15% of microcapsules in the first and second layer were submitted to salt spray chamber test. The samples were exposed for 720 h.

All experiments were performed in triplicate.

RESULTS

SEM Images of the Obtained Microcapsules

Figure 2 shows the SEM images of the microcapsules produced containing the epoxy ester resin. The analysis of the images

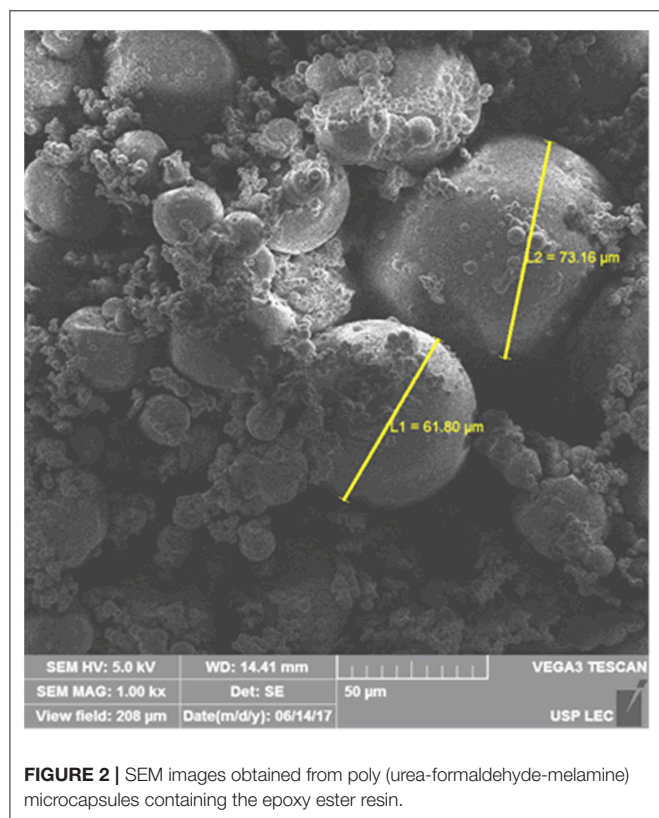


FIGURE 2 | SEM images obtained from poly (urea-formaldehyde-melamine) microcapsules containing the epoxy ester resin.

allows verifying that the obtained microcapsules have a wide distribution of size, where there is a population of microcapsules of smaller size, around $10\ \mu\text{m}$ and another population of larger size, with diameters in the order of $60\text{--}70\ \mu\text{m}$.

Microcapsules Size Distribution

Figure 3 shows the histogram of the numerical distribution and the curve of the accumulated value obtained by analyzing the sample of microcapsules containing the epoxy ester resin. The analysis by the numerical distribution of the sample helps in the understanding of what was observed by the microscopic techniques (Sánchez-Silva et al., 2011), where a large number of microcapsules with diameters below $30\ \mu\text{m}$ were observed and only the presence of some microcapsules with diameters around $75\ \mu\text{m}$ was detected.

The treatment of the data acquired by determining the numerical distribution enabled the determination of the numerical diameters D_{n10} , D_{n50} , and D_{n90} , which are presented in Table 2. These values show that 10% of the total number of microcapsules has size $<14\ \mu\text{m}$, 50% of the number of microcapsules has to size $<21\ \mu\text{m}$ and 90% of the microcapsules have to size $<110\ \mu\text{m}$.

The values presented by the numerical distribution are more consistent with what was observed by the images obtained with SEM, where a larger amount of microcapsules with diameters up to $30\ \mu\text{m}$ was observed.

FTIR-ATR Results From Pure Resin and Entire and Crushed Microcapsules

The microcapsules were chemically characterized, to ascertain whether the released material was, in fact, the epoxy ester resin. Figure 4 shows the spectra obtained by the FTIR-ATR technique during the characterization of the poly (urea-formaldehyde-melamine) microcapsules containing the epoxy ester resin and Table 3 shows the main characteristic absorption bands of the functional groups present on the epoxy ester resin and in the poly (urea-formaldehyde-melamine) polymer.

The epoxy ester resin, as its name suggests, exhibits in its structure the ester and epoxy functional groups, which in turn have characteristic absorptions in the infrared region of the spectrum. Therefore, we can identify by the spectrum of the resin (black spectrum) in Figure 4 the presence of bands, in a total of three, that are characteristic of the epoxy group. The first band in the region of $\sim 1,263\ \text{cm}^{-1}$ corresponds to the symmetrical axial

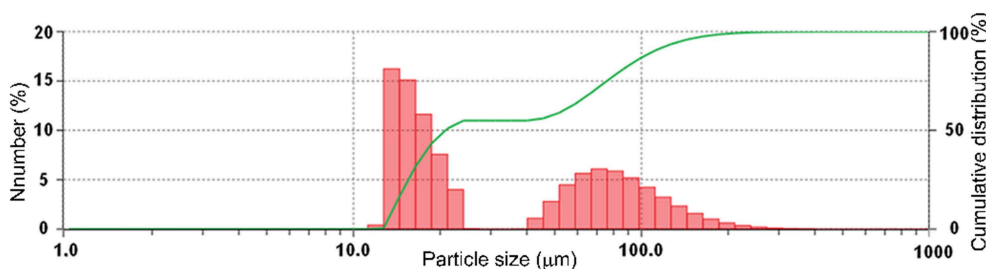


FIGURE 3 | Histogram of the numerical distribution and cumulative value curve of poly (urea-formaldehyde-melamine) microcapsules containing the epoxy ester resin.

TABLE 2 | Numeric diameters Dn10, Dn50, and Dn 90 obtained for poly(urea-formaldehyde-melamine) microcapsules containing in their core an epoxy ester resin.

Parameter	Diameter (μm)
Dn10	14
Dn50	21
Dn90	110

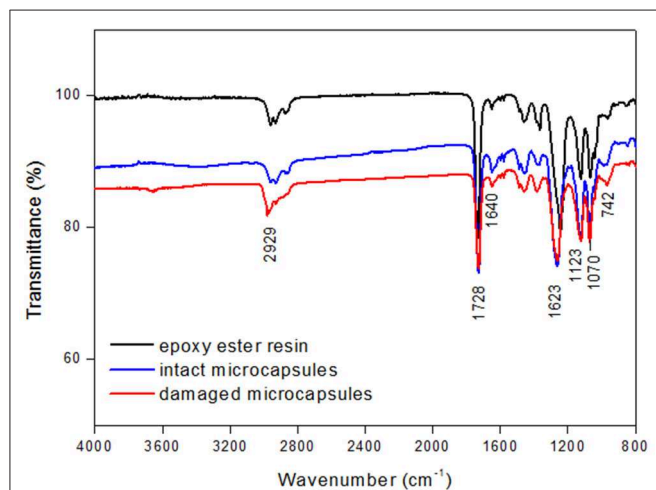


FIGURE 4 | FTIR-ATR spectra obtained for the epoxy ester resin prior to the microencapsulation process, for the intact microcapsules containing the resin and for the broken microcapsules containing the epoxy ester resin.

deformation of the epoxy ring, which occurs by the expansion and contraction of all ring bonds. The second band, around 966 cm^{-1} , can be attributed to the asymmetric axial deformation of the ring, where contraction of C–O type bonds and expansion in C–C type bonds occurs. The third and last band characteristic of the epoxy function, located at $\sim 742\text{ cm}^{-1}$, corresponds to the symmetric deformation in the plane of the C–O–C bond. The presence of the ester functional group on the resin can be visualized by the presence of the band at $\sim 1,728\text{ cm}^{-1}$, which is characteristic of the C=O bond.

In **Figure 4**, the spectrum presented for the intact microcapsules shows bands characteristic of the epoxy ester resin, which proves that the healing agent was microencapsulated. There is also a peak in the $\sim 1,640\text{ cm}^{-1}$ region, which is attributed to the stretching of the N–H bonds present in the compounds constituting the polymeric wall of the microcapsules.

The gravimetric assays showed that microcapsules contain $86 \pm 4\text{ wt. \%}$ of encapsulating resin. This value is similar to studies where linseed oil and Tung oil were encapsulated.

EIS Results for Samples Without Defect

The impedance diagrams were obtained after 6 h, 7 and 28 days of immersion in the electrolyte of the coated samples without defect. **Figure 5** shows the EIS diagrams obtained for the different microcapsules conditions under study and the

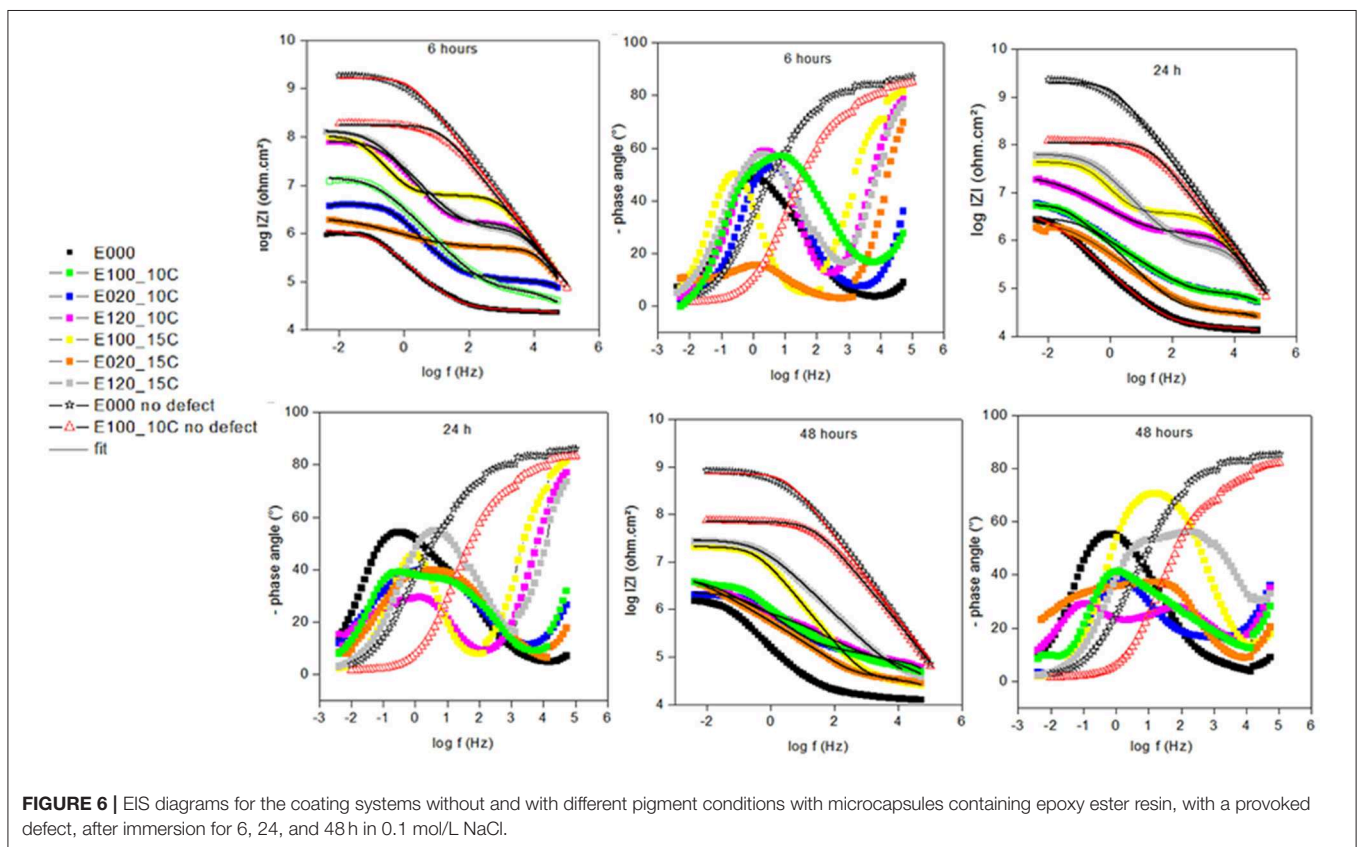
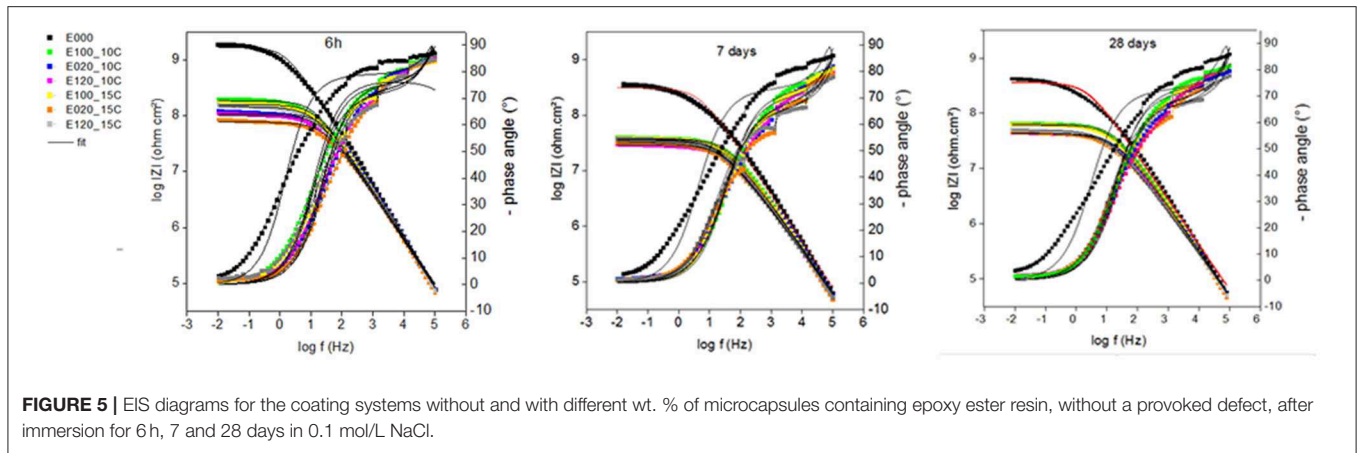
TABLE 3 | Characteristic absorption bands and the related functional groups present in the epoxy ester resin and in the poly(urea-formaldehyde-melamine) walls of the microcapsules are shown (Chike et al., 1993; Vařková and Křsálek, 2011; Knop et al., 2014; Singh et al., 2015; Khorasani et al., 2017).

Functional groups	Wave number (cm^{-1})
C–H aliphatic	3,000–2,840
C=O	1,750–1,730
N–H	1,626–1,645
C–N	$\sim 1,547$
Epoxy ring (axial deformation)	$\sim 1,263$
C=C aromatic (Bisphenol A)	1,300–1,000
Epoxy ring (asymmetric axial deformation)	950–860
Epoxy ring	865–785

condition without any microcapsules. The EIS diagrams show that the presence of the self-healing particles in the coating system affected the anticorrosive barrier properties. Comparing the samples containing microcapsules with the sample without microcapsules, it is observed the decay of an order of magnitude in impedance modulus values in the low-frequency region for the microcapsules samples. The traditional coating—without microcapsules—presented values around $1.88 \times 10^9\text{ ohm}\cdot\text{cm}^2$, whereas the self-repairing coatings presented values in the range 8.63×10^7 – $1.99 \times 10^8\text{ ohm}\cdot\text{cm}^2$, after 6 h of immersion.

This perturbation of the microcapsules in the coating systems is probably related to the presence of microcapsules larger than $20\text{ }\mu\text{m}$ (the average diameter is around $30\text{ }\mu\text{m}$) that normally causes a decrease in the barrier properties of any coating creating some preferential pathways for the electrolyte inside the coating. The lowest impedance modulus values were obtained for the highest percentage of microcapsules (15 wt. %) added in the coating and also when they were added only in the second layer.

The analysis of Bode (phase angle $\times \log f$) diagrams allows identifying a well-defined time constant in the HF region for all samples, which is related to the barrier protection properties of the coating. The presence of a single time constant, with high phase angle values and covering a large range of frequencies shows that the evaluated coating regions have no defects, making it impossible to sense the metal/electrolyte interface reactions. For the evaluation of the degradation over time of these systems by the EIS technique, it is verified that after 48 h of immersion the magnitude of decay in the impedance modulus was the same for all samples, showing that the barrier property was not affected and only the dielectric properties of the coating were altered by the microcapsules. This behavior indicates that the microcapsules affected the dielectric properties of the coating, but were not able to create effective preferential paths for the contact of the electrolyte with the substrate. However, it can be observed in the set of microcapsules samples that the systems containing the microcapsules in the first and second layers (E120), as well as the systems containing the microcapsules only in the second layer (E020), showed the more significant degradation after 48 h of immersion. These results indicate that the addition of the microcapsules in the second layer of the coating system is not the best option. This way, the best strategy to incorporate the



microcapsules in the presented coating scheme is only in the first layer of the coating system, whether with 10 or 15 wt. % on the coating solids.

EIS Results for Damaged Samples

To evaluate the self-healing effect of the different coating systems, the impedance spectra were obtained after 6, 24, and 48 h of immersion in the electrolyte. **Figure 6** shows the EIS diagrams of the coating systems in the different microcapsules conditions. For a better discussion of the self-healing effect, the EIS diagrams of the non-damaged coating systems E000 and E100_10C were also

joined. The sample E100_10C without defect was chosen, because it presented the best anticorrosive performance, in the first hours of immersion, among the microcapsules samples.

Based on the electrochemical behavior of the samples after 6 h of immersion, one can verify in the Bode $\log |Z| \times \log f$ diagrams that all the containing microcapsules and damaged samples presented impedance modulus values in LF region larger than the coating system without microcapsules and with defect (the negative reference). The higher total impedance presented for the microcapsules samples is associated with the formation of a protective film in the region of the defect by the

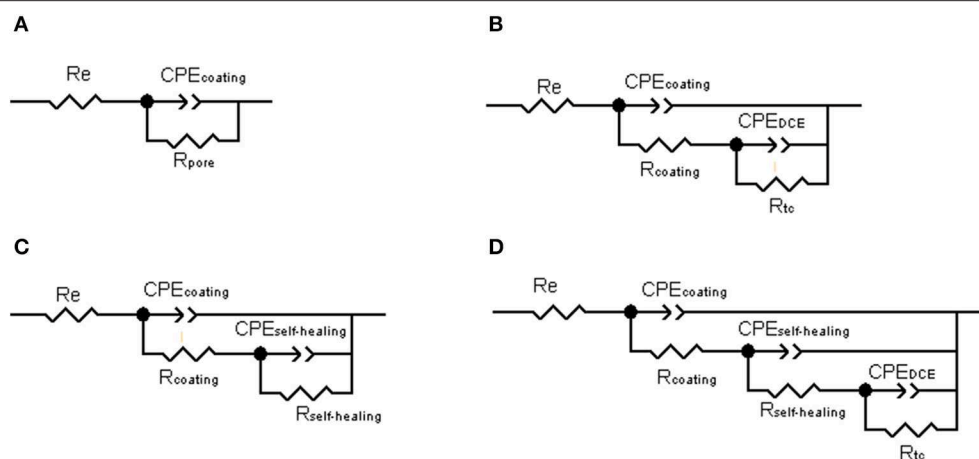


FIGURE 7 | Equivalent circuits for **(A)** intact coatings; **(B)** damaged coating without microcapsules; **(C)** damaged coating with microcapsules; and **(D)** damaged coating with microcapsules.

encapsulated epoxy ester resin released after the defect execution, promoting the self-healing effect. However, the degree of self-healing promoted by each microcapsules system was influenced by the incorporation conditions.

The coating systems added only in the second layer (E020) were the systems that presented the lowest self-healing performance, because the healing agent released during the execution of the defect is at a distance of $\sim 200\ \mu\text{m}$ (average thickness of the first layer) from the carbon steel surface. Also, the samples containing microcapsules only in the first layer showed that the best self-healing performance mainly by the system with the highest microcapsules concentration (E100_15C), most likely due to the higher amount of microcapsules available in the damaged region. The samples pigmented in the first two layers of coating system (E120) presented a very similar self-healing effect to the sample E100_15C and values very close to that of the microcapsules system without defect (E100_10C without defect), which indicates that the maximum protection of the self-healing agent was achieved for these three samples.

In the Bode diagrams (phase angle $\times \log f$) of **Figure 6**, the presence of two well-defined time constants for the samples with microcapsules and damaged is observed after 6 h of immersion. The time constant in HF is related to the self-healing film formed by the epoxy ester resin, released from the core of the microcapsules when the coating system has been damaged. However, the time constant in the LF regions is related to interface phenomena that, although present, are less active than the interface phenomena presented by the E000 condition (without microcapsules). By the evolution of time constants with immersion time, the usual degradation behavior of an organic coating could be observed for samples containing microcapsules, by the decay in the phase angle values and the shift of time constants to lower frequency regions. On the other hand, the sample without microcapsules does not present significant changes over time, showing the stability of the electrochemical system due to the absence of a protective film at the damaged site.

By the evaluation of the degradation of the self-healing films with time, it was confirmed that the films formed in samples

E100_15C and E120_15C presented high impedance modulus values in the LF region. Values that are even close to that of the microcapsules sample without defect (E100_10C without defect), showing that the film formed in the damaged region under the condition of higher microcapsules concentration provides more prolonged protection to the substrate.

From the results presented, the epoxy ester is an attractive alternative for self-healing coating systems, because showed highest self-healing results, when compared with linseed oil (Szaó et al., 2015; Behzadnasab et al., 2017) and Tung oil systems (Samadzadeh et al., 2011). The ester epoxy system also provides better-prolonged corrosion protection, since vegetable oils do not provide satisfactory protection after 24 h of electrolyte exposure.

The EIS data were adjusted with the equivalent circuits shown in **Figure 7**. The equivalent circuits were chosen by the best fit and with a plausible physical model. The intact systems were fitted by the circuit presented in **Figure 7A**, the damaged coating systems were adjusted with the equivalent circuit shown in **Figures 7B–D**. The circuit presented in **Figure 7B** was employed to fit the E000 data, due to this system does not have healing agent in its formulation, where R_s is the electrolyte resistance, CPE_{coating} and R_{coating} represent the capacitance and resistance of the coating, respectively, CPE_{DCE} represents the capacitance of the double layer and R_{tc} represents the resistance to charge transfer. The capacitance of the coating was expressed as a constant phase element (CPE) because it better represents the surface heterogeneities that are normally present in the coated metals. The circuits presented in **Figures 7C,D** were employed to fit the damaged coatings containing microcapsules, where the good self-healing systems could be fitted by circuit (**Figure 7C**), blocking the charge transfer phenomena, an effect that cannot be attributed to systems fitted by circuit (**Figure 7D**). Therefore, the elements $CPE_{\text{self-healing}}$ and $R_{\text{self-healing}}$ represent the capacitance and resistance of the self-healing film, respectively. In all circuit adjustment, the error values presented were in the range of 3–10% and the chi-squared values in the order of 10^{-4} .

TABLE 4 | Fitting results of EIS data for intact coated samples R ($\Omega\cdot\text{cm}^2$) and CPE-T ($\text{nF}\cdot\text{cm}^2/\text{S}\alpha^{-1}$), CPE-P (α).

Time	Sample	Parameters			
		Re	CPE-T	CPE-P	Rtc
6 h	E000	167	8.41×10^{-11}	0.88	1.67×10^9
	E100_10C	167	1.38×10^{-10}	0.85	1.84×10^8
	E020_10C	167	2.08×10^{-10}	0.84	1.09×10^8
	E120_10C	167	1.85×10^{-10}	0.82	1.01×10^8
	E100_15C	167	1.53×10^{-10}	0.84	1.58×10^8
	E020_15C	167	2.04×10^{-10}	0.82	7.65×10^7
	E120_15C	167	2.21×10^{-10}	0.80	1.43×10^8
7 days	E000	167	2.16×10^{-11}	0.82	3.09×10^8
	E100_10C	167	3.03×10^{-10}	0.81	3.72×10^7
	E020_10C	167	5.68×10^{-10}	0.75	3.37×10^7
	E120_10C	167	6.31×10^{-10}	0.76	2.87×10^7
	E100_15C	167	4.49×10^{-10}	0.78	3.67×10^7
	E020_15C	167	8.53×10^{-10}	0.73	3.13×10^7
	E120_15C	167	8.23×10^{-10}	0.73	3.61×10^7
28 days	E000	167	2.63×10^{-10}	0.80	3.59×10^8
	E100_10C	167	3.17×10^{-10}	0.81	6.31×10^7
	E020_10C	167	5.13×10^{-10}	0.76	4.36×10^7
	E120_10C	167	5.60×10^{-10}	0.77	4.26×10^7
	E100_15C	167	4.00×10^{-10}	0.79	6.08×10^7
	E020_15C	167	7.62×10^{-10}	0.74	4.33×10^7
	E120_15C	167	7.45×10^{-10}	0.75	4.89×10^7

Due to the high resistance of the painting systems, especially in the non-defective conditions, the studied frequency range did not allow the extraction of the Rs value directly from the EIS diagrams. For this reason, the value of Rs was kept fixed at $167 \Omega\cdot\text{cm}^2$, which is the resistance value of the electrolyte used.

Tables 4, 5 present the values obtained by the circuit model fitting for the EIS experimental data. From the values presented for the samples without damage, it is clear that the presence of microcapsules increased the capacitance of the coating and consequently decreased its resistance by one order of magnitude. Nevertheless, the exponent of the CPEcoating element had no significant variations with microcapsules incorporation, showing that the capacitive behavior of the coating has not been altered in the presence of the additive.

From the values presented for the damaged samples, it is observed that the damaged E000 sample showed an increase in the coating capacitance value, resulting in a decrease of the coating resistance value, Rcoating. This behavior results from the defect caused in the coating system, causing its protective properties to decrease, leading to exposure of the carbon steel substrate. Carbon steel exposure may be accompanied by the new circuit element present under damage condition, where the CPEDCE value of $1.0 \times 10^{-6} \text{ F}\cdot\text{cm}^2/\text{S}\alpha^{-1}$ is typical of corrosive or charge transfer processes at the metal/electrolyte interface (Szaó et al., 2015).

From the values presented for the damaged samples, it is clear that the self-healing film is present at the damaged region because the Rself-healing values are very close to the values presented

for E100_10C sample without damage. The CPEcoating and Rcoating parameters, for the self-repair condition, should be called self-healing CPE and Rself-healing, since the presence of the self-healing film is detected in these circuit elements. Besides, the high Rct value proves that the self-healing effect has been achieved in the microcapsules samples.

SVET Measurements

Figure 8 shows the SVET maps of the ionic currents densities measured above the surface of the carbon steel coated with an epoxy primer containing or not with 10 wt. % and 15% of microcapsules with an encapsulated epoxy ester resin and a provoked defect obtained after different immersion times in 0.01 mol/L NaCl. For the condition without microcapsules, the increasing anodic currents are evident for increasing immersion times, reaching the maximum value after 24 h of immersion. In the presence of microcapsules containing epoxy ester resin, both for 10 and 15 wt. % ratio microcapsules condition, after 6 h of immersion, a significant decrease in ionic currents is evidenced characterizing the self-healing process with active protection in the defect site. Even for 24 h of immersion, no anodic current density appeared in the defect site proving the self-healing properties of the coating system.

Pull-Off Adhesion Test

The results of the pull-off strength of coated samples and the type of failure occurred are presented in **Table 6** for different microcapsules conditions. By the average pull-off strength values

TABLE 5 | Fitting results of EIS data for coated damaged samples R ($\Omega\cdot\text{cm}^2$) and CPE-T ($\text{nF}\cdot\text{cm}^2/\text{S}\alpha^{-1}$), CPE-P (α).

Sample		Parameters									
		Re	CPE _{coating-T}	CPE _{coating-P}	R _{coating}	CPE _{self-healing-T}	CPE _{self-healing-P}	R _{self-healing}	CPE _{DCE-T}	CPE _{DCE-P}	R _{ct}
6 h	E000	167	2.21×10^{-9}	0.67	—	—	—	—	1.00×10^{-6}	0.68	1.17×10^6
	E100_10C	167	6.97×10^{-9}	0.60	1.49×10^5	6.97×10^{-9}	0.60	1.46×10^7	—	—	—
	E020_10C	167	3.94×10^{-10}	0.78	1.13×10^5	1.15×10^{-7}	0.77	4.11×10^6	—	—	—
	E120_10C	167	6.48×10^{-11}	0.92	1.61×10^6	1.07×10^{-11}	0.82	8.02×10^7	—	—	—
	E100_15C	167	8.01×10^{-11}	0.89	6.13×10^6	3.13×10^{-10}	0.85	1.01×10^8	—	—	—
	E020_15C	167	4.71×10^{-11}	0.95	4.80×10^5	6.80×10^{-10}	0.44	1.73×10^6	—	—	—
	E120_15C	167	7.94×10^{-11}	0.90	1.29×10^6	1.07×10^{-8}	0.73	1.36×10^8	—	—	—
24 h	E000	167	3.27×10^{-8}	0.49	1.60×10^4	—	—	—	1.41×10^{-6}	0.64	4.17×10^6
	E100_10C	167	1.71×10^{-10}	0.89	7.18×10^4	3.59×10^{-7}	0.53	7.70×10^6	—	—	—
	E020_10C	167	5.20×10^{-10}	0.77	5.46×10^5	1.87×10^{-7}	0.48	4.48×10^6	—	—	—
	E120_10C	167	7.93×10^{-11}	0.91	1.31×10^6	1.06×10^{-7}	0.52	2.26×10^7	—	—	—
	E100_15C	167	9.61×10^{-11}	0.89	3.70×10^6	2.03×10^{-8}	0.83	4.06×10^7	—	—	—
	E020_15C	167	3.64×10^{-10}	0.81	3.01×10^4	6.28×10^{-7}	0.56	2.51×10^6	—	—	—
	E120_15C	167	9.61×10^{-11}	0.90	7.90×10^5	1.11×10^{-8}	0.74	6.43×10^7	—	—	—
48 h	E000	167	7.65×10^{-8}	0.45	1.62×10^4	—	—	—	1.56×10^{-6}	0.70	1.89×10^6
	E100_10C	167	7.01×10^{-8}	0.43	1.60×10^5	2.84×10^{-7}	0.67	2.21×10^6	—	—	—
	E020_10C	167	4.88×10^{-10}	0.84	3.94×10^5	5.85×10^{-7}	0.32	1.01×10^7	—	—	—
	E120_10C	167	9.52×10^{-11}	0.91	7.49×10^4	1.85×10^{-7}	0.52	9.10×10^5	8.01×10^{-7}	0.68	3.61×10^6
	E100_15C	167	2.36×10^{-9}	0.69	3.47×10^4	2.24×10^{-8}	0.83	2.13×10^7	—	—	—
	E020_15C	167	5.96×10^{-10}	0.78	3.50×10^4	2.47×10^{-7}	0.65	3.32×10^5	7.23×10^{-7}	0.43	7.61×10^6
	E120_15C	167									

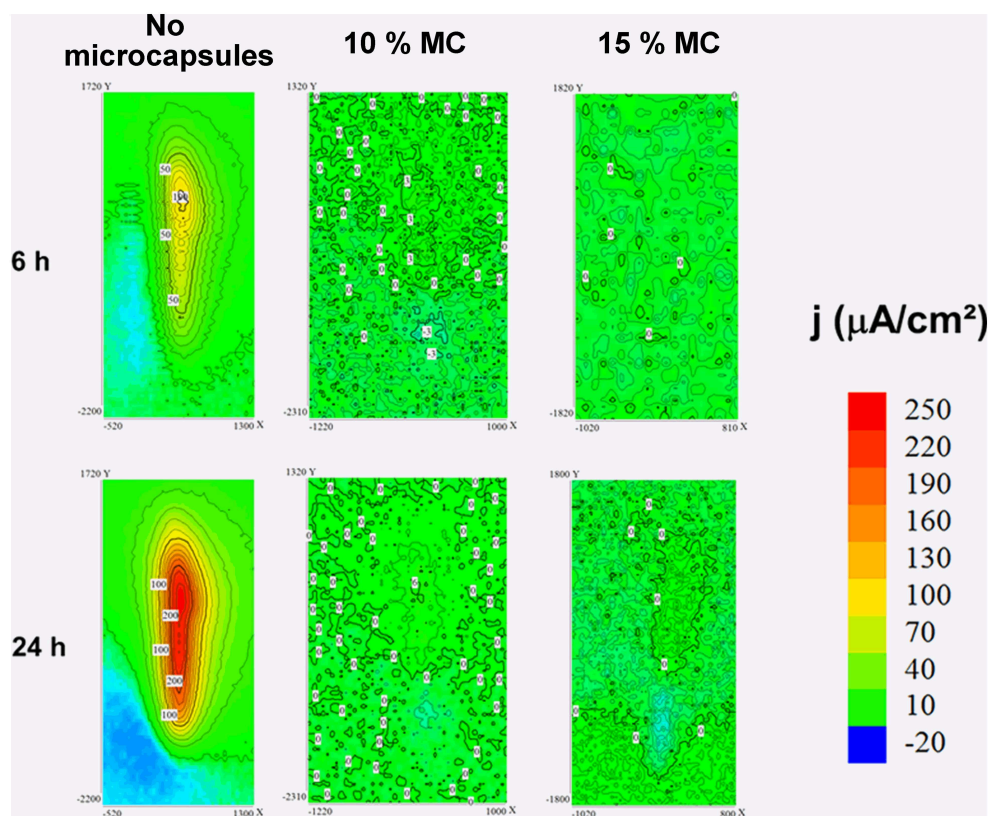


FIGURE 8 | Ionic current densities maps over a provoked defect on coated panels for microcapsules conditions: without microcapsules, with 10 wt. % of microcapsules containing epoxy ester resin, with 15 wt. % of the same microcapsules and the surface aspect after immersion.

TABLE 6 | Pull off strength of coated samples and observed type of failure.

Sample	Mean value of pull off strength (MPa)	Standard deviation	Failure mode
E000	6.5	0.7	Adhesive B/C
E100_10C	6.7	0.3	Adhesive B/C
E020_10C	5.9	0.2	Adhesive B/C
E120_10C	6.3	0.1	Adhesive B/C
E100_15C	6.3	0.4	Adhesive B/C
E020_15C	5.7	0.3	Adhesive B/C
E120_15C	6.1	0.1	Adhesive B/C

and the locus of failure presented by the samples, there is no way to affirm that there was a gain or a decrease in the adhesion properties of the coating systems in the presence of the microcapsules. However, what draws attention in this set of results is the low value obtained of pull-off tension for the type of applied coating, since its specification, according to PETROBRAS N-2680 standard, requires a tension of detachment above 12 MPa. Since great care was taken during the preparation of the substrate, which is evidenced by the adhesion of the first layer of the coating system to the substrate, there are indications that the coating used did not meet the expected quality.

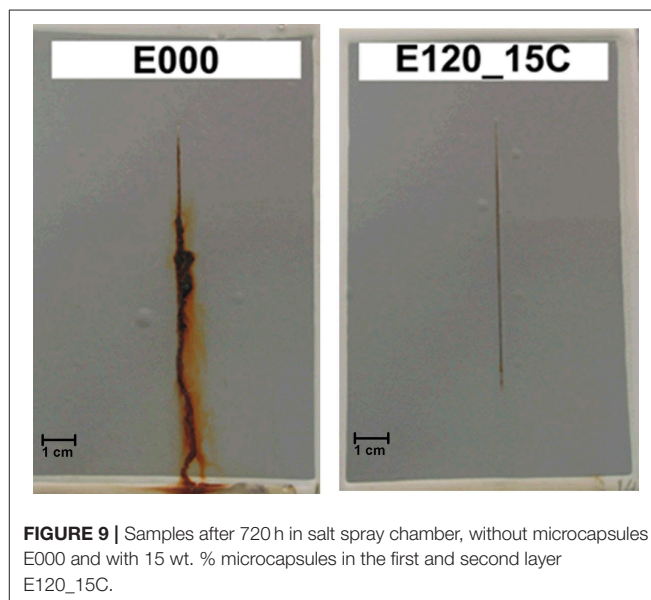


FIGURE 9 | Samples after 720 h in salt spray chamber, without microcapsules E000 and with 15 wt. % microcapsules in the first and second layer E120_15C.

By visual analysis of the regions where the coating was detached and by the posting dollies, it is noted that there are no differences in the type of failure between the different

painting systems studied. The detachment always occurred at the interface of the first and second layers of coating, either in the coated samples containing or not microcapsules. Therefore, we can conclude that poly (urea-formaldehyde-melamine) microcapsules containing the epoxy ester resin did not impair the tack properties of the coating system as a whole. Indeed, against the worst prognostic, this paper shows excellent results proving that the microcapsules do not spoil the adhesion properties of the pigmented coating and they do not show cohesive failure.

Salt Spray Chamber Results

The salt spray results are presented in **Figure 9**. From the images, it is observed that the pure epoxy coating cannot provide an anticorrosive protection in the scratch zone, due to a large number of observed corrosion products in the damaged region, as a result of iron oxidation. This result shows that the coating system without microcapsules cannot protect the carbon steel against aggressive species and consequently from the corrosion phenomena after damaged. On the other hand, in the self-healing coating, there are no visible corrosion products in the defect region. It suggests that the healing material was released on the damaged zone and a new protective layer was formed in the scratch area. Comparing the two samples it is clear that the microcapsules system increase the coating anticorrosion properties after mechanical damage, due to the self-healing effect. These results are in agreement with the EIS results, where the microcapsules system presented better anti-corrosion properties after damaging.

CONCLUSIONS

The loading of the coating system with the self-healing microcapsules caused a decrease in the total impedance of each coating system, showing that there was a certain disturbance of the coating system in the presence of the microcapsules. However, the self-healing effect can be verified for all samples containing microcapsules by all electrochemical techniques and corrosion tests employed in this work.

The higher concentration (15 wt. %) of microcapsules in the coating system provided a better self-healing film, with better anticorrosive performance than those with 10 wt. %. Also, the presence of microcapsules only in the second layer of the coating

system did not present satisfactory self-healing effects, due to the difficulty of the healing agent reaching the substrate.

The pull-off adhesion tests were significant in proving that the presence of the microcapsules did not in any way damage the adhesion or cohesion properties of the coating system, regardless the layer applied or the number of microcapsules added in the coating.

DATA AVAILABILITY STATEMENT

The datasets generated for this study are available on request to the corresponding author.

AUTHOR CONTRIBUTIONS

FC performed most of the experimental work because it was part of his Ph.D. thesis. He also gave important contribution to the discussion of data and bibliographic findings. AK acted as a project manager at Petrobras from which the laboratory received financial support. He advised about the performing long term SSC test and pull off strength adhesion test for practice importance in real life. He has contributed with the final discussion of these tests results. IA was the head of the Electrochemistry and Corrosion Laboratory at Polytechnic School at USP. She had been the Ph.D. advisor of FC and has acted as the coordinator of the research project. She had planned the work and paper, and had participated in the deep discussion of results.

FUNDING

The authors declare that this study received funding from PETROBRAS. The funder was not involved in the study design, collection, analysis, interpretation of data, the writing of this article, or the decision to submit it for publication.

ACKNOWLEDGMENTS

The authors were thankful for Petrobras for financial support (Project SAP: 4600508473) and CNPq for doctorate scholarship for FC (Proc 140309/2013-6). The authors were thankful to the Chemical Engineering Department of the FEI University Center, located in the city of São Bernardo do Campo for FTIR-ATR analysis.

REFERENCES

- Adamczak, M., Para, G., Simon, C., and Warszyński, P. (2013). Natural oil nanoemulsions as cores for layer-by-layer encapsulation. *J. Microencapsul.* 30, 479–489. doi: 10.3109/02652048.2012.752536
- Behzadnasab, M., Mirabedinia, S. M., Esfandeha, M., and Farnoodb, R. R. (2017). Evaluation of corrosion performance of a self-healing epoxy-based coating containing linseed oil-filled microcapsules via electrochemical impedance spectroscopy. *Prog. Org. Coatings* 105, 212–224. doi: 10.1016/j.porgcoat.2017.01.006
- Bekas, D. G., Tsirka, K., Baltzis, D., and Paipetis, A. S. (2016). Self-healing materials: a review of advances in materials, evaluation, characterization and monitoring techniques. *Compos. B Eng.* 87, 92–119. doi: 10.1016/j.compositesb.2015.09.057
- Cailleux, E., and Pollet, V. (2009). "Investigations on the development of self-healing properties in protective coatings for concrete and repair mortars," in *2nd International Conference on Self Healing Materials* (Brussels), 120.
- Chike, K. E., Myrick, M. L., Lyon, R. E., and Angel, S. M. (1993). Raman and near-infrared studies of an epoxy resin. *Appl. Spectrosc.* 47, 1631–1635. doi: 10.1366/0003702934334714
- Cotting, F., and Aoki, I. V. (2016). Smart protection provided by epoxy clear coating doped with polystyrene microcapsules containing silanol and Ce (III) ions as corrosion inhibitors. *Surf. Coatings Technol.* 303, 310–318. doi: 10.1016/j.surfcoat.2015.11.035

- Ebrahimiya, A., Khorram, M., Hassanajili, S., and Javidi, M. (2018). Modeling and optimization of the parameters affecting the *in-situ* microencapsulation process for producing epoxy-based self-healing anti-corrosion coatings. *Particuology* 36, 59–69. doi: 10.1016/j.partic.2017.01.010
- Fayyad, E. M., Almaadeed, M. A., and Jones, A. (2015). Encapsulation of tung oil for self-healing coatings in corrosion applications. *Sci. Adv. Mater.* 7, 2628–2638. doi: 10.1166/sam.2015.2583
- Huang, M., and Yang, J. (2011). Facile microencapsulation of HDI for self-healing anticorrosion coatings. *J. Mater. Chem.* 21, 11123–11130. doi: 10.1039/c1jm10794a
- Khorasani, S. N., Ataei, S., and Neisiany, R. E. (2017). Microencapsulation of a coconut oil-based alkyd resin into poly(melamine-urea-formaldehyde) as shell for self-healing purposes. *Prog. Org. Coatings* 111, 99–106. doi: 10.1016/j.porgcoat.2017.05.014
- Knop, W. R., Meier, M. M., and Pezzin, S. H. (2014). Preparação e caracterização de microcápsulas de poli (ureia-formaldeído) preenchidas com diciclopentadieno. *Rev. Mater.* 19, 266–273. doi: 10.1590/S1517-70762014000300010
- Liu, J., Gong, G., Zhong, Y., Gu, Y., and Zhang, F. (2015). Preparation of poly(urea-formaldehyde) microcapsules filled with epoxy resins via *in-situ* polymerization method. *Hecheng Shuzhi Ji Suliao/China Synth. Resin Plast.* 32, 1–9.
- Montemor, M. F. (2014). Functional and smart coatings for corrosion protection: a review of recent advances. *Surf. Coatings Technol.* 258, 17–37. doi: 10.1016/j.surfcoat.2014.06.031
- Montemor, M. F., Pinto, R., and Ferreira, M. G. S. (2009). Chemical composition and corrosion protection of silane films modified with CeO₂ nanoparticles. *Electrochim. Acta* 54, 5179–5189. doi: 10.1016/j.electacta.2009.01.053
- NACE International (2016). *IMPACT—International Measures of Prevention, Application and Economics of Corrosion Technologies Study* (Houston, TX).
- Petrobras, Paulo, U. D. S., Aoki, I. V., Lachtermacher, M. G., Coelho, J. F. C., A, K., et al. (2012). *Revestimento Autorregenerante Contendo Agentes de Autorreparação*. Rio de Janeiro.
- Samadzadeh, M., Boura, S. H., Peikari, M., Ashrafi, A., and Kasirha, M. (2011). Tung oil: an autonomous repairing agent for self-healing epoxy coatings. *Prog. Org. Coatings* 70, 383–387. doi: 10.1016/j.porgcoat.2010.08.017
- Sánchez-Silva, L., Rodríguez, J. F., and Sánchez, P. (2011). Influence of different suspension stabilizers on the preparation of Rubitherm RT31 microcapsules. *Colloids Surf. A Physicochem. Eng. Asp.* 390, 62–66. doi: 10.1016/j.colsurfa.2011.09.004
- Singh, A. P., Gunasekaran, G., Suryanarayana, C., and Balaji Naik, R. (2015). Fatty acid based waterborne air drying epoxy ester resin for coating applications. *Prog. Org. Coatings* 87, 95–105. doi: 10.1016/j.porgcoat.2015.05.012
- Siva, T., and Sathiyarayanan, S. (2015). Self healing coatings containing dual active agent loaded urea formaldehyde (UF) microcapsules. *Prog. Org. Coatings* 82, 57–67. doi: 10.1016/j.porgcoat.2015.01.010
- Szaó, T., Telegdia, J., and Nyikos, L. (2015). Linseed oil-filled microcapsules containing drier and corrosion inhibitor—their effects on self-healing capability of paints. *Prog. Org. Coatings* 84, 136–142. doi: 10.1016/j.porgcoat.2015.02.020
- Tracton, A. A. (2007). *Coating Materials and Surface Coating*. New York, NY.
- Vakhitov, T. R., Katnov, V. E., Grishin, P. V., Stepin, S. N., and Grigoriev, D. O. (2017). Biofriendly nanocomposite containers with inhibition properties for the protection of metallic surfaces. *Proc. R. Soc. A Math. Phys. Eng. Sci.* 473:20160827. doi: 10.1098/rspa.2016.0827
- Vášková, H., and Křesálek, V. (2011). “Raman spectroscopy of epoxy resin crosslinking,” in *Proceedings of the 13th WSEAS International Conference on Automatic Control, Modelling & Simulation*, 357–361.
- White, S. R., Sottos, N. R., Geubelle, P. H., Moore, J. S., Kessler, M. R., Sriram, S. R., et al. (2001). Autonomic healing of polymer composites. *Nature* 409, 794–797. doi: 10.1038/35057232
- Zhang, C., Wang, H., and Zhou, Q. (2018). Preparation and characterization of microcapsules based self-healing coatings containing epoxy ester as healing agent. *Prog. Org. Coatings* 125, 403–410. doi: 10.1016/j.porgcoat.2018.09.028

Conflict of Interest: AK was employed by the company PETROBRAS.

The remaining authors declare that the research was conducted in the absence of any commercial or financial relationships that could be construed as a potential conflict of interest.

Copyright © 2019 Cotting, Koebisch and Aoki. This is an open-access article distributed under the terms of the Creative Commons Attribution License (CC BY). The use, distribution or reproduction in other forums is permitted, provided the original author(s) and the copyright owner(s) are credited and that the original publication in this journal is cited, in accordance with accepted academic practice. No use, distribution or reproduction is permitted which does not comply with these terms.



Effects of TiO₂ Nanoparticles on the Overall Performance and Corrosion Protection Ability of Neat Epoxy and PDMS Modified Epoxy Coating Systems

Ammar Shafaamri^{1*}, Chiam H. Cheng¹, Iling A. Wonnice Ma¹, Shahid B. Baig¹, Ramesh Kasi^{1*}, Ramesh Subramaniam¹ and Vengadaesvaran Balakrishnan²

¹ Department of Physics, Center for Ionics University of Malaya, University of Malaya, Kuala Lumpur, Malaysia, ² UM Power Energy Dedicated Advanced Centre (UMPEDAC), University of Malaya, Kuala Lumpur, Malaysia

OPEN ACCESS

Edited by:

Flavio Defforian,
University of Trento, Italy

Reviewed by:

Benjamin Salas Valdez,
Universidad Autónoma de Baja
California, Mexico
Sébastien Touzain,
Université de la Rochelle, France

*Correspondence:

Ammar Shafaamri
ammarsafaamri@um.edu.my
Ramesh Kasi
rameshkasi@um.edu.my

Specialty section:

This article was submitted to
Environmental Materials,
a section of the journal
Frontiers in Materials

Received: 21 March 2019

Accepted: 06 December 2019

Published: 13 January 2020

Citation:

Shafaamri A, Cheng CH, Wonnice Ma IA, Baig SB, Kasi R, Subramaniam R and Balakrishnan V (2020) Effects of TiO₂ Nanoparticles on the Overall Performance and Corrosion Protection Ability of Neat Epoxy and PDMS Modified Epoxy Coating Systems. *Front. Mater.* 6:336. doi: 10.3389/fmats.2019.00336

Epoxy-TiO₂ nanocomposite coatings were prepared by the utilization of the solution intercalation method with the presence of the sonication process and the influence of embedding different loading ratios of TiO₂ nanoparticles within neat epoxy resin was investigated. To further improve the corrosion protection performance and to fulfill the hydrophobicity of the developed coated surfaces, the epoxy polymeric resin was modified with polydimethylsiloxane (PDMS) and different loading ratio of TiO₂ nanoparticles was introduced to the modified polymeric matrix to fabricate PDMS modified epoxy nanocomposite coating systems. All developed coating systems were characterized by means of Fourier transform infrared (FTIR) spectroscopy and differential scanning calorimetry (DSC) to investigate the chemical structure and the glass transition temperatures (T_g) of the developed coating systems, respectively. The morphology, topology, optical properties, and the wettability were also examined by field emission scanning electron microscope (FESEM), energy dispersive X-rays analyzer (EDX), atomic force microscopy (AFM), ultraviolet-visible spectroscopy (UV-vis), and contact angle measurement (CA), respectively. Moreover, the electrochemical behavior and the barrier properties of the developed coating films were investigated via electrochemical impedance spectroscopy (EIS). The findings revealed a good curing level with higher T_g values for all developed nanocomposite coating systems and confirmed the efficiency of the sonication process in developed well-dispersed TiO₂ within the polymeric matrix. Also, the obtained results revealed the ability of certain amount of TiO₂ nanoparticles in enhancing the corrosion protection performance of epoxy based coating systems. The compatibility of epoxy resin, PDMS, and TiO₂ nanoparticles was also confirmed by achieving the hydrophobicity and obtaining the best corrosion protection performance.

Keywords: epoxy, polydimethylsiloxane (PDMS), TiO₂ nanoparticles, nanocomposite coatings, hydrophobic, electrochemical impedance spectroscopy (EIS)

INTRODUCTION

Due to atmospheric interaction with the environment, corrosion can be defined as the degradation of metallic material via electrochemical reaction on its surface, where it can cause damage and destruction of the material. Moreover, it can lead to an economic burden to a country and put risk to human being's health and safety. Preservation to protect metallic material by applying protective coating is the best practice to overcome most of the corrosion issues and consequences across the globe. The polymeric coating is to provide barrier property on material surface and has been an outstanding choice for anticorrosion purpose due to its production accessibility. However, polymer resin has its shortcoming sustainability that it contains free volume, micro-voids, and exhibits hydrophilicity due to their polar group which gives strong affinity toward water molecules (Ammar et al., 2016b; Guo et al., 2018). These drawbacks lead corrosion process through diffusion of corrosive agents such as oxygen, water molecules, and aggressive anions, create deterioration pathways to reach the coating-metal interface. This action is known as penetration which caused localized corrosion on the material surface that responsible for the damage via hydrolytic degradation (Zaarei et al., 2008; Heidarian et al., 2010; Brusciotti et al., 2013; Verma et al., 2019). A huge number of researches have been done to improve the barrier properties of the polymeric coating in the past decades (Dolatzadeh et al., 2011; Heidarian et al., 2011; Shen and Zuo, 2014; Matin et al., 2015; Mohamad Saidi et al., 2018; Zheng et al., 2019). By incorporating nano-sized fillers into the polymer resin, it is aimed that this effort will enhance the anticorrosion and barrier properties of the polymer coating via various mechanisms, such as filling up the pores and reducing the matrix defects, bowing, bridging and deflecting the cracks (Ammar et al., 2016c). Also, the inorganic nano-sized filler tends to function as a connecting bridge linking between the matrix molecules, thus reducing the total free volume and promotes cross-linking (Shi et al., 2009; Heidarian et al., 2010; Atta et al., 2019). These mechanisms, in turn, delay the penetration activity which slows down the diffusion of corrosive agents in the coating layer from reaching to the coating-metal interface, thus decreasing the corrosion rate on the material surface. One of the utilizable nano-size filler is Titanium dioxide (TiO_2) nanoparticles which have been used extensively due to its ability to provide a photocatalytic effect (Liqiang et al., 2003). This means that it is capable to release a huge number of electrons when exposed to ultraviolet light radiation. These electrons then initiate the photo-induced redox reaction on the corrosion causing agents that are adsorbed on the coating surface, further curbing corrosion reaction. Worth to note that ultraviolet light can release radicals which will be able to break the molecular structure of neat polymeric coating layer. Nevertheless, this mechanism provides it an antimicrobial property to kill bacteria that are present on the coating surface, which may also act as corrosion causing agent (Fu et al., 2005; Evans and Sheel, 2007). By that, TiO_2 nanoparticles are extensively used due to their anti-fouling, self-cleaning and also odor-inhibition properties resulting from the photocatalytic effect they exhibit.

However, due to the high porosity and hydrophilicity properties possessed by the polymer resin, it drags down the performance of anticorrosion properties by the developed coating system as water molecule is one of the most easily be-in-contact corruptions causing agent. Silicones are categorized as a type of high-valued polymers due to its capability to affect the efficacy of various applications in the industrial field (Eduok et al., 2017; Liao et al., 2018). It gives a significant impact on the industrial applied due to its molecular structure that may exist in assorted forms (Pouget et al., 2009). Silicone polymers are widely used as polydimethylsiloxane (PDMS) which is an inorganic polymer and has the properties of being hydrophobic contributed by its non-polar $-\text{CH}_3$ group that gives the coating low surface energy (Ammar et al., 2017). Massive research works have been conducted in the past few years (Sung and Lin, 1997; Velan and Bilal, 2000; Ahmad et al., 2005) to determine the optimum mixing ratio between epoxy resin and PDMS. It has been agreed that the mixing ratio of 90:10 w/w gives the most optimum performance, especially on the research outcome performed by Ananda Kumar together with his research team (Kumar and Narayanan, 2002; Kumar et al., 2002, 2006; Duraibabu et al., 2014).

In this study, a simple preparation method was developed to prepare the epoxy- TiO_2 nanocomposite coating systems. As a result, a homogeneous solution with different TiO_2 loading ratios incorporated in epoxy resin was successfully prepared. Then, additional systems were amended with PDMS as modifier into epoxy- TiO_2 nanocomposite to develop epoxy-PDMS hybrid polymeric coating systems. The aims for both developed coating systems are to study the effect of low concentration of TiO_2 in two different polymeric based, epoxy and epoxy-PDMS matrices. The structure, thermal, and optical properties of all developed coating systems were investigated by FTIR, DSC, and UV-Vis, respectively. Moreover, FESEM, EDX, and AFM were employed to reveal the morphologies of the developed systems. The wettability of the resultant systems was determined by using contact angle method. As for, the barrier properties of the developed coating systems and the corrosion protection performance were investigated via EIS after exposing the cold rolled mild steel coated substrates to 3.5% NaCl solution up to 30 days.

EXPERIMENTAL

Materials

Epoxy resin (EPIKOTE 828) produced from a polycondensation reaction between bisphenol A and epichlorohydrin with an equivalent weight of 184–190 g/eq and viscosity of 12,000–14,000 cP at room temperature was purchased from Asachem (Malaysia) and used as the base resin. Modifier used was hydroxyl-terminated polydimethylsiloxane (HT-PDMS) with a viscosity of 750 cSt and a density of 0.97 g/ml at room temperature was supplied by Sigma-Aldrich (Malaysia) and used as the modifier for the epoxy resin. In order to develop the hybrid epoxy-PDMS polymeric matrix, 3-aminopropyltriethoxysilane (KBE-903) purchased from Shin-Etsu Chemical Co. Ltd (Japan) was used as the coupling agent. The development of all

nanocomposite coating systems was carried out via the utilization of titanium (IV) oxide nanoparticles of anatase crystalline structure with diameter < 25 nm and density of 3.9 g/mL at room temperature which was supplied by Sigma-Aldrich (Malaysia). Cycloaliphatic amine with an amine value of 260–285 mg KOH/g and an equivalent weight of 113 g/eq and acted as the curing agent and purchased from Hexion (Malaysia). All listed chemicals were used as received from the supplier without any further modification or purification.

Substrates Preparation and Coating Application

Cold rolled mild steel substrates with dimensions of $5 \times 7.5 \times 0.1$ cm were employed as the tested substrate to be coated. The steel panels were first degreased and cleaned using acetone then the pretreated specimens were subjected to sandblasting process according to ASTM D609 standard to achieve Sa 2½ surface profile followed by wiping the resulted surfaces with acetone once again to clean off the dust and any other impurities deposited from the sandblasting process. The brushing method was used to developed all coating films which were kept to dry for 7 days at room temperature. The dry film thickness was selected to be in the range of 75 ± 5 µm and was tested via using Elcometer 456 thickness gauge for three replicate coated panels. The coated steel substrates were used to perform FESEM and EIS tests. However, free films were cast onto Teflon plates in order to obtain FTIR testing samples. Transparent glass plates with a size of $2.54 \times 7.62 \times 0.12$ cm were also prepared and subjected to one side coating in order to perform AFM, contact angle measurements and ultraviolet-visible spectroscopy tests.

Preparation of Coating Systems

Neat epoxy coating system designated as (E) and cured with cycloaliphatic amine at mixing ratio (10:6) was developed and used as the reference system. The epoxy and curing agent blend was subjected to continuous stirring for 15 min at 750 rpm prior to the coating application. Different loading ratio of TiO₂ nanoparticles specifically, 0.1, 0.2, and 0.3 wt. % were utilized in order to prepare three different systems of epoxy-based nanocomposite coating systems named as ET1, ET2, and ET3, respectively. For this end, the different loading ratios of TiO₂ nanoparticles were first introduced to the calculated amount of the cycloaliphatic amine curing agent with the assistance of sonication process for 30 min. Then the epoxy resin was added and the resulting blend was subjected to sonication process for 10 min followed by constant stirring for 15 min at 750 rpm. Better dispersion state of the TiO₂ nanoparticles was expected to be achieved by introducing the nanofillers to the curing agent first followed by mixing the resulting blend with the epoxy base resin. This idea was supported by the 2017 work of Pourhashem et al., that reported the efficiency of this method in developing better dispersion of graphene oxide nanosheets within epoxy resin with the presence of polyamide curing agent which is characterized with lower viscosity comparing to epoxy resin (Pourhashem et al., 2017). To further improve the corrosion protection performance and to fulfill the hydrophobicity of the developed coated surfaces, the epoxy resin was modified with PDMS at (9:1)

mixing ratio with the presence of 3-aminopropyltriethoxysilane as a coupling agent. Prior to the addition of the curing agent, epoxy resin, PDMS, and a stoichiometric equivalent of 3-aminopropyltriethoxysilane were mixed using a glass rod until the mixture appeared to be homogeneous. Then the resulting blend together with the calculated amount of cycloaliphatic amine curing agent was magnetically stirred for 15 min at 750 rpm and then applied on both sides of cold rolled mild steel substrate as EP coating system. Then, the modified epoxy-PDMS polymeric blend was used as the host matrix for different loading ratios of TiO₂ nanoparticles specifically, 0.1, 0.2, and 0.3 wt. % in order to fabricate EPT1, EPT2, and EPT3 nanocomposite coating systems, respectively. The TiO₂ nanoparticles and cycloaliphatic amine blends were subjected to 30 min of sonication process prior to the addition of epoxy resin, PDMS and 3-aminopropyltriethoxysilane. The resulting mixtures were then subjected to sonication process for 10 min and mechanical stirring for 15 min at 750 rpm.

Characterization

Fourier Transform Infrared Spectroscopy (FTIR)

Fourier transform infrared spectroscopy (FTIR) was utilized for structural analysis. ATR-Nicolet iS10 Spectrometer from Thermo Fisher Scientific (USA) was used to obtain FTIR transmission spectra with a 32-scan data accumulation between the wavenumber of 400–4,000 cm⁻¹ at a resolution of 4.0 cm⁻¹ was acquired for all recorded spectra.

Differential Scanning Calorimetry (DSC)

The glass transition temperatures (*T_g*) of all developed coating systems was investigated by differential scanning calorimetry (DSC) using Perkin Elmer DSC800 (USA). The temperature range was varied from 25°C to 300°C with heat rate at 20°C/min under nitrogen condition with flow rate with 20 ml/min.

Field Emission Scanning Electron Microscope (FESEM)

The surface morphology and the dispersion state of the nano TiO₂ nanoparticles within the polymeric matrix was investigated by using field emission scanning electron microscopy (FESEM) FEI Quanta 450 FEG equipped with an energy dispersive X-rays analyzer (EDX) for elements mapping. It is worth to be mentioned that the coated steel panels were subjected to the application of a thin layer of a platinum coating before carried out the tests in order to minimize the charging effects.

Atomic Force Microscopy

A Bruker Multimode 8 AFM was employed for topography imaging and to measure the surface roughness of all coating systems. The measurement of the effect of TiO₂ nanoparticle in the coating system was conducted in the contact mode equipped with Scan Asyst-Air (Bruker) SPM tip (0.4 N/m spring constant). The 3D 5 µm² scanned areas were sampled at 769 equidistant points at a low scan rate of 1 Hz.

Ultraviolet-Visible (UV-Vis) Spectroscopy

To determine the photocatalytic effects of the incorporated TiO₂ nanoparticles, ultraviolet-visible (UV-vis) spectroscopy was used

with UV-3101PC (Shimadzu, Kyoto, Japan) UV-vis spectrometer in transmission mode at a wavelength range of 200–800 nm on medium-speed scanning. The UV-vis spectrometer was set in absorbance mode at the wavelength between 200 and 800 nm range and medium scanning speed. Measurements were carried out on a set of three different replicate coated glass plates.

Contact Angle (CA) Measurement

Contact Angle (CA) measurements were conducted in order to evaluate the wettability of coated surface and distinguish the effects of the embedded TiO_2 nanoparticles and modification epoxy resin with PDMS on the surface hydrophobicity state. By using Optical Contact Angle 15EC (Germany) instrument, the static contact angles were obtained by placing 5 drops of 9 μL distilled water at five different points on each coating samples with the use of a needle that located close enough to the coated surface to render the kinetic energy of the droplets negligible. Measurements were repeated for three times on three different coated samples. The results in the form of images were captured instantly and the average of five measurements was reported with $<1^\circ$ measurement error.

Electrochemical Impedance Spectroscopy (EIS)

In order to evaluate the anticorrosion performance and the barrier properties for all the developed coating systems, electrochemical impedance spectroscopy (EIS) was employed. The EIS was brought in action using a classical three electrode system consisting of 3 cm^2 area of the coated sample exposed to 3.5% NaCl distilled water solution as working electrode, a saturated calomel electrode SCE as a reference electrode and pyrolytic graphite electrode functioning as a counter electrode. All the components and connections were placed inside a Faraday cage to minimize external noise during measurement. Gamry PCI4 G300 potentiostat with 100 kHz–10 mHz frequency range at open circuit potential with a sinusoidal AC perturbation of 10 mV root mean square (rms) potential perturbation was used to perform the tests was utilized to complete the test. All the data obtained from EIS were analyzed by Gamry Echem Analyst of Version 6.03. EIS measurements were found to be reproducible after repeating the tests for three different coated substrates.

RESULTS AND DISCUSSION

Fourier Transform Infrared Spectroscopy (FTIR)

Figure 1A shows the FTIR spectra for TiO_2 nanoparticles, epoxy resin, and epoxy- TiO_2 nanocomposite coating systems. Most of the peaks in the coating systems can be traced back to the epoxy resin. Note that the epoxy resin spectrum in **Figure 1A** is the uncured epoxy resin.

The FTIR spectrum of TiO_2 nanoparticle with anatase crystalline structure showed a broad peak at 700–850 cm^{-1} and was attributed to Ti-O stretching vibration (Vasei et al., 2014). With the incorporation of TiO_2 nanoparticles into epoxy resin (ET1, ET2, and ET3), it can be slightly observed on the overlapping peaks that occurred between 700 and 850 cm^{-1} due to low percentage of TiO_2 nanoparticles presence in the epoxy

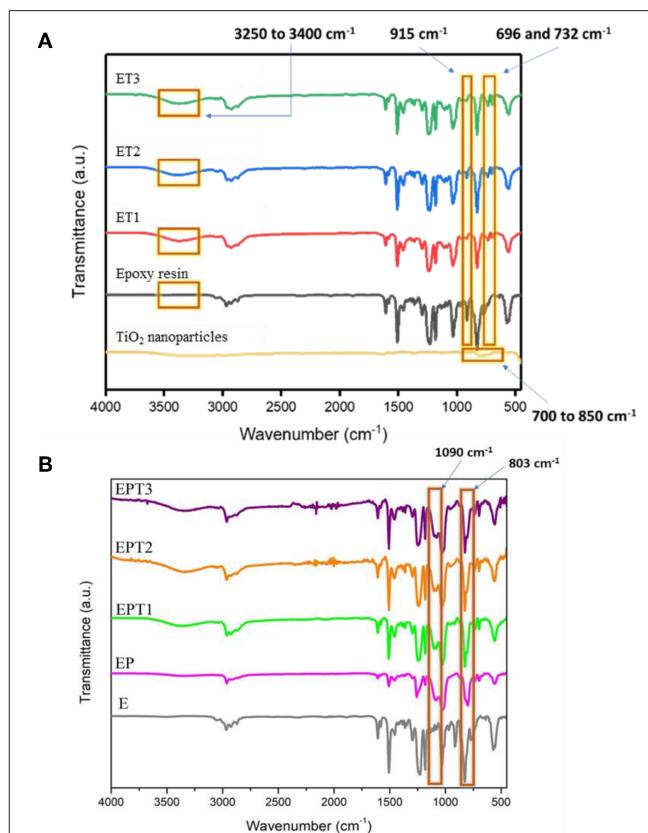


FIGURE 1 | FTIR spectrum for **(A)** TiO_2 nanoparticles, epoxy resin, and all developed epoxy- TiO_2 nanocomposite coating systems and **(B)** for E, EP, EPT1, EPT2, and EPT3 coating systems.

matrix. Compared with epoxy resin spectrum, the absorption band at 696–732 cm^{-1} varies with the nanocomposites were corresponded to Ti-O-Ti linkages in conjunction with the amine group of curing agent and epoxy matrix. This proves that TiO_2 nanoparticles are successfully obtained and incorporated into the organic matrix as the epoxy resin is being cured.

The absorption peak at 915 cm^{-1} of unmodified epoxy resin indicates the C-O deformation in the epoxide group, however, the decreased in the intensity of the peak at 915 cm^{-1} in the spectra of cured nanocomposite systems evincing the opening of the epoxide ring during curing reaction. Many studies have reported the curing reactivity of epoxy resin by using amine curing agents (Ansari et al., 2014; Moura et al., 2018). As reported by Ma et al., the curing state of epoxy resin with diamine curing agent at room temperature could be assigned to the disappearance of the absorption peak at 915 cm^{-1} in the cured neat epoxy (Ma et al., 2017). Also, the emergence of a new peak at 3,250–3,400 cm^{-1} in the cured systems instead of unmodified epoxy resin affirmed the existence of secondary amine, which is due to the stretching of the N-H bond. These peaks further assured the curing agent successfully functioned to cure the coating mixture into a film. This to be said that almost all epoxy resins are converted into

insoluble solid film due to the formation of three-dimensional thermoset networks by curing agent during the curing period (Shi et al., 2009; Ma et al., 2017).

Figure 1B depicts the FTIR spectra for unmodified epoxy resin (E), epoxy-PDMS hybrid (EP), and PDMS modified epoxy nanocomposite coating systems which are EPT1, EPT2, and EPT3. Note that 3-Aminopropyltriethoxysilane (3-APS) was used to link between epoxy and PDMS resins, thus, the cross-linking between the two polymers can be observed at some fundamental peaks. With the peaks that originate from the consequences of curing reaction as mentioned earlier still to be seen here, the new emerging peak at 803 and 1,090 cm^{-1} is ascribed to the stretching of Si-O-Si and Si-C bond which is not seen in the unmodified epoxy resin. This affirmed that PDMS was successfully incorporated with epoxy forming the desired hybrid coating systems. The coupling mechanism between epoxy and PDMS can be divided into two stages where the first stage involves the opening of the epoxide ring to react with the amino group of the 3-APS, where the primary amine tends to transform to the tertiary amine. During the second stage, PDMS tends to react with epoxy by the endorsement of the alkoxy group in 3-APS, forming the final modified epoxy-silicone structure. Moreover, the disappearance of the band 915 cm^{-1} of the unmodified epoxy spectrum has attributed the opening of the epoxide ring which revealed the intercalation of the curing agent in the epoxy matrix. A similar observation of cured epoxy-PDMS has also been reported by Ammar et al. (2016b). Also from **Figure 1B**, it can be seen the intensity spectra of EPT1, EPT2, and EPT3 are slightly increased as the amount of TiO_2 increased. This to be said that the presence of TiO_2 nanoparticle within the hybrid polymer matrices is observable on the overlapping peaks occurred between 700 and 850 cm^{-1} as in ET systems (**Figure 1A**). Dan et al. (2018) have reported the possible reason for weak peak appearance which almost invisible on these peaks could be due to the low content of TiO_2 filler in the host domain and possibly can be observed at high loading concentration of TiO_2 , that is, 10 wt.%.

Differential Scanning Calorimetry (DSC)

The DSC thermographs of E, EP, and all TiO_2 nanocomposite coating systems were illustrate in **Figures S1–S8**. Moreover, the glass transition temperatures (T_g) values were tabulated

in **Table 1**. A single glass transition temperature was observed in all reported thermographs which indicate the good curing state of the coating films and the proper crosslinking among the coating components (Radoman et al., 2014; Ammar et al., 2016b). However, the changes in the T_g values could be utilized as an indicator that illustrates the influences of PDMS and TiO_2 nanoparticles on the cross-linked structure of the epoxy polymeric matrix. As tabulated in **Table 1**, the incorporation 0.1 wt. % of TiO_2 nanoparticles within the epoxy polymeric matrix had the most pronounced effect on the T_g value which increased from 127.9°C for neat epoxy coating system to ~144°C ET1. Similar observations were reported by Radoman et al. (2015), who claimed that the epoxy resin is able to exhibit higher T_g values when it reinforced with TiO_2 nanoparticles due to the role of these particles in reducing the segments mobility at the nanoparticles-epoxy interfaces by the presence of physical attractive interactions.

Apart from that, further increasing the concentration of TiO_2 nanoparticles within the epoxy host matrix did not result in higher T_g values, contrarily, relatively lower T_g values, comparing to ET1 coating system, were recorded for ET2 and ET3 systems. This reduction in the T_g values could be ascribed to the insufficient dispersion of TiO_2 nanoparticles and its tendency to agglomerate and cluster at the high concentrations. This trend of the nanoparticles physically hinders the curing process of the coating system by blocking the formation of the continuous crosslinked network, hence, increasing the free volume and the mobility of the segments (Polizos et al., 2011; Kumar et al., 2016).

On the other hand, modifying the epoxy resin with PDMS has also influence the glass transition temperature of the resultant coating system which recorded an increment in the T_g value at 134.3°C. This was found in good correlation with FTIR results and further confirmed the good crosslinked structure among epoxy and PDMS resin. The effects of the TiO_2 nanoparticles on the thermal properties of the PDMS-epoxy polymeric matrix were found to be similar to their influences to the neat epoxy polymeric matrix as the coating system with 0.1 wt. % of TiO_2 loading ratio, EPT1, demonstrated the highest T_g value. Whereas, higher concentrations of TiO_2 nanoparticles reduce the T_g values due to the agglomeration tendency of the nanoparticles.

Surface Morphology

In order to examine the dispersion state of the embedded TiO_2 nanoparticles within the epoxy polymeric matrix, FESEM, and EDX techniques were utilized and the recorded images were illustrated in **Figure 2**. In addition to studying the distribution of the nanoparticles within the surface area, the surface properties, and phase distribution can be evaluated via FESEM. Moreover, the EDX mapping helps on gaining more understanding about the element distribution in the coating film and investigating the dispersion state of TiO_2 nanoparticles at the specimen surface. All developed epoxy-based nanocomposite coatings demonstrated surfaces free of microcracks or phase separation which is clear evidence on the effectiveness of the curing process. Moreover, the vital role of the sonication process was observed in all FESEM images that revealed a good dispersion of the nanoparticles. Due to the attraction among the nanoparticles

TABLE 1 | The glass transition temperatures (T_g) values of all developed coating systems.

System	T_g (°C)
E	127.9
ET1	143.9
ET2	137.5
ET3	135.3
EP	134.2
EPT1	142.3
EPT2	136.8
EPT3	131.4

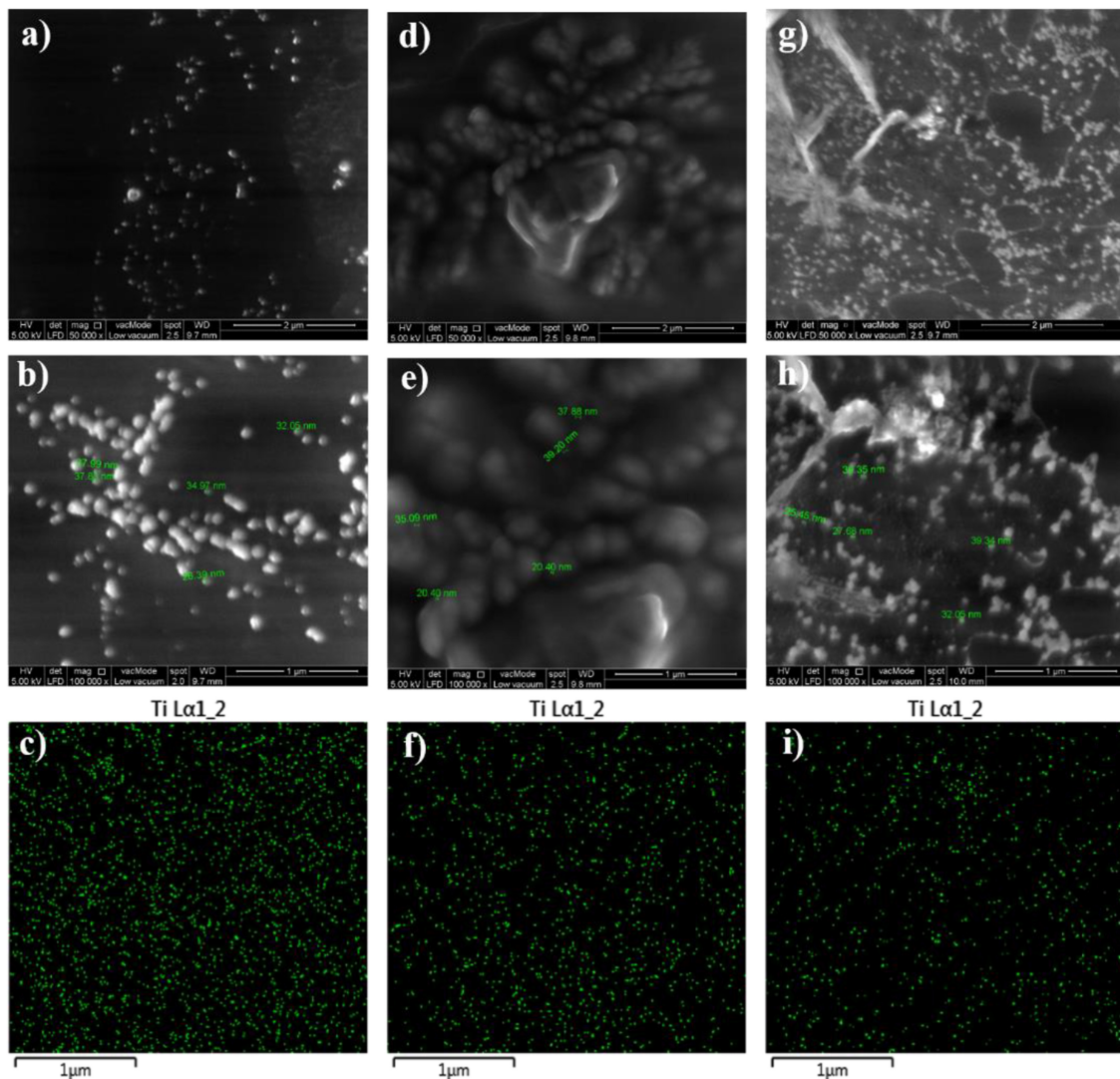


FIGURE 2 | FESEM images at x50000 and x100000 magnifications together with EDX mapping images for ET1 (a–c), ET2 (d–f), and ET3 (g–i).

and its tendency to form relatively larger agglomerated particles, the agglomeration increases as the TiO₂ nanoparticle loading ratio exceeds 0.1 wt. %. Moreover, the proper dispersion state of TiO₂ nanoparticles was further confirmed by EDX mapping results which illustrate the distribution of Ti element on the coated surfaces. In addition, the surface morphology of the TiO₂ nanocomposite coatings that developed after modifying the epoxy host matrix with PDMS resin was investigated and the FESEM and EDX images were illustrated in **Figure 3**. Surface free of cracks and phase separation confirms the compatibility of the coating components and the good curing level of the coating films. However, it was noticed that as the loading ratio of the TiO₂ nanoparticles increase, larger clusters were observed in the FESEM images especially for EPT3 coating systems. That could be attributed due to the tendency of the nanoparticles to agglomerate at the high loading ratio and to the increase of the particles amount within the unit area. EDX mapping images

were also collected for this set of samples and the results revealed the existence of well-dispersed Ti element within the coating film which is considered as a clear evidence on the appropriate introduction of TiO₂ nanoparticles within the hybrid PDMS-epoxy polymeric matrix.

Atomic Force Microscopy (AFM)

The topological properties of the developed coating systems and the changes in the surface roughness were investigated by means of AFM. **Figure 4** illustrates the 3 D topographical images of neat epoxy and all developed epoxy-TiO₂ nanocomposite coating systems. The AFM result of the neat epoxy coating system revealed a root mean square height (Sq) equal to 15.5 nm, whereas, Sq values at 2.5, 3.6, and 10.2 nm were recorded to ET1, ET2, and ET 3 coating systems, respectively. The high surface roughness of the neat epoxy coating system could be attributed to the solvent evaporation during the curing period

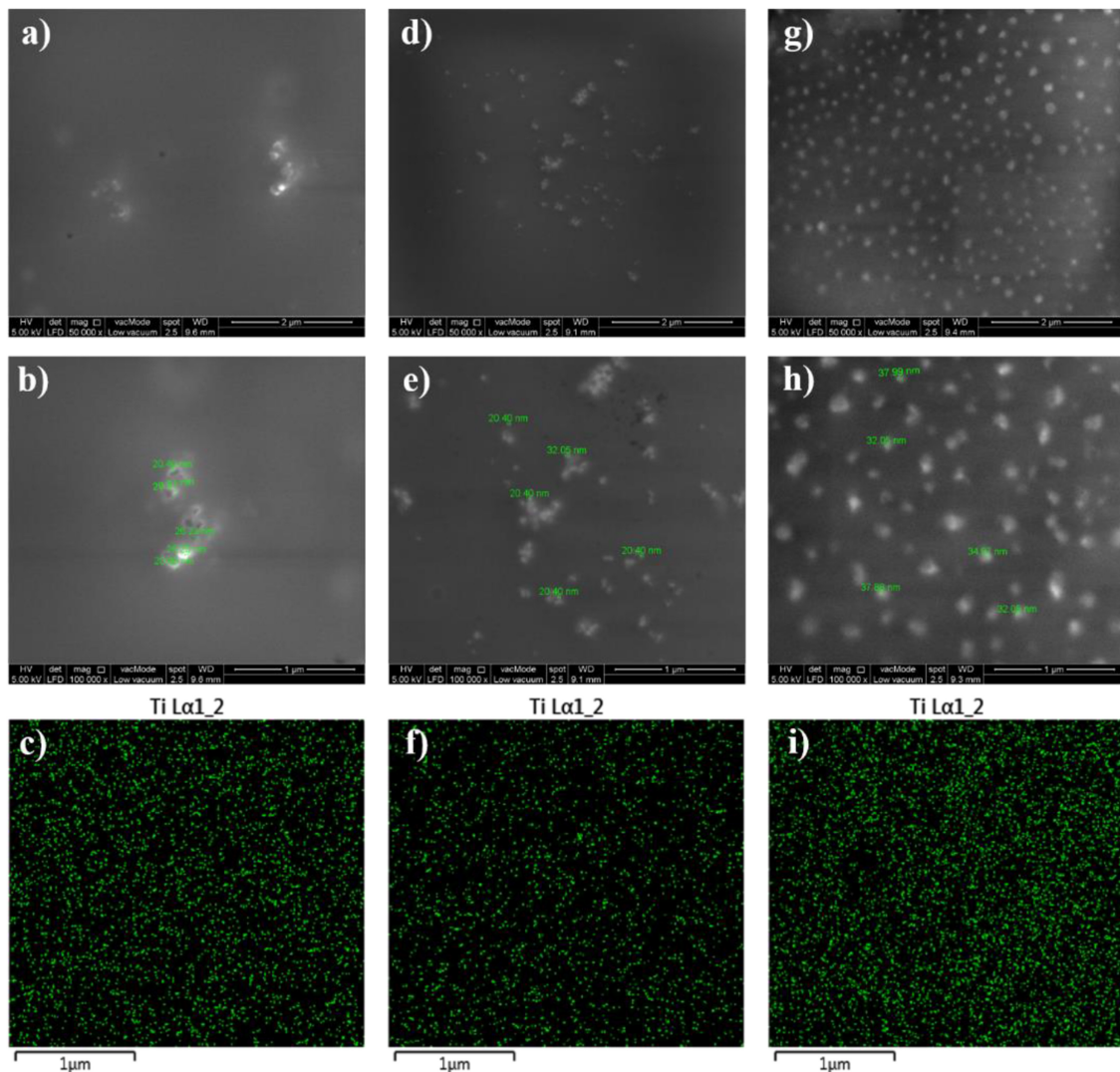


FIGURE 3 | FESEM images at x50000 and x100000 magnifications together with EDX mapping images for EPT1 (a–c), EPT2 (d–f), and EPT3 (g–i).

of the epoxy coating film which led to the formation of some holes that reduces the surface evenness (Dan et al., 2018). In contrary, a significant reduction on the surface roughness was realized after the incorporation of TiO_2 nanoparticles within the epoxy polymeric matrix especially for 0.1 and 0.2 wt. % loading ratios. That, in turn, could be considered as strong evidence on the proper dispersion state of the nano TiO_2 particles and the efficiency of the sonication process in developing a good level of dispersion state and further improving the cross-linked structure by releasing the trapped solvent from the nano-polymeric blend. However, higher surface roughness was recorded with the application of the ET3 coating system due to tendency of the TiO_2 nanoparticles to agglomerate at the higher loading ratio, therefore, increasing the cluster size of the particles (Goyat et al., 2018).

The influences of modifying the epoxy base resin with PDMS, with and without the presence of TiO_2 nanoparticles, on the

surface roughness of the resultant coated surfaces was also investigated by means of AFM and the findings in the form of 3 D topographical images were illustrated in **Figure 5**. Sq values of 5.8, 5.6, 4.1, and 12.6 nm were recorded for EP, EPT1, EPT2, and EPT3 coating systems, respectively. Comparing the Sq value of neat epoxy coating system, the addition of the PDMS has significantly reduced the roughness which could be corresponded to the greater level of crosslinking with the achievement of the better curing process. This observation was found in strong agreement with FTIR results and further confirm the compatibility among epoxy and PDMS resins. In the case of the addition 0.1 and 0.2. wt. % TiO_2 nanoparticles within the PDMS modified epoxy matrix, the AFM results did not show considerable alterations among the surface roughness which indicate the good dispersion state. However, increasing the loading ratio up to 0.3 wt. % led to change the nature of the surface toward more roughness due to the existence of a greater

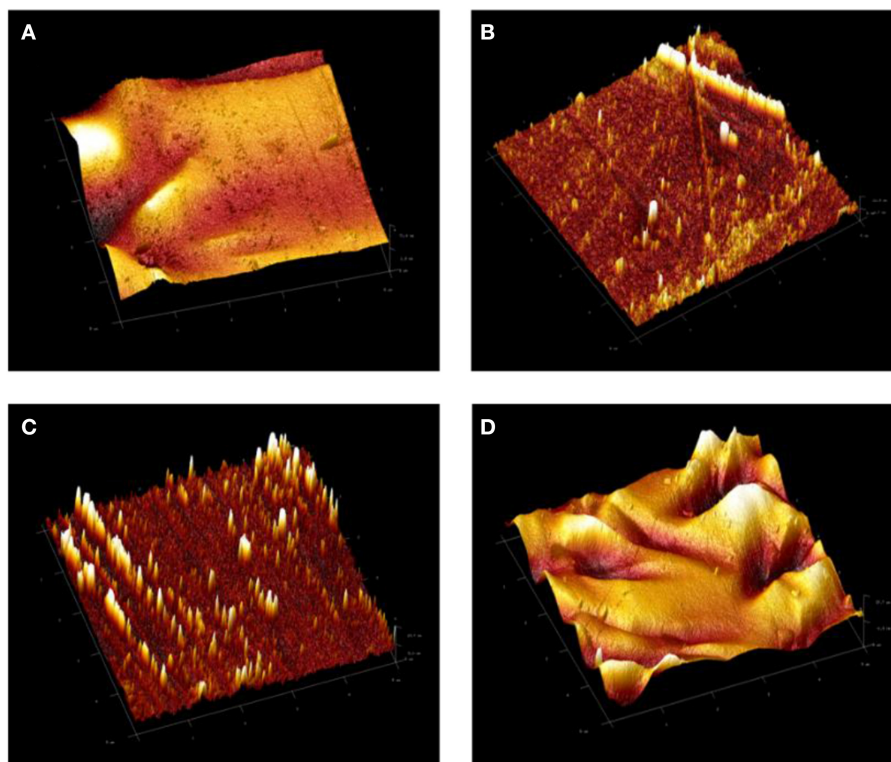


FIGURE 4 | 3D atomic force microscopy (AFM) images of (A) neat epoxy, E, coating system and (B) ET1, (C) ET2, and (D) ET3 epoxy-TiO₂ nanocomposite coating systems.

number of TiO₂ nanoparticles within the unit area, therefore, agglomeration formation.

Ultraviolet-Visible (UV-Vis) Spectroscopy

Ultraviolet-visible (UV-vis) spectroscopy was used to determine the optical properties of TiO₂ nanoparticles within the epoxy polymeric matrix. **Figure 6** shows the UV-vis absorbance spectra of all developed coating systems. As TiO₂ have a wide bandgap between valence and conduction band of 3.2 eV, it tends to absorb shorter wavelength with high energy to excite its electron (Pugachevskii, 2013), typically at the UV range below 400 nm where it does not have a specific peak within this region (Gouda and Aljaafari, 2012; Karkare, 2014; Rathod and Waghuley, 2015). Therefore, when TiO₂ nanoparticles have been incorporated within the epoxy coating, it tends to broaden the absorption region of the epoxy and significantly enhance the existing absorption intensity at around 250 nm, which is also within the TiO₂ absorption range. It can be seen that the absorption at UV range is enhanced with the incorporation of TiO₂ nanoparticles. However, as the loading ratio of incorporated TiO₂ nanoparticle increased, the UV absorption intensity at around 250 nm shows a lowering trend, this is due to the fact that UV-vis absorbance highly depends on the TiO₂ particle size (Kormann et al., 1988; Gutierrez et al., 2008). The lowering of the absorbance intensity arises from composites' cluster morphology. The absorption intensity of all coating

system developed using epoxy-PDMS hybrid polymeric matrix namely, EP, EPT1, EPT2, and EPT3 is lower compared to neat epoxy coating. This can be attributed due to the formation of intercalation network among the two polymers and changed the conformational structure of neat epoxy coating. However, when the TiO₂ nanoparticles were embedded within the epoxy-PDMS hybrid matrix, broadening, and increasing of absorption intensity at the same wavelength peak observed as the amount of TiO₂ nanoparticles increased. This observation can further confirm that TiO₂ nanoparticle tends to enhance the UV absorption within their active absorption region. Due to its light-respond capability, it can be suggested on the future work that the presence of TiO₂ nanoparticle in coating development can improve the photogenerated cathodic protection of metals and might help from discoloration of coating product under UV illumination.

Contact Angle (CA) Measurement

Water contact angle measurements (CA) were carried out for all prepared coating systems in order to investigate the wettability state of the developed coated surfaces and to determine the roles of the incorporated PDMS resin and the embedded TiO₂ nanoparticles in manipulating the wettability characters of epoxy-based coatings. **Table 2** tabulate all contact angle values with its correspondent drop image at the respective coating surfaces. The hydrophilic nature of the epoxy coatings was

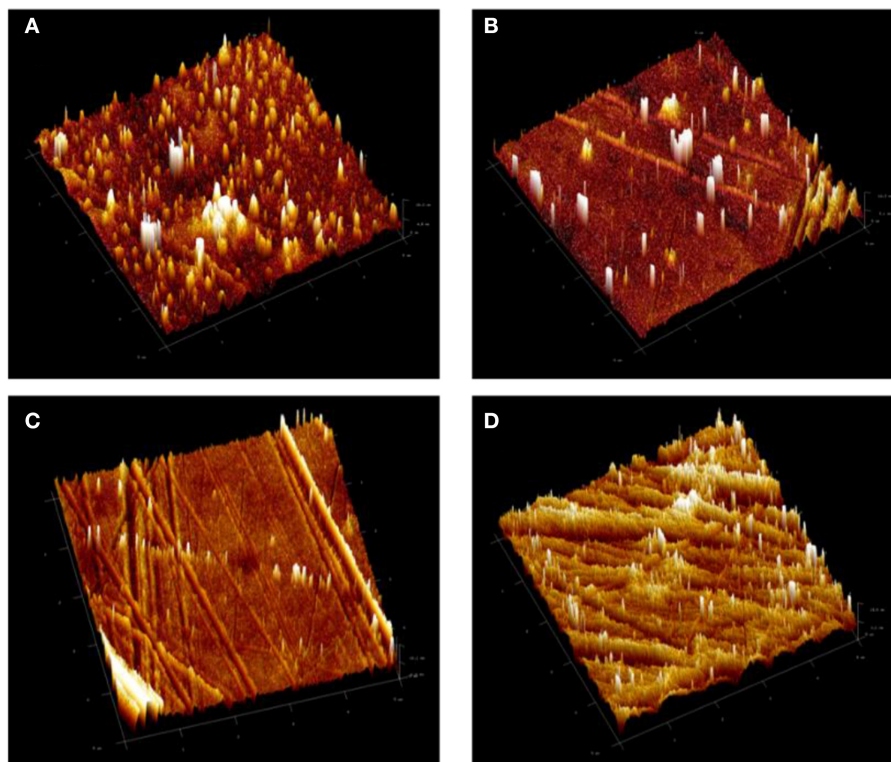


FIGURE 5 | 3D atomic force microscopy (AFM) images of (A) PDMS modified epoxy, EP, coating system and (B) EPT1, (C) EPT2, and (D) EPT3 PDMS modified epoxy-TiO₂ nanocomposite coating systems.

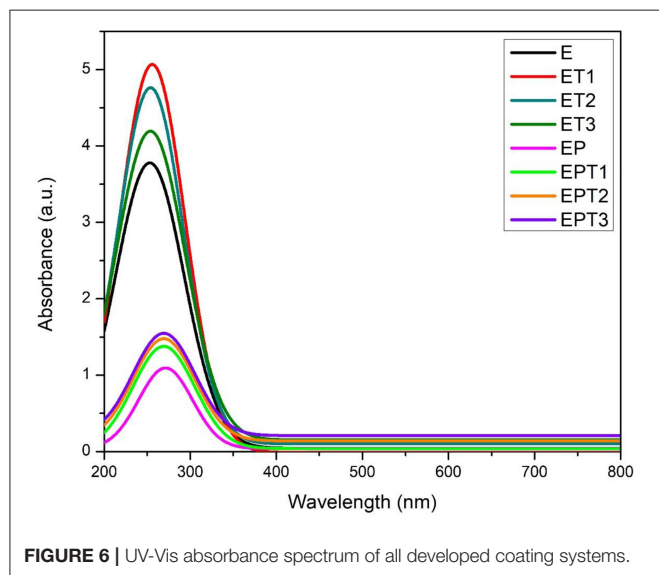


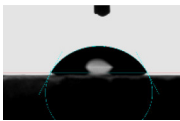
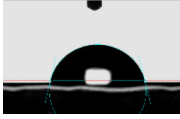
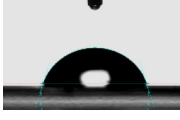


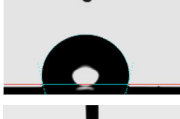


FIGURE 6 | UV-Vis absorbance spectrum of all developed coating systems.

confirmed as the substrate coated with the E coating system demonstrated a CA value equal to $\sim 63^\circ$. The introducing TiO₂ nanoparticles within the epoxy polymeric matrix was able to enhance the wettability of the coating film toward more hydrophobicity. However, as the surface is characterized as a hydrophobic surface when the contact angle values reach

or exceed 90° , none of the utilized loading ratios of TiO₂ nanoparticles has resulted in that. Despite that, an increase of $\sim 14^\circ$ in the CA values was gained by the surface coated with the ET1 coating system further confirm the excellent dispersion state of the 0.1 wt. % TiO₂ nanoparticles among the epoxy matrix. This observation could be attributed due to the fact that the existence of the appropriate amount of inorganic nanoparticles within the polymeric based coating system could alter the surface roughness and results in more hydrophobicity (Park et al., 2014). It was interesting to note that CA results were found to be in strong agreement with AFM findings as the substrate coated with E coating systems shows a higher value of surface roughness. This explains the lower contact value of neat epoxy coating system since the rougher surface area will lead to the spreading of the water droplet among the grooves (Asadi et al., 2019). While the incorporation of TiO₂ nanoparticles, with the assist of the sonication process, resulting in a lower degree of surface roughness, hence, shifting the wettability state toward more hydrophobic nature (Vázquez-Velázquez et al., 2018). It is worth mentioning that no further improvement was realized with the application of ET2 and ET3 coating systems due to the tendency of the nanoparticles at the higher loading rates to agglomerate and affect the bulk properties rather than the surface characteristics (Ramezanzadeh et al., 2011).

A hydrophobic surface was recorded after the application of EP coating with CA value almost reached 100° . This

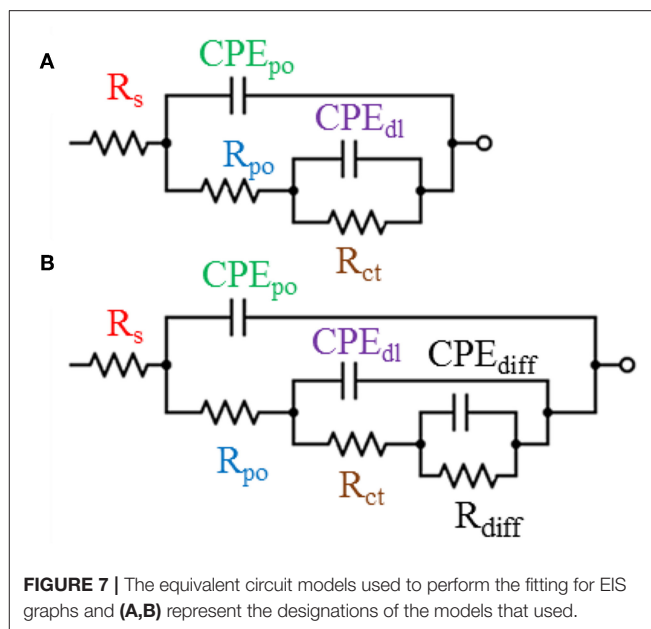
TABLE 2 | The water contact angle values of all developed coating systems.

System	Contact angle ($^{\circ}$)	Drop image
E	62.9 ± 0.5	
ET1	77.1 ± 0.7	
ET2	72.2 ± 0.4	
ET3	69.6 ± 0.4	
EP	99.7 ± 0.5	
EPT1	103.2 ± 0.3	
EPT2	100.9 ± 0.4	
EPT3	98.2 ± 0.3	

result was in complete agreement with finding reported by many researchers who proved the ability of PDMS resin to enhance the hydrophobicity of epoxy coatings due to its low surface energy (Eduok et al., 2017). The highest CA value obtained by EPT1 coating system which further confirms the compatibility among the coating components, the good cross-linked structure of the coating film and proper dispersion of TiO_2 nanoparticles with the hybrid epoxy-PDMS polymeric matrix.

Electrochemical Impedance Spectroscopy (EIS)

Electrochemical impedance spectroscopy was performed to investigate the effects of adding different loading ratios of TiO_2 nanoparticles on the barrier properties and the corrosion protection performance of the epoxy-based coating systems. Moreover, EIS was also utilized to investigate the role of PDMS in improving the electrochemical behavior



of epoxy coating and epoxy- TiO_2 nanocomposite coating against corrosion. After exposing the coated samples to 3.5% NaCl solution, the EIS measurements were carried out periodically and the collected results were presented graphically with Bode and Nyquist plots after 1 and 30 days of immersion time.

To explain the electrochemical behavior of all developed coating systems after different periods of immersion time, two models of the equivalent circuits were utilized and illustrated in **Figure 7**. As the exposure time elapsed, the electrolyte attempted to penetrate through the coating film toward the coating–substrate interface causing the initiation of the corrosion reaction. However, the corrosion protection obtained by the coating film at this stage could be understood by analyzing the electrochemical response with the assist of Model A of the equivalent circuit which composes of the following elements: a resistor R_{po} and a constant phase element (CPE_{po}), which describes the electrolyte resistance through the film pores, and its associated (CPE_{po}). Also, this model includes a parallel combination of a resistor which represents the charge transfer resistance (R_{ct}) and constant phase element as the double layer capacitance (CPE_{dl}). The aforementioned components represent the resistance obtained by the coating film against the corrosion reaction. In order to distinguish the coating systems that are unable to withstand corrosion and failed in isolating the substrate's surface to be in direct contact with the penetrated electrolyte, Model B of the equivalent circuit was introduced. In addition to the previous elements that used to build up Model A, new constant phase element and resistor were added to Model B namely constant phase element of corrosion products diffusion capacitance (CPE_{diff}) and corrosion products diffusion resistance (R_{diff}). Hence, by mean of Model B, the resistance obtained by the coating film against the diffusion of the corrosion

products from the substrate active sites at the coating-substrate interface could be represented. It is worth mentioning that both proposed equivalent circuit models include a resistor element R_s which serves as the solution resistance and had no significant technical or theoretical information about the developed coating systems, therefore, it was not included in this study (Ammar et al., 2016c).

Figure 8 illustrates the Bode and Nyquist plots for neat epoxy and all developed epoxy-TiO₂ nanocomposite coating systems after 1 day of immersion time. Even after this short period of exposure, the poor barrier properties and weak corrosion protection performance was obvious for E coating system as two-time constants and corresponded two semicircles was observed in Bode and Nyquist pots, respectively. Model B of the equivalent circuit was found to obtain the best numerical fitting for the EIS data which further indicates the initiation of the corrosion process and the formation of the corrosion products that cause the delamination of the coating film from the metal substrate. Similar observations were published by Pourhashem et al., who have investigated the corrosion protection performance of epoxy-based coating systems applied to mild steel substrates. The reported results indicate the poor barrier properties of neat epoxy coating system after only 1 day of exposure time to 3.5%

NaCl electrolyte even when it is applied at a larger thickness up to $150 \pm 10 \mu\text{m}$ (Pourhashem et al., 2017). Moreover, the weak corrosion protection performance of epoxy based coating systems after such a short period of immersion time was reported by several researchers who studied the performance of neat epoxy coating films that applied with different thickness specifically at $120 \mu\text{m}$ (Chang et al., 2014), $130 \mu\text{m}$ (Li et al., 2015), and $250 \mu\text{m}$ (Wang et al., 2018).

However, the incorporation of different loading rates of TiO₂ nanoparticles within the epoxy polymeric matrix has significantly enhanced the barrier properties of the coating films as only a slight bending of the Bode plots at the low-frequency region, as well as, one semicircle in the Nyquist plots which both fitted with model A of the equivalent circuit. These findings could be attributed to the vital role of the incorporated TiO₂ nanoparticles in modifying the network structure of the epoxy polymeric matrix where the embedded nanoparticles contributed in reorganizing the polymeric matrix by the physical interactions due to Van Der Waal's force that helps in closing up the pores of the epoxy matrix, hence, forcing the penetrated electrolyte to travel a longer distance in order to reach the substrate surface and lead to the corrosion reaction initiation (Ramezanzadeh et al., 2016b; Basiru et al., 2018). However, as the immersion

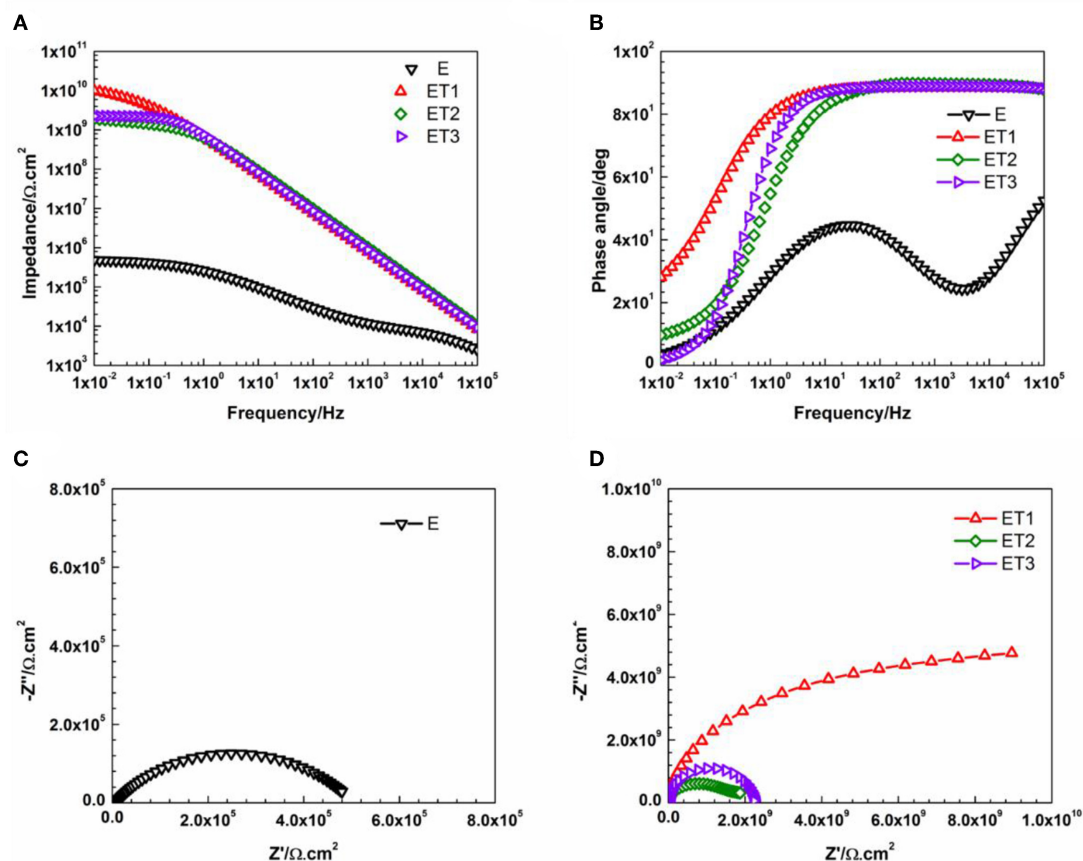


FIGURE 8 | Representative (A) Bode plots and (B) phase angle plots for all prepared epoxy-based coating systems, (C) Nyquist plot for E coating system, and (D) Nyquist plots for all epoxy-TiO₂ nanocomposite coating systems after 1 day of immersion.

time elapsed and reached 30 days, only ET1 coating system which loading with 0.1 wt. % of TiO_2 nanoparticles manage to obtain performance stability and perfectly protect the steel substrate from being corroded. The observation of Bode and Nyquist plots of ET1 coating systems, illustrated in **Figure 9**, interestingly demonstrated no changes over the immersion time period and still holding the ability to be fitted by means of

Model A of the equivalent circuit. This, in turn, implied that this small amount of TiO_2 nanoparticles was sufficient to enhance the overall performance of the coating film as the EIS finding was in strong agreement with all previously reported results.

On the other hand, all other developed coating systems namely, E, ET2, and ET3, failed to obtain the desired protection performance against corrosion as two-time constants in Bode

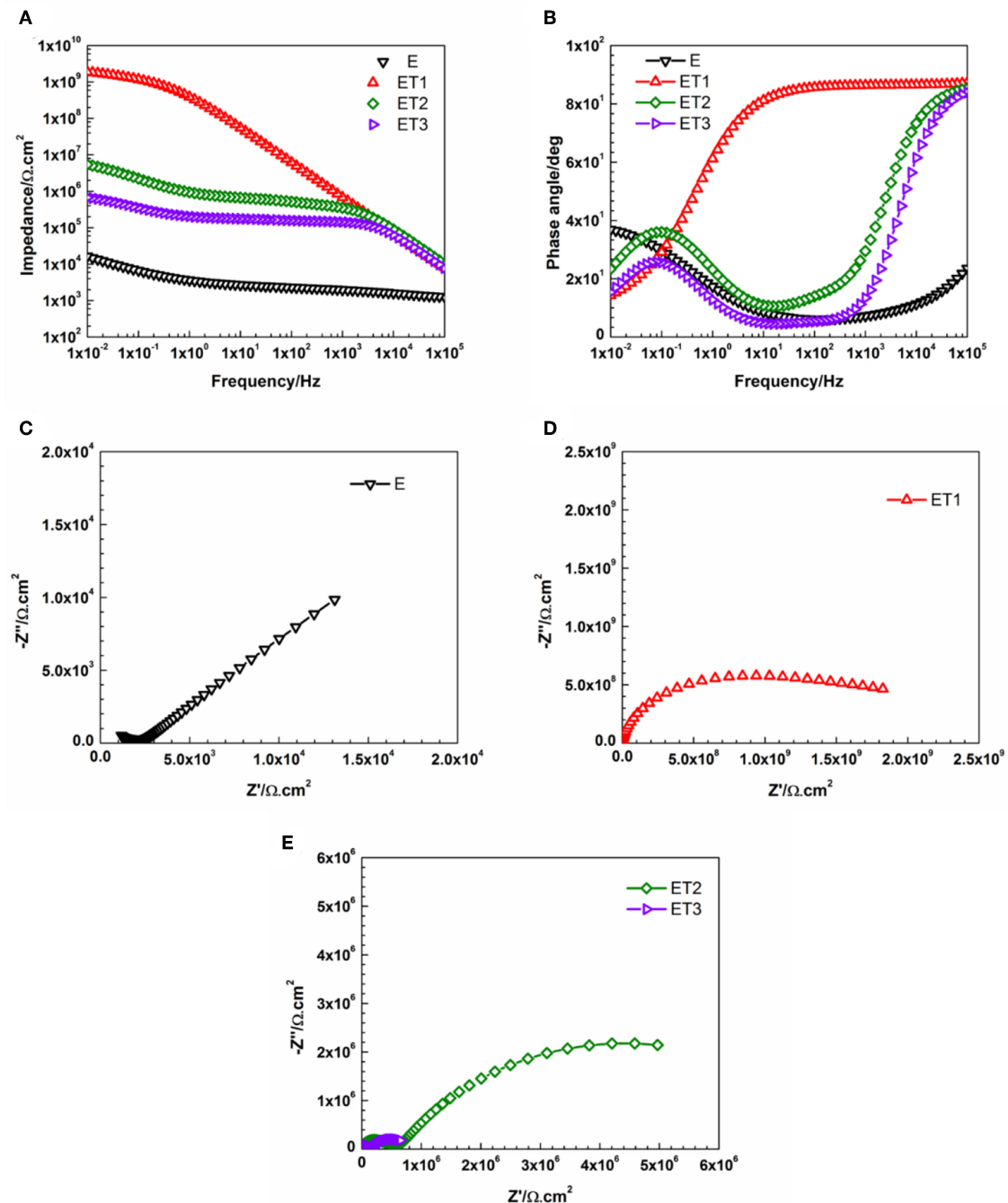


FIGURE 9 | Representative (A) Bode plots and (B) phase angle plots for all prepared epoxy-based coating systems, (C) Nyquist plot for E coating system, (D,E) Nyquist plots for all epoxy- TiO_2 nanocomposite coating systems after 30 days of immersion.

plots and two semicircles in Nyquist plots were observed and Model B of the equivalent circuit was utilized to obtain the fitting. The poor corrosion protection performance of E coating system could be attributed to the weak barrier properties of the epoxy polymeric matrix due to the presence of voids at the coating film surface and pores through the bulk structure of the coating layer. Yi et al. (2018) reported that the creation of the voids and the pores is due to the evaporation of the solvent during the curing process and the shrinkage of the coating layer. Moreover, the existence of these pores increases the free volume within the epoxy polymeric matrix and consider the main responsible of the creation of the diffusion pathways that permit the corrosive agents to penetrate through the coating

film, hence, the degradation of the corrosion protection ability (Ramezanzadeh et al., 2016a). The most pronounced effect of TiO_2 nanoparticles was realized with its loaded at 0.1 wt. %, within ET1 coating system. That could be attributed to the proper dispersion of the nano reinforcing agents within the polymeric matrix, hence, reducing the porosity and zigzagging the diffusion pathway. However, the EIS findings revealed that the further addition of TiO_2 nanoparticles did not significantly enhance the corrosion protection performance of the polymeric matrix. The 2016 work of Kumar et al., discuss the effects of different concentrations of TiO_2 nanoparticles on the epoxy matrices and have concluded that the higher loading ratios of TiO_2 could affect its dispersion state and led to the formation of larger

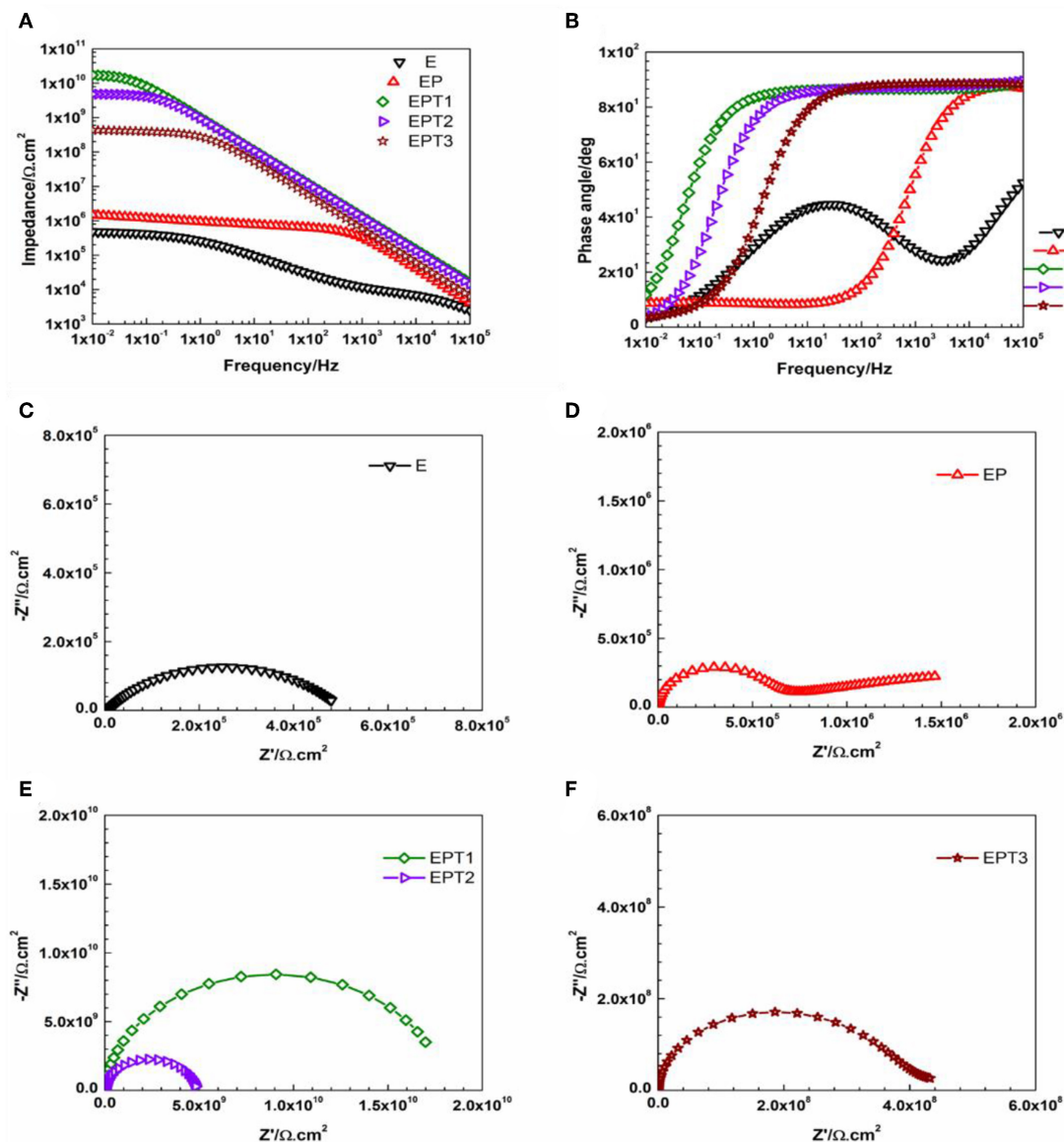


FIGURE 10 | Representative (A) Bode plots and (B) phase angle plots for E, EP, and all PDMS modified epoxy nanocomposite coatings, and Nyquist plots for (C) E, (D) EP, (E) EPT1 and EPT2, (F) EPT3 coating systems after 1 day of immersion.

clusters, hence, alter the contact among the nanoparticles and the epoxy matrix and narrow their interaction that is essential for the interfacial adhesion (Kumar et al., 2016). Furthermore, the numerical values of all parameters that have been obtained by fitting the EIS data of E coating system and all epoxy-TiO₂ nanocomposite coating systems after 1 and 30 days of immersion time with its respective equivalent circuit models were tabulated in **Tables S1, S2**, respectively.

Recently, several studies confirmed the development of better corrosion protection performance of polymeric based coating systems that possess hydrophobic nature (Huang et al., 2019; Zhang et al., 2019; Zhu et al., 2019). Therefore, the wettability of the developed coated surfaces become to be considered as

one of the indicators about the corrosion protection ability of the coating system. In this study, attempts have been made to enhance the hydrophobicity by modifying the epoxy base resin with PDMS. From **Figures 10, 11**, which represent the Bode and Nyquist plots of E, EP and all PDMS modified epoxy nanocomposite coating systems after 1 and 30 days of immersion time, respectively, it can be seen that utilizing PDMS resin as a modifier have enhanced the barrier properties of the coating film and ensure the performance stability of the coating system over the whole periods of immersion time. Even though the EIS data for EP coating system was found to be perfectly fitted with Model A of the equivalent circuit after 1 and 30 days of immersion time, but the bending of

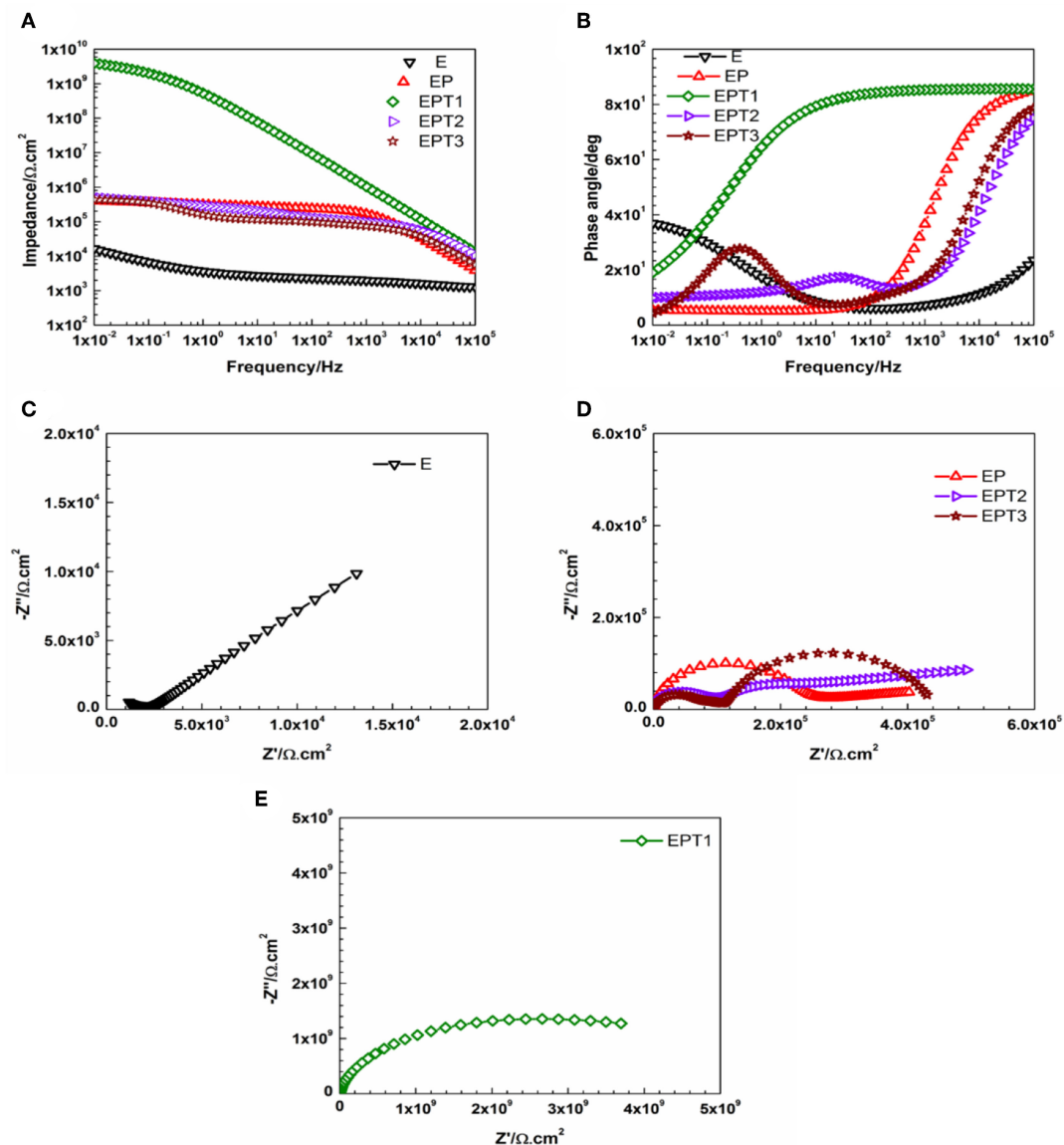
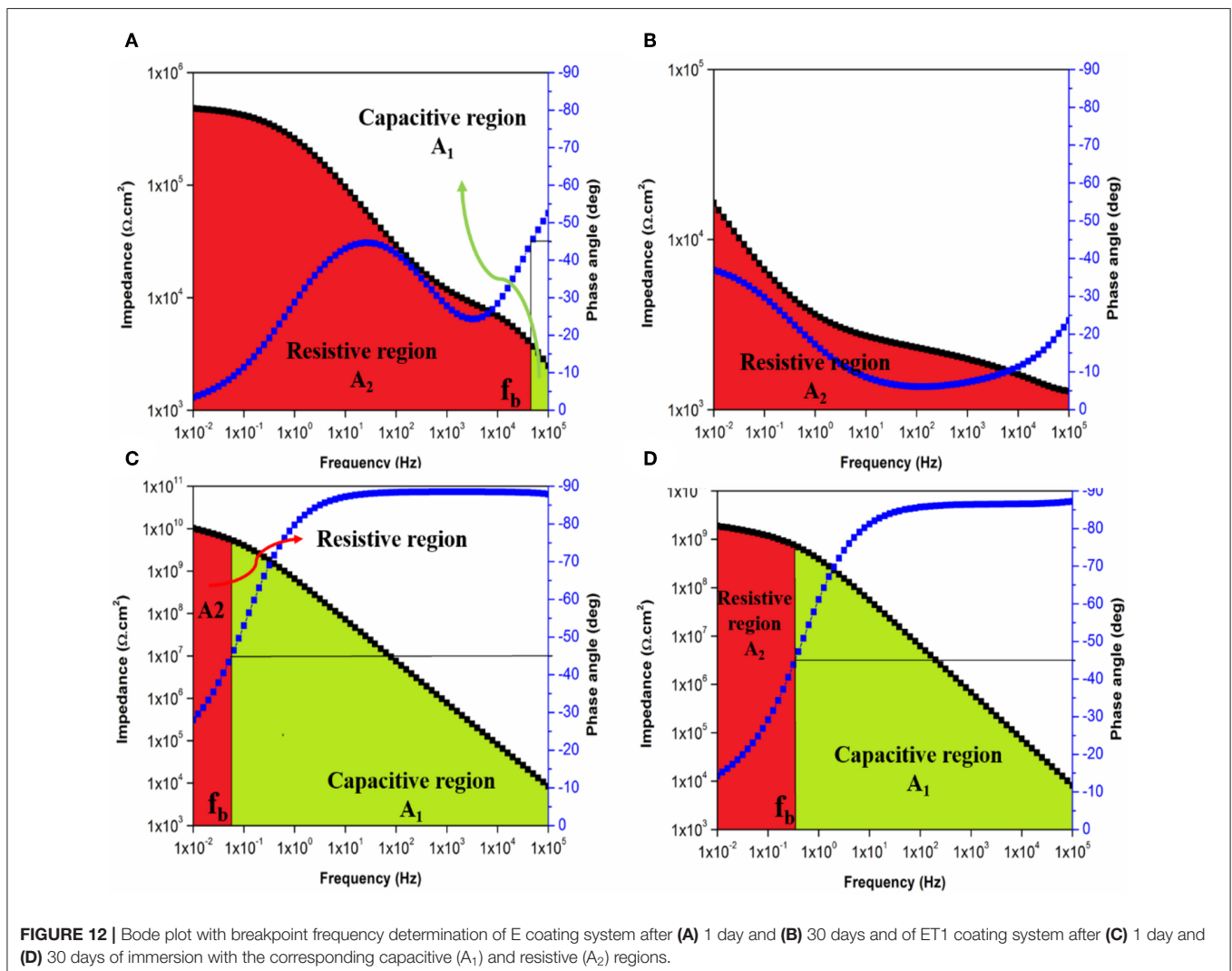


FIGURE 11 | Representative (A) Bode plots and (B) phase angle plots for E, EP, and all PDMS modified epoxy nanocomposite coatings, and Nyquist plots for (C) E, (D) EP, EPT2, and EPT3, (E) EPT1 coating systems after 30 days of immersion.

the Bode plot at the high-frequency region and the small diameter of the semicircle in the Nyquist plot indicate a fair corrosion ability. Similar observations were reported by Ammar et al. who utilized the breakpoint frequency concept to the analysis the stability of the epoxy-PDMS hybrid coating system and concluded with that fact that as the immersion time elapsed, larger resistive region and relatively smaller capacitive region are observed in the area under the Bode plot which resulted from the shifting of the breakpoint frequency values toward the higher frequencies region, hence a reduction of the barrier properties of the coating film is occurring (Ammar et al., 2017).

Among all developed EP nanocomposite coating systems, the most pronounced enhancement was recorded for EPT1 coating system as a Bode plot with slight bending at the low-frequency region and Nyquist plot with one semicircle after 1 and 30 days of immersion time indicate the capacitive behavior and the stability of the coating film over the whole period of exposure without any significant signs for coating deterioration or loss of the intact barrier properties. Model A of the equivalent

circuit was used to obtain the numerical fitting for both EIS graphs after 1 and 30 days of immersion time. Furthermore, it was interesting to notice that 0.1 wt. % of TiO_2 nanoparticles was found to be the optimum loading ratio that results in the best corrosion protection performance for both utilized polymeric matrices namely, neat epoxy and PDMS modified epoxy matrix. Apart from that, more stability against corrosion was realized for EPT1 coating system with higher impedance values over the whole periods of immersion. This could be attributed due to the role of the PDMS modifier in obtaining the hydrophobicity to the coating film. The relation among the hydrophobic character of the coated surface and its barrier properties could be explained as increasing the hydrophobicity will lead to minimizing the areas of the surface that are in direct contact with the aqueous electrolyte solution, hence, reducing the electrolyte absorption within the coating film and enhance its barrier properties. Moreover, the existence of good dispersed TiO_2 nanoparticles within the PDMS modified epoxy matrix magnified the protection obtained by the coating film against the penetration of the electrolyte toward the coating—substrate



interface by filling up the matrix pores and zigzagging the diffusion pathways (Ammar et al., 2016a). However, as in epoxy-TiO₂ nanocomposites that mentioned above, further increasing the loading ratio of TiO₂ nanoparticles up to 0.2 and 0.3 wt. % did not show any additional improvement to the corrosion protection performance which could also attributed to the tendency of the nanoparticles to agglomerate at the high loading ratios. Furthermore, the numerical values of all parameters that have been obtained by fitting the EIS data of E, EP, and all PDMS modified epoxy nanocomposite coating systems after 1 and 30 days of immersion time with its respective equivalent circuit models were tabulated in **Tables S3, S4**, respectively.

In the ideal coating system, the applied layer covers the enter surface area of the specimen and acts as a perfect capacitor. However, as the electrolyte penetrates and reaches the substrate, it tends to settle in the microporous at the coating-substrate interface and leads to promote the corrosion process. Hence, the performance at these spots is considered

as a resistive behavior. Therefore, analyzing the areas under the bode plot and its interpretations, with the assist of breakpoint frequency values, could play a vital role in obtaining a better understanding of corrosion processes at the coating—substrate interfaces and its implications for film delamination and loss of adhesion that lead to the degradation of the protection system. Zhang et al. (2007) have investigated the delamination of TiO₂-epoxy nanocomposite coating system based on the relation suggested by Hirayama and Haruyama (1991):

$$f_b = \frac{S}{2\pi\epsilon\rho} \quad (1)$$

Where, S is the ratio of delaminated area to the original area, ρ is the coating resistivity and ϵ is the dielectric constant. Hence, the breakpoint frequency and its changes over the different period of immersion time for a giving coating system is proportional to the delaminated area. To that end, the impedance and phase angles values were plotted

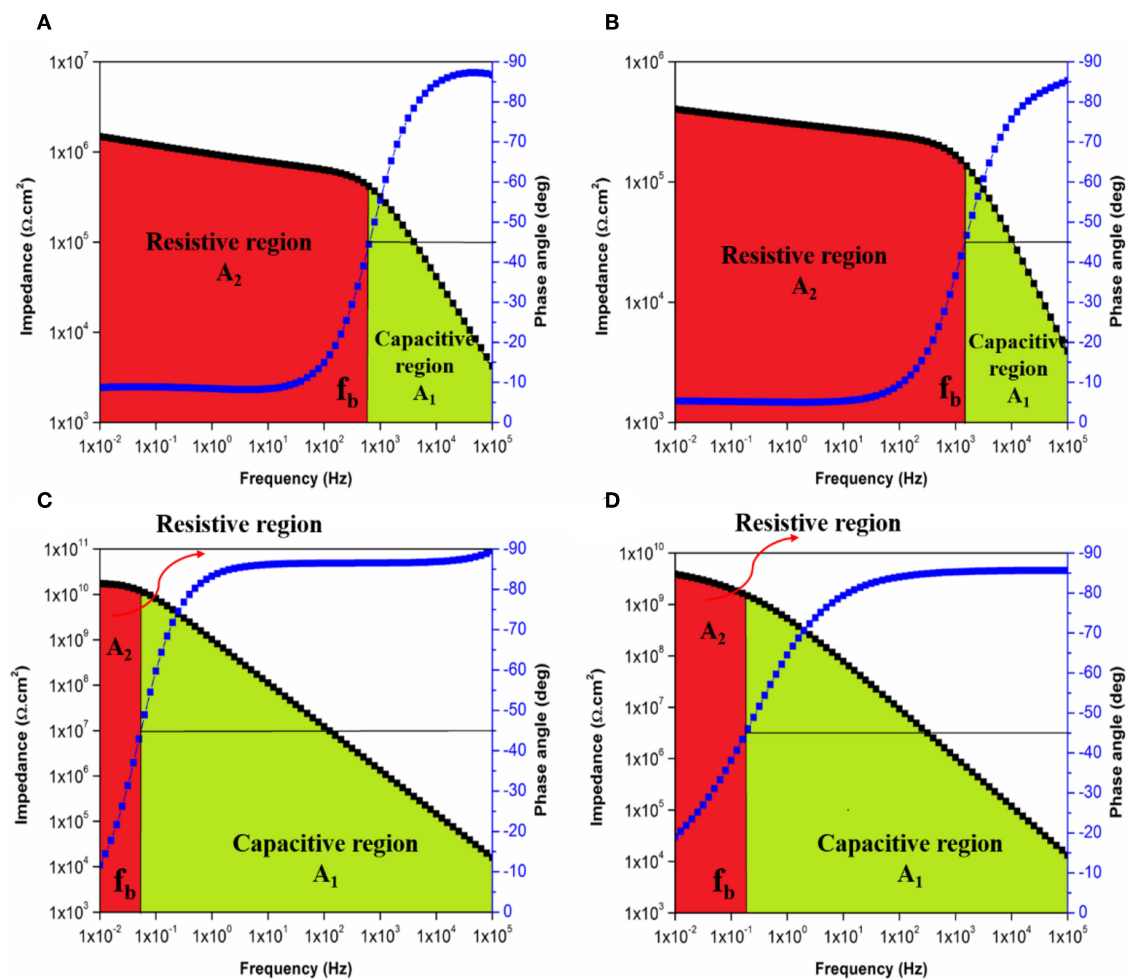


FIGURE 13 | Bode plot with breakpoint frequency determination of EP coating system after (A) 1 day and (B) 30 days and of EPT1 coating system after (C) 1 day and (D) 30 days of immersion with the corresponding capacitive (A₁) and resistive (A₂) regions.

as functions to their frequencies. After that, the intersection of the breakpoint frequency (f_b), which is defined as the frequency at 45° phase angle, with the impedance curve was considered to distinguish the different areas under the Bode plots.

With respect to the immersion time, the performance of the applied coatings could be evaluated based on the regions under the Bode plot. An intact character of the coating system is realized when the phase angle remains higher than 45° over the whole tested frequency range the area under the Bode plot is recognized as a capacitive region. While in the case of observing two areas under the Bode plot namely, capacitive and resistive regions, coating film undergoing corrosion is considered (Javidparvar et al., 2019). The failure of the coating system is confirmed when only a resistive region is observed below the Bode plot. **Figures 12A–D** illustrate the areas under Bode plot for E and ET1 coating systems based on its f_b values after 1 and 30 days of immersion. While the plots of ET2 and ET3 were illustrated in **Figures S9, S10**. **Figure 12A** shows both capacitive and resistive areas under the Bode plot of the E coating system after 1 day of immersion time. As the immersion time elapsed, only the resistive region was observed in **Figure 12B** which further indicates the poor corrosion protection performance of neat epoxy coating system. Apart from that, the incorporation 0.1 wt. % of TiO_2 nanoparticles within the epoxy polymeric matrix has significantly enhanced the barrier properties of the coating film as the lower value of breakpoint frequency was recorded, hence, relatively smaller resistive regions in the low-frequency range and larger capacitive regions are observed in **Figures 12C,D**. No further improvement was realized with increasing the TiO_2 concentrations within the epoxy polymeric matrix as higher f_b values and increased size of the resistive regions over the capacitive regions were recorded in **Tables S1, S2** and **Figures S11, S12**.

In the same manner, the influences of PDMS on the TiO_2 -epoxy nanocomposite coating systems were discussed by means of breakpoint frequencies and the areas under Bode plots were illustrated in **Figures 13A–D** for EP and EPT1 coating systems. Whereas, **Figures S11, S12** show the areas under bode plots of EPT2 and EPT3, respectively. Comparing to the neat epoxy coating system, modifying the epoxy resin with PDMS has resulted in shifting the f_b values toward the lower frequency region, therefore, increases the size of the capacitive region over the resistive region as observed in **Figures 13A,B**. The most pronounced improvement was realized, in **Figure 13C**, for EPT1 coating system as the lowest f_b values, the largest capacitive region and smallest resistive region were recorded after 1 day of immersion time. Moreover, the remarkable stability of the aforementioned coating system against the initiation of corrosion whereby the coating layer successfully prevented the penetration of corrosive agents was confirmed due to the non-significant changes in the f_b values up to 30 days of immersion time. However, no further improvement was recorded as the loading ratio of TiO_2 nanoparticles reached 0.2 and 0.3 wt. % due to

the tendency of the nanoparticles to agglomerate and form larger clusters.

CONCLUSION

Different loading ratios of TiO_2 nanoparticles were introduced within epoxy resin by the utilization of the solution intercalation method with the presence of the sonication process. Several characterization techniques were employed to evaluate the overall performance of the developed nanocomposite coating systems. FTIR and DSC results revealed the achievement of proper crosslinked structure of the epoxy-based coating systems with the presence of cycloaliphatic amine curing agent and the observation of single glass transition temperature in all recorded thermographs. Moreover, the dispersion state of TiO_2 nanoparticles within the epoxy was investigated by FESEM and EDX. The Findings confirmed the efficiency of the sonication process and room temperature curing process in achieving good dispersion of TiO_2 nanoparticles especially when it is loaded at 0.1 wt. %. The incorporation of TiO_2 nanoparticles demonstrated a photocatalytic effect on the coating film as increased the absorbance at UV region. Lower surface roughness, higher CA values and better corrosion protection performance were recorded for all TiO_2 nanocomposite coating systems and the most pronouncing effect was realized with the utilization of 0.1 wt. % loading ratio. The reported finding revealed the compatibility of TiO_2 nanoparticles to be embedded within the epoxy matrix and its ability to physically interact with the epoxy network resulting in high T_g values and better barrier properties via reducing the porosity and zigzagging the diffusion pathway of the polymeric matrix. Furthermore, PDMS resin was used to modify the epoxy-based resin and the hybrid polymeric matrix was used to host different loading ratio of TiO_2 nanoparticles. Similiter to epoxy- TiO_2 nanocomposites, good curing level with proper dispersion state of TiO_2 nanoparticles were recorded with the presence of PDMS modifier. The low surface energy of PDMS resin led to alter the wettability of the epoxy resin toward more hydrophobic character. Moreover, 0.1 wt. % of TiO_2 nanoparticles was also confirmed to be the optimum concentration that significantly enhanced the barrier properties and corrosion protection ability of the coating film. Therefore, PDMS resin was confirmed to be a suitable modifier that is able to enhance the hydrophobicity of the resulting coated surfaces without alter the curing level, glass transition temperature, dispersion state and the corrosion protection performance of TiO_2 -epoxy nanocomposite coating systems.

DATA AVAILABILITY STATEMENT

All datasets generated for this study are included in the article/**Supplementary Material**.

AUTHOR CONTRIBUTIONS

AS, CC, and IW prepared the samples, carried out the characterizations, data analysis, and wrote the manuscript. SB

and VB assisted in performing the tests and data analysis. RK and RS supervised the overall research work and finalized the manuscript.

ACKNOWLEDGMENTS

Authors would like to thank the University of Malaya and the Ministry of Education, Malaysia for supporting this study by

providing the fundamental research grants FP036-2018A and IIRG007C-19IISS.

SUPPLEMENTARY MATERIAL

The Supplementary Material for this article can be found online at: <https://www.frontiersin.org/articles/10.3389/fmats.2019.00336/full#supplementary-material>

REFERENCES

- Ahmad, S., Gupta, A., Sharmin, E., Alam, M., and Pandey, S. (2005). Synthesis, characterization and development of high performance siloxane-modified epoxy paints. *Prog. Org. Coat.* 54, 248–255. doi: 10.1016/j.porgcoat.2005.06.013
- Ammar, S., Ramesh, K., Ma, I., Farah, Z., Vengadaesvaran, B., Ramesh, S., et al. (2017). Studies on SiO₂-hybrid polymeric nanocomposite coatings with superior corrosion protection and hydrophobicity. *Surf. Coat. Technol.* 324, 536–545. doi: 10.1016/j.surfcoat.2017.06.014
- Ammar, S., Ramesh, K., Vengadaesvaran, B., Ramesh, S., and Arof, A. (2016a). Formulation and characterization of hybrid polymeric/ZnO nanocomposite coatings with remarkable anti-corrosion and hydrophobic characteristics. *J. Coat. Technol. Res.* 13, 921–930. doi: 10.1007/s11998-016-9799-z
- Ammar, S., Ramesh, K., Vengadaesvaran, B., Ramesh, S., and Arof, A. (2016b). Amelioration of anticorrosion and hydrophobic properties of epoxy/PDMS composite coatings containing nano ZnO particles. *Prog. Org. Coat.* 92, 54–65. doi: 10.1016/j.porgcoat.2015.12.007
- Ammar, S., Ramesh, K., Vengadaesvaran, B., Ramesh, S., and Arof, A. (2016c). A novel coating material that uses nano-sized SiO₂ particles to intensify hydrophobicity and corrosion protection properties. *Electrochim. Acta* 220, 417–426. doi: 10.1016/j.electacta.2016.10.099
- Ansari, F., Galland, S., Johansson, M., Plummer, C. J., and Berglund, L. A. (2014). Cellulose nanofiber network for moisture stable, strong and ductile biocomposites and increased epoxy curing rate. *Compos. Part A* 63, 35–44. doi: 10.1016/j.compositesa.2014.03.017
- Asadi, F., Jannesari, A., and Arabi, A. (2019). Epoxy siloxane/ZnO quantum dot nanocomposites: Model-fitting and model-free approaches to kinetic analysis of non-isothermal curing process. *Progr. Org. Coat.* 135, 270–280. doi: 10.1016/j.porgcoat.2019.06.006
- Atta, A. M., Mohamed, N. H., Rostom, M., Al-Lohedan, H. A., and Abdullah, M. M. (2019). New hydrophobic silica nanoparticles capped with petroleum paraffin wax embedded in epoxy networks as multifunctional steel epoxy coatings. *Prog. Org. Coat.* 128, 99–111. doi: 10.1016/j.porgcoat.2018.12.018
- Basiru, Y., Ammar, S., Ramesh, K., Vengadaesvaran, B., Ramesh, S., and Arof, A. (2018). Corrosion protection performance of nanocomposite coatings under static, UV, and dynamic conditions. *J. Coat. Technol. Res.* 15, 1035–1047. doi: 10.1007/s11998-017-0038-z
- Brusciotti, F., Snihirova, D. V., Xue, H., Montemor, M. F., Lamaka, S. V., and Ferreira, M. G. (2013). Hybrid epoxy-silane coatings for improved corrosion protection of Mg alloy. *Corros. Sci.* 67, 82–90. doi: 10.1016/j.corsci.2012.10.013
- Chang, K.-C., Hsu, M.-H., Lu, H.-I., Lai, M.-C., Liu, P.-J., Hsu, C.-H., et al. (2014). Room-temperature cured hydrophobic epoxy/graphene composites as corrosion inhibitor for cold-rolled steel. *Carbon* 66, 144–153. doi: 10.1016/j.carbon.2013.08.052
- Dan, S., Gu, H., Tan, J., Zhang, B., and Zhang, Q. (2018). Transparent epoxy/TiO₂ optical hybrid films with tunable refractive index prepared via a simple and efficient way. *Prog. Org. Coat.* 120, 252–259. doi: 10.1016/j.porgcoat.2018.02.017
- Dolatzadeh, F., Moradian, S., and Jalili, M. M. (2011). Influence of various surface treated silica nanoparticles on the electrochemical properties of SiO₂/polyurethane nanocoatings. *Corros. Sci.* 53, 4248–4257. doi: 10.1016/j.corsci.2011.08.036
- Duraibabu, D., Ganeshbabu, T., Manjumeena, R., and Dasan, P. (2014). Unique coating formulation for corrosion and microbial prevention of mild steel. *Prog. Org. Coat.* 77, 657–664. doi: 10.1016/j.porgcoat.2013.12.002
- Eduok, U., Faye, O., and Szpunar, J. (2017). Recent developments and applications of protective silicone coatings: a review of PDMS functional materials. *Prog. Org. Coat.* 111, 124–163. doi: 10.1016/j.porgcoat.2017.05.012
- Evans, P., and Sheel, D. (2007). Photoactive and antibacterial TiO₂ thin films on stainless steel. *Surf. Coat. Technol.* 201, 9319–9324. doi: 10.1016/j.surfcoat.2007.04.013
- Fu, G., Vary, P. S., and Lin, C.-T. (2005). Anatase TiO₂ nanocomposites for antimicrobial coatings. *J. Phys. Chem. B* 109, 8889–8898. doi: 10.1021/jp0502196
- Gouda, M., and Aljaafari, A. I. (2012). Augmentation of multifunctional properties of cellulosic cotton fabric using titanium dioxide nanoparticles. *Adv. Nanopart.* 1, 29–36. doi: 10.4236/anp.2012.13005
- Goyat, M., Rana, S., Halder, S., and Ghosh, P. (2018). Facile fabrication of epoxy-TiO₂ nanocomposites: a critical analysis of TiO₂ impact on mechanical properties and toughening mechanisms. *Ultrason. Sonochem.* 40, 861–873. doi: 10.1016/j.ultrsonch.2017.07.040
- Guo, J., Yuan, S., Jiang, W., Lv, L., Liang, B., and Pehkonen, S. O. (2018). Polymers for combating biocorrosion. *Front. Mater.* 5:10. doi: 10.3389/fmats.2018.00010
- Gutierrez, J., Tercjak, A., Garcia, I., Peponi, L., and Mondragon, I. (2008). Hybrid titanium dioxide/PS-b-PEO block copolymer nanocomposites based on sol-gel synthesis. *Nanotechnology* 19:155607. doi: 10.1088/0957-4484/19/15/155607
- Heidarian, M., Shishesaz, M., Kassiriha, S., and Nematollahi, M. (2010). Characterization of structure and corrosion resistivity of polyurethane/organoclay nanocomposite coatings prepared through an ultrasonication assisted process. *Prog. Org. Coat.* 68, 180–188. doi: 10.1016/j.porgcoat.2010.02.006
- Heidarian, M., Shishesaz, M., Kassiriha, S., and Nematollahi, M. (2011). Study on the effect of ultrasonication time on transport properties of polyurethane/organoclay nanocomposite coatings. *J. Coat. Technol. Res.* 8, 265–274. doi: 10.1007/s11998-010-9297-7
- Hirayama, R., and Haruyama, S. (1991). Electrochemical impedance for degraded coated steel having pores. *Corrosion* 47, 952–958. doi: 10.5006/1.3585208
- Huang, W., Xiao, Y., Huang, Z., Tsui, G. C., Yeung, K., Tang, C., et al. (2019). Super-hydrophobic polyaniline-TiO₂ hierarchical nanocomposite as anticorrosion coating. *Mater. Lett.* 258:126822. doi: 10.1016/j.matlet.2019.126822
- Javidparvar, A. A., Naderi, R., and Ramezanzadeh, B. (2019). Epoxy-polyamide nanocomposite coating with graphene oxide as cerium nanocontainer generating effective dual active/barrier corrosion protection. *Compos. Part B Eng.* 172, 363–375. doi: 10.1016/j.compositesb.2019.05.055
- Karkare, M. M. (2014). “Estimation of band gap and particle size of TiO₂ nanoparticle synthesized using sol gel technique,” in *2014 International Conference on Advances in Communication and Computing Technologies ICACACT 2014* (Mumbai: IEEE), 1–5. doi: 10.1109/EIC.2015.7230747
- Kormann, C., Bahnemann, D. W., and Hoffmann, M. R. (1988). Preparation and characterization of quantum-size titanium dioxide. *J. Phys. Chem.* 92, 5196–5201. doi: 10.1021/j100329a027
- Kumar, K., Ghosh, P., and Kumar, A. (2016). Improving mechanical and thermal properties of TiO₂-epoxy nanocomposite. *Compos. Part B Eng.* 97, 353–360. doi: 10.1016/j.compositesb.2016.04.080
- Kumar, S. A., Alagar, M., and Mohan, V. (2002). Studies on corrosion-resistant behavior of silicized epoxy interpenetrating coatings over mild steel surface by electrochemical methods. *J. Mater. Eng. Perform.* 11, 123–129. doi: 10.1361/105994902770344178

- Kumar, S. A., Balakrishnan, T., Alagar, M., and Denchev, Z. (2006). Development and characterization of silicone/phosphorus modified epoxy materials and their application as anticorrosion and antifouling coatings. *Prog. Org. Coat.* 55, 207–217. doi: 10.1016/j.porgcoat.2005.10.001
- Kumar, S. A., and Narayanan, T. S. (2002). Thermal properties of siliconized epoxy interpenetrating coatings. *Prog. Org. Coat.* 45, 323–330. doi: 10.1016/S0300-9440(02)00062-0
- Li, P., He, X., Huang, T.-C., White, K. L., Zhang, X., Liang, H., et al. (2015). Highly effective anti-corrosion epoxy spray coatings containing self-assembled clay in smectic order. *J. Mater. Chem. A* 3, 2669–2676. doi: 10.1039/C4TA06221C
- Liao, M., Schneider, A. F., Laengert, S. E., Gale, C. B., Chen, Y., and Brook, M. A. (2018). Living synthesis of silicone polymers controlled by humidity. *Eur. Polym. J.* 107, 287–293. doi: 10.1016/j.eurpolymj.2018.07.023
- Liqiang, J., Xiaojun, S., Weimin, C., Zili, X., Yaoguo, D., and Honggang, F. (2003). The preparation and characterization of nanoparticle TiO₂/Ti films and their photocatalytic activity. *J. Phys. Chem. Solids* 64, 615–623. doi: 10.1016/S0022-3697(02)00362-1
- Ma, I. W., Sh, A., Ramesh, K., Vengadaesvaran, B., Ramesh, S., and Arof, A. (2017). Anticorrosion properties of epoxy-nanochitosan nanocomposite coating. *Prog. Org. Coat.* 113, 74–81. doi: 10.1016/j.porgcoat.2017.08.014
- Matin, E., Attar, M., and Ramezanzadeh, B. (2015). Investigation of corrosion protection properties of an epoxy nanocomposite loaded with polysiloxane surface modified nanosilica particles on the steel substrate. *Prog. Org. Coat.* 78, 395–403. doi: 10.1016/j.porgcoat.2014.07.004
- Mohamad Saidi, N., Shafaamri, A. S., Wonnice Ma, I. A., Kasi, R., Balakrishnan, V., and Subramaniam, R. (2018). Development of anti-corrosion coatings using the disposable waste material. *Pigment Resin Technol.* 47, 478–484. doi: 10.1108/PRT-03-2018-0030
- Moura, J. H. L., Heinen, M., da Silva, R. C., Martini, E. M., and Petzhold, C. L. (2018). Reinforcing anticorrosive properties of biobased organic coatings through chemical functionalization with amino and aromatic groups. *Prog. Org. Coat.* 125, 372–383. doi: 10.1016/j.porgcoat.2018.09.021
- Park, E. J., Yoon, H. S., Kim, D. H., Kim, Y. H., and Kim, Y. D. (2014). Preparation of self-cleaning surfaces with a dual functionality of superhydrophobicity and photocatalytic activity. *Appl. Surf. Sci.* 319, 367–371. doi: 10.1016/j.apsusc.2014.07.122
- Polizos, G., Tuncer, E., Sauers, I., and More, K. L. (2011). Physical properties of epoxy resin/titanium dioxide nanocomposites. *Polym. Eng. Sci.* 51, 87–93. doi: 10.1002/pen.21783
- Pouget, E., Tonnar, J., Lucas, P., Lacroix-Desmazes, P., Ganachaud, F., and Boutevin, B. (2009). Well-architected poly (dimethylsiloxane)-containing copolymers obtained by radical chemistry. *Chem. Rev.* 110, 1233–1277. doi: 10.1021/cr8001998
- Pourhashem, S., Vaezi, M. R., Rashidi, A., and Bagherzadeh, M. R. (2017). Exploring corrosion protection properties of solvent based epoxy-graphene oxide nanocomposite coatings on mild steel. *Corros. Sci.* 115, 78–92. doi: 10.1016/j.corsci.2016.11.008
- Pugachevskii, M. (2013). Ultraviolet absorption spectrum of laser-irradiated titanium dioxide nanoparticles. *Tech. Phys. Lett.* 39, 36–38. doi: 10.1134/S1063785013010239
- Radoman, T. S., Džunuzović, J. V., Jeremić, K. B., Grgur, B. N., Miličević, D. S., Popović, I. G., et al. (2014). Improvement of epoxy resin properties by incorporation of TiO₂ nanoparticles surface modified with gallic acid esters. *Mater. Design* 62, 158–167. doi: 10.1016/j.matdes.2014.05.015
- Radoman, T. S., Terzić, N., Spasojević, P. M., Džunuzović, J. V., Marinković, A. D., Jeremić, K. B., et al. (2015). Synthesis and characterization of the surface modified titanium dioxide/epoxy nanocomposites. *Adv. Technol.* 4, 7–15. doi: 10.5937/savteh1501007R
- Ramezanzadeh, B., Attar, M., and Farzam, M. (2011). A study on the anticorrosion performance of the epoxy-polyamide nanocomposites containing ZnO nanoparticles. *Prog. Org. Coat.* 72, 410–422. doi: 10.1016/j.porgcoat.2011.05.014
- Ramezanzadeh, B., Haeri, Z., and Ramezanzadeh, M. (2016a). A facile route of making silica nanoparticles-covered graphene oxide nanohybrids (SiO₂-GO); fabrication of SiO₂-GO/epoxy composite coating with superior barrier and corrosion protection performance. *Chem. Eng. J.* 303, 511–528. doi: 10.1016/j.cej.2016.06.028
- Ramezanzadeh, B., Niroumandrad, S., Ahmadi, A., Mahdavian, M., and Moghadam, M. M. (2016b). Enhancement of barrier and corrosion protection performance of an epoxy coating through wet transfer of amino functionalized graphene oxide. *Corros. Sci.* 103, 283–304. doi: 10.1016/j.corsci.2015.11.033
- Rathod, P., and Waghuley, S. (2015). Synthesis and UV-Vis spectroscopic study of TiO₂ nanoparticles. *Int. J. Nanomanuf.* 11, 185–193. doi: 10.1504/IJNM.2015.071925
- Shen, S., and Zuo, Y. (2014). The improved performance of Mg-rich epoxy primer on AZ91D magnesium alloy by addition of ZnO. *Corros. Sci.* 87, 167–178. doi: 10.1016/j.corsci.2014.06.020
- Shi, X., Nguyen, T. A., Suo, Z., Liu, Y., and Avci, R. (2009). Effect of nanoparticles on the anticorrosion and mechanical properties of epoxy coating. *Surf. Coat. Technol.* 204, 237–245. doi: 10.1016/j.surfcoat.2009.06.048
- Sung, P.-H., and Lin, C.-Y. (1997). Polysiloxane modified epoxy polymer networks—I. Graft interpenetrating polymeric networks. *Eur. Polym. J.* 33, 903–906. doi: 10.1016/S0014-3057(96)00214-5
- Vasei, M., Das, P., Cherfouth, H., Marsan, B., and Claverie, J. P. (2014). TiO₂@C core-shell nanoparticles formed by polymeric nano-encapsulation. *Front. Chem.* 2:47. doi: 10.3389/fchem.2014.00047
- Vázquez-Velázquez, A., Velasco-Soto, M., Pérez-García, S., and Licea-Jiménez, L. (2018). Functionalization effect on polymer nanocomposite coatings based on TiO₂-SiO₂ nanoparticles with superhydrophilic properties. *Nanomaterials* 8, 369. doi: 10.3390/nano8060369
- Velan, T. T., and Bilal, I. M. (2000). Aliphatic amine cured PDMS-epoxy interpenetrating network system for high performance engineering applications—Development and characterization. *Bull. Mater. Sci.* 23, 425–429. doi: 10.1007/BF02708394
- Verma, S., Mohanty, S., and Nayak, S. (2019). A review on protective polymeric coatings for marine applications. *J. Coat. Technol. Res.* 16, 307–338. doi: 10.1007/s11998-018-00174-2
- Wang, C., Wang, H., Hu, Y., Liu, Z., Lv, C., Zhu, Y., et al. (2018). Anti-corrosive and scale inhibiting polymer-based functional coating with internal and external regulation of TiO₂ Whiskers. *Coatings* 8:29. doi: 10.3390/coatings8010029
- Yi, C., Rostrom, P., Vahdati, N., Gunister, E., and Alfantazi, A. (2018). Curing kinetics and mechanical properties of epoxy based coatings: the influence of added solvent. *Prog. Org. Coat.* 124, 165–174. doi: 10.1016/j.porgcoat.2018.08.009
- Zaare, D., Sarabi, A. A., Sharif, F., and Kassiriha, S. M. (2008). Structure, properties and corrosion resistivity of polymeric nanocomposite coatings based on layered silicates. *J. Coat. Technol. Res.* 5, 241–249. doi: 10.1007/s11998-007-9065-5
- Zhang, H., Bao, W., Deng, Z., Zhang, S., and Ji, Z. (2019). Next-generation composite coating system: nanocoating. *Front. Mater.* 6:72. doi: 10.3389/fmats.2019.00072
- Zhang, X., Wang, F., and Du, Y. (2007). Effect of nano-sized titanium powder addition on corrosion performance of epoxy coatings. *Surf. Coat. Technol.* 201, 7241–7245. doi: 10.1016/j.surfcoat.2007.01.042
- Zheng, S., Bellido-Aguilar, D. A., Huang, Y., Zeng, X., Zhang, Q., and Chen, Z. (2019). Mechanically robust hydrophobic bio-based epoxy coatings for anti-corrosion application. *Surf. Coat. Technol.* 363, 43–50. doi: 10.1016/j.surfcoat.2019.02.020
- Zhu, G., Cui, X., Zhang, Y., Chen, S., Dong, M., Liu, H., et al. (2019). Poly (vinyl butyral)/graphene oxide/poly (methylhydrosiloxane) nanocomposite coating for improved aluminum alloy anticorrosion. *Polymer* 172, 415–422. doi: 10.1016/j.polymer.2019.03.056

Conflict of Interest: The authors declare that the research was conducted in the absence of any commercial or financial relationships that could be construed as a potential conflict of interest.

Copyright © 2020 Shafaamri, Cheng, Wonnice Ma, Baig, Kasi, Subramaniam and Balakrishnan. This is an open-access article distributed under the terms of the Creative Commons Attribution License (CC BY). The use, distribution or reproduction in other forums is permitted, provided the original author(s) and the copyright owner(s) are credited and that the original publication in this journal is cited, in accordance with accepted academic practice. No use, distribution or reproduction is permitted which does not comply with these terms.



Polypyrrole/Metal Oxides-Based Composites/Nanocomposites for Corrosion Protection

Niteen Jadhav*, Subramanyam Kasisomayajula and Victoria Johnston Gelling

Department of Coatings and Polymeric Materials, North Dakota State University, Fargo, ND, United States

OPEN ACCESS

Edited by:

Marco Salerno,
Italian Institute of Technology (IIT), Italy

Reviewed by:

Arunas Ramanavicius,
Vilnius University, Lithuania
Wan Jeffrey Basirun,
University of Malaya, Malaysia

*Correspondence:

Niteen Jadhav
n3.uict@gmail.com

Specialty section:

This article was submitted to
Environmental Materials,
a section of the journal
Frontiers in Materials

Received: 18 July 2019

Accepted: 30 March 2020

Published: 05 May 2020

Citation:

Jadhav N, Kasisomayajula S and
Gelling VJ (2020) Polypyrrole/Metal
Oxides-Based
Composites/Nanocomposites
for Corrosion Protection.
Front. Mater. 7:95.
doi: 10.3389/fmats.2020.00095

Corrosion is of paramount interest to researchers all around the world owing to its disastrous impact on both the economy and people's safety. New strategies based on novel materials have been employed to mitigate corrosion. Conducting polymer-based nanocomposites are a class of materials which have shown promise for corrosion protection. This paper will focus on the specific case of the Conducting polymer-based nanocomposites for corrosion protection, and one important case will be discussed in detail. Corrosion protection offered by Polypyrrole (PPy)/Fe₂O₃ based composite coating for cold rolled substrate is characterized in this paper by electrochemical impedance spectroscopy and open circuit potential measurements. It was found that PPy/Fe₂O₃ based composite coating provides better corrosion performance after 40 days exposure to ASTM B117 salt fog test conditions. This improved performance was attributed to the increased surface area of PPy and passivating nature of the composite resulting from the redox activity provided by PPy.

Keywords: polypyrrole, corrosion, coatings, composites, nanocomposites, electrochemical impedance spectroscopy, iron oxide

INTRODUCTION

Corrosion is an electrochemical process by which metals or metal alloys go back to their oxide form. Generally, products of corrosion reaction are the most thermodynamically stable forms of the metals and metal alloys. It is in that stable form (oxide) of metal in which it exists in the ores. Huge amounts of energy are required to bring the metal oxide to metal or metal alloy form. The same amount of energy is released once the metal comes into contact with a conducive environment for corrosion (water, oxygen, salts, etc.) resulting in the formation of metal oxide (corrosion product). Microscopic strain, faults, defects, and impurities in the metal surface are responsible for its thermodynamic instability. Corrosion can be aqueous or atmospheric depending on the environment to which the metal is exposed.

Corrosion cannot be stopped as it is a thermodynamically favorable process. However, it can be mitigated by using several strategies. Design control, judicious alloy selection, overdesign, cathodic protection, organic coatings, metallic coatings (inorganic coatings), or plating are the avenues used for corrosion protection. Use of organic coatings is widely employed for the corrosion protection of the metals and their alloys owing to the application flexibility, cost effectiveness, ability to protect in different environments, and other performance attributes of this method. Traditional coating technologies protect by different mechanisms such as barrier, sacrificial, and active (corrosion inhibitors). These coatings have their own advantages and disadvantages. With the changing

environment of the 21st century and an increasing demand for ecofriendly materials, researchers have been encouraged to work on innovative materials for corrosion protection. A combination of the protection mechanism is one of the ways to improve the corrosion resistance of the organic coating. In this paper we will be discussing the active corrosion protection offered by conducting polymers in combination with the passive protection imparted by the inorganic oxide pigments. This combination ultimately results in the conducting polymer composite coatings.

Conducting polymers are an important class of materials which have shown promise in areas such as batteries, sensors, actuators, electromagnetic shielding, semiconductors, and corrosion protection (Das and Prusty, 2012; Ratautaite et al., 2013; Deshpande et al., 2014). Their conductivity, ease of synthesis, and pigment-like nature make them a suitable candidate to be used in coatings for corrosion protection. Polyaniline (PANI), polypyrrole (PPy), and polythiophene (PTh) belong to the family of intrinsically conducting polymers. Polypyrrole is one of the most important members of this class of polymers. Polypyrrole possesses the necessary electrical conductivity and environmental stability for corrosion protection application for metals and their alloys. Significant progress has been made in the last 30 years toward the application of PPy for the protection of metal alloys. There are papers which discuss the milestones in the development of several avenues based on PPy for corrosion protection of metal substrates (Jadhav et al., 2013; Deshpande et al., 2014).

Composites combine unique properties of two or more materials to impart beneficial functionalities. Nanocomposites involve one phase in nanometer dimension. A high surface to volume ratio of nanoparticles render properties which are not attainable in the case of regular particle sizes of the same material. This paper will detail the various composites/nanocomposites of PPy with several materials.

Among many conductive polymer composites/nanocomposites, the composites/nanocomposites prepared using PPy as the conductive polymer have been extensively investigated for the corrosion protection of various metals and their alloys. Recent studies have demonstrated that the incorporation of nanoparticles into conductive polymers such as PPy can increase the surface area of the conductive polymers and thereby provide improved electrochemical interactions with corrosive species and metal substrates. Although PPy composites/nanocomposites can be prepared via several synthetic methods, the most commonly used ones are electrochemical and chemical oxidation methods. Some more information about these preparation methods is provided in **Table 1**.

Iron oxide is an anticorrosive pigment and is a workhorse of red oxide primers which provide decent corrosion protection to mild steel. Polypyrrole/ Fe_2O_3 and PPy/ Fe_3O_4 composites were synthesized on iron electrochemically and were found to provide corrosion protection by maintaining substrate in a passive state (Garcia et al., 2002). Core and shell PPy/ Fe_2O_3 pigment composites were synthesized by chemical oxidative polymerization (Jadhav and Gelling, 2012). The layer of PPy on Fe_2O_3 was in nanometer range, rendering PPy/ Fe_2O_3 as a nanocomposite. The corrosion performance testing of these core

TABLE 1 | Conducting polymer-based nanocomposites synthesis methods.

Method	Chemical	Electrochemical
Composite obtained as	Powder, film	Directly on substrate but can be scraped to form powder
Doping with counterions	Possible	Possible
Special needs	Chemical oxidant needed	Potential needed
Production	Bulk production possible	Rapid production possible
Conductivity of composite	High	Very high

and shell particles is described in this paper below. Shell of PPy in nanometer thickness range on Fe_2O_3 effectively increases the redox active surface area in the nanocomposite.

MATERIALS AND METHODS

Coatings were prepared on sandblasted and hexane degreased cold rolled steel substrate. Coatings were formulated at 10% Pigment Volume Concentration (PVC) for Fe_2O_3 pigment and Fe_2O_3 /PPy composite pigment and 1:1 stoichiometric ratio of EPON 830 and Epicure 3015 were used. MEK was used to reach application viscosity for proper drawdown application on the cold rolled steel surface. The coatings were applied with a drawdown bar on cleaned cold rolled steel substrate. Coatings were cured at an ambient temperature for 8 days for full development of the protective properties. Final dry film thickness of the coatings was 75–85 μm .

The coatings were exposed to salt spray test conditions according to ASTM B 117. Corrosion performance was monitored by electrochemical impedance spectroscopy (EIS) with Gamry Reference 600 Potentiostats with Gamry Framework Version 5.58/EIS 300 software. For EIS, AC perturbation of 10 mV over a frequency range of 100,000–0.01 Hz at 10 points/decade was applied. For EIS experiments 5% NaCl was used as electrolyte. Experiments were performed in triplicates and data is collected from representative samples. The cell area for the EIS measurements was 7.1 cm^2 . Open circuit potential (OCP) measurements were also performed with the same set up used in EIS experiments.

RESULTS AND DISCUSSION

A three-electrode cell consisting of substrates with coating as working electrode, saturated calomel as reference electrode, and platinum mesh as a counter electrode was employed for performing EIS. As observed in **Figures 1, 2**, low frequency (0.01 Hz) impedance was very high initially for both Fe_2O_3 and Fe_2O_3 /PPy coatings. As the duration of the salt spray exposure increased, a drop in low frequency impedance was observed for both Fe_2O_3 and Fe_2O_3 /PPy coatings. The drop-in impedance in this case represents a decrease in protection offered by the coating to the corrosion (Le Thu et al., 2001). It represents the electrolyte ingress through the developed pores in the coating

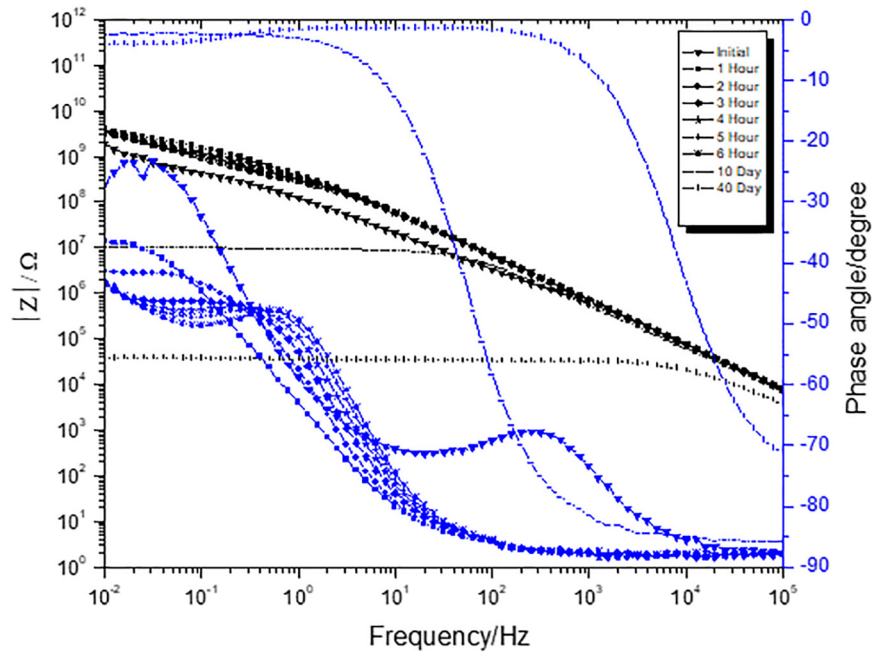


FIGURE 1 | Bode plot of 10 % PVC of Fe₂O₃ coating.

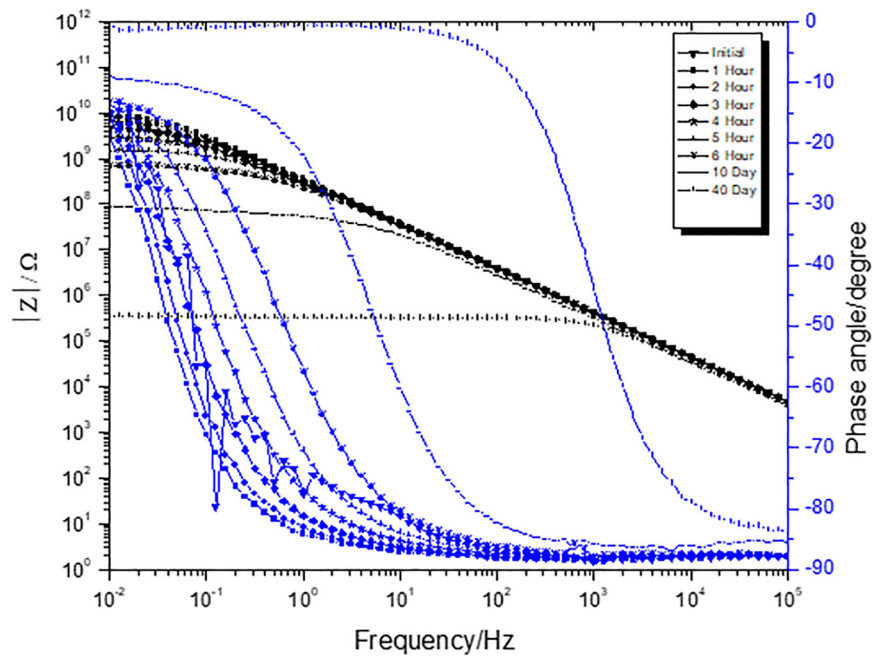


FIGURE 2 | Bode plot of 10 % PVC of Fe₂O₃/PPy coating.

(Amirudin and Thieny, 1995). An appearance of a second time constant in Fe₂O₃ coating indicates the start of the corrosion reaction at coating and cold rolled steel interface.

The EIS data was modeled by using ZView 2 software from Scribner Associates Inc. EIS data was fitted to Randles circuit model equivalent circuit. Randles circuit model consists of

solution resistance and a constant phase element which is in parallel with coatings resistance (R_c). Resistance for both Fe₂O₃ and Fe₂O₃/PPy coatings was plotted against the duration of the exposure in salt spray (Figure 3). Initially R_c was higher for Fe₂O₃/PPy coating as compared with both Fe₂O₃ coating. Even though the value of R_c decreased with the duration of exposure

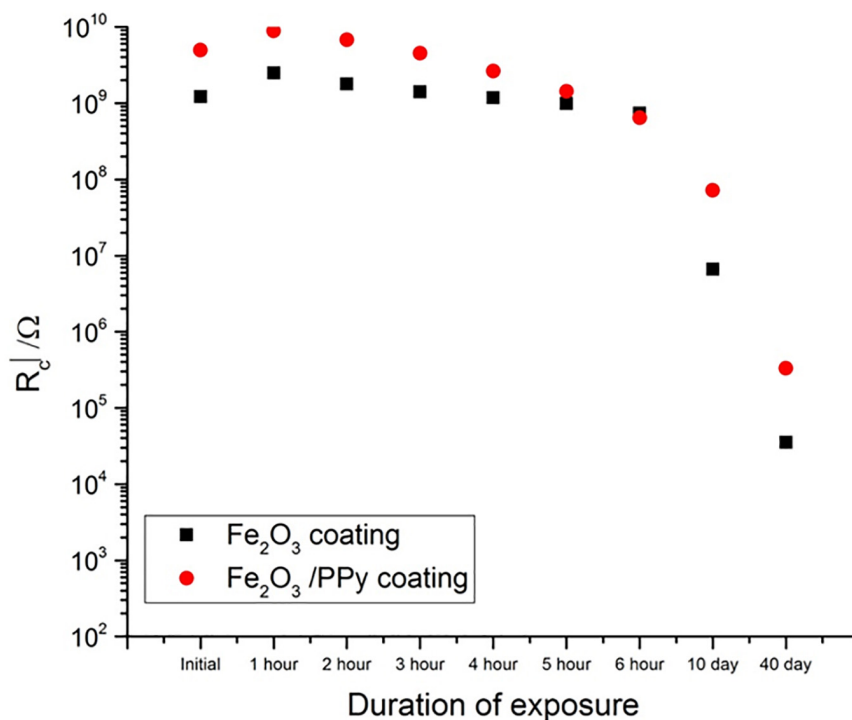


FIGURE 3 | Change in coating resistance (R_c) with time of exposure.

to salt spray, it increased for Fe₂O₃/PPy coating and was still higher than that of Fe₂O₃ coating for the same duration of exposure. This suggested better corrosion performance offered by Fe₂O₃/PPy coating.

Simultaneously with EIS experiments, OCP values were also collected. As shown in **Figure 4**, OCP of the Fe₂O₃ coating was more toward the OCP of the cold rolled steel. For Fe₂O₃/PPy coating, OCP was more positive initially whereas it decreased over time as the duration to the salt spray exposure increased. Similar behavior was observed earlier in the case of PPy doped with sulfate anions. The more positive values of the OCP were attributed to the doped nature of the PPy (Ocón et al., 2005). Polypyrrole tends to be reduced and also serve as an oxidant to passivate underlying iron substrate, thereby further increasing corrosion protection (Spinks et al., 2002). The increased corrosion protection offered in the case of Fe₂O₃/PPy coating can also be attributed to the increased surface area of PPy for redox reactions and interactions with metal substrates and corrosive ions (Mahmoudian et al., 2011). The reduced PPy can also scavenge oxygen and get oxidized, thereby decreasing the rate of cathodic reaction and corrosion (Yan et al., 2010).

The efficiencies of the nanocomposites of inorganic pigments with PPy have been well documented in literature. In order to provide more evidence of the efficiency of the Fe₂O₃/PPy composite coating, we are providing a brief account of research. Polypyrrole/ZnO nanocomposites/composites can be synthesized by electrochemical or chemical oxidative polymerization (Moghaddam et al., 2009; Batool et al., 2012). Polypyrrole/ZnO nanocomposite was electrochemically prepared

on mild steel with 10% loading of ZnO and was compared for corrosion protection with just PPy. Nanorod morphology was obtained for ZnO in the nanocomposite. It was found that the OCP of nanocomposite was more positive than just PPy and EIS measurements confirmed lower water uptake and lower capacitance suggesting better corrosion protection by PPy/ZnO nanocomposite (Hosseini et al., 2011). Polypyrrole/ZnO nanocomposites have also been obtained by chemical oxidative polymerization (Valença et al., 2015). Prepared PPy/ZnO nanocomposites were incorporated in epoxy coating at 0.2 w/w% loading and applied on SAE 1020 carbon steel. Electrochemical impedance spectroscopy and OCP measurements exhibited improved corrosion protection at lower loading of PPy/ZnO nanocomposites.

Polypyrrole/SiO₂ composite was synthesized by chemical oxidative polymerization using FeCl₃ as an oxidizer (Ruhi et al., 2014). The composite particles were added to epoxy powder coatings with the help of ball milling process. The composite particle concentrations added to epoxy powder coatings were 1–4 wt% with increments of 1 wt%. The addition of PPy/SiO₂ composite at 3 wt% was found to provide optimum and superior corrosion performance on low carbon steel as observed in EIS and ASTM B117 salt fog exposures. The passivating ability of PPy in the defect/scribe was also noticed in Tafel experiments. Polypyrrole/SiO₂ composite also exhibited improved corrosion protection for 316 stainless steel (Qun, 2017). In another attempt, multilayered coatings of PPy (obtained electrochemically) and SiO₂ (deposited electrophoretically) were applied on AISI 304 stainless steel (Grari et al., 2015). The oxidizing ability of PPy

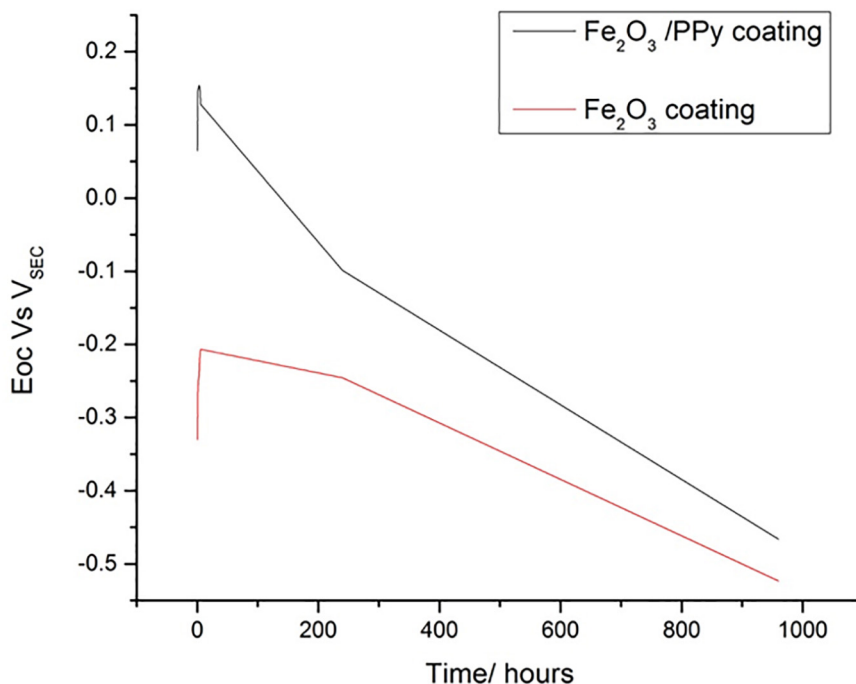


FIGURE 4 | Open circuit potential (OCP) with time of exposure.

leads to passivation along with added resistance of SiO₂ results in improved corrosion protection. Oxalate ion doped PPy/SiO₂ nanocomposite on carbon steel was also found to improve corrosion protection in polyvinylbutyral (PVB) binder matrix (Van et al., 2018). Multi-material composite of chitosan, PPy, and SiO₂ was studied for the corrosion protection of mild steel (Rui et al., 2015). High cross linking is provided by chitosan for added barrier performance.

Polypyrrole/Al₂O₃ composite was electrochemically synthesized and was characterized for corrosion performance on 316 stainless steel (Yan et al., 2017). Improved barrier and increased charge transfer resistance, hence a lesser corrosion rate, was evident in 3.5 wt% NaCl constant immersion. Doped PPy composite films were prepared on stainless steel with alumina nanoparticles as the second phase (Ali, 2014). This composite was found to inhibit any increase in pH, thereby limiting the delamination process. Comparison of PPy/Al₂O₃, PPy/ZnO, PPy/TiO₂, PPy/CeO₂, and PPy/SnO₂ nanocomposites was performed after they were synthesized by electrodeposition on the surface of mild steel (Babaei-Sati et al., 2019). The best corrosion protection was observed for PPy/Al₂O₃ nanocomposites. This was attributed to the lowest reduction potential (−2.33 V) exhibited by Al₂O₃ compared to other metal oxides, which ensures stability and less porosity under corroding situations. Hybrid composites of PPy deposited on alumina were incorporated in zinc rich epoxy primers found to improve corrosion performance on cold rolled steel by reducing the rate of zinc self-corrosion and blocking oxidizing entities (Gergely et al., 2011). Similar results were obtained in another study (Gergely et al., 2013). Nanocomposite of PPy and

alumina was found to improve adhesion and corrosion resistance on Al 2024-T3 substrate (Tallman et al., 2008).

Polypyrrole containing composite pigments (PPy on aluminum flake surface) have been synthesized and used for the corrosion protection of metal substrates. Different morphologies of PPy on an aluminum flake surface resulted in improved corrosion performance on aluminum 2024-T3 surface (Jadhav et al., 2013). Incorporation of dopants (phosphates, nitrates, tungstate, and vanadate) on the backbone of PPy in these composites on an aluminum surface (as a single particle) resulted in better corrosion performance (Jadhav et al., 2012, 2015; Jensen et al., 2014). This ensured the intelligent release of corrosion inhibiting dopant at scribe in the event of corrosion as well as barrier properties provided by aluminum flakes, and the passivating nature of PPy in one composite particle for the overall corrosion protection of the substrate.

Mica provides improved corrosion protection by barrier mechanism because of its high aspect ratio and inert nature. Combining mica with PPy results in improved corrosion protection as there is the added advantage of active nature of PPy at coating metal interface and its dopant release ability in the event of defect or corrosion. Various organic surfactant dopants were incorporated on the backbone of PPy which was formed on mica flakes. The improved corrosion resistance on cold rolled steel was attributed to the decreased diffusion due to increased impediment for chloride ion ingress (Jadhav et al., 2018). Polypyrrole/mica composite with zinc as a pigment in epoxy coatings also exhibited improved corrosion protection (Qi and Gelling, 2009). Micaceous iron oxide (MIOx) is also another laminar flake pigment which provides barrier protection

and passivation owing to its oxide nature. Micaceous iron oxide laminar flakes of different sizes (5, 10, and 30 μm) were used for preparation of PPY/MIOx composites pigments. Composite pigments with MIOx 30 μm size were selected for the corrosion resistance application on cold rolled surface. Improved corrosion protection was observed with PPY/MIOx due to the combination of impact from the passivating nature of PPY and the barrier properties exhibited by MIOx (Jadhav and Gelling, 2013).

TiO₂ is a pigment which is widely used for hiding in paints and coatings. As it is already present in the protective coatings, combining it with an active corrosion provider such as PPY will improve overall corrosion performance. Polypyrrole/TiO₂ composite on AISI 1010 mild steel exhibited improved corrosion protection as observed in weight loss and salt spray measurements (Lenz et al., 2003). Polypyrrole/TiO₂ composites at 6.5 wt% concentration resulted in improved corrosion performance on AISI 1010 mild steel (Ferreira et al., 2001). Polypyrrole/TiO₂ nanocomposite and PPY/co-doped TiO₂ nanocomposite exhibited improved corrosion protection on AISI steel as observed in EIS, OCP, and Potentiodynamic polarization measurements. An insignificant decrease in the impedance was observed for 3.5 wt% NaCl immersion of the coatings (Ladan et al., 2017). The increased surface area of PPY on TiO₂ particles was attributed to high chances on the surface of PPY for oxygen reduction (Mahmoudian et al., 2013). Passive film formation in case of PPY/V-doped TiO₂ resulted in improved corrosion performance (Chen et al., 2019). Polypyrrole/TiO₂ and PPY/tungstate doped TiO₂ exhibited improved corrosion performance on cold rolled steel substrates due to effective PPY surface area increase and passivation after tungstate release in the event of corrosion (Jadhav and Gelling, 2015).

REFERENCES

- Ali, E. (2014). Influence of electrosynthesis conditions and Al₂O₃ nanoparticles on corrosion protection effect of polypyrrole films. *Anti-Corrosion Methods Mater.* 61, 146–152. doi: 10.1108/ACMM-07-2012-1193
- Amirudin, A., and Thieny, D. (1995). Application of electrochemical impedance spectroscopy to study the degradation of polymer-coated metals. *Prog. Org. Coat.* 26, 1–28. doi: 10.1016/0300-9440(95)00581-1
- Babaei-Sati, R., Basiri Parsa, J., and Vakili-Azghandi, M. (2019). Electrodeposition of polypyrrole/ metal oxide nanocomposites for corrosion protection of mild steel—A comparative study. *Synth. Met.* 247, 183–190. doi: 10.1016/j.synthmet.2018.12.009
- Batool, A., Kanwal, F., Imran, M., Jamil, T., and Siddiqi, S. A. (2012). Synthesis of polypyrrole/zinc oxide composites and study of their structural, thermal and electrical properties. *Synth. Met.* 161, 2753–2758. doi: 10.1016/j.synthmet.2011.10.016
- Chen, Z., Yang, W., Xu, B., Chen, Y., Qian, M., Su, X., et al. (2019). Corrosion protection of carbon steels by electrochemically synthesized V-TiO₂/polypyrrole composite coatings in 0.1 M HCl solution. *J. Alloys Compd.* 771, 857–868. doi: 10.1016/j.jallcom.2018.09.003
- Das, T. K., and Prusty, S. (2012). Review on conducting polymers and their applications. *Polym. Plast. Technol. Eng.* 51, 1487–1500. doi: 10.1080/03602559.2012.710697
- Deshpande, P. P., Jadhav, N. G., Gelling, V. J., and Sazou, D. (2014). Conducting polymers for corrosion protection: a review. *J. Coatings Technol. Res.* 11, 473–494. doi: 10.1007/s11998-014-9586-7
- Ferreira, C. A., Domenech, S. C., and Lacaze, P. C. (2001). Synthesis and characterization of polypyrrole/TiO₂ composites on mild steel. *J. Appl. Electrochem.* 31, 49–56. doi: 10.1023/A:1004149421649

CONCLUSION

Polypyrrole/Metal oxides composites/nanocomposites have shown promise for corrosion protection. In this study, after exposure to salt spray test conditions, a lower drop in coating resistance in the case of Fe₂O₃/PPY coating as compared to Fe₂O₃ coating suggested better corrosion protection is offered by Fe₂O₃/PPY coating. An increased surface area for the interaction of ions with PPY and the passivating ability of PPY was responsible for the improved corrosion protection offered by Core and shell Fe₂O₃/PPY particles-based coatings.

DATA AVAILABILITY STATEMENT

The datasets generated for this study are available on request to the corresponding author.

AUTHOR CONTRIBUTIONS

All authors contributed to the manuscript.

ACKNOWLEDGMENTS

The authors would like to thank the U.S. Army Research Laboratory under grant nos. W911 NF-04-2-0029, W911NF-09-2-0014, W911NF-10-2-0082, and W911NF-11-2-0027 for supporting this research.

- Garcia, B., Lamzoudi, A., Pillier, F., Nguyen, H., Le, T., and Deslouis, C. (2002). Oxide/polypyrrole composite films for corrosion protection of iron. *J. Electrochem. Soc.* 149, B560–B566.
- Gergely, A., Bertóti, I., Török, T., Pfeifer, E., and Kálmán, E. (2013). Corrosion protection with zinc-rich epoxy paint coatings embedded with various amounts of highly dispersed polypyrrole-deposited alumina monohydrate particles. *Prog. Org. Coatings* 76, 17–32. doi: 10.1016/j.porgcoat.2012.08.005
- Gergely, A., Pfeifer, E., Bertóti, I., Török, T., and Kálmán, E. (2011). Corrosion protection of cold-rolled steel by zinc-rich epoxy paint coatings loaded with nano-size alumina supported polypyrrole. *Corros. Sci.* 53, 3486–3499. doi: 10.1016/j.corsci.2011.06.014
- Grari, O., Taouil, A. E., Dhouibi, L., Buron, C. C., and Lallemand, F. (2015). Multilayered polypyrrole-SiO₂ composite coatings for functionalization of stainless steel: characterization and corrosion protection behavior. *Prog. Org. Coatings* 88, 48–53. doi: 10.1016/j.porgcoat.2015.06.019
- Hosseini, M. G., Bagheri, R., and Najjar, R. (2011). Electropolymerization of polypyrrole and polypyrrole-ZnO nanocomposites on mild steel and its corrosion protection performance. *J. Appl. Polym. Sci.* 121, 3159–3166. doi: 10.1002/app.33952
- Jadhav, N., and Gelling, V. (2015). Titanium dioxide/conducting polymers composite pigments for corrosion protection of cold rolled steel. *J. Coatings Technol. Res.* 12, 137–152. doi: 10.1007/s11998-014-9613-8
- Jadhav, N., and Gelling, V. J. (2013). Synthesis and characterization of micaceous iron Oxide/Polypyrrole composite pigments and their application for corrosion protection of cold-rolled steel. *Corrosion* 70, 464–474. doi: 10.5006/0980
- Jadhav, N., Jensen, M. B., and Gelling, V. (2015). Tungstate and vanadate-doped polypyrrole/aluminum flake composite coatings for the corrosion protection of aluminum 2024-T3. *J. Coatings Technol. Res.* 12, 259–276. doi: 10.1007/s11998-014-9633-4

- Jadhav, N., Matsuda, T., and Gelling, V. (2018). Mica/polypyrrole (doped) composite containing coatings for the corrosion protection of cold rolled steel. *J. Coatings Technol. Res.* 15, 363–374. doi: 10.1007/s11998-017-9974-x
- Jadhav, N., Vetter, C. A., and Gelling, V. J. (2012). Characterization and Electrochemical Investigations of Polypyrrole/Aluminum Flake Composite Pigments on AA 2024-T3 Substrate. *ECS Trans.* 41, 75–89.
- Jadhav, N., Vetter, C. A., and Gelling, V. J. (2013). The effect of polymer morphology on the performance of a corrosion inhibiting polypyrrole/aluminum flake composite pigment. *Electrochim. Acta* 102, 28–43. doi: 10.1016/j.electacta.2013.03.128
- Jadhav, N. G., and Gelling, V. J. (2012). Novel, facile method for the synthesis of iron oxide/polypyrrole core and shell particles, in: *Polym. Mater. Sci. Eng.* 2012:536.
- Jensen, M. B., Peterson, M. J., Jadhav, N., and Gelling, V. J. (2014). SECM investigation of corrosion inhibition by tungstate- and vanadate-doped polypyrrole/aluminum flake composite coatings on AA2024-T3. *Prog. Org. Coatings* 77, 2116–2122. doi: 10.1016/j.porgcoat.2014.05.019
- Ladan, M., Basirun, W. J., Kazi, S. N., and Rahman, F. A. (2017). Corrosion protection of AISI 1018 steel using Co-doped TiO₂/polypyrrole nanocomposites in 3.5% NaCl solution. *Mater. Chem. Phys.* 192, 361–373. doi: 10.1016/j.matchemphys.2017.01.085
- Le Thu, Q., Bierwagen, G. P., and Touzain, S. (2001). EIS and ENM measurements for three different organic coatings on aluminum. *Prog. Org. Coatings* 42, 179–187. doi: 10.1016/S0300-9440(01)00171-0
- Lenz, D. M., Delamar, M., and Ferreira, C. A. (2003). Application of polypyrrole/TiO₂ composite films as corrosion protection of mild steel. *J. Electroanal. Chem.* 540, 35–44. doi: 10.1016/S0022-0728(02)01272-X
- Mahmoudian, M. R., Alias, Y., Basirun, W. J., and Ebadi, M. (2013). Effects of different polypyrrole/TiO₂ nanocomposite morphologies in polyvinyl butyral coatings for preventing the corrosion of mild steel. *Appl. Surf. Sci.* 268, 302–311. doi: 10.1016/j.apsusc.2012.12.082
- Mahmoudian, M. R., Basirun, W. J., Alias, Y., and Ebadi, M. (2011). Synthesis and characterization of polypyrrole/Sn-doped TiO₂ nanocomposites (NCs) as a protective pigment. *Appl. Surf. Sci.* 257, 8317–8325. doi: 10.1016/j.apsusc.2011.03.075
- Moghaddam, A. B., Nazari, T., Badraghi, J., and Kazemzad, M. (2009). Synthesis of ZnO nanoparticles and electrodeposition of Polypyrrole/ZnO nanocomposite film. *Int. J. Electrochem. Sci.* 4, 247–257.
- Ocón, P., Cristobal, A. B., Herrasti, P., and Fatas, E. (2005). Corrosion performance of conducting polymer coatings applied on mild steel. *Corros. Sci.* 47, 649–662. doi: 10.1016/j.corsci.2004.07.005
- Qi, X., and Gelling, V. (2009). “Polypyrrole coated mica flake as a pigment for corrosion protection,” in *Proceedings of the DoD Corrosion Conference*, Washington, DC, 2009.
- Qun, Y. (2017). Electrochemical synthesis of polypyrrole-SiO₂ composite coating on 316 stainless steel for corrosion protection. *Anti-Corrosion Methods Mater.* 64, 452–460. doi: 10.1108/ACMM-02-2016-1650
- Ratautaite, V., Ramanaviciene, A., Oztekin, Y., Voronovic, J., Balevicius, Z., Mikoliunaite, L., et al. (2013). Electrochemical stability and repulsion of polypyrrole film. *Colloids Surf. A Physicochem. Eng. Asp.* 418, 16–21. doi: 10.1016/j.colsurfa.2012.10.052
- Ruhi, G., Bhandari, H., and Dhawan, S. K. (2014). Designing of corrosion resistant epoxy coatings embedded with polypyrrole/SiO₂ composite. *Prog. Org. Coatings* 77, 1484–1498. doi: 10.1016/j.porgcoat.2014.04.013
- Ruhi, G., Modi, O. P., and Dhawan, S. K. (2015). Chitosan-polypyrrole-SiO₂ composite coatings with advanced anticorrosive properties. *Synth. Met.* 200, 24–39. doi: 10.1016/j.synthmet.2014.12.019
- Spinks, G. M., Dominis, A. J., Wallace, G. G., and Tallman, D. E. (2002). Electroactive conducting polymers for corrosion control. *J. Solid State Electrochem.* 6, 85–100. doi: 10.1007/s100080100211
- Tallman, D. E., Levine, K. L., Siriprom, C., Gelling, V. G., Bierwagen, G. P., and Croll, S. G. (2008). Nanocomposite of polypyrrole and alumina nanoparticles as a coating filler for the corrosion protection of aluminium alloy 2024-T3. *Appl. Surf. Sci.* 254, 5452–5459. doi: 10.1016/j.apsusc.2008.02.099
- Valença, A., Sa, D. P., Alves, K. G. B., de Melo, C. P., and Bouchonneau, N. (2015). Study of the Efficiency of Polypyrrole/ZnO Nanocomposites as additives in anticorrosion coatings. *Mater. Res.* 18, 273–278.
- Van, V. T. H., Hang, T. T. X., Nam, P. T., Phuong, N. T., Thom, N. T., Devilliers, D., et al. (2018). Synthesis of Silica/Polypyrrole Nanocomposites and application in corrosion protection of carbon steel. *J. Nanosci. Nanotechnol.* 18, 4189–4195. doi: 10.1166/jnn.2018.15198
- Yan, M., Vetter, C. A., and Gelling, V. J. (2010). Electrochemical investigations of polypyrrole aluminum flake coupling. *Electrochim. Acta* 55, 5576–5583. doi: 10.1016/j.electacta.2010.04.077
- Yan, Q., Li, C., Huang, T., and Yang, F. (2017). Electrochemical synthesis of polypyrrole-Al₂O₃ composite coating on 316 stainless steel for corrosion protection. *AIP Conf. Proc.* 1820:30005. doi: 10.1063/1.4977262

Conflict of Interest: The authors declare that the research was conducted in the absence of any commercial or financial relationships that could be construed as a potential conflict of interest.

Copyright © 2020 Jadhav, Kasisomayajula and Gelling. This is an open-access article distributed under the terms of the Creative Commons Attribution License (CC BY). The use, distribution or reproduction in other forums is permitted, provided the original author(s) and the copyright owner(s) are credited and that the original publication in this journal is cited, in accordance with accepted academic practice. No use, distribution or reproduction is permitted which does not comply with these terms.



Protective and Suppressing Electromagnetic Interference Properties of Epoxy Coatings Containing Nano-Sized NiZn Ferrites

Andrzej Miszczyk*

Department of Electrochemistry, Corrosion and Materials Engineering, Faculty of Chemistry, The Gdansk University of Technology, Gdansk, Poland

Nano-crystalline ferrites with the chemical formula $\text{Ni}_x\text{Zn}_{(1-x)}\text{Fe}_2\text{O}_4$, where $x = 0, 0.2, 0.4, 0.6, 0.8, 1.0$, were synthesized using a co-precipitation method. The obtained ferrites were investigated by X-ray diffraction (XRD). The corrosion inhibiting behavior of nano-sized ferrites was tested using carbon steel samples and 10% aqueous ferrite extracts. Results were compared with previous data obtained for micro-sized ceramic ferrites. Nanoparticles show more favorable properties regarding inhibiting corrosion processes on steel. Two Millimeter thick epoxy coatings on steel containing 10% vol. of nano-sized ferrites has been investigated as a microwave absorber. The microwave reflectivity of the coating was measured within the range from 6.5 to 15 GHz. Both the nano- and micro-sized ferrites included in the coatings exhibited different reflection loss spectra. The greatest attenuation on a level of 8–16 dB was observed. The nano-ferrite-filled epoxy coating exhibited a higher minimum reflection frequency in comparison with the micro-ferrite-filled coating. A frequency shift of 1–2 GHz was observed.

Keywords: corrosion, pigment, NiZn ferrites, microwave absorption, EMI

OPEN ACCESS

Edited by:

Michele Fedel,
University of Trento, Italy

Reviewed by:

Wan Jeffrey Basirun,
University of Malaya, Malaysia
Da-Hai Xia,
Tianjin University, China

*Correspondence:

Andrzej Miszczyk
andrzej.miszczczyk@pg.edu.pl

Specialty section:

This article was submitted to
Environmental Materials,
a section of the journal
Frontiers in Materials

Received: 01 August 2019

Accepted: 19 May 2020

Published: 23 June 2020

Citation:

Miszczczyk A (2020) Protective and Suppressing Electromagnetic Interference Properties of Epoxy Coatings Containing Nano-Sized NiZn Ferrites. *Front. Mater.* 7:183. doi: 10.3389/fmats.2020.00183

INTRODUCTION

After the withdrawal of effective anti-corrosive but toxic pigments, it is necessary to introduce new non-toxic pigments in protective coatings. An interesting and desirable option is to use for this purpose materials that in addition to anti-corrosion properties show other useful properties. Materials that meet these expectations include ferrites. In addition to anti-corrosive properties, they have the ability to suppress electromagnetic waves. This is important now due to the presence of so-called electromagnetic smog in the environment and the problems of electromagnetic interference.

Electromagnetic interference (EMI) is an issue which happens with electric or electronic devices when the operation of a device is disturbed, interrupted or degraded by any undesirable, natural or artificial in origin, electromagnetic radiation. Any electronic device can potentially create electromagnetic interference. The increasing number of electronic systems and the use of microwaves in both civil and military fields have resulted in a growth in EMI (Weston, 2001; Zeddami et al., 2009; Kharissova et al., 2015; Koyssuka, 2019; Suarez et al., 2019). This kind of pollution can lead to serious disturbance or damage to electronic equipment. Human health aspects are also of importance (Paniagua et al., 2009). Microwaves can interact with the biosystem causing diverse physiological impacts (Banik et al., 2003; Breckenkamp et al., 2003). One practical approach for EMI shielding relies on the use of microwave absorber. In addition, there has been

the development of stealth technologies for reducing the radar cross-section (RCS). These work by absorption of the electromagnetic radar signal by a coating material applied on the surface of the target (Vinoy and Jha, 1996). This kind of camouflage of military objects is of great interest today when radar technology has reached a high level of excellence.

A range of materials which act as electromagnetic wave absorbers has been developed (Nicolaescu, 2006; Duan and Guan, 2017; Koysuka, 2019). For significant attenuation, the absorber material ought to possess electric and magnetic dipoles which will interact with the electromagnetic field of the radiation (Simms and Fusco, 2005; Landy et al., 2008; Wang et al., 2009). In this way, it attenuates radiated electromagnetic energy and transforms it to heat. Composite coatings filled with magnetic ferrites reduce the radiation caused by the use of electromagnetic sources in the environment and can be used to protect electronic devices against external unwanted electromagnetic fields. Therefore they have been recently investigated in many studies that concentrate on their microwave absorbing properties (Yusoffa and Abdullah, 2004; Dosoudil et al., 2006; Abbas et al., 2007; Bueno et al., 2008; Zhao et al., 2009; Kharissova et al., 2015; Grigoriev et al., 2016; Suarez et al., 2019). The properties of ferrite composite materials obtained by mixing ferrite particles with a resin can also be partially controlled by processing conditions. The conducted investigations have been concerned with particular materials and specific preparation methods.

A ferrite is usually described by the general chemical formula MFe_2O_4 , where M represents a metal in a bivalent state, e.g., Fe^{2+} , Zn^{2+} , Ni^{2+} , Co^{2+} , Mn^{2+} , Cu^{2+} (Miszczyk and Darowicki, 2011). Depending on the type of metal, magnetic (e.g., Fe^{2+} , Ni^{2+} , Co^{2+} , Mn^{2+}) or non-magnetic (e.g., Zn^{2+} , Ca^{2+} , Cu^{2+}) ferrites may be obtained. They show typically high chemical stability, high magnetic loss and high resistivity. In general, studies show that ferrites behave in different coating formulations as active anti-corrosive pigments (Sekine and Kato, 1986; Abu Ayana et al., 1997; Kalendova, 2000; Zubielewicz and Gnot, 2004; Kalendova and Vesely, 2008; Miszczyk and Darowicki, 2011). They passivate the metal substrate, forming an insoluble, protective layer of hydroxides of metals contained in ferrite pigment. This effect is promoted by creating an alkaline environment in cathode areas at the interface between the coating and the substrate. In addition, ferrite pigments can also form inhibitive zinc soaps in certain binders (Kalendova, 2000).

Recently great attention has been paid to nano-sized ferrites (Poddar et al., 2009; Priyadharsinia et al., 2009; Vermaa et al., 2009; Vinas et al., 2015; Kefeni et al., 2017; Sarkar et al., 2018). Also in the field of coating protection, the use of nanoparticles as active pigments in protective coatings seems potentially promising. Nanoparticles have a much larger active surface, so they can be used with a much smaller amount (Shi et al., 2019). They can also be located much closer to the protected area, which can increase their effectiveness. The significant properties of ferrites change as the size of the particles turns into the nanometric magnitude (Awschalom and Vincenzo, 1995; Shi et al., 1996; Chen and Zhang, 1998; Hernando, 1999; Kodama and Berkowitz, 1999; Ehrhardt et al., 2002; Shenoy et al., 2004; Andrade et al., 2009). There are several methods of preparation

of nano-sized ferrite particles including auto-combustion (Sileo et al., 2002), hydrothermal synthesis (Dias et al., 1997), mechano-chemical synthesis (Shi et al., 2000), co-precipitation followed by calcination (Abraham, 1994), sol-gel processes (Pradeep et al., 2008), etc. Among these processes, co-precipitation has been shown to be an easy and promising technique for the preparation of nano-sized ferrite particles.

The anticorrosive properties of some micro- and nano-sized ferrite pigments have been documented (Sekine and Kato, 1986; Abu Ayana et al., 1997; Kalendova, 2000; Zubielewicz and Gnot, 2004; Kalendova and Vesely, 2008; Miszczyk and Darowicki, 2011; Chaudhry et al., 2015, 2017; Grigoriev et al., 2016). Although conventional anticorrosive pigments containing lead or hexavalent chromium (VI) (zinc chromate) cannot be used formally these days due to the environmental and human hazard, there is still a need for effective active anti-corrosive pigments. Non-toxic ferrites may be the answer to this demand. Therefore, they are used as drug carriers in order to target specific sites in the human body (Rana et al., 2007). The concomitant anticorrosive and microwave absorption properties of these pigments offer functionalities not found in traditional coatings and it makes them attractive as an additive to multifunctional protective coatings (Miszczyk and Darowicki, 2011).

In this work, epoxy-NiZn ferrite composites prepared by use of conventional ceramic (micro-sized polycrystalline structure) and the aqueous precipitation (nano-crystalline structure) followed by calcination methods were investigated. The anticorrosive and microwave absorbing properties of epoxy composites containing obtained ferrites were compared experimentally.

MATERIALS AND METHODS

Ferrites with the chemical formula $Ni_xZn_{(1-x)}Fe_2O_4$ ($x = 0, 0.2, 0.4, 0.6, 0.8, 1.0$) were synthesized by using traditional ceramic (Miszczyk and Darowicki, 2011) and aqueous co-precipitation methods.

The ferrite was prepared in micro-sized form by heating thoroughly mixed powders of nitrates $Fe(NO_3)_3 \cdot 9H_2O$, $Zn(NO_3)_2 \cdot 6H_2O$ and $Ni(NO_3)_2 \cdot 6H_2O$ of reagent grade purity (min. 99%) at $1200^\circ C$ at ambient atmosphere for 2 h and later natural cooling after switching off the oven. Ferrite powders were later processed by mechanical grinding of sintered ferrite during ca. 5 h in a ball mill, followed by washing with water and drying at $80^\circ C$ for 24 h (Miszczyk and Darowicki, 2011).

The ferrite in nano-sized form was prepared by the co-precipitation method. The starting materials were the same reagent grade purity nitrates $Fe(NO_3)_3 \cdot 9H_2O$, $Zn(NO_3)_2 \cdot 6H_2O$ and $Ni(NO_3)_2 \cdot 6H_2O$. Desired amounts of $Fe(NO_3)_3 \cdot 9H_2O$, $Zn(NO_3)_2 \cdot 6H_2O$ and $Ni(NO_3)_2 \cdot 6H_2O$ were mixed to yield a clear aqueous solution. The mixed solution was placed in a water bath at $90^\circ C$, and then NaOH solution (6 mol/l) was added dropwise with intensive stirring. During the precipitation, the reaction solution was vigorously stirred with a magnetic stirrer. After reaction completion, the precipitates were kept stirred in the reaction solution for 2 h at a temperature of

90°C. The co-precipitated powders were filtered and washed with deionized water many times, followed by washing with ethyl alcohol and filtering. The washed powders were dried at 80°C during 24 h. Density and oil number were determined in order to obtain the proper formulation of the composite. For comparison, Fe₂O₃ nanoparticles were also synthesized via a co-precipitation method using iron chloride hexahydrate (FeCl₃ 6H₂O) as a precursor.

The precipitates were calcined at 300, 400, 500, and 600°C for 2 h and ground in a ball-mill for 5 h. After analysis of the XRD pattern, only the powder calcined at 600°C was afterwards tested. XRD analysis was performed on a Philips X'Pert diffractometer with Cu K α radiation in the 2 θ range from 10° to 80° by steps of 0.02°. The identification of compounds was conducted using the ICDD database.

Composite materials have been prepared by mixing ferrite particles with an epoxy resin (Epidian-5, from Sarzyna-Organika Chemical Company in Nowa Sarzyna, Poland, clear epoxy resin with molecular mass ≤ 700 u, diglicidyl ether of bisphenol A) using stirrer during 1 h (800 turns per min). After that, a proper amount of hardener (Z1 from Sarzyna-Organika Chemical Company in Nowa Sarzyna, Poland, triethylenetetramine) was added. Composites containing 10%vol of ferrites were prepared on a low carbon steel substrate (Q-panel). The thickness of all coatings was 2 mm, which was arbitrarily chosen.

In order to measure microwave absorption properties of the prepared coatings, the reflection coefficients were determined by using Site Master™ (Anritsu) S820D and WR90 waveguide connected by APC-7 mm coaxial line. Measurements were made in the 6.5–15 GHz range by collecting 256 frequency points using the reflection method (Chen et al., 2004). Before the experiments, the set-up was calibrated using three standards, which are required to eliminate the directivity, reflection tracking and source match errors. 1/8, 3/8 offset shorts and termination were used.

In order to assess the properties of nano-ferrites as corrosion inhibitors, electrochemical tests of carbon steel in 10% aqueous extracts from nano-pigments, obtained after 2 weeks, were performed. The electrochemical cell consisted of the carbon steel (S235JR) sample with an area of 1 cm², as a working electrode, saturated calomel electrode (SCE) as a reference electrode, and a platinum mesh as a counter electrode. Electrochemical measurements were made using ModuLab XM ECS (Solartron Analytical–Ametek SI, USA). Polarization tests were carried out with the scan rate of 10 mV/s and potential range of –150 mV to +600 mV with respect to open circuit potential (OCP).

AFM studies were conducted by means of an AFM device Ntegra Prima (NT-MDT, Russian Federation) supplemented with a magnetic tip. In this case, the magnetic forces, acting on a magnetized tip by the sample, are measured and local magnetic properties of the surface in the form of a map were registered.

RESULTS AND DISCUSSION

Characterization of the obtained ferrite samples was carried out by X-ray diffraction (XRD) analysis of powders. **Figure 1** shows

as an example the XRD patterns of the as-precipitated powder of nickel ferrite and after being calcined at 300, 400, 500, and 600°C. The as-precipitate and calcined at 300 and 400°C powders were amorphous. They show broad and unresolved peaks. The XRD patterns of powders calcined at 500 and 600°C show a clear pattern, which corresponds to the known structure of a spinel-type lattice of ferrite. All of the peaks indicated that the obtained ferrite is NiFe₂O₄. Their position agrees with the standard pattern presented in **Figure 1** based on the International Center for Diffraction Data (ICDD)–Powder Diffraction File (data set 44-1485). Apart from the most intense peak located at the diffraction angle of 2 θ = 35.691°, corresponding to the (311) reflection plane, other peaks are located at 2 θ = 30.301°, 37.331°, 43.381°, 53.831°, 57.381°, 62.021° and 74.581°.

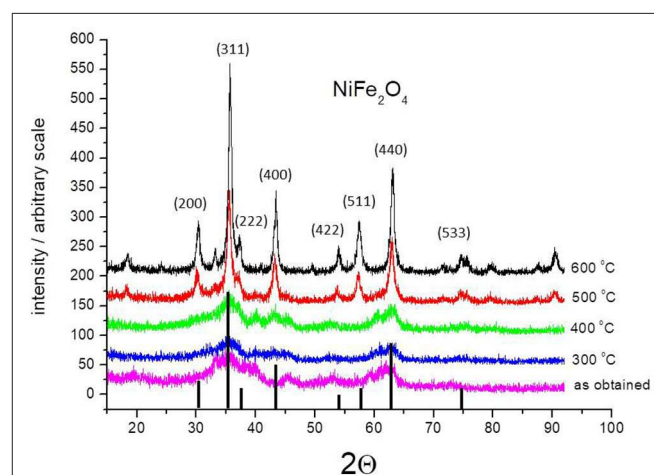


FIGURE 1 | XRD pattern of the as-prepared NiFe₂O₄ nanoparticles as obtained and annealed at different temperatures. The figure includes the standard XRD pattern for nickel ferrite (ICDD file No. 44-1485).

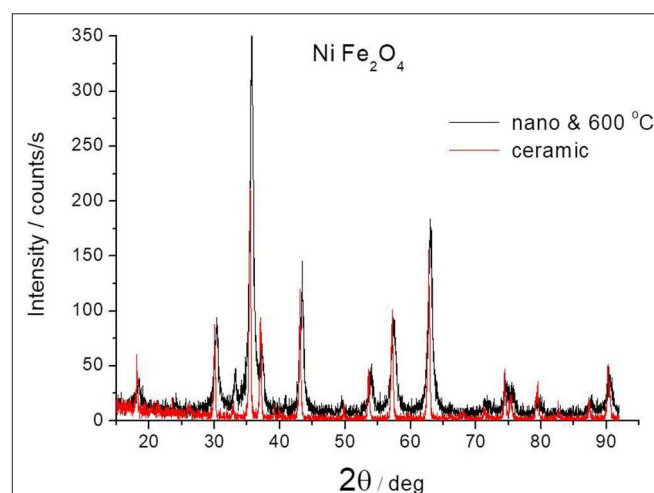


FIGURE 2 | Comparison of XRD pattern of NiFe₂O₄ ferrites obtained by ceramic method at 1200°C or by co-precipitation method and after annealing at 600°C.

Figure 2 shows a comparison of the XRD pattern of the ceramic ferrite (calcined at 1200°C) with the same one obtained by co-precipitation method and calcined at 600°C. There are no essential differences between them in relation to the position of the peaks. There are differences in peak widths that result from the size of the crystallites. Ceramic ferrites are sharper due to larger crystallite sizes. This indicates that particles with significantly smaller crystallite sizes were obtained using the co-deposition method. The results for ferrite with nano-crystalline structure presented below refer to powder obtained by the co-precipitation method and followed by calcination at 600°C.

Figure 3 shows XRD patterns for all nano-crystalline ferrites obtained by the co-precipitation method and followed by calcination at 600°C. It also includes a standard nickel ferrite pattern based on ICDD data for comparison. All samples exhibit a single phase with a spinel structure. The average grain size (D) of ferrites was calculated from the diffraction

peak of the (311) plane using the Debye-Scherrer formula (Armstrong and Karceff, 1999):

$$D = 0.9\lambda / (\beta \cos\theta) \quad (1)$$

where λ is the X-ray wavelength, β is the half-maximum breadth and θ is the Bragg angle of the (311) plane. According to the obtained data and formula (1), the average particle size of the nano-crystalline NiZn ferrites is found to be ca. 20 nm. The individual particles of the poly-crystalline ferrites were typically 120–180 nm in diameter.

In order to verify the size of particles obtained by co-deposition, AFM measurements of the composite cross-section containing these particles were performed. Utilizing the magnetic properties of ferrite particles, a magnetic tip was also used. **Figure 4** shows the obtained diagrams. The classic AFM technique does not allow for clear observation of nanoparticles embedded in the epoxy binder. The application of the tip covered with a magnetic layer causes that the phase of the tip oscillations changes when it interacts with the magnetic area. This causes a phase shift recorded in the image (the unit on the vertical axis in **Figure 4B** is degree). **Figure 4** demonstrates (light areas in **Figure 4A** and dark areas in **Figure 4B**) that the particle sizes do not exceed several hundred nm and that they are most likely the result of the agglomeration of individual crystallites. This phenomenon is typical for such particles if no special surface treatment has been performed (Kefeni et al., 2017).

The microwave absorption property was presented using microwave loss efficiency. **Figures 5–10** show the reflection loss of composites containing the investigated ferrites. Each figure compares composites filled by poly-crystalline (ceramic) and nano-crystalline ferrites. The reflection loss (R_L) is given by the difference between the incident and reflected signal level expressed in logarithmic scale according to the equation (Chen et al., 2004):

$$R_L(\text{dB}) = 10\log(P_r/P_o) \quad (2)$$

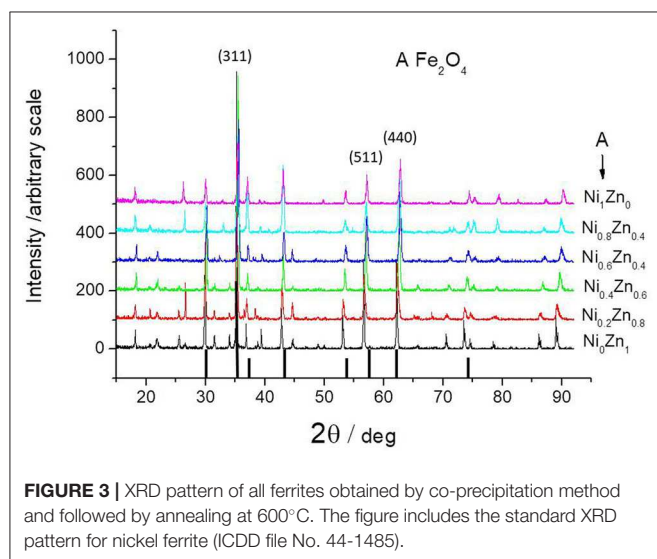


FIGURE 3 | XRD pattern of all ferrites obtained by co-precipitation method and followed by annealing at 600°C. The figure includes the standard XRD pattern for nickel ferrite (ICDD file No. 44-1485).

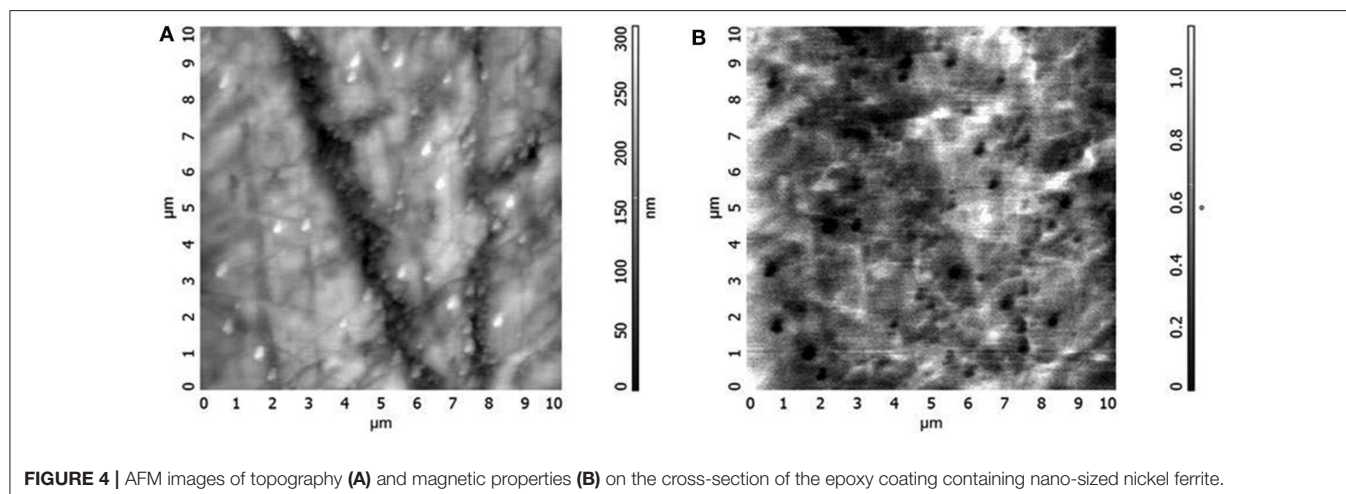
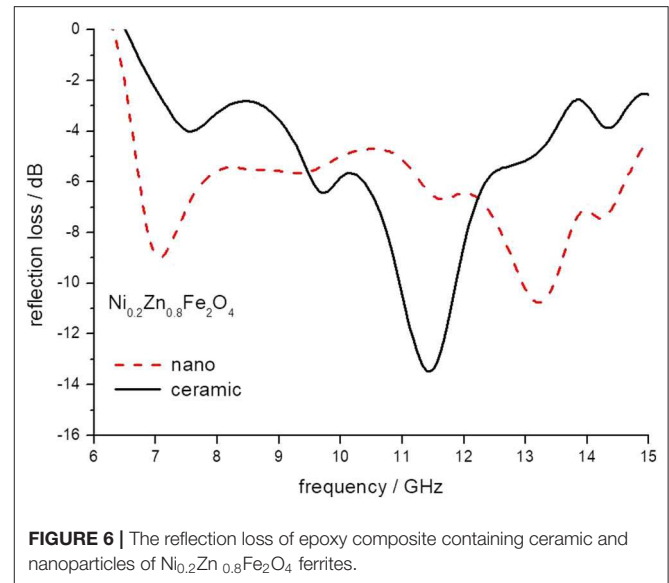
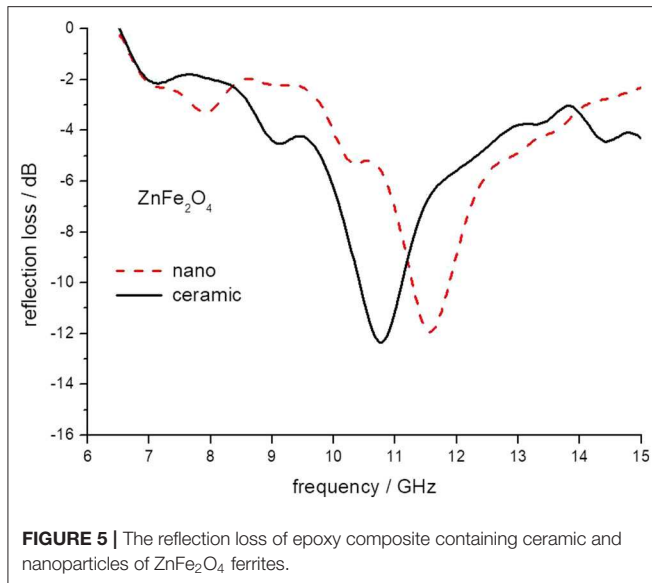


FIGURE 4 | AFM images of topography (A) and magnetic properties (B) on the cross-section of the epoxy coating containing nano-sized nickel ferrite.



where: P_r —the power of the reflected wave,
 P_o —the power of the incident wave.
 Based on transmission line theory, the reflection loss (R_L) for a single layer absorbing material backed by a conductor is given by

$$R_L = 20\log|(Z_{in} - Z_0)/(Z_{in} + Z_0)| \quad (3)$$

where: $Z_0 = \sqrt{\frac{\mu_0}{\epsilon_0}}$ is the impedance of free space and the input impedance (Z_{in}) at the air-material interface is given by

$$Z_{in} = Z_0 \sqrt{\frac{\mu_0}{\epsilon_0}} \tanh[j(2\pi fd/c) \sqrt{\frac{\mu_r}{\epsilon_r}}] \quad (4)$$

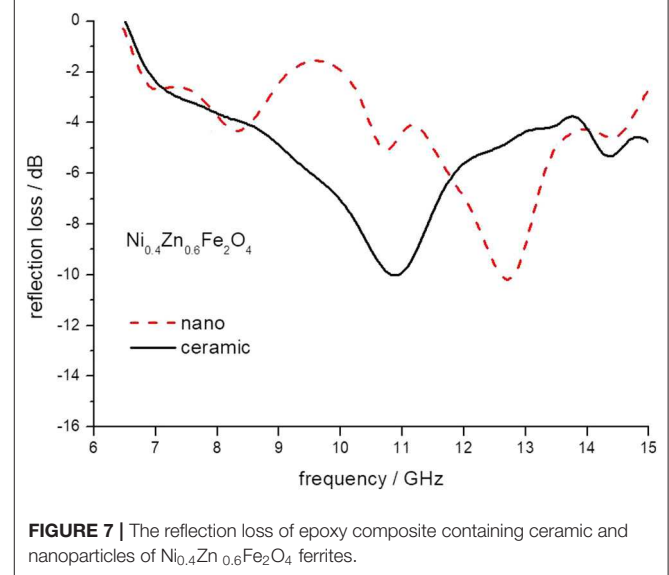
where ϵ_0 is the dielectric constant of free space, $\epsilon_r = \epsilon' - j\epsilon''$ is the complex permittivity, μ_0 is the permeability of free space, $\mu_r = \mu' - j\mu''$ is the complex permeability, f is the frequency of the incident wave, c is the velocity of light in free space and d is the thickness of absorber. The imaginary unit is denoted by j .

There are two conditions to achieve low R_L values:

- the incident wave should transmit from the air (free space) into the materials with minimum reflection,
- a material should attenuate the absorbed wave.

In order to implement the first condition, impedance matching between the material surface and free space is required. The second condition requires that the energy of electromagnetic waves inside material transform into other forms of energy, e.g., heat. In this case, specific high magnetic and electrical loss properties of the material are required. Electromagnetic waves supply energy to material by means of electric and magnetic fields. These fields can exert forces and carry charges and magnet moments in the material.

Electromagnetic wave energy can be absorbed and dissipated to heat through magnetic and dielectric losses (Equations 3,



4). This can be quantified by reflection loss (Equation 2). The minimum value of the reflection loss shows the frequency of the wave, which has the highest attenuation. It means maximum absorption of the microwave power for a particular sample thickness.

The minimum of reflection loss for each ferrite composite is presented in **Figure 11** as a function of the content of nickel in ferrite. It seems that both micro- and nano-sized ferrites containing the composite exhibit much the same values of attenuation, except nickel ferrite. However, there is a clear shift in the frequency of maximum attenuation, **Figure 12**. Composites containing nano-ferrites exhibit a higher frequency of maximum attenuation. Probably, it is related to the domains' wall mobility at a lower frequency. The resonance frequency f is

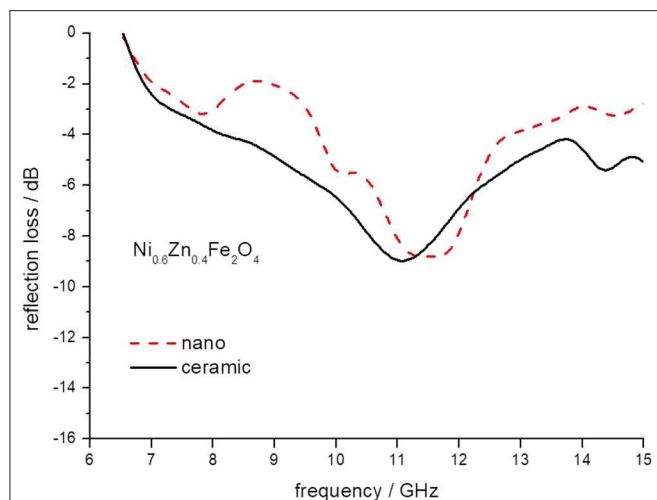


FIGURE 8 | The reflection loss of epoxy composite containing ceramic and nanoparticles of $\text{Ni}_{0.6}\text{Zn}_{0.4}\text{Fe}_2\text{O}_4$ ferrites.

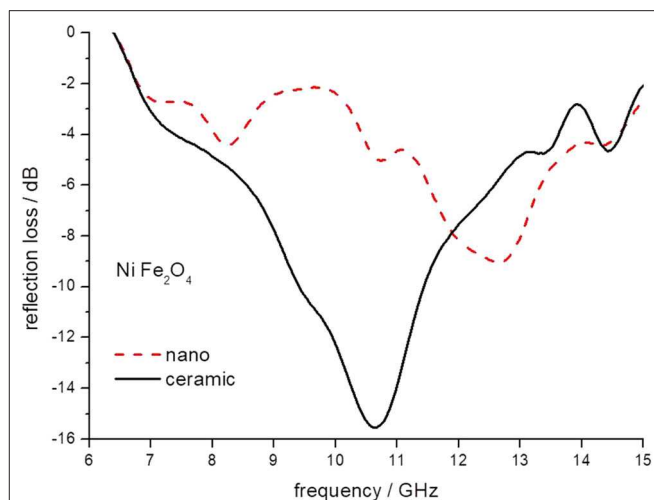


FIGURE 10 | The reflection loss of epoxy composite containing ceramic and nanoparticles of NiFe_2O_4 ferrites.

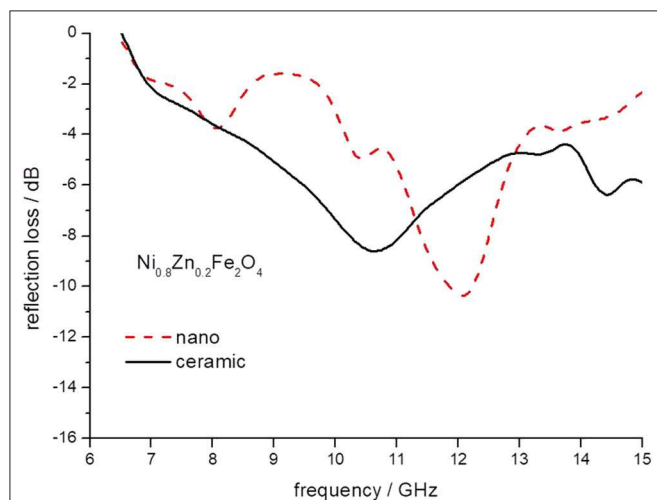


FIGURE 9 | The reflection loss of epoxy composite containing ceramic and nanoparticles of $\text{Ni}_{0.8}\text{Zn}_{0.2}\text{Fe}_2\text{O}_4$ ferrites.

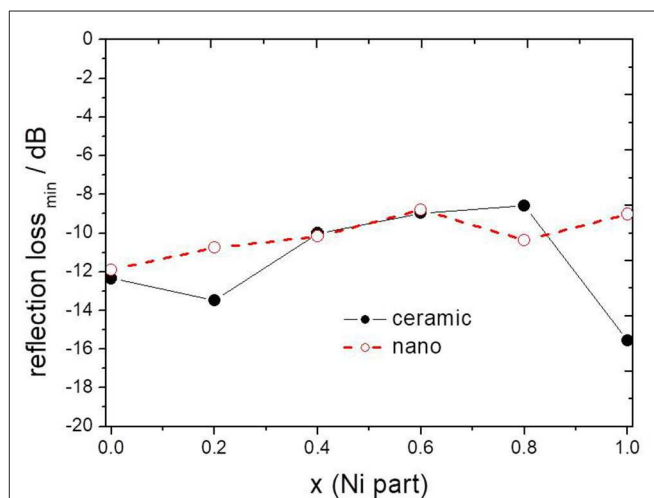


FIGURE 11 | The maximum value of attenuation depending on x (Ni content) in composite containing ceramic and nanoparticles of $\text{Ni}_x\text{Zn}_{(1-x)}\text{Fe}_2\text{O}_4$.

proportional to the anisotropy field H_a according to the equation (Chikazumi, 1997):

$$f = (\gamma/2\pi)H_a \quad (5)$$

where: γ is gyromagnetic ratio,

H_a is crystal anisotropy field.

These results suggest an increase in the crystal anisotropy field in nano-sized ferrites as compared to micro-sized ferrites. It seems that there is certain intrinsic randomness with regard to size and orientation of the nanostructures and this depends on the preparation technique used and can be specific for a particular method of preparation.

Until now, the anticorrosive properties of ferrites obtained by the ceramic method have been studied (Kalendova, 2000; Zubielewicz and Gnot, 2004; Kalendova and Vesely, 2008; Deya et al., 2010; Miszczyk and Darowicki, 2011; Hao et al., 2012; Kalendova et al., 2014; Benda and Kalendova, 2017; Chaudhry et al., 2017). In this work, a test of nano-sized ferrites was made and the obtained results were compared with the results for the same ferrites but obtained by the ceramic method, previously published (Miszczyk and Darowicki, 2011).

In order to assess the properties of nano-ferrites as corrosion inhibitors, electrochemical tests of carbon steel in 10% aqueous extracts from nano-pigments, obtained after 2 weeks, were performed.

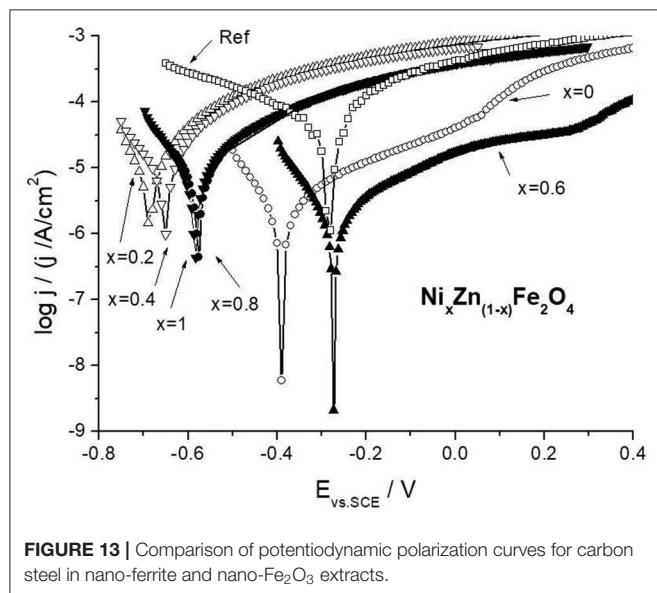
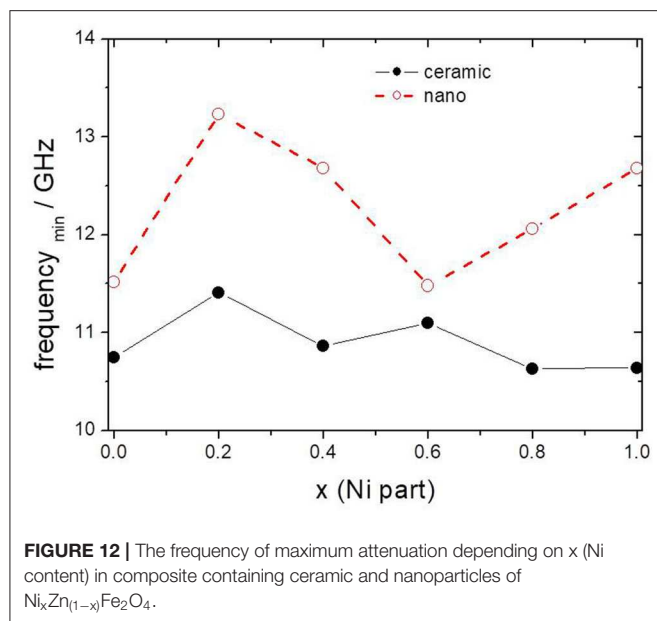
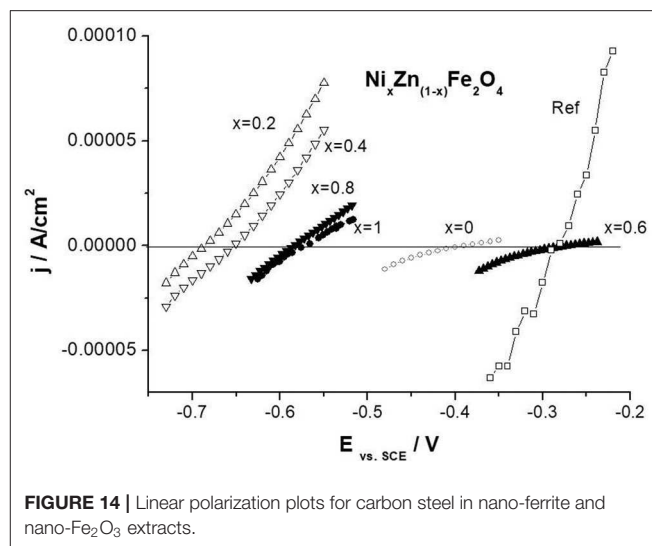


Figure 13 shows the polarization curves for the carbon steel samples immersed in the ferrite extracts after 1 h of sample immersion. There are significant differences in the electrochemical behavior of steel samples in various extracts. This indicates the activity of the studied nano-pigments in relation to the steel surface. As can be seen from the figure, the obtained polarization curves differ both in the corrosion potential and in the exchange current density from which the steel corrosion rate depends directly. The corrosion potential becomes more negative compared to the reference extract, which indicates the effect of pigments on the cathodic reaction. Also, the other slope of the cathodic portion for ferrite extracts as compared to the reference extract confirms this assumption. We observe much lower values of exchange current density, demonstrating the inhibitory effect of pigments.



Electrochemical studies were also performed using the linear polarization method, **Figure 14**. The polarization resistance was calculated from the slope of the potential vs. current density plots around the corrosion potential (using a linear portion of experimental polarization curve containing both the anodic and cathodic branches).

As a result of a carried out electrochemical measurements polarization resistances, corrosion potential and the corrosion current density for carbon steel in Fe_2O_3 and ferrite extracts were collected. **Table 1** shows the results obtained. The analogous polarization resistances determined for ceramic ferrites (of micro-size) have also been presented (Miszczyk and Darowicki, 2011). In general, all ferrites with the exception of zinc ferrite show a higher polarization resistance for the nano form. This demonstrates the potentially beneficial effect of ferrites in the form of nano-size for use in protective coatings.

CONCLUSIONS

Nano-sized NiZn ferrites described by the formula $\text{Ni}_x\text{Zn}_{(1-x)}\text{Fe}_2\text{O}_4$, where $x = 0, 0.2, 0.4, 0.6, 0.8, 1.0$, were prepared by means of a co-precipitation method. The electrochemical behavior of carbon steel in 10% aqueous ferrite extracts was tested and compared with previous results obtained for micro-sized ceramic ferrite. The carried out tests indicate more favorable inhibiting properties of ferrites in the form of nanoparticles. An epoxy coating containing 10% vol. of obtained ferrites as a coating capable of attenuating electromagnetic radiation in the microwave range was tested. The results of coating microwave reflectivity over a range of frequencies from 6.5 to 15 GHz were presented.

The conclusions are as follows:

1. Based on selected electrochemical tests, better anti-corrosion inhibition properties of pigments in the form of nano were found.

TABLE 1 | The polarization resistance (in Ωcm^2), corrosion potential (in V vs. SCE) and the corrosion current density (in $\mu\text{A}/\text{cm}^2$) of carbon steel electrode determined in Fe_2O_3 and nano-sized ferrite extracts.

Pigment	Fe_2O_3	$\text{Ni}_x\text{Zn}_{(1-x)}\text{Fe}_2\text{O}_4$					
		$x = 0$	$x = 0.2$	$x = 0.4$	$x = 0.6$	$x = 0.8$	$x = 1$
Nano-sized	940	14,080	2,650	2,500	16,190	3,160	1,710
	−0.282	−0.392	−0.690	−0.655	−0.374	−0.578	−0.583
	35.5	1.15	3.90	3.22	0.84	2.34	2.21
Micro-sized*	851	924	1,343	1,482	1,752	1,609	2,893

*Data comes from Miszczyk and Darowicki (2011).

For comparison, the polarization resistance for the micro-sized pigments is given in the last line.

- Both nano- and micro-sized ferrites of the same composition embedded in epoxy matrix exhibit much the same reflection loss. For 2 mm thick coatings maximum attenuation on level of 8–16 dB was observed.
- Nano-ferrite filled epoxy coatings exhibit higher minimum reflection frequency in comparison with ceramic-filled coatings with the same composition. A frequency shift of 1–2 GHz was observed.
- Nano-ferrites obtained by co-precipitation method needed significantly lower calcining temperature, ca. 600°C in comparison with micro-sized ferrites obtained by traditional ceramic solid-state reaction, which demand a temperature of 1200°C.
- The use of AFM technique equipped with a magnetic tip enables effective observation of the presence of magnetic nano-sized particles of ferrites used as pigments in an epoxy coating.

The tested NiZn ferrites are suitable as microwave shielding and absorbing materials for potential application in the reduction of EMI. In combination with anti-corrosion properties, they might be a reasonable and cost-effective addition to modern multifunctional coatings providing additional benefits, including reduction or elimination of EMI problems.

DATA AVAILABILITY STATEMENT

The datasets generated for this study cannot be shared at this time as the data also forms part of an ongoing study.

AUTHOR CONTRIBUTIONS

AM have made a substantial, direct and intellectual contribution to this work, starting with the idea, carrying out research, working out the results, and formulating the manuscript.

REFERENCES

- Abbas, S. M., Dixit, A. K., Chatterjee, R., and Goel, T. C. (2007). Complex permittivity, complex permeability and microwave absorption properties of ferrite-polymer composite. *J. Magn. Magn. Mat.* 309, 20–24. doi: 10.1016/j.jmmm.2006.06.006
- Abraham, T. (1994). Economics of ceramic magnet. *Am. Ceram. Soc. Bull.* 73, 62–73.
- Abu Ayana, Y. M., El-Sawy, S. M., and Salah, S. H. (1997). Zinc-ferrite pigment for corrosion protection. *Anti-Corros. Method. M.* 44, 381–388. doi: 10.1108/00035599710367681
- Andrade, A. L., Souza, D. M., Pereira, M. C., Fabris, J. D., and Domingues, R. Z. (2009). Magnetic properties of nanoparticles obtained by different chemical routes. *J. Nanosci. Nanotechnol.* 9, 2081–2087. doi: 10.1166/jnn.2009.423
- Armstrong, N., and Karceff, W. (1999). A maximum entropy method for determining column-length distributions from size-broadened X-ray diffraction profiles. *J. Appl. Cryst.* 32, 600–613. doi: 10.1107/S0021889899000692
- Awschalom, D. D., and Vincenzo, D. P. D. (1995). Complex dynamics of mesoscopic magnets. *Phys. Today* 48, 43–49. doi: 10.1063/1.881448
- Banik, S., Bandyopadhyay, S., and Ganguly, S. (2003). Bioeffects of microwave—a brief review. *Bioresour. Technol.* 87, 155–159. doi: 10.1016/S0960-8524(02)00169-4
- Benda, P., and Kalendova, A. (2017). Development and preparation of oxide mixture-based pigments for anticorrosion paints. *Pigm. Resin Technol.* 46, 342–355. doi: 10.1108/PRT-01-2016-0012
- Breckenkamp, J., Berg, G., and Blettner, M. (2003). Biological effects on human health due to radiofrequency/microwave exposure: a synopsis of cohort studies. *Radiat. Environ. Biophys.* 42, 141–154. doi: 10.1007/s00411-003-0203-x
- Bueno, A. R., Gregorib, M. L., and Nobrega, M. C. S. (2008). Microwave-absorbing properties of $\text{Ni}_{0.50}\text{-xZn}_{0.50}\text{-xMe}_2\text{xFe}_2\text{O}_4$ (Me=Cu, Mn, Mg) ferrite-wax composite in X-band frequencies. *J. Magn. Magn. Mat.* 320, 864–870. doi: 10.1016/j.jmmm.2007.09.020
- Chaudhry, A. U., Mittal, V., Hashmi, M. I., and Mishra, B. (2017). Evaluation of $\text{Ni}_{0.5}\text{Zn}_{0.5}\text{Fe}_2\text{O}_4$ nanoparticles as anti-corrosion pigment in organic coatings for carbon steel. *Anti-Corros. Method. M.* 64, 644–653. doi: 10.1108/ACMM-10-2016-1725
- Chaudhry, A. U., Mittal, V., and Mishra, B. (2015). Nano nickel ferrite (NiFe_2O_4) as anti-corrosion pigment for API 5L X-80 steel: an electrochemical study in acidic and saline media. *Dyes Pigm.* 118, 18–26. doi: 10.1016/j.dyepig.2015.02.023
- Chen, L. F., Ong, C. K., Neo, C. P., and Varadan, V. V., Varadan, V. K. (2004). *Microwave Electronics - Measurement and Materials Characterization*. Chichester, UK: John Wiley & Sons. doi: 10.1002/0470020466
- Chen, Q., and Zhang, Z. J. (1998). Size-dependent superparamagnetic properties of MgFe_2O_4 spinel ferrite nanocrystallites. *Appl. Phys. Lett.* 73, 3156–3158. doi: 10.1063/1.122704
- Chikazumi, S. (1997). *Physics of Ferromagnetism*. Oxford: Clarendon Press.
- Deya, C., Blustein, G., del Amo, B., Romagnoli, R. (2010). Evaluation of eco-friendly anticorrosive pigments for paints in service conditions. *Prog. Org. Coat.* 69, 1–6. doi: 10.1016/j.porgcoat.2010.03.011
- Dias, A., Moreira, R. L., and Mohallem, N. D. S. (1997). Sintering studies of hydrothermal NiZn ferrites. *J. Phys. Chem. Solids* 58, 543–549. doi: 10.1016/S0022-3697(96)00162-X

- Dosoudil, R., Usakova, M., Franek, J., Slama, J., and Olah, V. (2006). High-frequency EMI noise suppression by polymer-based composite magnetic materials. *J. Magn. Magn. Mat.* 304, 755–757. doi: 10.1016/j.jmmm.2006.02.216
- Duan, Y., and Guan, H. (2017). *Microwave Absorbing Materials*. Singapore: Pan Stanford Publishing. doi: 10.1201/9781315364704
- Ehrhardt, H., Campbell, S. J., and Hofmann, M. (2002). Structural evolution of ball-milled ZnFe₂O₄. *J. Alloys Compd.* 339, 255–260. doi: 10.1016/S0925-8388(01)02011-4
- Grigoriev, D. O., Vakhtov, T., and Stepin, S. N. (2016). “Ferrites as Non-Toxic Pigments for Eco-Friendly Corrosion Protection Coatings, chap. 3,” in: *Biobased and Environmental Benign Coatings* (Salem, MA: Scrivener Publishing; Hoboken, NJ: John Wiley & Sons). doi: 10.1002/9781119185055.ch3
- Hao, Y., Liu, F., and Han, E. (2012). Inhibitive behavior and mechanism of a ferrite inhibition pigment in epoxy paints. *J. Electrochem. Soc.* 159, C403–C410. doi: 10.1149/2.049209jes
- Hernando, A. (1999). Magnetic properties and spin disorder in nanocrystalline materials. *J. Phys.: Condens. Matter* 11, 9455–9482. doi: 10.1088/0953-8984/11/48/308
- Kalendova, A. (2000). Alkalising and neutralising effects of anticorrosive pigments containing Zn, Mg, Ca, and Sr cations. *Prog. Org. Coat.* 38, 199–206. doi: 10.1016/S0300-9440(00)00103-X
- Kalendova, A., and Vesely, D. (2008). The properties of ZnFe₂O₄ as an anticorrosion pigment dependent upon the structure of initial Fe₂O₃. *Anti-Corros. Method. M.* 55, 175–190. doi: 10.1108/00035590810887673
- Kalendova, A., Vesely, D., and Kohl, M. (2014). Synthesis of Me₂TiO₄ and MeFe₂O₄ spinels and their use in organic alkyd resin-based anticorrosion coatings. *Corros. Rev.* 32, 51–72. doi: 10.1515/correv-2013-0050
- Kefeni, K. K., Msagati, T. A. M., and Mamba, B. B. (2017). Ferrite nanoparticles: Synthesis, characterisation and applications in electronic device. *Mater. Sci. Eng. B* 215, 37–55. doi: 10.1016/j.mseb.2016.11.002
- Kharissova, O. V., Dias, H. V. R., and Kharisov, B. I. (2015). Magnetic adsorbents based on micro- and nano-structured materials. *RSC Adv.* 5, 6695–6719. doi: 10.1039/C4RA11423J
- Kodama, R. H., and Berkowitz, A. E. (1999). Atomic-scale magnetic modelling of oxide nanoparticles. *Phys. Rev. B* 59, 6321–6336. doi: 10.1103/PhysRevB.59.6321
- Koysuka, Y. (2019). *Electromagnetic Wave Absorbers: Detailed Theories and Applications*. Hoboken, NJ: John Wiley & Sons. doi: 10.1002/9781119564430
- Landy, N. I., Sajuyigbe, S., Mock, J. J., Smith, D. R., and Padilla, W. J. (2008). Perfect metamaterial absorber. *Phys. Rev. Lett.* 100:207402. doi: 10.1103/PhysRevLett.100.207402
- Miszczyk, A., and Darowicki, K. (2011). Study of anticorrosion and microwave absorption properties of NiZn ferrite pigments. *Anti-Corros. Method. M.* 58, 13–22. doi: 10.1108/0003559111097657
- Nicolaescu, I. (2006). Radar absorbing materials used for target camouflage. *J. Optoelectron. Adv. M.* 8, 333–338. Available online at: https://old.joam.inoe.ro/arhiva/pdf8_1/Nicolaescu.pdf (accessed June 8, 2020).
- Paniagua, J. M., Rufo, M., Jimenez, A., Antolin, A., and Sanchez, M. (2009). Electrical stimulation vs thermal effects in a complex electromagnetic environment. *Sci. Total Environ.* 407, 4717–4722. doi: 10.1016/j.scitotenv.2009.04.034
- Poddar, A., Bhowmik, R. N., De, A., and Sen, P. (2009). Magnetic response of NiFe₂O₄ nanoparticles in polymer matrix. *J. Magn. Magn. Mat.* 321, 2015–2020. doi: 10.1016/j.jmmm.2009.01.010
- Pradeep, A., Priyadarsini, P., and Chandrasekaran, G. (2008). Sol-gel route of synthesis of nanoparticles of MgFe₂O₄ and XRD, FTIR and VSM study. *J. Magn. Magn. Mater.* 320, 2774–2779. doi: 10.1016/j.jmmm.2008.06.012
- Priyadarsinia, P., Pradeepa, A., Sambasiva Raob, P., and Chandrasekaran, G. (2009). Structural, spectroscopic and magnetic study of nanocrystalline Ni-Zn ferrites. *Mater. Chem. Phys.* 116, 207–213. doi: 10.1016/j.matchemphys.2009.03.011
- Rana, S., Gallo, A., Srivastava, R. S., and Misra, R. D. K. (2007). On the suitability of nanocrystalline ferrites as a magnetic carrier for drug delivery: functionalization, conjugation and drug release kinetics. *Acta Biomaterialia* 3, 233–242. doi: 10.1016/j.actbio.2006.10.006
- Sarkar, N. N., Rewatkar, K. G., Nanoti, V. M., and Tayade, N. T. (2018). “Soft ferrite: a brief review on structural, magnetic behavior of nanosized spinel ferrites, Chap. 9,” in: *Magnetic Oxides and Composites* (Materials Research Forum).
- Sekine, I., and Kato, T. (1986). Corrosion-protective properties of various ferrite paint films. *Ind. Eng. Chem. Product Res.* 25, 7–10. doi: 10.1021/i300021a002
- Shenoy, S. D., Joy, P. A., and Anantharaman, M. R. (2004). Effect of mechanical milling on the structural, magnetic and dielectric properties of coprecipitated ultrafine zinc ferrite. *J. Magn. Magn. Mater.* 269, 217–226. doi: 10.1016/S0304-8853(03)00596-1
- Shi, C. H., Shao, Y., Wang, Y., Liu, B., and Meng, G. (2019). Evolutions of the protection performances of epoxy coatings containing different concentrations of submicron-sheet zinc phosphate pigment. *Colloids Surf. A* 577, 378–395. doi: 10.1016/j.colsurfa.2019.05.084
- Shi, J., Gider, S., Babcock, K., and Awschalom, D. D. (1996). Magnetic clusters in molecular beams, metals, and semiconductors magnetic clusters in molecular beams, metals, and semiconductors. *Science* 271, 937–941. doi: 10.1126/science.271.5251.937
- Shi, Y., Ding, J., and Yin, H. (2000). CoFe₂O₄ nanoparticles prepared by the mechanochemical method. *J. Alloys Compd.* 308, 290–295. doi: 10.1016/S0925-8388(00)00921-X
- Sileo, E. E., Rotelo, R., and Jacobo, S. E. (2002). The effect of rare earth substitution on the magnetic properties of Ni_{0.5}Zn_{0.5}M_xFe_{2-x}O₄ (M: rare earth). *Physica B* 320, 261–263. doi: 10.1016/S0921-4526(02)00706-8
- Simms, S., and Fusco, V. (2005). Thin radar absorber using an artificial magnetic ground plane. *Electron. Lett.* 41, 1311–1313. doi: 10.1049/el:20053236
- Suarez, A., Victoria, J., Torres, J., Martinez, P. A., Alcarria, A., Martos, J., et al. (2019). Effectiveness assessment of a nanocrystalline sleeve ferrite core compared with ceramic cores for reducing conducted EMI. *Electronics (MDPI)* 8:800. doi: 10.3390/electronics8070800
- Verma, V., Pandeya, V., Singha, S., Aloysiusa, R. P., Annapoornib, S., and Kotanala, R. K. (2009). Comparative study of structural and magnetic properties of nano-crystalline Li_{0.5}Fe_{2.5}O₄ prepared by various methods. *Physica B* 404, 2309–2314. doi: 10.1016/j.physb.2009.04.034
- Vinas, S. L., Simeonidis, K., Li, Z. A., Ma, Z., Myrovali, E., Makridis, A., et al. (2015). Tuning the magnetism of ferrite nanoparticles. *J. Magn. Magn. Mat.* 415, 20–23. doi: 10.1016/j.jmmm.2016.02.098
- Vinoy, K. J., and Jha, R. M. (1996). *Radar Absorbing Materials: From Theory to Design and Characterization*. Boston: Kluwer Academic Publishers.
- Wang, B., Koschny, T., and Soukoulis, C. M. (2009). Wide-angle and polarization-independent chiral metamaterial absorber. *Phys. Rev. B* 80, 033108. doi: 10.1103/PhysRevB.80.033108
- Weston, D. A. (2001). *Electromagnetic Compatibility, Principles and Applications*. 2nd ed. Basel; New York, NY: Marcel Dekker.
- Yusoff, A. N., and Abdullah, M. H. (2004). Microwave electromagnetic and absorption properties of some LiZn ferrites. *J. Magn. Magn. Mat.* 269, 271–280. doi: 10.1016/S0304-8853(03)00617-6
- Zeddami, A., Gautier, A., and Tlich, M. (2009). Electromagnetic environment and telecommunications: towards a cognitive electromagnetic compatibility. *C.R. Physique* 10, 4–12. doi: 10.1016/j.crhy.2009.02.001
- Zhao, D. L., Zeng, Q. L., and Shen, M. (2009). Fabrication and microwave absorbing properties of Ni-Zn spinel ferrites. *J. Alloys Compd.* 480, 634–638. doi: 10.1016/j.jallcom.2009.01.130
- Zubielewicz, M., and Gnot, W. (2004). Mechanisms of non-toxic anticorrosive pigments in organic waterborne coatings. *Prog. Org. Coat.* 49, 358–371. doi: 10.1016/j.porgcoat.2003.11.001

Conflict of Interest: The author declares that the research was conducted in the absence of any commercial or financial relationships that could be construed as a potential conflict of interest.

Copyright © 2020 Miszczyk. This is an open-access article distributed under the terms of the Creative Commons Attribution License (CC BY). The use, distribution or reproduction in other forums is permitted, provided the original author(s) and the copyright owner(s) are credited and that the original publication in this journal is cited, in accordance with accepted academic practice. No use, distribution or reproduction is permitted which does not comply with these terms.

Advantages of publishing in Frontiers



OPEN ACCESS

Articles are free to read
for greatest visibility
and readership



FAST PUBLICATION

Around 90 days
from submission
to decision



HIGH QUALITY PEER-REVIEW

Rigorous, collaborative,
and constructive
peer-review



TRANSPARENT PEER-REVIEW

Editors and reviewers
acknowledged by name
on published articles

Frontiers

Avenue du Tribunal-Fédéral 34
1005 Lausanne | Switzerland

Visit us: www.frontiersin.org

Contact us: info@frontiersin.org | +41 21 510 17 00



REPRODUCIBILITY OF RESEARCH

Support open data
and methods to enhance
research reproducibility



DIGITAL PUBLISHING

Articles designed
for optimal readership
across devices



FOLLOW US

@frontiersin



IMPACT METRICS

Advanced article metrics
track visibility across
digital media



EXTENSIVE PROMOTION

Marketing
and promotion
of impactful research



LOOP RESEARCH NETWORK

Our network
increases your
article's readership